University of Southampton

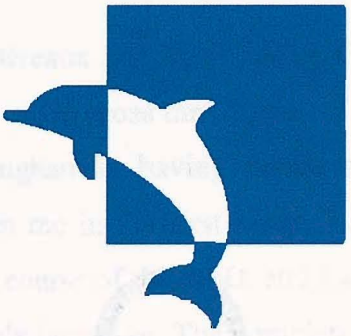

PENETRANT DIFFUSION IN POLYETHYLENE: THE IMPACT OF WATER ON THE PERFORMANCE OF NOVEL XLPE CABLE DESIGNS.

By

Laurent Luc BARRÉ.

A thesis submitted for the degree of

Doctor of Philosophy,

A study funded by the National Grid Transco.

National Grid Transco

Southampton, 07/2004.

Faculty of engineering and applied science.

DECLARATION OF AUTHORSHIP

I, Laurent Luc BARRÉ

declare that the thesis entitled:

PENETRANT DIFFUSION IN POLYETHYLENE: THE IMPACT OF WATER ON THE PERFORMANCE OF NOVEL XLPE CABLE DESIGNS.

and the work presented in it are my own. I confirm that:

- this work was done wholly or mainly while in candidature for a research degree at this University;
- where any part of this thesis has previously been submitted for a degree or any other qualification at this University or any other institution, this has been clearly stated;
- where I have consulted the published work of others, this is always clearly attributed;
- where I have quoted from the work of others, the source is always given. With the exception of such quotations, this thesis is entirely my own work;
- I have acknowledged all main sources of help;
- where the thesis is based on work done by myself jointly with others, I have made clear exactly what was done by others and what I have contributed myself;
- parts of this work have been published as:

A.S. Vaughan, Y. Zhao, L.L. Barré, S.J. Sutton, S.G. Swingler. "On additives, morphological evolution and dielectric breakdown in low density polyethylene" - European Polymer Journal 39 (2003) 355-365.

Signed: ...  .....

Date: Southampton, the 27th of October 2004.

ACKNOWLEDGEMENTS

I wish to thank Dr. Yves Béreaux and Prof. Didier Graebling for their initial and invaluable "push" which led me to cross the Channel. I am also extremely grateful to my supervisor Dr. Alun Vaughan for having chosen me to carry out this research, without having actually seen me in the first place. I am indebted to him since he helped me during the whole course of this PhD, and I am grateful that he could cope with my use of Shakespeare's language. The completion of this research would not have been possible without the valuable input brought by Dr. Simon Sutton thanks to several discussions. Also, I would like to thank Dr. Steve Dodd for his kind and fruitful help and advice.

I also wish to thank my industrial employer, National Grid Transco.

On a more personal level, I would like to thank my wife Alexandra for her patience and support, and also to my family.

UNIVERSITY OF SOUTHAMPTON

ABSTRACT

FACULTY OF ENGINEERING AND APPLIED SCIENCE

Doctor of Philosophy

Penetrant diffusion in polyethylene: The impact of water on the performance of novel XLPE cable designs.

By Laurent Luc BARRÉ.

Power cables consist of concentric arrangements of layers designed to respond to specific technological requirements. The ambition of the present work is to devise a way to prevent durably the occurrence of detrimental electrical breakdowns induced by the progressive penetration of water within such structures, by the means of studying materials or systems that already are, or could be, integrated into the design of a cable.

Preliminary investigations were directed at evaluating the effect of composition and thermal conditioning on the subsequent morpho-mechanical structure of model materials, which potentially reflect the behaviour of existing LDPE-based insulating materials. This was done prior to investigating water uptake kinetics using the same model materials as above. What was revealed is the considerable influence of additives and thermal processing on the morphology and molecular mobility of such systems. Additionally, such materials exhibit sorption characteristics that were shown to respond to Fickian characteristics.

Afterwards, two materials whose potential applicability to forming water retention layers were probed using ageing methods that ideally reproduce those they would be subjected to, were they incorporated in power cables. One of these two systems is a biomaterial whose water-binding capacities were shown to remain constant, albeit with a propensity to exhibit marked depolymerisation characteristics. The other material is a superabsorbent whose nature was not precisely known, but which nonetheless proved to be as functional as the above biomaterial, from a water-trapping standpoint.

Humidité, cause de tous les maux.

Gustave Flaubert.
(1821/1880)

TABLE OF CONTENTS

LIST OF FIGURES

LIST OF TABLES

Glossary

Anomer: Type of molecular configuration of hexoses involving the C1-C6 ring closure.

Chirality: Geometric property of a spatial arrangement of atoms that cannot be superimposed onto its mirror image.

Endo/Exocycle: Descriptors of the relative orientation of atoms or groups of atoms attached to non-bridging atoms. If the group is orientated towards the highest numbered bridge it is given the description *exo;* if it is orientated away from the highest numbered bridge it is given the description *endo*.

Epimer: Isomers that have the opposite configuration at only one or two or more tetrahedral (stereogenic) centres present in the respective molecular entities. In our case, the notion of epimer characterises a monosaccharide which differ in configuration around a single, or two carbon atoms.

Chapter 1

Background and materials presentation

1.1 General remarks on the appearance and modern use of polymers

Synthetic polymers appear nowadays remarkably diverse as they meet varied functions within innumerable mass market applications. A key reason for this is the ease with which most polymers can be moulded and shaped. This confers on those materials an unprecedented versatility in utilization: from pen lids to elastomeric joints sent in spacecrafts, from shopping bags to multi-layered milk bottles, from acoustic insulation materials to shoe soles, from liquid crystal displays to shock absorbers, synthetic polymers can be found in simple objects and as parts of complex systems. However, this emergence of synthetic polymers arose as a result of fairly recent discoveries. Effectively, the first polymeric materials started to appear only about a hundred years ago, towards the end of the 19th century. The very first commercial appearance of a synthetic "plastic", referred to as Celluloid[1], initiated the revolutionary leap that led to more recent discoveries of other synthetic polymers. Celluloid, whose name became notorious since 1868, was followed in 1906 by Bakelite, a phenolic resin. The real breakthrough in the polymer field, however, relates to the conjecture by Staudinger in 1920 regarding the true nature of a polymer. Other well-known polymers have been discovered since then. For instance, the discovery of Nylon in the 1930's[2] allowed the manufacture of parachute cloth, clothes as well as fishing lines. Ziegler and Natta respectively discovered polyethylene and polypropylene in 1953 and 1954. At the present time, synthetic polymers are mainly derived from processed oils as well as from vegetable or animal sources. As a result, hundreds, if not thousands of synthetic polymers exist nowadays; fortunately, it appears possible to sort them as a function of their physical and chemical properties. This permits the construction of classes and families of polymers, since groups of them tend to possess common properties.

[1] A product named after nitrocellulose processed with camphor.

[2] Nylon is derived from polymerization reactions between acids and amines.

Generally speaking, most synthetic polymers appear as long macromolecular assemblies made of organic elements, and it is mostly from their size that they derive most of their properties.

In contrast to mankind's relatively recent discovery of synthetic polymers, natural polymers have been part of nature since the emergence of living plants and animals. A protein such as casein coming from milk can be used as a glue sealant but it also gives a polymer called paracasein once processed with formaldehyde. At the same time, natural polymers, also referred to as biopolymers, are used by living creatures as their genetic material or, alternatively, as vital food reserves and essential bodily fluids. For instance, deoxyribonucleic acid, also known as DNA, is a molecule that contains hereditary information. This macromolecule is now commonly recognized as being a polymer in the sense that it consists of millions of repeat units. Among other well-known biopolymers, one can find diverse assemblies of poly-proteins and also carbohydrates, a family which includes, among other substances, starch, cellulose and polysaccharides; all these molecules provide essential support for living plants and animals. Of course, biopolymers exhibit similar characteristics to that of their synthetic cousins. For example, DNA also shows self-organizing properties, in the sense that it can adopt helical conformations as well as linearly condensed structures in response to electro-biological stimuli. Thus, biopolymers can also crystallize, form complex structures, store energy and information and such qualities are fundamentally related to their macromolecular nature. In this sense, they reflect their synthetic counterparts, while being used for rather different purposes, as part of many biological processes.

To conclude, the enormous appeal of polymers is linked to their flexible processing ability. In addition, it would be wrong to deny that the low price of a number of unprocessed materials does not reinforce the overall attractiveness of polymeric materials. As we have already indicated, polymers are employed in the most complex systems, and the high-voltage industry is no exception to this.

1.2 High-voltage cables: a polymer-based structure

A modern power cable is a complex, engineered structure. It contains many coaxial layers with complementary functions, and many of these layers are made of polymeric materials. When it comes to the transport of currents at high voltage, the primary problems high-voltage cables must face relate to electrical insulation. Nevertheless,

other important technological issues must also be addressed beyond this concern. In this section, we provide a short summary dealing with the history of materials linked to electrical insulation in power cables. We then examine the internal architecture of a modern power cable, to emphasize the precise context of this study, since the latter does not exclusively relate to insulating materials. We ultimately present the model materials examined in the experimental part of this thesis and, as we associate them to their functions, we give a more accurate description of their composition and alternative uses outside power cable applications.

1.2.1 Brief reminder of the history behind electrical insulation in power cables

The need for electrical insulation is great in power transmission, since massive flows of current must be solely restricted to the conductors. A natural rubber known as gutta percha served as an early insulating material for cables [1]. Later designs involved layers of paper impregnated with oils and such systems are still being used nowadays [1]. However, such cables possess a major drawback, namely the possible leakage of oil that can lead to pollution and the potential for fires [1]. Alternatively, synthetic polymers such as low-density polyethylene (LDPE) and polyvinyl chloride (PVC) are also utilized as insulators [2,3], but it is LDPE that is primarily employed for its intrinsically high dielectric stability. An improved version of LDPE started being used from the 1960's: crosslinked polyethylene or XLPE. The passage from LDPE to XLPE was due to the fact that the latter possesses rather better mechanical characteristics at high temperatures, i.e. reduced softening properties. This enables XLPE to cope with hypothetical short temperature excursions [4,5] which is increasingly important since the magnitudes of the transmitted power has increased significantly in a few decades. In the 1960's, European polymer-insulated power cables could tolerate voltages up to 50 kV [6]; as suggested by more recent work [7], modern cables have been required to withstand ten times higher voltages since the late 1980's. Also, in the 1960's, 11 to 50 kV power cables using polyethylene insulation were required to withstand temperatures of ca. 70°C when fully loaded [6]. These days, normal running temperatures are reported to range from 70°C [8] to 90°C [5], a value which depends obviously on the current flowing in the conductor. According to Boubakeur et al. [5], 400 kV cables can, exceptionally, reach overload temperatures as high as 250°C.

1.2.2 Schematic description of a contemporary power cable

One way to deal with the work described in this thesis is to divide it up in a way that resembles the architecture of a power cable. The latter can be viewed as a coaxial multilayered structure in which one finds layers responding specifically to different technological criteria. In order to illustrate this point, fig.1.1 provides a schematic representation of a high-voltage cable[3] inspired from general descriptions provided by different workers [3,9,10]. If we start from its core, a power cable comprises arrangements or bundles of copper conductors. Then, one finds a primary semi-conducting shield that consists of a carbon-black filled cross-linkable ethylene-based copolymer. The primary role of this layer concerns effects attributable to the surface irregularities of the copper conductors. It can alternatively be seen as a stress control layer, meant to ensure that the electric field generated by a cable remains symmetrical. Around this first layer, one finds an XLPE layer, which is wrapped in another semi-conducting layer. The obvious role for the XLPE layer is electrical insulation, while the role for the outer semi-conducting layer is to confine voltage gradients to the inner parts of the cable. Depending on the cable type, for instance, as seen from an ABB 115 kV cable, the above structure can then be surrounded by a thin layer, which contains water-trapping substances. Water-trapping layers are habitually found in the structure of submarine cables where such devices are designed to restrict water penetration along the cable's core. Additional water-trapping particles can also be introduced into the spaces left between the bundles of copper conductors [11]. Finally, the external layers can be wrapped in a metallic tape or sheath and, occasionally, the entire structure can also be encased in an external jacket or sheath.

Since our research topic is primarily linked to the occurrence of water permeation in a high-voltage cable, our main attention is directed at those layers which may be subjected to water-related hazards. Therefore, it is essential to consider the environmental conditions under which a power cable must operate.

[3] The geometrical scale and relative thicknesses of the different layers indicated in fig.1.1 are not shown to scale.

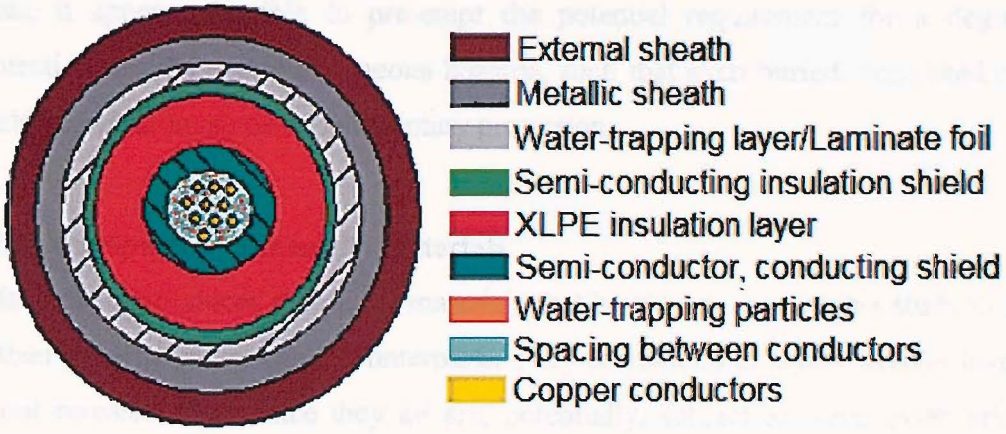

Figure 1.1: Schematic representation of a high-voltage cable comprising a water-trapping layer.

1.2.3 Installation and external constraints for power cables

Transmission lines can either appear as underground cables or overhead conductors depending on the constraints imposed by the surrounding area [12]; in some cases, underground installation costs are 4 to 33 times higher than that for overhead conductors [12]. This means that cables are generally buried only in populated zones, i.e. urban areas. Here, London represents an excellent example, where transmission cables have to be installed underground, as part of the so-called London Project. Buried cables can be installed in pipes, ducts or ventilated pipes but some are also buried directly in the ground. An obvious advantage of this is that overhead conductors are exposed to variable environmental conditions, such as wind and sleet loads [13]. On the other hand, cable cooling is a major issue for underground installations, since overhead conductors are cooled by natural air circulation. Thus, controlled conditions are needed to ensure that a cable can function correctly. In an ideal scenario, well protected power cables will never be exposed to aqueous systems. Although the long-term threat of water ingress is more obvious for submarine cables, we cannot totally reject the possibility that ducted or buried cables might, at some point, be exposed to water. The reasons for this could include:

- Unnoticed manufacture imperfections could compromise the local integrity of a cable.
- Partial, accidental perforation of some external layers could occur during installation or maintenance.
- Flooding or leakage in urban areas might result the cable being exposed to water, even in a previously clean and dry duct.

Thus, it appears sensible to pre-empt the potential requirement for a degree of protection against potential aqueous hazards, such that even buried, ventilated cables could benefit from some supplementary protection.

1.2.4 Description of our model materials

This section introduces the model materials that have been used in this study in place of their genuine power cable counterparts. They correspond to layers directly involved in our research topic since they all are, potentially, subject to water permeation or water uptake. Firstly, polyethylene-based materials relate to the electrical insulation layer. Then, the other two systems correspond to two distinct hydrophilic materials that can be seen as potential water-blocking systems. The following sections provide more detailed descriptions of our systems.

1.2.4.1 Classification of our LDPE-based materials

Insulating layers made of LDPE or XLPE were considered in this study, since water permeation can induce specific electrical breakdown mechanisms. Our approach does not include any experimental work related to breakdown and, consequently, we do not wish to expand much further on such mechanisms; we nonetheless wish to point out that failures related to water absorption generally involve water-treeing, and that many studies in the literature provide this much needed connection between water uptake and breakdown strength reductions in LDPE-based insulating materials [14-17]. If AC breakdown values are reported to decrease proportionally to the moisture content absorbed by XLPE [15], water uptake additionally appears to be accelerated by the voiding generated by treeing mechanisms [18,19]. In view of this, we developed an additional interest in a related family of ethylene-based materials, namely ethylene-vinyl-acetate (EVA) copolymers; our interest in these stems from the fact that EVA materials are reported to exhibit water-tree suppressant properties [8,20,21] since they may inhibit mechanical damage attributable to cavity growth phenomena, as discussed later on in the case of pure polyethylene (PE).

1.2.4.1.1 Chemical structure and typical uses for polyethylene

Polyethylene possesses a simple chemical structure, being the simplest synthetic macromolecule. PE is built from a polyaddition reaction of ethylenic monomers

classically represented as -(CH_2-CH_2)- units. Depending on the polymerization process, low or high-density polyethylene can form. LDPE, or branched polyethylene, is obtained via high pressure processes, whereas low pressure procedures requiring catalysts, lead to linear polyethylene chains. Thus, polyethylene derived from natural gas at pressures higher than a thousand bars leads to LDPE, a material that commonly contains 20 to 40 side branches per 1000 carbons of the main backbone [22]. In any case, PE is a semi-crystalline material. It is employed extensively in the food and packaging industry for its barrier properties, in the market of household goods for its low price, or, alternatively, in the chemical industry for its intrinsic inertness, e.g. for the transport of certain acids. However, our interest in LDPE comes from the fact that it is frequently employed for electrical insulation, since it exhibits excellent dielectric properties. As far as we can state, literature studies [4,5,8,15] repeatedly provide evidence that LDPE or crosslinked LDPE are insulating materials preferentially employed in power cables. However, one could argue that any polyolefin could provide an equivalent, if not superior insulating behaviour to that of PE-based compounds. It appears possible to envisage using HDPE as an insulating material; but in practice, an extruder requires additional power to process it at some 30°C higher than for LDPE[4] [6]; more seriously, rapid cooling stages also imply greater volume contractions leading to the formation of internal voids and delamination of the insulator from the conductor [6]. In the case of polypropylene (PP), Mayoux reports that the latter exhibits a restricted temperature capability since it is accompanied by a significant variation in capacitance with temperature [23], which is a drawback.

1.2.4.1.2 Borealis Oy polyethylene compounds

Our first material consists of an LDPE that is supposedly, free of any additives. Our second material contains at least one unidentified antioxidant, which has been added to the pure material. Our third compound combines the content of the previous one with an unknown quantity of unreacted dicumyl peroxide (DCP). From now on, we will respectively refer to our LDPE-based materials as Material A, B or C. Initially, we carried out a literature research aimed at reviewing the likely composition of each of the above materials. From different literature studies [2,24-27], we learn that insulating materials derived from chemically crosslinked LDPE must withstand

[4] LDPE extrusion temperatures are situated between 180°C and 270°C [6].

thermally-activated alterations during crosslinking[5]. Several workers [2,25-27] indicate that a critical balance between a primary phenolic or amine reagent is employed to inhibit scorch[6]; a bifunctional sulfur or phosphorous-based antioxidant being also required to prevent long-term thermal oxidation. Hence, the initial amount and type of antioxidant appears closely linked to the initial amount of DCP present in the material [15,26], but also to the latter's future running conditions. This leads to a likely description of Material C's composition. It appears important to specify that classical XLPE compounds initially comprise a few percent of DCP in mass, typically 1 to 3% [5,8,28]. Once DCP has been activated, the final gel contents are found to reach a maximum with an initial content of 2 to 3% of DCP [28]; this maximum reaches typically 80% to 90%, a result that can also depend to some extent on the molecular characteristics of the branched polyethylene, for example, the degree of branching [24,28]. Also, the amount of gel formed by crosslinking is a quantity likely to increase noticeably due to long-term ageing reactions occurring during service conditions.

1.2.4.1.3 Chemical structure and utilizations of EVA copolymers

Ethylene-vinyl acetate is a rather more complex macromolecule than polyethylene, since it is composed of a distribution of ethylene and vinyl acetate units. The vinyl acetate unit is shown schematically in fig.1.2. EVA copolymers are commonly employed as alternative materials instead of polyethylene for applications that require a better mechanical flexibility than polyethylene [22], even though the presence of vinyl acetate is detrimental to the chemical inertness of the material. EVA is employed in the food packaging industry and, for instance, some flexible gloves are prepared from such materials. It is also utilized as an insulating material in the cable industry.

---

[5] The thermo-chemical activation of DCP leading to the formation of a network due to a succession of chemical reactions that can be summarized as the following three-steps reaction [5,26,27]:-

(i) $ROOR \rightarrow 2RO^{\bullet}$

(ii) $RO^{\bullet} + -CH_2-CH_2-CH_2- \rightarrow -CH_2-CH^{\bullet}-CH_2- + ROH$

(iii) $2\ -CH_2-CH^{\bullet}-CH_2 \rightarrow 1$ HC-CH bridge

Thus, DCP reactions with polyethylene chains leads to the formation of alkyl radical and cumyl alcohol groups, as the original peroxy groups combine with hydrogen atoms extracted from the LDPE chain [5,26,27].

[6] Scorch is an alternative name given to premature crosslinking [2].

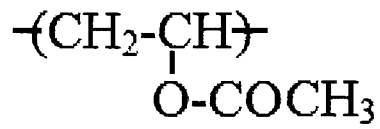

Fig.1.2: A vinyl acetate repeat unit.

1.2.4.1.4 Dupont de Nemours random ethylene-vinyl-acetate copolymers[7]

Our pellets of Elvax® 40W consist of a randomly distributed copolymer of vinyl acetate and ethylene units. The latter is said to contain a residual quantity of butylated hydroxy-toluene, in addition to 0.3% of residual vinyl acetate groups. It also contains an anti-blocking adhesive additive of unspecified nature. The final compound contains approximately 40% vinyl acetate by weight. According to the manufacturer, Elvax's main application area is in electrical distribution equipment and wires. Elvax® 40W compounds are specifically reported to be employed as materials for wire and cable applications, such as ignition wire jackets, heater cable insulators, power cable shields, among other potential uses; The principal appeal of this material being that Elvax is designed to create a controlled-adhesion interface between the insulating and semi-conductive layers of a cable, thus allowing the outer semi-conductive layer to be peeled away when needed to make repairs or terminations. EVA-based materials are sometimes filled with carbon to be used as wire sheathing materials [23].

1.2.4.2 Description of the water-trapping materials

National Grid Transco initially provided us with two different materials of unknown origin. At the time, the only certainty was that such systems could serve as water-blocking systems in power cables. Here, we provide further details about both materials; the identity of the first one was determined prior to carrying out further experiments, whereas the second material has still not been precisely identified.

1.2.4.2.1 Water-blocking materials supplied by the National Grid Transco

Here is a detailed account of what we originally knew about our water-blocking systems:

[7] Informations provided about Elvax was taken from the product information sheets sent by Dupont de Nemours.

- The first system takes the form of a raw powder. Comparative studies between this material and a set of known commercial gums[8] were performed by Raman spectroscopy. Thus, we identified it as being a polysaccharide, more specifically guar gum, which is alternatively called guar or guaran. Fig.1.3 contains a micrograph of raw guar powder. Although this image does not show it, this gum was completely unrefined, since crude fibres were also found in the bulk of the material. It must be specified that the guar powder provided by National Grid Transco was the one actually used to perform the totality of our experiments.
- Our second system is considerably more complex than the previous one. It comprises absorbent particles grafted between non-woven fabrics. Interestingly, fig.1.4 shows that our absorbent particles might be glued to the fabric, see the right part of the micrograph. The appearance of patches of glue in this system is consistent with the fact that the absorbent particles could not be easily detached from the supporting fabric when the system is dry. Examination of industrial systems sold for water-trapping purposes, for instance in submarine cable technology, demonstrates that these effectively consist of absorbent particles glued between fabrics. Such systems are sometimes referred to as laminate foils.

[8] We gratefully acknowledge the shipment of guar, locust and xanthan gums by TIC GUMS. Throughout this work, we considered that the TIC PRETESTED® Gum Guar 8/22 NF/FCC Powder and the National Grid Transco guar powder were equivalent, even though the latter was clearly unrefined. We also utilized TIC PRETESTED® Locust Bean Gum POR/A powder and a xanthan gum for comparative purposes.

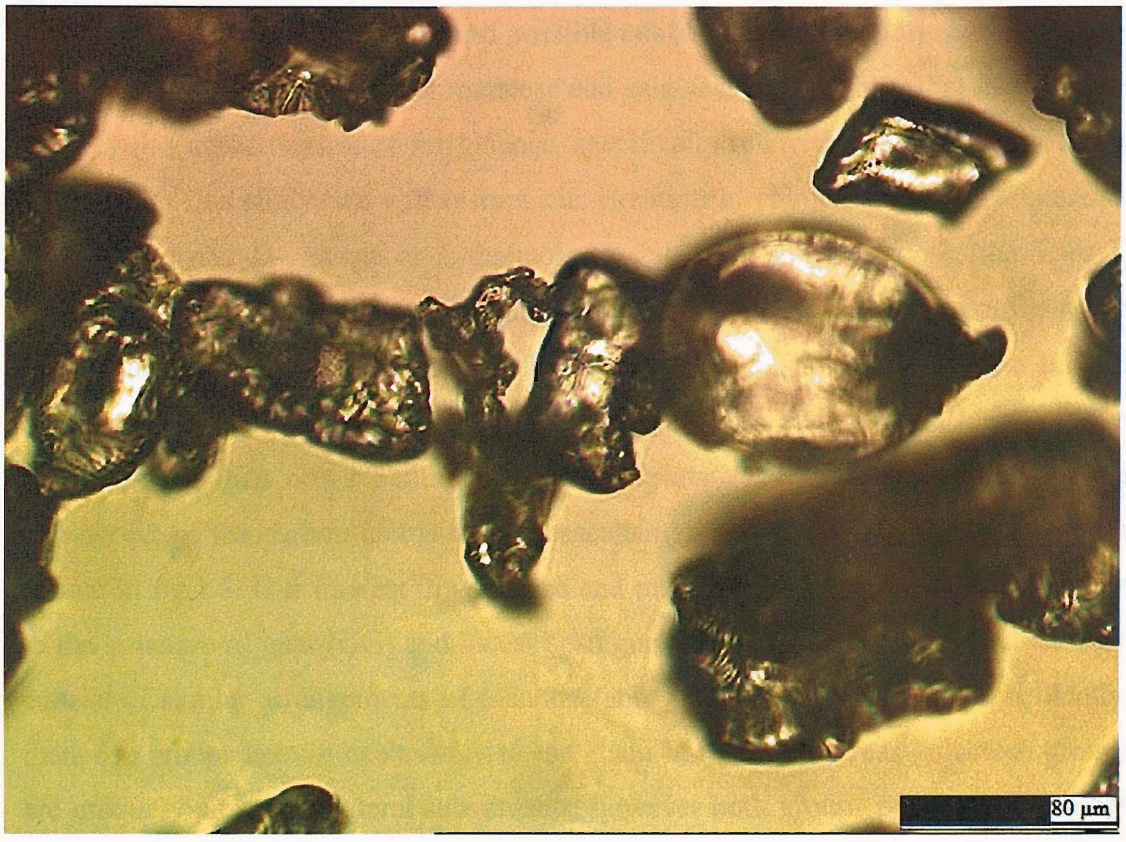

Figure 1.3: Magnified images of raw guar particles (transmission mode).

Figure 1.4: Magnified images of an absorbent particle (left) and of its non-woven backing fabrics (transmission mode).

1.2.4.2.2 IUPAC nomenclature and possible conformations for polysaccharides

Conventional representations for mannose and galactose groups show that the latter are two regular diastereoisomers for glucose, specifically referred to as epimers. For the purposes of this study, we will restrict our attention to epimers such as D-mannose, D-galactose and D-glucose or L-mannose, L-galactose and L-glucose; the L or D prefix depends on the epimeric configuration, which relates to the chiral configuration around a specific carbon atom. To clarify this, fig.1.5 shows the acyclic Fischer representations for the D-epimers of mannose, galactose and glucose, knowing that L-epimers are their non-superimposable counterparts[9]. Conventionally, one starts the numbering of the carbon atoms of monosaccharides at the CHO group of atoms, as shown in fig.1.5. Our interest in galactose and mannose configurations directly relate to the structure of guar (GG) and locust bean gum (LBG) macromolecules, since both consist of similar arrangements of mannose and galactose groups. More specifically, mannose groups belong exclusively to the chain backbone whereas galactose groups are uniquely present as lateral substituents; however both groups preferentially adopt cyclic forms in these polysaccharides, especially in their solid state. To visualize this, fig.1.6 shows the simplest plane projection of a GG repeat unit made of one lateral galactose group attached to one mannose ring within the main chain. In addition to epimerism, the cyclic form of both mannose and galactose groups assumes the creation of a new chiral centre; it is situated at their so-called anomeric centre which is, in simpler terms, the location of their ring closure. Consequently, two new possible conformations appear for both mannose and galactose groups and such configurations are conventionally referred to as α and β conformers or more specifically anomers. It must be noted that these anomeric configurations do not exhibit the same probability of existence; this means that the formation of α and β-anomers is somewhat biased by the thermodynamic preference for polar groups bonded to C-1, thus making for a general preference between these two conformers [29]. To sum up, GG and LBG macromolecules possess mannose groups bound by (C1-C4) or 1-4 linkages, whereas pendant galactose groups are bound by (C1-C6) or 1-6 linkages. GG and LBG are polysaccharides mainly consisting of a linear backbone of β-1,4-linked mannose units with randomly attached pendant α-1,6-linked galactose units. Fig.1.6 appears restricted

[9] This implies that their Fischer represetation would only invert the hydrogen and the hydroxy group at the epimeric carbon, however our 2D representation would not permit the 2 forms to be distinguished.

in the sense that the 3D structure is much more complex. As a result, the number of spatial configurations for GG and LBG molecules is high.

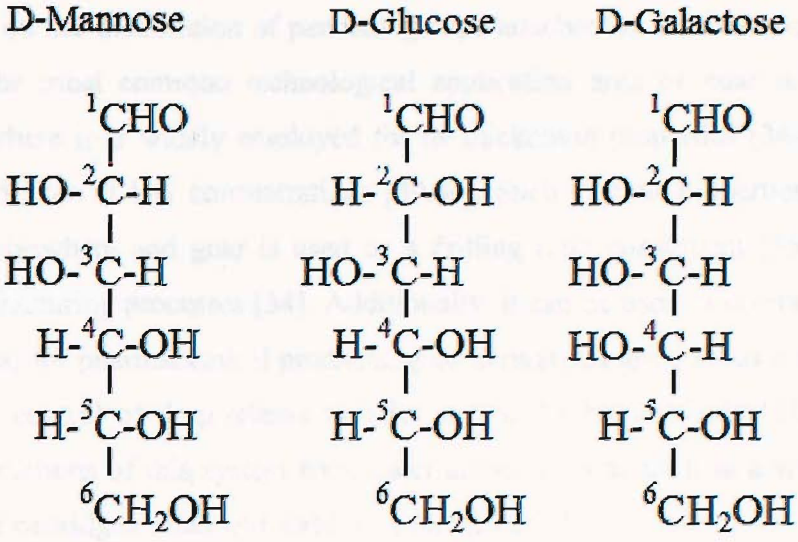

Figure 1.5: Fischer representations for D-Mannose and D-Galactose, epimers to D-Glucose at carbons C-2 and C-2/C-4.

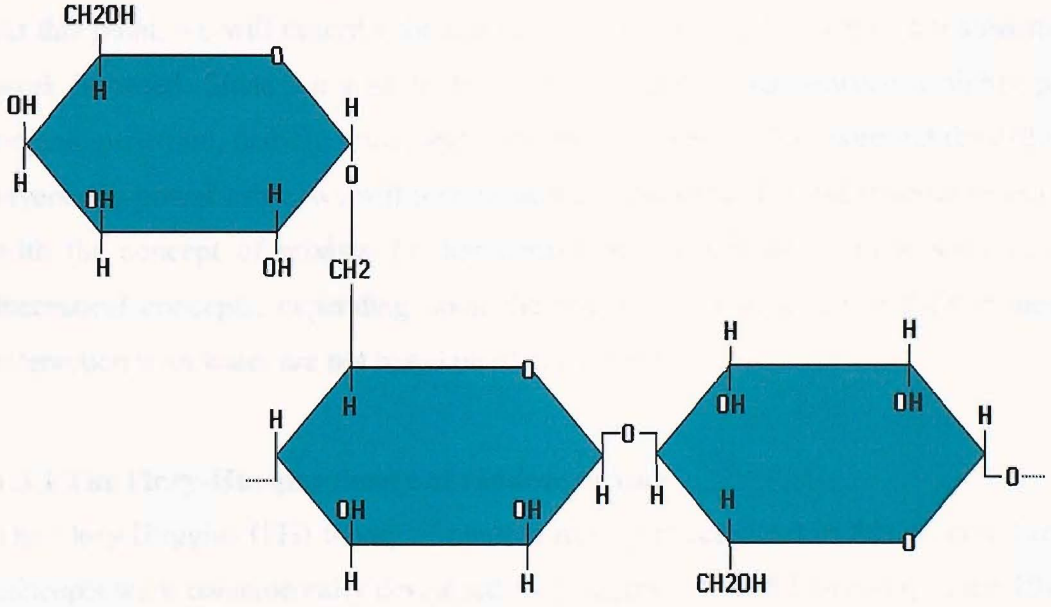

Figure 1.6: The simplest 2D representation for the structure of guar-redrawn from Bayerlein [30].

1.2.4.2.3 Utilizations of guar gum

In its natural state, guar is one member of a family of such materials that are used by plants as natural food reserves [31,32]. Other related biopolymers include locust bean gum, tara gum, fenugreek gum, which differ from guar only in terms of their galactose

to mannose ratios [30-33]. Specifically, GG is employed for its propensity to form hydrogen bonds with water molecules [30] and its solubility degree is strongly dependent on the distribution of pendant groups attached to the main backbone [30]. Possibly the most common technological application area of guar is in the food industry, where it is widely employed for its thickening properties [34-38] which is pronounced even at low concentrations [39,40]. Such viscous properties can also be exploited elsewhere and guar is used as a drilling mud constituent [35] and during hydraulic fracturing processes [34]. Additionally, it can be used in diverse specialized applications; for pharmaceutical products, guar derivatives are used as coatings taking part in the control of drug-release kinetics within the human body [41], whilst the strong interactions of this system with water allows it to be used as a water-blocking systems for cartridges filled with explosive powders [30].

1.3 Physical descriptions for the concept of mixing

At this point, we will describe the theoretical basis on which much of our subsequent work is based. Since we wish to focus on the interactions between a highly polar organic penetrant, namely water, and some model materials that represent the different layers of a power cable, we will present here the statistical thermodynamics associated with the concept of mixing. Further considerations will differentiate such general theoretical concepts, depending upon the materials involved, since their modes of interaction with water are not based on identical mechanisms.

1.3.1 The Flory-Huggins theory of random mixing

The Flory-Huggins (FH) theory of random mixing is described in this section. Similar concepts were coincidentally developed by Huggins [42] and Flory [43] in the 1940's. The FH model consists in a statistical thermodynamic description which conveys quantitative information about the mixing of a polymer with a foreign substance, which might be another polymer or a solvent. The mathematical aspects required to understand FH theory relate to quantities borrowed from combinatorial calculus. The latter leads to estimates such as the number of possible permutations or equivalent rearrangements of molecular units placed on a regular lattice. It is then used to quantify an entropic term, thanks to Boltzmann's law. We do not wish to describe how this combinatorial term is calculated, since it would not fundamentally increase our global

understanding of the model. Instead, we emphasise here the physical meaning of the latter, its limitations and its scientific contribution to our subject. Thus, the following sub-sections introduce the physical implementation of the FH theory, starting from basic thermodynamic considerations. Then, we will review the approximations used to construct this model, before discussing those elements of the model that take on a critical aspect with regard to our experimental work. We eventually present the notion of an interaction parameter, both in the context of the FH theory, and also in the context of a modified version of the theory that takes into account the concept of excluded volume.

1.3.1.1 Definitions for the free enthalpy of mixing and the chemical potential

When two chemical species are mixed, the potential energy of each of the molecules constituting the system changes, since the surroundings of some molecules will then differ from their original state. In physical terms, the behaviour of a mixture of N_1 molecules of solvent and N_2 molecules of solute can be quantified using the free enthalpy of mixing ΔG_m and, also, through variations in the chemical potential of the solvent, $\Delta\mu_1$. The definition of the free enthalpy is the following:

$$G = H - TS \qquad \text{(eq.1.1)}$$

where G, H, S and T respectively stand for the free energy (or Gibbs potential), the enthalpy, the entropy and the absolute temperature of a given system. The change in free enthalpy from an initial value, G^o, is then:

$$\Delta G_m = G - G^o \qquad \text{(eq.1.2)}$$

Thus, ΔG_m is the change in free enthalpy induced by mixing the constituents which is not the simple sum of the free energy of the constituents considered separately. This quantity will further be expressed as the difference between the heat of mixing and the entropy of mixing of the system, see eq.1.15. Then, $\Delta\mu_1$ is the variation of the chemical potential for the solvent:

$$\Delta\mu_1 = \mu_1 - \mu_1^o = [\partial(\Delta G_m)/\partial N_1]_{T,P,N_2} \qquad \text{(eq.1.3)}$$

This is the derivative of eq.1.2 when T, P and N_2 are taken as fixed variables. ΔG_m and, more importantly, $\Delta\mu_1$ will be utilized subsequently.

1.3.1.2 Variations in the entropy and enthalpy of mixing in the lattice theory

FH theory is based upon a statistical description of the variation in the entropy of mixing, ΔS_m, a quantity evaluated from the number of possible configurations accessible to any random mixture of N_1 molecules of solvent and N_2 molecules of polymer. ΔS_m is then obtained directly from Boltzmann's law:

$$\Delta S_m = -k_B \ln(\Omega) \qquad \text{(eq.1.4)}$$

where k_B and Ω respectively stand for Boltzmann's constant and the combinatorial estimate representing the number of configurations determined as being the total number of ways to place N_2 polymeric units in a 3D lattice. From this, one can evaluate the entropy of mixing, which corresponds to the difference between the entropy of the mixed constituents, S_m, and the entropy of the constituents taken separately, S^o:

$$\Delta S_m = S_m - S^o = -k_B (N_1 \ln(\Phi_1) + N_2 \ln(\Phi_2)) \qquad \text{(eq.1.5)}$$

where ϕ_1 and ϕ_2 respectively represent the volume fractions of the two components of the mixture, namely the solvent and the polymer. The next step involves an evaluation of ΔH_m, the variation of the enthalpy of mixing, by using three elementary interactions: solvent-solvent, ε_{11}; segment-segment, ε_{22}; and solvent-segment ε_{12}, (see fig.1.7). The formation of two interactions of the *1-2* type happens at the expense of one interaction of the *1-1* type and one interaction of the *2-2* type. Thus, the energy associated with the creation of a *1-2* type contact, also termed the contact or interchange energy, $\Delta\varepsilon_{12}$, becomes:

$$\Delta\varepsilon_{12} = (\varepsilon_{11} + \varepsilon_{22})/2 - \varepsilon_{12} \qquad \text{(eq.1.6)}$$

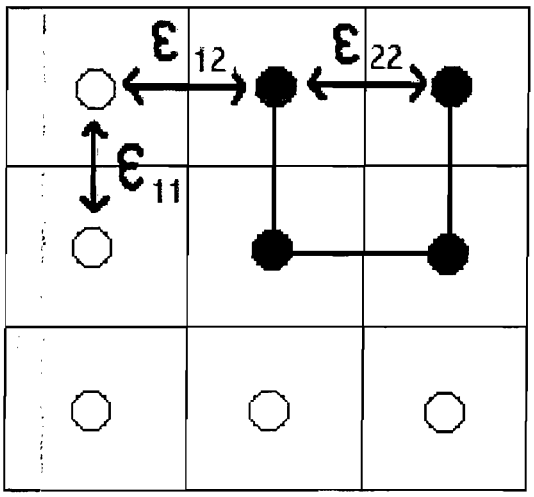

Figure 1.7: 2D representation of the lattice model comprising a short loop of segments from a polymer chain surrounded by solvent molecules.

Using the interchange energy term derived above, we then consider that the total variation of the heat of mixing simply results from the addition of the individual interchange energy contributions[10]:

$$\Delta H_m = p_{12}\Delta\varepsilon_{12} \qquad \text{(eq.1.7)}$$

where p_{12} represents the number of interactions of the *1-2* type formed in the mix. The following assumption is that each segment is surrounded by z neighbours in total; hence, a polymeric chain can be split into x segments of equal volume. If the characteristic volume for a monomeric unit compares to the characteristic volume of the solvent, x can be seen as the degree of polymerization of the polymer and as a cell unit in respect to the lattice theory. Thus, p_{12} can be evaluated as follows; the number of adjacent cells to those occupied by the polymeric segments for a whole chain equals[11]:

$$(z-2)x+2 \equiv (z-2)x \qquad \text{(eq.1.8)}$$

If we then assume that the mixture can be considered to be a homogeneous distribution of its constituents, then $[(z-2)x]\,\phi_1$ adjacent cells will be occupied by solvent molecules. This quantity also represents the number of *1-2* interactions per macromolecule. For N_2 chains, the result is straightforward. It gives:

$$\Delta H_m = p_{12}\Delta\varepsilon_{12} = (z-2)xN_2\Phi_1\Delta\varepsilon_{12} \qquad \text{(eq.1.9)}$$

This quantity can be expressed in a slightly different way since, from the definition of ϕ_2, we have[12]:

$$xN_2\phi_1 = N_1\phi_2 \qquad \text{(eq.1.10)}$$

Thus:

$$\Delta H_m = N_1\phi_2(z-2)\Delta\varepsilon_{12} \qquad \text{(eq.1.11)}$$

Another expression can be obtained instead of this equation. In the case of an almost apolar mix, one can consider the geometric average obtained from ε_{11} and ε_{22}[13]:

$$\Delta\varepsilon_{12} = (\sqrt{\varepsilon_{11}}/2 - \sqrt{\varepsilon_{22}}/2)^2 \qquad \text{(eq.1.12)}$$

---

[10] Since the FH model does not take into account changes in volume, the variation of the enthalpy is implicitly identified as being the variation in internal energy; hence (eq.1.7) takes this form.

[11] Macromolecules are considered to be sufficiently long, that terms relating to the first and last segments can be neglected.

[12] $\phi_1 = N_1V_1/(N_1V_1 + N_2V_2) = N_1/(N_1 + xN_2)$ and $\phi_2 = xN_2/(N_1 + xN_2)$

[13] From (eq.1.6), $\sqrt{\varepsilon_{11}\varepsilon_{22}} \equiv \varepsilon_{12}$. This relationship is valid when no secondary type interaction favours bonding between the 1-2 contacts.

Thus eq.1.11 can be rewritten in the following form:

$$\Delta H_m = V\Phi_1\Phi_2(\delta_1 - \delta_2)^2 \qquad \text{(eq.1.13)}$$

where V stands for the volume of the mixture, provided that the solubility parameters are defined as follows, where δ_i represents the solubility parameter of each species:

$$\delta_i = (\varepsilon_{ii}(z-2)/2V_i^o)^{1/2} \qquad \text{(eq.1.14)}$$

We know from thermodynamics that, to dissolve a polymeric substance in a solvent, the change in the free enthalpy of mixing, ΔG_m, must be negative. From (eq.1.1), we have:

$$\Delta G_m = \Delta H_m - T\Delta S_m \qquad \text{(eq.1.15)}$$

where ΔS_m stands for the change in the entropy of mixing, a quantity that is always positive. If ΔH_m is negative, mixing is possible in all cases; in addition, assuming that eq.1.13 is valid, mixing is also possible if ΔH_m is small, implying that the solubility parameters of the mixing species are similar in values. This means that a good polymeric solvent often exhibits a solubility parameter extremely close to that of the polymer to be dissolved.

1.3.1.3 Introduction of a dimensionless interaction parameter

We can rearrange eq.1.11 such that a new factor appears in this equation[14]:

$$\Delta H_m = RT\chi_{12}N_1\phi_2 \qquad \text{(eq.1.16)}$$

Here, χ_{12} is a dimensionless factor known as the Flory-Huggins interaction parameter; it derives its meaning from the expression:

$$\chi_{12} = (z-2)(\Delta\varepsilon_{12}/RT) \qquad \text{(eq.1.17)}$$

where the product $RT\chi_{12}$ physically represents the energy associated with the interaction of one mole of solvent with the pure polymer ($\Phi_2=1$). At this point, we can substitute the derived expressions for ΔH_m and ΔS_m into eq.1.15. Thus, the expression for the free enthalpy of mixing becomes:

$$\Delta G_m = RT(N_1 \ln\phi_1 + N_2 \ln\phi_2 + \chi_{12}N_1\phi_2) \qquad \text{(eq.1.18)}$$

and:

$$\Delta\mu_1 = RT(\ln(1-\phi_2) + (1-1/x)\phi_2 + \chi_{12}\phi_2^2) \qquad \text{(eq.1.19)}$$

[14] NB: For practical reasons, (eq1.13) was multiplied by Avogadro's number to deal with molar quantities instead of molecular ones; and so forth for all the following equations.

The behaviour of the quantity $\Delta\mu_1$ varies with both T, Φ_2, x and χ_{12}. To illustrate this, we have constructed the example shown in fig.1.8 using a value of 100 for x. If T is fixed, the quantity $\Delta\mu_1/RT$ can be studied as a function of Φ_2, where χ_{12} can be viewed as an adjustable parameter. When the interaction parameter strictly remains below a critical value χ_{12C} introduced further on, $\Delta\mu_1/RT$ decreases monotonically with Φ_2. When χ_{12} exceeds this critical value, the curve displays a maximum and a minimum which are an indication of the presence of two phases. Between the two cases, for a given temperature, one can find an inflexion point as shown in fig.1.8. The critical value for χ_{12} is obtained by solving the following:

$$\partial(\Delta\mu_1)/\partial\phi_2 = \partial^2(\Delta\mu_1)/\partial\phi_2^2 = 0 \qquad \text{(eq.1.20)}$$

which gives:

$$\chi_{12c} = 0.5(1+x^{-0.5})^2 \qquad \text{(eq.1.21)}$$

Fig.1.9 was generated from the latter equation to illustrate the fact that χ_{12C} converges towards 0.5 as values for x become larger[15].

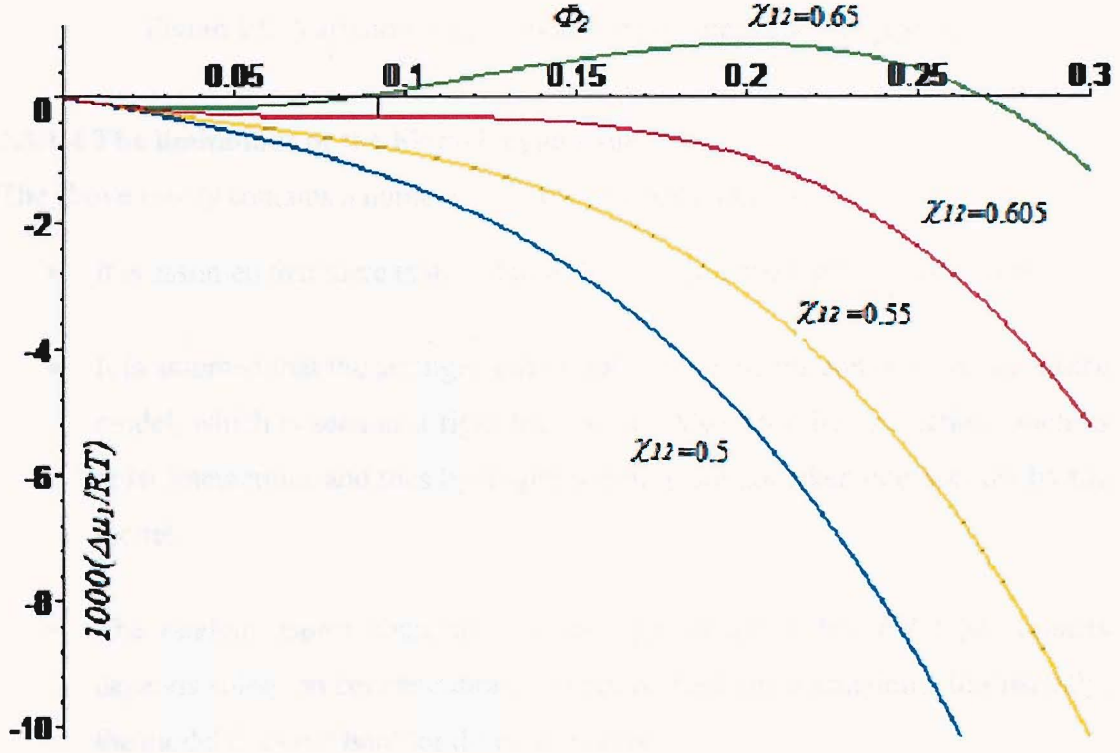

Figure 1.8: Influence of χ_{12} on the variation of the chemical potential of the solvent.

[15] For x=100, χ_{12C} =0.605.

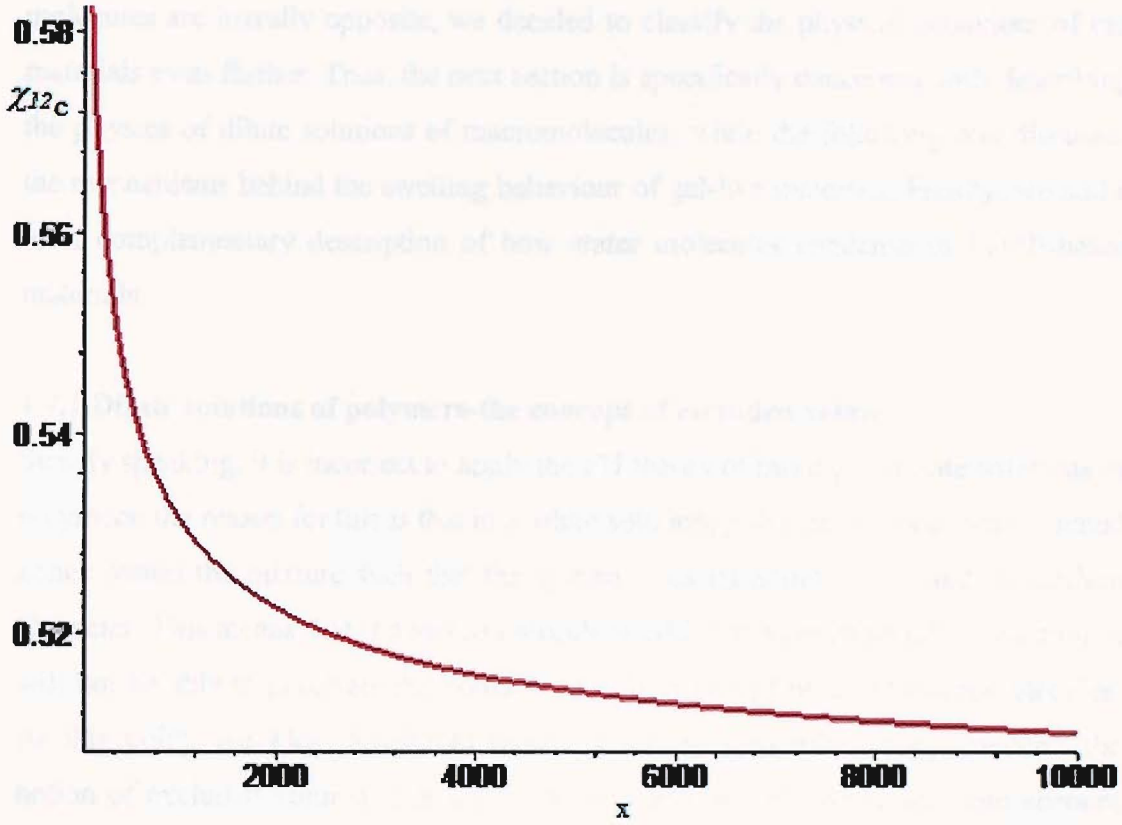

Figure 1.9: Variations of χ_{12C} with the polymerization degree, x.

1.3.1.4 The limitations of the Flory-Huggins theory

The above theory contains a number of significant assumptions:

- It is assumed that there is no volume change upon mixing the constituents.
- It is assumed that the arrangement of polymer segments conforms to the lattice model, which is seen as a rigid framework. Also, specific interactions such as polar interactions and thus hydrogen bonding, are not taken into account by the model.
- The random aspect characterizing the appearance of the *1-2* type contacts depends solely on concentration, and not on specific interactions. Intrinsically, the model does not hold for dilute solutions.

1.4 Experimental implications of the Flory-Huggins theory

We introduced extremely dissimilar materials earlier in this chapter. While LDPE is strongly hydrophobic in nature, the very opposite is the case for our two water-trapping materials. Since the propensity of our materials to bind with water

molecules are literally opposite, we decided to classify the physical behaviour of our materials even further. Thus, the next section is specifically concerned with describing the physics of dilute solutions of macromolecules, while the following one discusses the mechanisms behind the swelling behaviour of gel-like materials. Finally, we add a brief complementary description of how water molecules condense in LDPE-based materials.

1.4.1 Dilute solutions of polymers-the concept of excluded volume

Strictly speaking, it is incorrect to apply the FH theory of mixing to dilute solutions of polymers; the reason for this is that in a dilute solution, polymer chains occupy isolated zones within the mixture such that the system loses its homogeneity and its random character. This means that if a macromolecule is added to an existing dilute solution, it will not be able to penetrate the domains already occupied by other macromolecules. At this point, the Flory-Krigbaum theory develops a complementary concept: the notion of excluded volume. The latter was primarily introduced to take into account the impossibility of finding the centre of mass of one macromolecule in the vicinity of another and we illustrate this in fig.1.10. The dimensional parameters shown on the latter figure, namely Q and u, respectively correspond to the hydrodynamic radius of a solvated macromolecule and to the excluded volume we are talking about. For this spherical object, one can quantify the value for u:

$$u = (32/3)\pi Q^3 \qquad \text{(eq.1.22)}$$

In this case, the variation of the entropy of mixing takes into account the excluded volume:

$$\Delta S_m = -RN_2(\ln\phi_2 - (N_a u / 2V_1 x)\phi_1 + o(\phi)) \qquad \text{(eq.1.23)}$$

where N_a stands for Avogadro's number, V_1 for the molar volume of the solvent, u the excluded volume and higher order terms that will be neglected. Since we are concerned with a dilute solution, we can neglect any thermal reactions. Since $\Delta H_m=0$, eq.1.15 can be employed without considering this component and thus:

$$\Delta\mu_1 = -RT(\phi_2 / x + (N_a u / 2V_1 x^2)\phi_2^2 + o(\phi)) \qquad \text{(eq.1.24)}$$

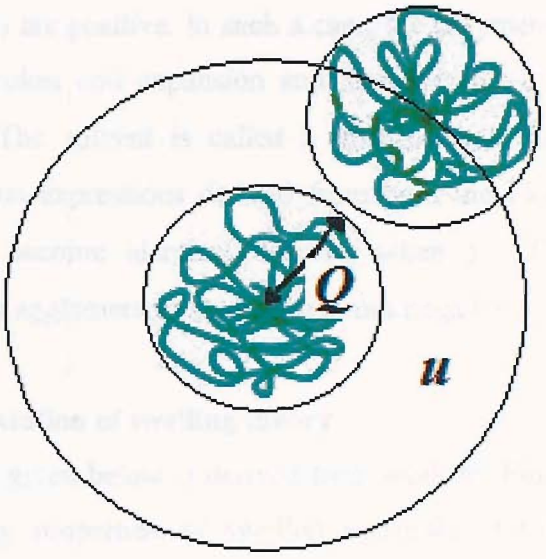

Figure 1.10: Schematic representation of the excluded volume *u*.

At this point, we can define the solute's concentration c_2:

$$\phi_2 = c_2 V_1 x / M_2 \qquad \text{(eq.1.25)}$$

where M_2 stands for the molecular mass of the sample. Eq.1.24 then becomes:

$$\Delta\mu_1 = -c_2 RTV_1 (1/M_2 + (N_a u / 2M_2^2)c_2 + o(c_2)) \qquad \text{(eq.1.26)}$$

This can alternatively be rewritten as follows:

$$\Delta\mu_1 = -c_2 RTV_1 \sum_i A_i c_2^i \qquad \text{(eq.1.27)}$$

where $A_o = 1/M_2$ and $A_1 = N_a u / 2M_2^2$. Importantly, the Flory-Krigbaum theory links the excluded volume to the FH interaction parameter via:

$$u = 2(1/2 - \chi_{12}) x^2 V_1 F(x) / N_a \qquad \text{(eq.1.28)}$$

where *F(x)* is a strictly decreasing monotonic function of *x*. The difference between the Flory-Huggins and Flory-Krigbaum theories solely consists of this additional term, which accounts for the dilute nature of a solution. From the latter theory:

$$\Delta\mu_1 = -RT(\phi_2 / x + (1/2 - \chi 12) F(x) \phi_2^2 + o(\phi))$$

(eq.1.29)

This expression is comparable to eq1.19, since ϕ_2 is small in a dilute solution, and eq.1.19 then gives:

$$\Delta\mu_1 = -RT(\phi_2 / x + (1/2 - \chi_{12})\phi_2^2) \qquad \text{(eq.1.30)}$$

From the previous expressions, we can see how the second virial coefficient A_2 relates to χ_{12} and how the excluded volume depends on the latter parameter, and vice-versa.

coefficients u and A_1 are positive. In such a case, the polymer/solvent interactions are favoured. This provokes coil expansion and increases the excluded volume. When $\chi_{12}=1/2$, $u=A_1=0$. The solvent is called a theta-solvent. At this particular point, $F(x)=1$. The previous expressions derived from both the Flory-Huggins and Flory-Krigbaum theories become identical. Finally, when $\chi_{12}>1/2$, macromolecules in solution tend to form agglomerates since u becomes negative.

1.4.2 A short presentation of swelling theory

The swelling theory given below is derived from work by Flory, which describes the equilibrium swelling properties of swollen materials, but not swelling kinetics. Swelling can be summarized thanks to a single equation that links the number of crosslinks X present in a given volume V_c of collapsed network to V_1, χ_{12} and Φ_2:

$$\phi_2 = (XV_1/(V_c(1/2-\chi_{12})))^{3/5} \qquad \text{(eq.1.31)}$$

Since elastic forces oppose the osmotic force that tends to reduce concentration gradients [44], the physical interpretation for this equation is that equilibrium conditions are met when the elastic forces generated in a swollen network and the osmotic pressure are balanced. Swelling depends on the type of solvent/polymer interactions and structures, and, in this respect, we need to distinguish extreme cases such as water swelling in polyethylene and in our superabsorbent material. Unlike PE, our superabsorbent swells water to a great extent; it is a material that can be swollen by up to a thousand times its own weight, without falling apart. We can define the affinity of PE and water on the basis of the difference of their solubility, and since water and PE exhibit respective solubility parameters of 47.4 $MPa^{1/2}$ and 16 $MPa^{1/2}$ [22], we can already predict that their reciprocal affinity has to be very limited. This implies that the only way to reduce the magnitude of ΔH_m, see for instance eq.1.13, is by considering values for Φ_1 close to 0. Fedors [45] considered a limiting form of one of Flory's equations regarding the equilibrium solubility of water in hydrocarbon polymers:

$$\phi_1 = \exp(-1-\chi_1) = \exp(-1.34-(\upsilon_1/RT)(\delta_1-\delta_2)^2) \qquad \text{(eq.1.32)}$$

where Φ_1 is the volume fraction of liquid absorbed at equilibrium and v_1 the molar volume of water. For ethylene-propylene rubbers, values for Φ_1 are ~$2x10^{-4}$ [45]. However, very often, water uptake greatly exceeds that expected for equilibrium solubility [45], because polar impurities attract water molecules. Also, experimental parameters such as oxidation levels and temperature have significant effects on

solubility and water uptake levels. In practice, water solubility in PE appears also to be linked to the level of oxidation within the material. Experimental work [46,47] has shown that the overall permeability of branched PE remains constant, even under a broad range of oxidation levels. Conclusions from the same studies show that if solubility increases, diffusivity decreases accordingly, and, by chance, cancels out with the solubility variations. Temperature variations are also reported to have strong effects on the most hydrophobic materials [48]. For example, a series of three different elastomers were found to exhibit a higher permeability when the temperature was increased [49].

The accumulation of water droplets leads to the formation of growing cavities and this condensation phenomenon is also known as clustering.

1.4.3 Water clustering in polyethylene

Due to the extreme lack of polarity of polyethylene macromolecules, water molecules develop a propensity to group into a finite number of clusters distributed throughout the bulk. This behaviour has already been observed experimentally for PE [50], thanks to optical evidence related to the opacity of the material. What tends to happen, in the case of hydrophilic materials, is that once water starts diffusing into the bulk, subsequent water molecules tend to agglomerate with either the previous ones or other polar species, as a result of the lack of affinity between the two substances. Water molecules group and interact with each other in their surroundings.

The equation quantifying the interactions of water molecules is the following [48,51]:

$$G_{11} = \int\!\!\ldots\!\int (1 + \sum_{ij} f_{ij} + \sum_{ij} \sum_{kl \neq ij} f_{ij} f_{kl} + \ldots) dq \qquad \text{(eq.1.33)}$$

It is sometimes called the cluster integral (G_{11}) [52,53]. This equation is derived from statistical thermodynamic concepts, where the f terms in it stand for the molecular interactions in pairs and higher order terms represent the interaction of three or more molecules at a time. This equation can be used to evaluate the mean number of water molecules in the neighbourhood of another water molecule. One can show that the latter quantity is proportional to the following quantity, $c_1 G_{11}$ [52,53]:

$$c_1 G_{11} = (1 - \Phi_1)(\partial \ln \Phi_1 / \partial \ln a_1)_{p,T} - 1 \qquad \text{(eq.1.34)}$$

where c_1 and a_1 stand for the molar concentration and activity of water. Starkweather [52] reports that the tendency of water to form clusters increases steadily with the

global humidity level. In practice, it will also be important to know how damaging growing cavities can be. Alternatively, it might be useful to know whether water clusters formed in PE are large enough to exhibit the well-known characteristics of bulk water for experimental purposes; to quote Ugalde et al. [54], a single water molecule has neither a melting nor a boiling point.

1.5 Overview of the following chapters

This thesis is a detailed account of work carried out using model materials that potentially represent two of the layers within a power cable; LDPE-based systems for the insulation layer and two different water-blocking systems for a layer with this purpose. The following is a brief summary of the work presented in each chapter:

Chapter 2, provides essential information about sample preparation and our testing techniques. We also introduce the nomenclature used throughout the following results chapters.

Chapter 3, considers the morphology and molecular mobility characterizing our LDPE-based systems.

Chapter 4, investigates experimental diffusion kinetics of water in LDPE-based materials and LDPE/EVA blends using both analytical and numerical methods.

Chapter 5, aims at quantifying, via viscometry, the hydrophilic character of guar molecules subjected to accelerated ageing conditions.

Chapter 6, complements the data obtained by viscometry. Data obtained from spectroscopic techniques such as Fourier-Transform Infrared and Raman spectroscopy are discussed.

Chapter 7, comprises the analysis of the ageing behaviour of our synthetic superabsorbent material.

Chapter 8, finally, summarizes the above results, draws conclusions and contains a proposal for future work based on the ensemble of our results.

Chapter 2

Experimental techniques and sample preparation

2.1 Introduction

This section provides specific information about the experimental techniques, sample preparation procedures and nomenclatures used throughout the subsequent results chapters. The presentation of our different testing techniques has been arranged in such a way that principal procedures are dealt with at first. Supplementary or preparation methods are described afterwards.

2.2 Main testing techniques

2.2.1 Differential scanning calorimetry (DSC)

Thermal analysis of synthetic polymers has been routinely performed with a Perkin-Elmer DSC7 model. Our data were acquired and processed using Pyris software. The majority of our experiments were carried out on LDPE-based compounds to examine structural variations resulting from the thermal treatment of such materials.

2.2.1.1 Principle of the method

A power-compensated DSC measures the enthalpy variations in a sample as a function of temperature, or time, if the temperature is fixed. Fig.2.1 illustrates the key elements of the instrument. This demonstrates that DSC employs two separate heating furnaces; the latter being related to the sample and reference holders. In practice, sample and reference specimens are heated simultaneously according to the same thermal program and the temperature of each is determined separately. Any measured differences in temperature, reported as $\Delta\theta$ in fig.2.1, form the basis of the DSC technique. Since both sample holders possess separate heating and cooling systems, the system adjusts the

sample's heat flux so that temperature gradients are constantly nullified. It is this constant feedback process that is referred to as the power compensation principle [55]. To normalize DSC data, it is important to measure precisely the sample mass, reported as *m* in fig.2.1.

Thus, the DSC technique allows the measurement of endothermic and exothermic processes, attributable either to chemical reactions or thermodynamic transitions within the samples; the measured parameter being the rate of change of enthalpy *H*, *dH/dT* or specific heat capacity C_p, and the main input parameter the heating rate, *dT/dt*. In view of this, it is necessary to calibrate the instrument prior to starting any experiment so that experimental data can be confidently reproduced.

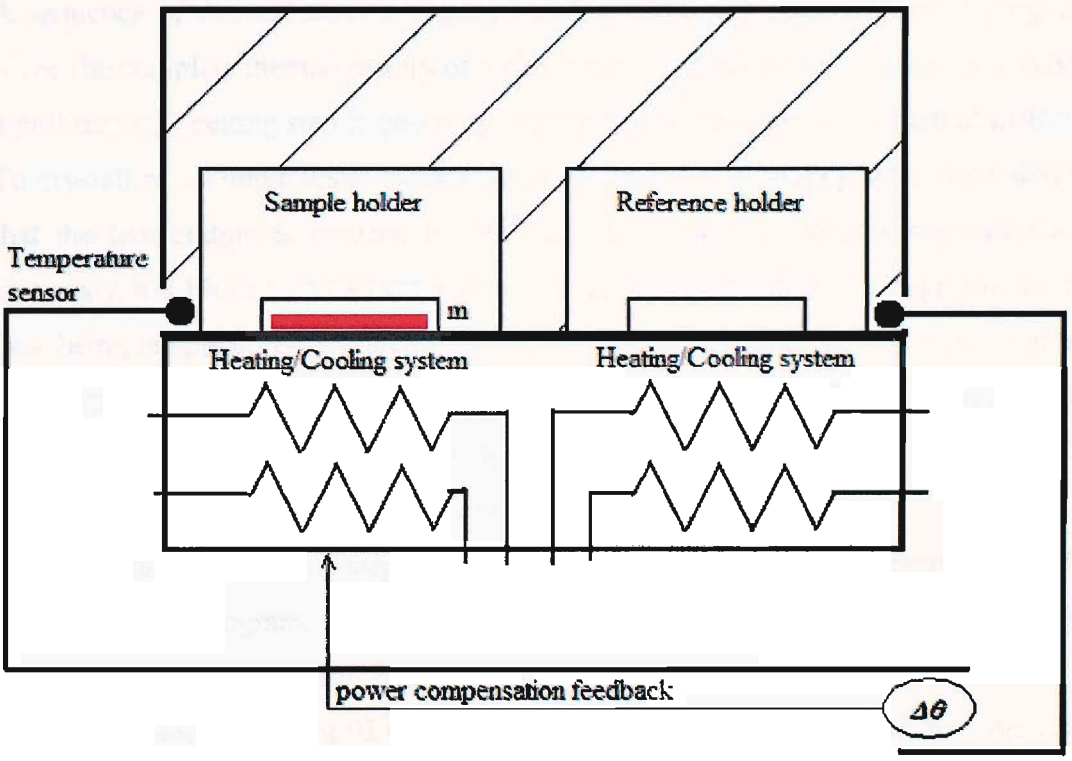

Figure 2.1: Schematic representation of a DSC testing chamber (*m* denotes the sample mass and $\Delta\theta$ the measured temperature difference between furnaces).

2.2.1.2 Calibration and sample encapsulation

High-purity indium was used to calibrate the instrument, on a daily basis. This operation was achieved by monitoring shifts in the indium melting peak along the temperature axis. Calibration was always carried out using the same thermal program. The temperature of the sample holder was initially set to 150°C, and, a sufficient amount of time was left for the instrument to stabilize; and only then was the melting

ramp initiated, up to a final temperature of 160°C[1]. Since indium is expected to exhibit a sharp melting peak at 156.6°C, one can use the temperature at which the melting peak appears as a new calibration input, prior to reiterating the calibration process as many times as needed until the peak's temperature coincide with the literature value for the melting of indium.

Routinely, samples were weighed prior to their encapsulation; their mass was adjusted so that it ranged between 5 and 10 mg; whenever possible, samples were cut as thin and even slices, to ensure optimum thermal contact with the sample holder.

2.2.1.3 Typical thermal programs and sample nomenclature

A sequence of thermal steps is required to form a comprehensive thermal program. Since the complete thermal history of a given sample is not always known in advance, a preliminary, melting step is generally needed to erase any previous thermal history[2]. To crystallize a sample under isothermal conditions, a fast cooling stage is needed so that the temperature is reduced to that desired, in order to achieve crystallization; obviously, a sufficient crystallization time is required to complete this stage, the former time being temperature-dependent. Further crystallization steps can then be carried out in a similar way, before the sample is finally quenched. Then, a heating stage can be started at a chosen rate. A common value reported for this parameter is 10°C/min [55], and this was the value we adopted for most melting scans.

Crystallization and melting steps were habitually implemented as successive parts of a single thermal program. For a given material, crystallization temperatures will be referred to as follows; for instance, (Mat.A/92C) indicates that Material A was crystallized isothermally at 92°C, with no mention of the required crystallization time. For obvious reasons, this nomenclature does not indicate explicitly that the sample was subjected to an initial melting phase prior to crystallization. Material C's nomenclature requires complementary details, since the latter can be crosslinked and experiments dealing specifically with crosslinking kinetics require a specific classification. Thus, (Mat.C/200/0.5) indicates that Material C was heated at 200°C for a period of half a minute. Then, (Mat.C/X/92C) indicates that a fully crosslinked sample of Material C

[1] For the calibration method, the heating rate was always set to 10°C/min.

[2] The melting trace of an unprocessed material treated "as received" also provides preliminary information about its nature in terms of crystallinity and melting temperature.

was crystallized isothermally at 92°C. Where critical for interpretation, the significance of this notation is reiterated at key points within the text.

2.2.2 Dynamic mechanical testing

Dynamic mechanical tests were carried out using a Rheometrics Solids Analyzer II (RSAII) linked to a host computer running the Rhios software package. Most experiments were executed on LDPE-based specimens whose thermal history was controlled by reproducing crystallization conditions equivalent to those employed throughout DSC experiments.

2.2.2.1 Principle of operation

The Rheometrics Solids Analyzer (RSAII) measures the viscoelastic properties of solid materials. This method involves imposing an oscillatory strain (~10%) on a sample via the cantilever testing geometry. The resulting sinusoidal stress is then measured and correlated with the input strain. If the sample behaves as an ideal elastic solid, then the resulting stress is in phase and proportional to the strain, according to Hooke's law:

$$\sigma = E\varepsilon \qquad \text{(eq.2.1)}$$

where σ and ϵ respectively stand for the in-phase stress and strain; E being Young's modulus. If the sample behaves as an ideal fluid, then the stress is proportional to the strain rate according to Newton's definition for shear viscosity:

$$\sigma = \eta(d\varepsilon / dt) \qquad \text{(eq.2.2)}$$

where η represents the sample's viscosity. In this case, the stress signal is out of phase with the strain, stress preceding strain by an angle of $\pi/2$. For viscoelastic materials, the phase shift between stress and strain occurs somewhere between the elastic and viscous extremes. Thus, the stress signal generated by a viscoelastic material can be separated into two components: an elastic stress in phase with strain and a viscous stress which is in phase with the strain rate (i.e. $\pi/2$ out of phase with the strain). The mechanical loss or loss tangent ($tan(\delta)$) is then obtained from the elastic and viscous components of the complex modulus. This quantity can be defined in the complex plane, being a composite quantity which contains contributions from both the elastic and viscous moduli, E' and E'':

$$E^* = E' + jE'' \qquad \text{(eq.2.3)}$$

The expression for the loss tangent is:

$$\tan\delta = E''/E' \qquad \text{(eq.2.4)}$$

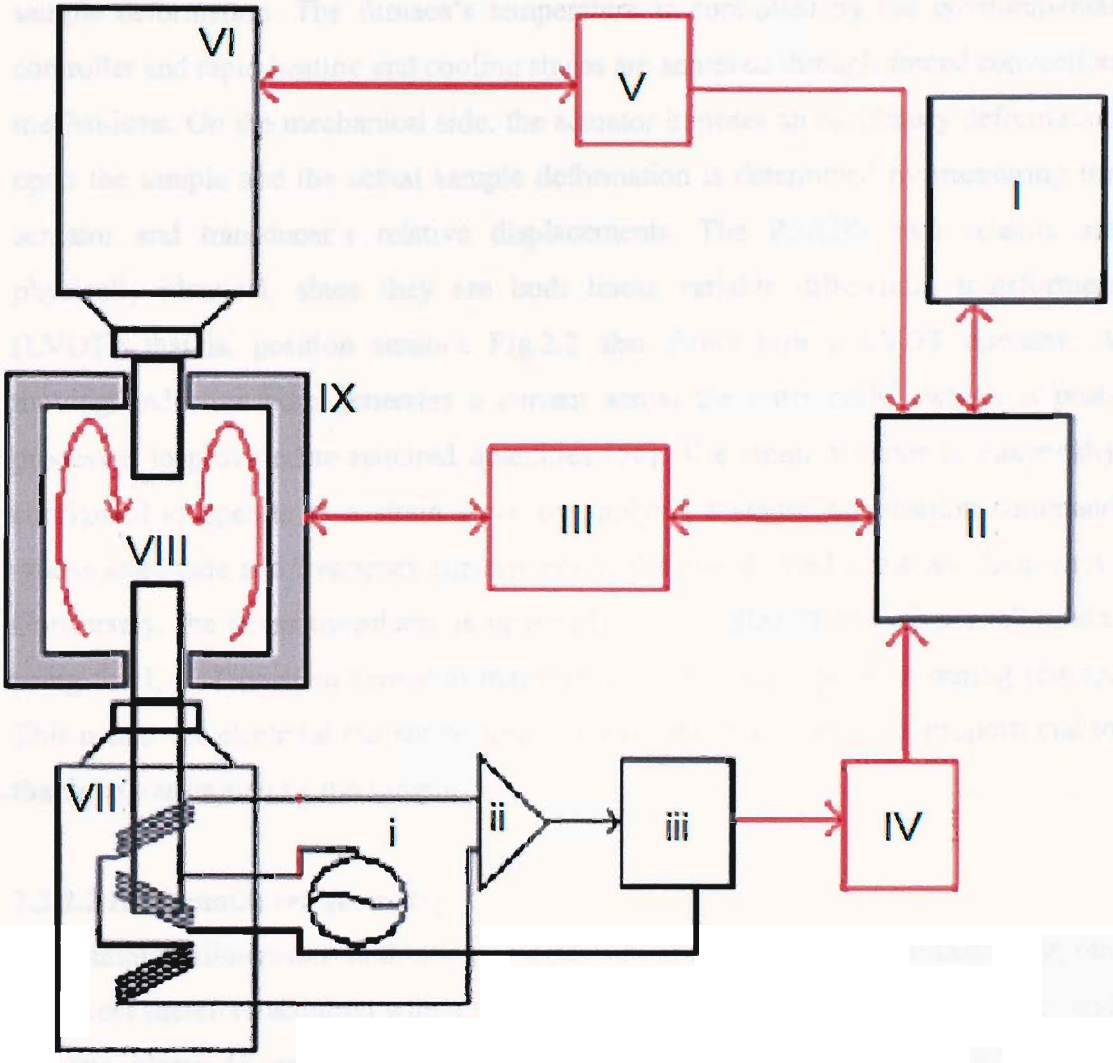

Figure 2.2: Schematic representation of the RSAII's architecture.

Fig.2.2 shows the RSAII's basic architecture. A sample is placed in a closed furnace between an actuator and the transducer that measures the resultant force generated by

sample deformation. The furnace's temperature is controlled by the environmental controller and rapid heating and cooling stages are achieved through forced convection mechanisms. On the mechanical side, the actuator imposes an oscillatory deformation upon the sample and the actual sample deformation is determined by measuring the actuator and transducer's relative displacements. The RSAII's two sensors are physically identical, since they are both linear variable differential transformers (LVDT); that is, position sensors. Fig.2.2 also shows how a LVDT operates. A moving, inductive core generates a current across the outer coils[3], which is post-processed to provide the required quantities [56]. The strain actuator is electrically configured to operate as a strain servo by applying a sinusoidal position command whose amplitude and frequency corresponds to the user-defined strain and frequency. Conversely, the stress transducer is operated in a so-called "force rebalance" mode, using the LVDT position sensor to maintain a constant axial position during testing. This means the electrical current required to maintain axial position is proportional to the force transmitted by the sample.

2.2.2.2 Dual cantilever geometry

The sample's dimensions and modulus determine the choice of fixture geometry; our data were therefore acquired with a dual cantilever fixture. This comprises a lower and an upper clamp designed to hold a solid, rectangular specimen in a horizontal attitude. When mounting the sample, the actuator grips the sample ends, while the transducer grips the centre of the specimen, see fig.2.3. The initial adjustment of clamping pretension to a zero initial static force is achieved by balancing a force-meter through a potentiometer. Importantly, sample dilatation effects are compensated by spring loaded clamps mounted onto the lower fixture, so that no further correction is needed during heating/cooling cycles.

[3] The central coil in fig.2.2 is a supply winding, whereas the outer coils are pickup windings [2.2].

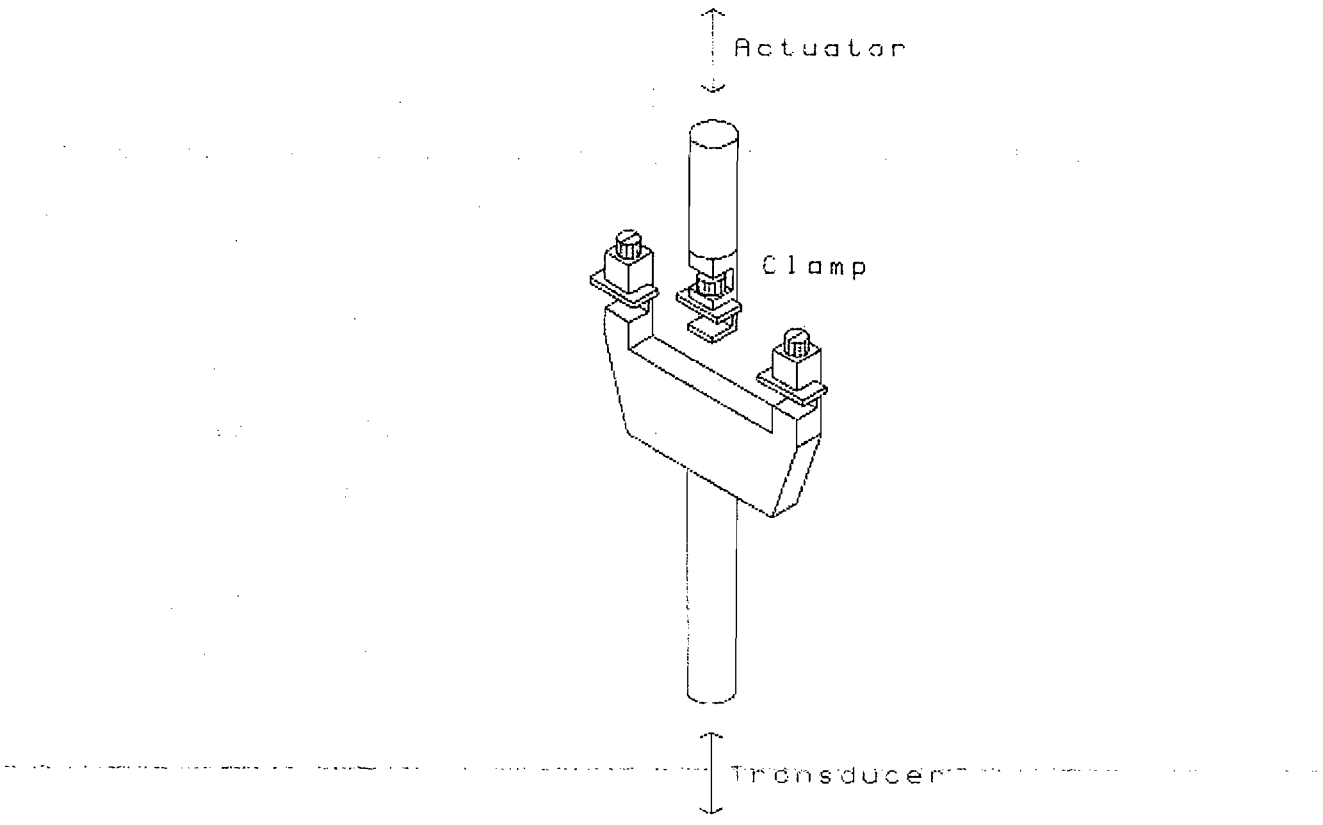

Figure 2.3: Dual cantilever testing fixture-taken from Greenway [1].

2.2.2.3 Sample preparation, nomenclature and testing methods

Samples were made from pellets placed between glass slides and pressed evenly on a hot plate. Thickness control was achieved using lateral glass slides as spacers. Once plaques were formed in this way and quenched either in air (SQ) or in water (FQ), they were cut with a razor blade to conform to the required testing dimensions. Typically, our strips were 5 mm wide and 2 mm thick. Then, annealing and crystallization treatments were carried out directly in the RSAII's furnace. In comparison to the automated DSC cooling method, these samples could either be quenched in air or water. Nevertheless, the crystallization and crosslinking protocols were derived from DSC results, and, hence, sample nomenclature remains as above. In addition, we distinguish (Mat.A/SQ) and (Mat.A/FQ) that respectively stand for a slowly or rapidly quenched sample of Material A.

Both isochronal and isothermal testing methods were applied to test our samples. Isochronal tests were generally carried out from 20 to 80°C, at a frequency of 1 Hz. Unlike DSC experiments though, heating cycles are not continuous. Isochronal methods require a choice of soaking time intervals, which we evaluated by probing the

value of Young's modulus as a function of time[4]. Isothermal tests were also performed, which explore the response of the sample to a range of frequencies. Our tests were carried out between 0.016 and 16 Hz and repeated at different temperatures, i.e. 20, 50 and 70°C. Finally, graphical time-temperature superposition methods were used to construct master relaxation curves.

2.2.3 Optical microscopy

A LEITZ Aristomet compound microscope was used in this study to examine the different microstructures formed in our LDPE-based materials. This microscope comprises a power-adjustable light source and an optional set of polarizers to observe optically anisotropic entities. A JVC CCD camera is additionally linked to the microscope such that microphotographs can be captured using Auto-Montage software.

2.2.3.1 Birefringence and crystallinity

There are different causes for birefringence, such as strain-induced, flow-induced or structural birefringence [57]. However, we were exclusively interested in the last of these, which is due to the formation of crystalline entities in LDPE. Specifically, PE chains fold to form thin lamellar arrangements, whose thickness and probability of occurrence are reduced by molecular branching [1]. Crystals generally consist of ordered arrangements of atoms that are optically anisotropic, which means that they have at least two principal refractive indices [58]. This forms the optical basis from which birefringence originates.

2.2.3.2 Sample preparation and nomenclature

LDPE-based samples were pressed on a hot plate at sufficiently high temperatures, that is, between 130 and 200°C, depending on the sample type. In practice, small amounts of materials were placed on a standard glass slide and melted before being made thinner by pressing down a cover slide placed on top of the sample. Crystallization and crosslinking treatments were performed using a temperature-controlled Mettler hot stage, and slow and fast quenching methods were carried out in a similar manner to

[4] 90 to 120 seconds were typically enough to reach constant values for E.

that used for the RSAII's samples. Hence, the sample nomenclature remains unchanged.

2.2.4 Viscometry

Dilute solution viscometry was carried out with an Ubbelohde viscometer. This instrument provided a way of probing the interactions between water and guar molecules.

2.2.4.1 Principle of the method

A viscometer is a container with a standard-sized orifice that controls the rate at which a given fluid flows. Thus, raw data derived from viscometry experiments are flow times; these are alternatively called efflux times. Fig.2.4 shows a schematic representation of an Ubbelohde viscometer immersed in a thermal bath. The viscometer consists of three vertical tubes: the largest tube, situated on the left-hand side of the figure, is connected to a reservoir, which is initially filled with the fluid to be tested. The active element of the viscometer is the thin capillary on the right-hand side of the diagram; the latter fills up a constant volume, including a bulb, which is situated above the capillary and is delimited by lower and upper marks. It is these marks that allow the efflux times to be recorded. In short, an Ubbelohde viscometer is a vertical capillary in which the tested fluid is subjected to pure shear. Physical parameters of interest can then be derived after measuring the efflux times for a series of fluids diluted sequentially to varying concentration levels. Analysis also necessitates a value for the efflux time of the pure solvent. Once the efflux times for the solution and the solvent, t and t_o, have been acquired, one starts by calculating the relative viscosity of the fluid, η_{rel}, using the following relationship[5]:

$$t / t_o = \eta_{rel} \qquad \text{(eq.2.5)}$$

Definitions for inherent and reduced viscosities, η_{red} and η_{inh}, can be established from that of the relative viscosity:

$$(\eta_{rel} - 1) / C = \eta_{red} \qquad \text{(eq.2.6)}$$

$$\ln(\eta_{rel}) / C = \eta_{inh} \qquad \text{(eq.2.7)}$$

Here, C stands for the concentration of the tested solutions.

[5] This formula assumes that the ratio between the densities of the tested fluid and that of the pure solvent is close to 1.

Plots derived from reduced or inherent viscosity versus concentration relate respectively, to analysis methods originally devised by Huggins and Kraemer [59,60]. Both methods are employed to derive a value for the intrinsic viscosity, that is, a viscosity value extrapolated to zero concentration. Graphically, one can find the intrinsic viscosity $[\eta]$ and a constant k by fitting experimental data to:

$$\eta_{red/inh} = k[\eta]^2 C + [\eta] \qquad \text{(eq.2.8)}$$

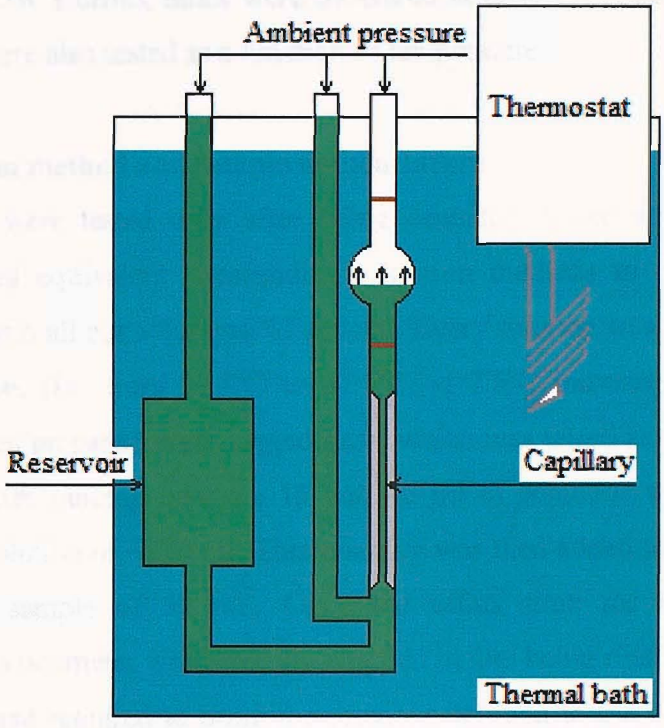

Figure 2.4: Schematic representation of an Ubbelohde viscometer immersed in a thermal bath.

2.2.4.2 Data acquisition

Recording efflux times from a viscometer is a straightforward task, and, in this study, all efflux times were recorded manually using a digital timer. However, contamination effects must be avoided, especially since multiple series of measurements were carried out with similar series of dilute solutions. Furthermore, we had actively to manage the fact that the viscometer could remain unused for periods of time.

2.2.4.2.1 Cleaning method and idle time management

An initial preparation of permanganic acid was first employed to rid the viscometer of any organic contaminant. Subsequently, the viscometer was stored entirely filled with the testing solvent, namely distilled deionised water (DDW), whenever it remained

unused. By doing so, we wished to prevent any residue from drying and adhering to the viscometer's surfaces, since such contamination could modify the efflux time for subsequently tested samples. Prior to starting any series of measurements with dilute solutions obtained from guar and DDW, the viscometer was routinely filled and rinsed three consecutive times with DDW. To check the grounds for this method, the efflux time for DDW was occasionally measured and compared to initial DDW's efflux times. These DDW's efflux times were measured at different temperatures since the guar solutions were also tested as a function of temperature.

2.2.4.2.2 Dilution method and sample nomenclature

Guar solutions were tested only after being centrifuged, see section 2.3.2. Once refined, we used equivalent "descending" dilution methods to perform series of measurements with all our solutions, 17 in total. Every solution was tested at least five flow temperatures (i.e. from 27.5°C to 57.5°C, at 7.5°C increments), apart from a reference solution prepared from unaged guar, which was tested at 7 temperatures. In practice, quantities ranging between 15 and 45 ml of solution[6] were taken from a refined parent solution of ~250 ml. This quantity was then added to DDW to give an initial solution sample of 50 ml[7]. Once the efflux time for this solution was determined, the viscometer was carefully emptied before being rinsed with the precise quantity of solvent required to bring the previous solution to the next concentration. The above method provided a way of recovering the maximum amount of the previous solution, by draining the viscometer's content with a known quantity of DDW. This method was repeated to give progressively more dilute samples. Typically, the final concentration of the solution was eventually 5 to 10 times lower than that of the initial 50 ml specimen.

We classified 16 aged guar samples as a function of their ageing conditions, see section 2.3.1.2. These were termed ($G50/O_2$), ($G50/N_2$), ($G90/O_2$) and ($G90/N_2$) in reference to the gas composition and temperature they were subjected to; N_2 and O_2 respectively standing for nitrogen and air. The duration of the ageing treatments was also included in the nomenclature; ($G50/O_2/24W$) is therefore a sample that has been aged in air for 24 weeks.

[6] A quantity that was generally augmented with the testing temperature but who also depended on the initial concentration of the parent solution.

[7] A minimal amount required to carry out a test.

2.2.5 Fourier-transform infrared spectroscopy

A Nicolet FTIR spectrometer linked to a computer running the Omnic software package was employed to collect infrared spectra. Infrared spectroscopy is a widely used technique in organic chemistry and it is mostly used for its capacity to detect IR-sensitive groups of atoms in organic molecules; in our case, this technique was primarily used to explore chemical modifications caused by accelerated ageing to guar molecules.

2.2.5.1 Description of the technique

A schematic representation of the optical bench used in direct transmission mode is given in fig.2.5. An infrared beam is split by a beamsplitter into two beams, which are directed along orthogonal paths to two distinct mirrors, to give an optical arrangement similar to a Michelson interferometer. Thus, one beam is reflected off a stationary mirror, while its counterpart is reflected off a moving mirror. The displacement of this mirror makes the length of the optical path variable when compared to the fixed distance between the stationary-mirror and the beamsplitter. When the rays recombine at the beamsplitter, the time-dependent difference in path lengths creates constructive and destructive interferences, which form the basis of an interferogram[8]. As such, the latter contains all the frequencies that make up a time-domain spectrum. This time-modulated signal goes through the sample which absorbs sample-specific wavelengths. A sensor finally collects these variations and the signal is processed using Fourier techniques, to give the final spectrum. Once processed, the final spectrum is displayed as absorbance versus wavenumber, ranging from 400 to 4000 cm^{-1}. The beam's photon energy E is calculated using the following relationship [61]:

$$E = h\nu = hc/\lambda \qquad \text{(eq.2.9)}$$

Here, h and c are Planck's constant and the speed of light, and ν stands for the frequency. Infrared energy levels range from 8 to 40 kJ/mol. This range encompasses vibrational frequencies in most covalent molecules [61]. The effect of energy on

[8] When the fixed mirror and moving mirror are equidistant from the beamsplitter, the amplitudes of all frequencies are in phase and interfere constructively. This position of zero path difference is where the interferogram centerburst or maximal light intensity occurs; but as the moving mirror is moved away from the beamsplitter, an optical path difference is generated. A pattern of constructive and destructive interferences is generated which depends on the position of the moving mirror and on the frequency of the radiation resulting in the complex time-modulation of light intensity.

fundamental absorption processes, essentially stretching, can be understood thanks to an uncomplicated mechanistic representation. Bonded atoms of known masses, i.e. m_1 and m_2, can be considered to be analogous to masses linked by a spring, with spring constant K. The natural frequency of a bond is them given by [61]:

$$\nu = (2\pi c)^{-1}[K/(m_1 m_2/(m_1 + m_2))]^{1/2} \qquad \text{(eq.2.10)}$$

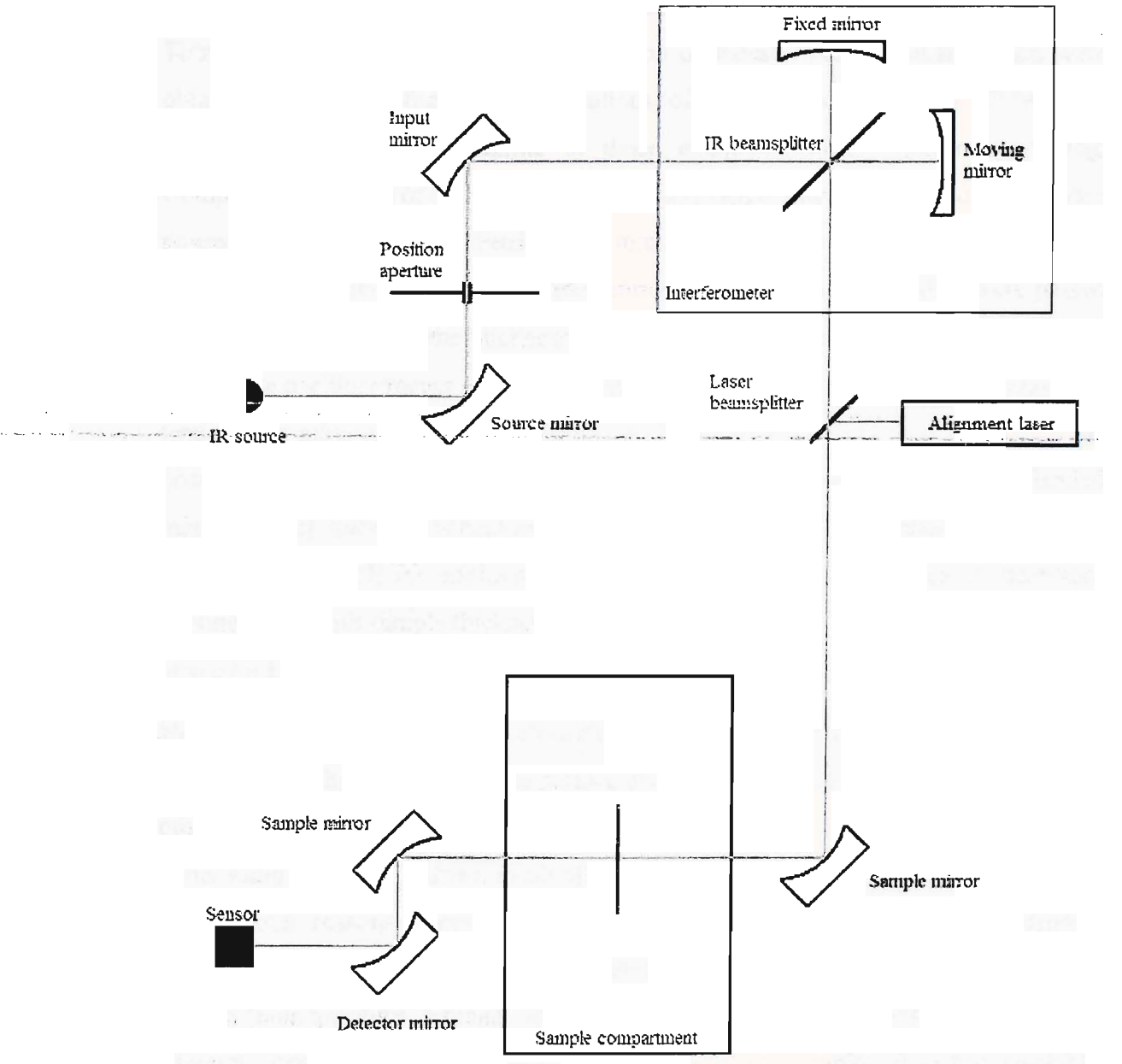

Figure 2.5: Schematic representation for the arrangement of the FTIR's optics in transmission mode.

This relationship provides fairly accurate values for stretching frequencies, but, more importantly, one can predict that identical atoms will require higher energies when covalent bonds are double or triple; this simply reflects the fact that the spring constant

K increases accordingly. This notion becomes important in interpreting a spectrum, and, generally, fundamental absorption modes are also be classified as a function of energy. Generally, bending requires less energy than stretching; asymmetric stretching requires more energy than symmetric stretching [61].

2.2.5.2 Sample preparation and nomenclature

Thin films were cast from soluble fractions of locust bean and guar, which were obtained from centrifuged dilute solutions of materials dissolved in DDW. The employed solutions were similar to those employed during viscometry testing. Comparable amounts of dilute solutions, typically ranging between 15 and 30 ml, were poured into standard glass Petri dishes and sufficient times were allocated for the DDW to evaporate completely. When completely dry, the resultant films were peeled from the glass surfaces; the thickness of these typically ranged from 5 to 10 μm. Even though the peeling process was difficult at times, due to the film's brittleness and their tendency to stick and coil up, our goal was to keep the sample thickness as low as possible. In practice, we followed empirical rules especially recommended for blended materials [62] since the optical properties of the tested specimens should obey Beer-Lambert's law [62]; for information, this law specifies that absorbance, A, decreases exponentially with sample thickness [63]:

$$A = ax = \log_{10}(I_o / I) \qquad \text{(eq.2.11)}$$

Here, a, x, I_o and I stand for the absorption coefficient, sample thickness, the intensity of the incident light on the sample surface and the intensity of light emerging from the other side of the sample.

Other samples, made of dried, insoluble guar fraction, could not be prepared as above, for obvious reasons. They were consequently cut and pressed in a diamond compression cell specifically designed to flatten and hold solid, uneven samples. Sample nomenclature remains identical to that used during viscometry testing although, since the diamond compression cell was only employed to test insoluble fractions, we do not specify sample type in the nomenclature.

2.2.5.3 Calibration and data acquisition

The calibration of the spectrometer requires the instantaneous composition of the gaseous atmosphere surrounding the sample in the testing chamber to be taken into

account. In practice, carbon dioxide and water vapour are strong infrared-absorbers [61]. Thus, a background spectrum was routinely acquired prior to placing any sample in the test chamber, and is, then, automatically subtracted from subsequent sample spectra. Both spectra are obtained by accumulating a given number of acquisitions at a discrete spectral resolution. We chose a resolution of 4 cm^{-1}, since lower values did not appear to improve significantly the spectral quality obtained from our samples. However, the total number of acquisitions was changed according to the sample holder. Standard spectra were obtained using 128 or 256 accumulations, whereas, when the diamond compression cell was used, this was increased up to 4096. This is due to the fact that the overall light transmission is greatly reduced when this device is employed, because of the diamond's size. Consequently, more accumulations are then required to improve the quality of the collected spectra.

2.2.6 Raman spectroscopy

A Renishaw RM1000 spectrometer linked to a host computer running Wire and GRAMS/32 software was employed to collect Raman spectra. Raman spectroscopy is generally seen as complementary to infrared spectroscopy, in the sense that not all molecular vibrations are both Raman and infra-red active [64]. In practice, Raman spectroscopy also differs from infrared spectroscopy because sample preparation is considerably easier; the technique becomes therefore more versatile. Data were collected to characterize guar and locust bean samples, again, to complement our viscometry data.

2.2.6.1 Description of the technique

Raman spectroscopy involves using monochromatic laser light[9] to excite a sample and, then, analyzing the energy distribution of the backscattered photons. Scattering mechanisms can be classified on the basis of the difference between the energy of the incident and scattered photons, this difference being transposed onto a frequency scale to provide a quantity denoted by the Raman shift, Δv. If the energy of the incident photon is equal to that of the scattered one ($\Delta v=0$), the process is called elastic or Rayleigh scattering, see fig.2.6. If the energy of the incident photon is different to that

[9] The spectroscope includes a Renishaw NIR 780TF semiconductor diode laser of wavelength 780nm with a maximum output power of 25mW.

of the scattered one, the process is called Raman scattering or inelastic scattering. The probability of inelastic scattering is drastically lower than that of elastic scattering, and, additionally, the occurrence of Anti-Stokes scattering is also much lower than Stokes scattering [64]. Fig.2.6 shows how the above scattering processes differ from one another.

Raman spectra are usually plotted in intensity or Raman counts versus Raman shift. Like their FTIR counterparts, Raman spectra can be split into distinct zones to facilitate interpretation.

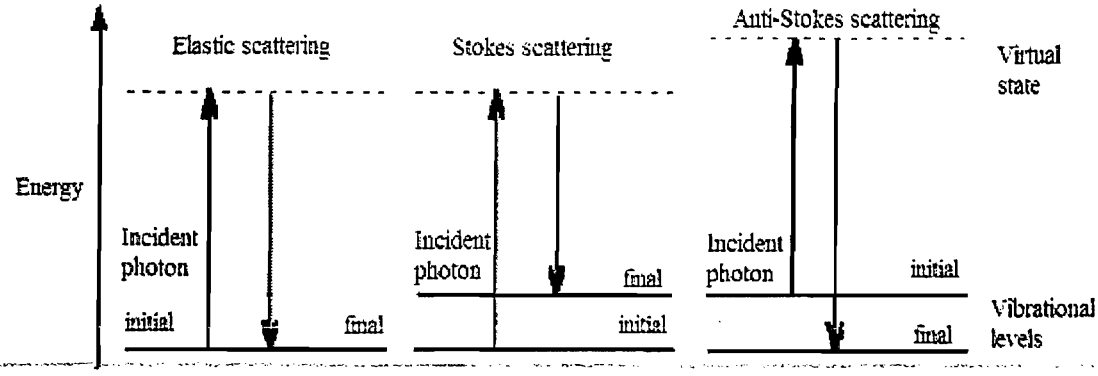

Figure 2.6: Illustration of Rayleigh and Raman scattering-redrawn from [64].

2.2.6.2 Sample preparation and nomenclature

Samples were generally prepared using a Specac press and a set of metallic dies. The advantage of this approach stems from the fact that mirror-like surfaces are used to compress powder or thin film samples to give pellets with smooth surfaces[10]. To avoid cross-contamination effects, the dies were routinely cleaned between every sample preparation. Uncompressed samples, such as raw guar powder, were also analyzed to probe the effect of sample preparation on the obtained spectra. Subsequent sample nomenclature follows once more that adopted for viscometry and FTIR spectroscopy.

2.2.6.3 Calibration and data acquisition

Prior to starting a series of experiments, the spectrometer was calibrated using a silicon standard. The resulting signal consists in a narrow peak whose intensity stabilizes after a while, hence experiments were only begun once the exciting laser had stabilized, typically after 60 minutes.

[10] Samples were obtained under a nominal pressure of two tons.

Throughout this study, the instrument was operated in non-confocal mode. This configuration was chosen to maximize signal throughput, thus reducing acquisition times. A great number of spectra were acquired individually using runs of 24-hours duration, involving the repeated acquisition (i.e. 2400) of spectra. For each, the signal was integrated over 30 s duration and extended to cover the required range (extended mode)[11]. Shorter runs were also carried out in a fixed range mode centred at a particular frequency. For this, 10 runs of 30 seconds each were, typically, acquired.

2.2.7 Conductivity measurements for liquid samples

Conductivity experiments were conducted on liquid samples prepared from our absorbent material. The key element of the experimental arrangement is a WAYNE KERR Universal Bridge B221 linked to a parallel plate capacitor that can be immersed in the liquid to be tested.

2.2.7.1 Principles of the method

Fig.2.7 shows a schematic representation of the experimental arrangement used to evaluate the conductivity and permittivity of liquid samples. To do this, a parallel plate electrode arrangement (i.e. a capacitor) is located, tightly, within a glass container, which also serves as the sample holder. This capacitor is linked to the testing bridge that generates an AC signal at a fixed frequency of 1591.5 Hz. Once calibrated and set to work, the bridge must be balanced manually. The latter possesses two distinct sets of knobs; one of which adjusts a resistive element while the other enables a reactive element to be varied. Obviously, the bridge can then only be balanced properly by adjusting both the above parts of the impedance in concert, which makes the experimental work difficult when dealing with rapidly evolving quantities. Fig.2.7 shows that an additional part of this experimental setup was a Philips PM3267 oscilloscope, which helps the bridge to be balanced with greater accuracy. Fig.2.7 also reveals a crucial part of the testing system; a copper screen which prevents discharges between the upper parts of the electrodes. It is essential to minimize stray capacitances since, otherwise, our readings would be biased and measured quantities would deviate

[11] Shorter runs enable any incongruous behaviour to be visualized during a run, since, in the instrument's extended scan mode, the display is refreshed only once one acquisition is fully terminated.

from those of the tested sample. Temperature control was achieved using to a TECHNE Tempette TE-8A temperature controller to regulate the bath temperature.

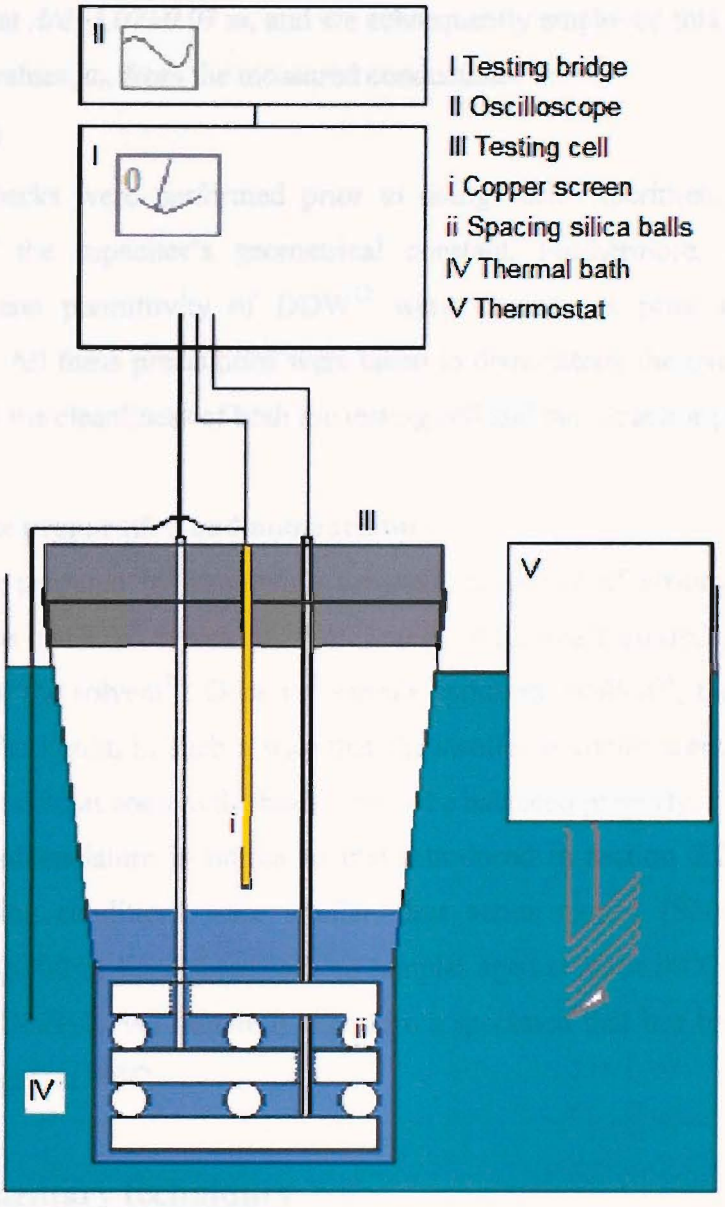

Figure 2.7: Schematic representation of the conductivity testing cell.

2.2.7.2 Calibration of the bridge and cell

Initial calibration of the bridge requires it to be zeroed both in open and short-circuit conditions. The capacitor's geometrical constant (A/d), where A and d respectively stand for the capacitor plate's surface and the gap between them, was initially determined for reproducibility and data processing issues. The capacitance of a parallel plate capacitor is obtained from the relationship:

$$C = \varepsilon_o \varepsilon_r A / d \qquad \text{(eq.2.12)}$$

where ϵ_o and ϵ_r respectively stand for the permittivity of space ($8.854x10^{-12}$ F/m) and the relative permittivity of the dielectric between the plaques (1.00054 for air). We determined that $A/d \sim 3.07 \pm 0.03$ m, and we subsequently employed this figure to derive conductivity values, σ_r, from the measured conductance σ:

$$\sigma = \sigma_r (A/d) \qquad \text{(eq.2.13)}$$

Systematic checks were performed prior to doing each experiment, to ensure the constancy of the capacitor's geometrical constant. Furthermore, values for the conductivity and permittivity of DDW[12] were carried out prior to starting any measurement. All these precautions were taken to demonstrate the overall stability of the bridge and the cleanliness of both the testing cell and the capacitor plates.

2.2.7.3 Sample preparation and nomenclature

Samples were prepared by immersing pre-weighed pieces of absorbent material in fixed quantities of DDW, typically 20 ml and the time was recorded as soon as each sample entered the solvent[13]. Once the sample appeared swollen[14], the capacitor was inserted into the liquid, in such a way that the swollen particles were dispersed, and readings were taken as soon as the bridge could be balanced properly.

The sample nomenclature is similar to that introduced in section 2.2.4.2.2 for guar samples. Ageing conditions were similar, thus series named ($S50/O_2$), ($S90/O_2$), ($S50/N_2$) and ($S90/N_2$) stand for absorbent samples aged at 50 or 90°C in nitrogen gas or in air. A ($S90/N_2/24W$) sample is therefore a specimen that has been aged for 24 weeks in nitrogen, at 90°C.

2.3 Supplementary techniques

This section provides brief information regarding supplementary techniques, which are mainly related to sample preparation. It also provides indications about how simple measurements were performed, for instance, how water diffusion was obtained by measuring mass variations over time with a microbalance.

---

[12] DDW conductivity levels were measured and the cell and capacitor cleaned again if required.

[13] In practice, readings were taken with DDW alone. We also allocated sufficient time for our readings to stabilize and for DDW to reach the temperature of the thermal bath.

[14] Typically after immersion times of about 30 to 60s.

2.3.1 Accelerated ageing and water diffusion procedures

Two different ovens, namely a stainless steel, PID-controlled HERAEUS oven and a HARVARD/LTE Qualivac oven, were used to expose a range of samples to accelerated ageing conditions. Typically, the HERAEUS oven was employed to speed up water diffusion processes in LDPE-based materials. Conversely, the vacuum system of the HARVARD/LTE oven provided us with a practical means of performing those accelerated ageing procedures requiring initial gas exchanges.

2.3.1.1 Samples used in water diffusion experiments

Plaques pressed from Materials A, B and C, and from some blended materials were immersed in sealed jars, filled with either distilled water (DW) or tap water. These samples were prepared in a way entirely identical to that employed to obtain samples for mechanical testing, (see section 2.2.2.3). However strict morphology control was not employed and the plaques were all simply quenched in air. Sealed jars filled with DW or tap water and containing immersed samples were placed in the HERAEUS oven set at a nominal temperature of 50°C; jars were opened periodically to perform weight measurements on our samples; water levels were routinely checked and topped up as required.

2.3.1.2 Accelerated ageing of guar and superabsorbent samples

Adequate numbers of flasks containing raw guar powder were first placed in the HARVARD/LTE oven. Once each was filled with a few grams of raw, unaged guar powder, lids were pre-positioned such that we could simultaneously press all of them with a ruler. Prior to sealing the flasks, an external pump was employed to replace air with nitrogen gas; to remove as much of air as possible, we repeated this substitution operation three times consecutively. Eventually, the oven's door was opened quickly and all the lids rapidly pressed at the same time. Afterwards, we carried out a rapid manual check of each individual flask, to ensure that all lids were securely closed. Accelerated ageing was then carried out in both ovens, with temperatures set at 50°C and 90°C. Samples were taken out of the ovens at different time intervals and labelled accordingly. Ageing times of 3, 6, 12 and 24 weeks were employed.

2.3.2 Method for preparative centrifugation (pelleting)

Centrifugation relies on the acceleration of a natural phenomenon, whose normal driving force is the Earth's gravitational field. For our specific needs, we made use of an increased centrifugal force field to separate, more rapidly, guar's insoluble fraction from its soluble counterpart; the latter was used, primarily, for viscometry, but also provided samples for FTIR and Raman analysis. The centrifugal and gravitational forces can be compared using the following pair of equations:

$$F_{centrifuge} = m\omega^2 R \qquad \text{(eq.2.14)}$$

$$F_{gravitational} = mg \qquad \text{(eq.2.15)}$$

Here, m, ω and R respectively stand for the sample mass, the angular velocity and the distance between the centre of rotation and the vial containing the liquid. The relative centrifugal force generated by the centrifuge is therefore given by the ratio between $F_{centrifuge}$ and $F_{gravitational}$.

Precipitation methods that are based upon preparative centrifugation are also referred to as pelleting [65]. Experimental control over the centrifugal force applied to aqueous guar samples hydrated for sufficient times sees the fraction of the material which is not truly soluble precipitate. Thus, adequate pelleting conditions allow insoluble residues to be compacted at the bottom of centrifuged flasks; hence, one can easily separate soluble from insoluble material. To do this, we employed a BB VVV centrifuge, which is able to reach a maximum speed of 5000 rpm. The centrifuging chamber comprises ten receptacles inclined at a fixed angle, and these receptacles are meant to hold a series of ten 15 ml vials. In practice, the angular velocity is selected by turning a graduated potentiometer, and a timer can be set to stop the centrifugation routine automatically. The rotor speed determines both the time required for pellet formation and its compactness. We determined satisfactory pelleting conditions by varying centrifugation times and speed; our conditions corresponded to a relative centrifugation force that ranged approximately from 750 to 1200 g, if we take into account the fact that the distance to the rotation centre varies between the top and the bottom of the vial. This corresponds to a nominal angular speed of 2000 rpm; this speed was selected in conjunction with centrifugal times of 15 minutes, which were routinely applied as pelleting conditions.

2.3.3 Preparation and nomenclature of our (EVA/LDPE) blends

Blends were obtained by a co-precipitation method from a solution of LDPE (Material A) and ELVAX® 40W. These were all prepared as follows:

100 ml of xylene was initially poured into a beaker and placed on a hot plate whose nominal temperature was high enough to dissolve the granules of polymer. In total, 2 grams of polymer, (i.e., a varying quantity of LDPE and its complement to 2 grams of ELVAX® 40W), were added in the beaker, and agitated using a magnetic stirrer. Once all the granules had dissolved, the beaker was cooled down to 80°C or below, before its contents were poured carefully into 100 ml of methanol. It is the abrupt change in solubility that makes the dissolved polymer precipitate rapidly to form a swollen gel. This gel was then filtered at room temperature with a standard filter paper, to collect the xylene/methanol mix. Blends were finally placed in Petri dishes and left to dry out for extended times, from which, samples were extracted and used as required.

Binary blends obtained from Borealis LDPE and ELVAX® 40W are named after their respective weight fractions, such that a (20/80) sample stands for a mix containing 80% of Material A, by weight, and 20% of ELVAX® 40W.

2.3.4 Weighing methods

An MC210P Sartorius microbalance was used to determine the mass of the samples used throughout this study. This microbalance possesses an automated calibration routine, which was used prior to starting any series of measurements. Its display implies a precision of a hundredth of a milligram and it needs, on average, ten seconds to reach a constant mass value, according to the manufacturer.

2.3.4.1 Water sorption experiments

Absorption and desorption experiments were performed using mains tap water or distilled deionised water by evaluating the variation in the mass of samples following their removal from jars filled with solvents, in which they were immersed. Since time is the key parameter in performing such experiments, the balance was always fully calibrated prior to starting to weigh the samples.

2.3.4.2 Preparation of distilled and distilled deionised water

DW was prepared with a BIBBY STERILIN W4000 still and was stored in a sealed jar. DDW was then obtained from our supply of DW using a MILLIPORE Milli-Q

water purification system. DDW was kept in a second jar. Purity levels for DDW were checked using the conductivity gauges (15MΩcm) that are part of the filtering device.

Chapter 3

The effect of additives and thermal conditioning on the morpho-mechanical properties of LDPE-based materials.

3.1 Introduction

We believe that an understanding of the properties of polymeric materials is intimately linked to their microstructure. For instance, insulating materials based on LDPE or XLPE materials appear more likely to undergo electrical breakdown via amorphous regions or at crystalline interfaces than in crystalline entities [66-68]. According to Barrie [48], the diffusion of water molecules in a polymer such as LDPE is also strongly linked to its microstructure, since crystalline structures, individually, form almost impassable barriers for some penetrants such as water. In short, the initial molecular composition of the material combined with processing conditions will be critical in determining its future characteristics and overall performance. Thus, this preliminary part of our work deals explicitly with the study of selected factors involved in the variation of the structural properties of our model materials. More specifically, we attempted to understand how the presence of additives affects their morpho-mechanical properties, by imposing various thermal treatments on them. First of all, we wanted to explore the role played by each additive in influencing the final microstructure of our materials. To begin with, we employed differential scanning calorimetry as a technique to probe both the crystallization kinetics and the consequent melting behaviour of Materials A and B; Material C's crosslinking kinetics, crystallization and melting behaviour were also followed, using this technique. After that, the comprehensive use of isothermal crystallization and melting procedures, mainly developed via calorimetry, stimulated the need for optical and mechanical tests; the latter were employed as a mean of completing our understanding of the molecular mobility which characterize the above LDPE-based systems. More precisely, dynamic

mechanical measurements were employed to characterize the α-relaxation of our three materials, whereas a number of optical micrographs were acquired to evaluate the effect of thermal treatments on the formation of large scale polycrystalline entities from the melt.

3.2 Differential calorimetry: procedures and results

DSC is an extremely versatile tool when it comes to imposing a set thermal history and evaluating its consequences for the structure of crystalline polymers. We started this part of the work by locating the temperature window from which isothermal crystallization can occur, and, by doing so, we observed marked differences in the behaviour of Materials A and B[1]. Thus, the following section introduces preliminary work carried out on the crystallization kinetics of Materials A and B, with the subjacent idea of exploring the temperature domain where our materials are able to crystallize isothermally. Then, we examine Material C's crosslinking kinetics. To do this, we varied the DCP activation time and temperature, to evaluate how long it takes for the subsequent melting trace to exhibit an invariant pattern[2]. After that, we discuss the effect of equivalent isothermal treatments on the consequent melting behaviour of our three materials. Finally, we consider the effect of the heating rate on the different features seen in our melting thermograms, since we need to know how heating rate variations influence dynamic reorganization effects.

3.2.1 Estimates for the semi-crystallization times of Materials A and B

Here, we compare numerical values for the semi-crystallization times ($t_{1/2}$) derived graphically from DSC isothermal crystallization traces; $t_{1/2}$ is simply an evaluation of the time required by a sample to reach 50% of its maximum crystallinity. We considered that the latter is attained once C_p becomes a constant. In practice, rigorously identical thermal programs were applied to Materials A and B, over a range of crystallization temperatures. Fig.3.1 exemplifies the approach we employed to obtain

[1] We originally followed the variations in C_p as a function of time for both materials, when subjected to identical thermal programs. Exothermic crystallization peaks could not be superimposed since Material A's trace always took longer times to reach a constant value for C_p.

[2] To do this, we implicitly assumed that an equivalent melting trace, i.e. a trace obtained from a unique isothermal crystallization method varies when DCP starts being activated. It simply means that DCP's activation somehow affects the crystallization and melting behaviour of Material C.

graphical estimates for $t_{1/2}$. The formation of an exothermic peak during isothermal crystallization indicates that a fraction of the material truly crystallizes at the selected crystallization temperature. To obtain numerical estimates for $t_{1/2}$, we decided to exploit sample-specific reference traces, which were obtained both for Material A and Material B; such traces are acquired by applying a thermal program similar to that aimed at crystallizing a sample under isothermal conditions, except that such thermal program is chosen to be exempt of any isothermal crystallization step, i.e. the ongoing thermal trace is characterized by a constant C_p value. As a result, we expected to collect a trace devoid of an exothermic peak. This is precisely what the reference curve seen in fig.3.1 demonstrates. To be applicable, our method then requires the subtraction of the two DSC traces, including the sample and reference traces. An estimate for the area between the two traces was obtained thanks to a subtraction routine in Sigma Plot, which then enables $t_{1/2}$ to be evaluated.

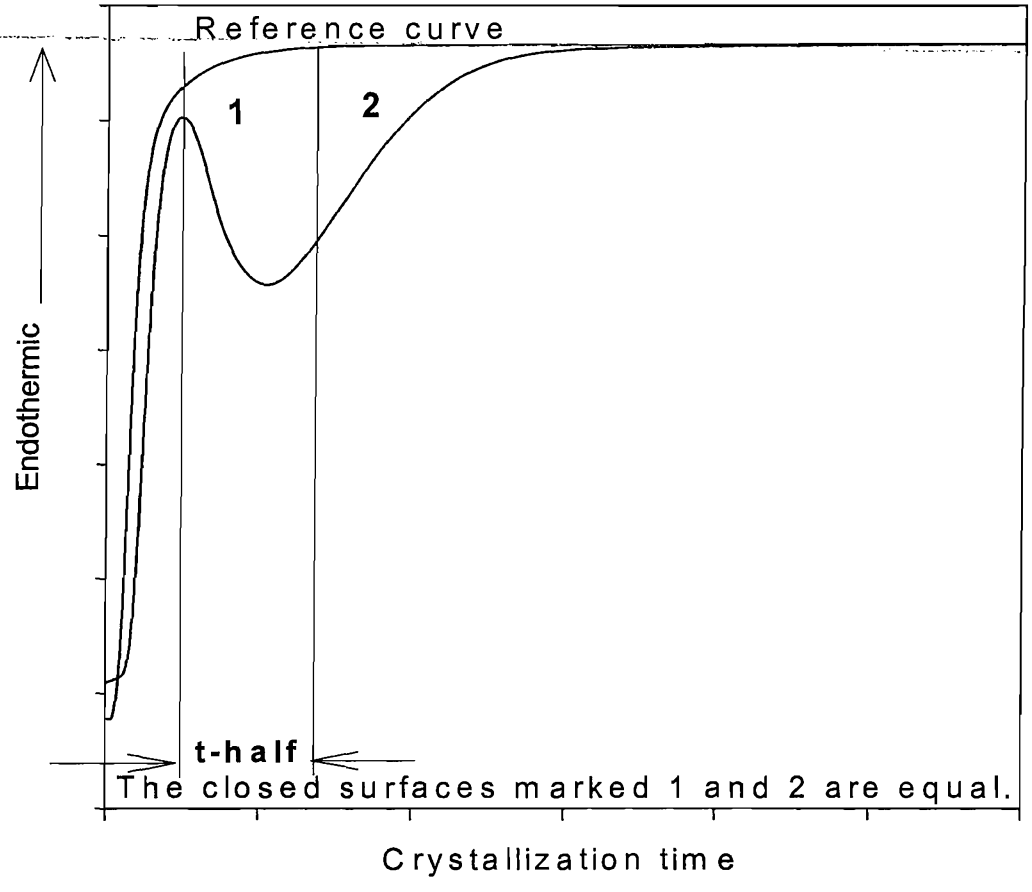

Figure 3.1: Example of the graphical subtraction method employed to obtain values for $t_{1/2}$.

Using this approach in a systematic way, we investigated the behaviour of our two materials, indicated (Mat.A/T) and (Mat.B/T), where T represents the crystallization temperature of 92, 96, 99, 102, 105 or 108°C[3]. Fig.3.2 is a plot of $t_{1/2}$ values versus crystallization temperature. However, crystallization traces obtained at high temperatures did not exactly rejoin the right-hand, flat baseline provided by the reference trace; this was more pronounced at lower temperatures for Material B than for Material A, i.e. for crystallization temperatures strictly exceeding 102°C. This is the reason why we decided not to derive approximate numerical estimates for $t_{1/2}$ at higher crystallization temperatures, even though we possess the corresponding experimental data. Also, melting traces obtained from Materials A and B invariably show that the fraction of material involved in isothermal crystallization reduces drastically above 102°C. It is a combination of these two factors that prevents us from obtaining reliable estimates for $t_{1/2}$ above 102°C. Nevertheless, we can still visualize the clear tendency for Material B to crystallize faster than Material A, since fig.3.2 clearly indicates that semi-crystallization times increase with crystallization temperatures[4]. Since Materials A and B are identical, except for the unidentified antioxidant in the latter system, we can infer that it is the presence of the latter which promotes Material B's faster crystallization rates.

If we then assume that crystalline entities formed within both materials grow at a rate which is purely temperature-dependent, reductions in crystallization times are likely to originate from an increase in nucleation density. Because of this, we propose, at this stage, that this pronounced difference in crystallization kinetics originates from the presence of antioxidant in Material B.

[3] In order to minimize variations attributable to sample preparation, unique samples were utilized to derive our two series of data for $t_{1/2}$.

[4] This is evidently the case for the crystallization times themselves; the latter were originally estimated by following ongoing traces during DSC runs.

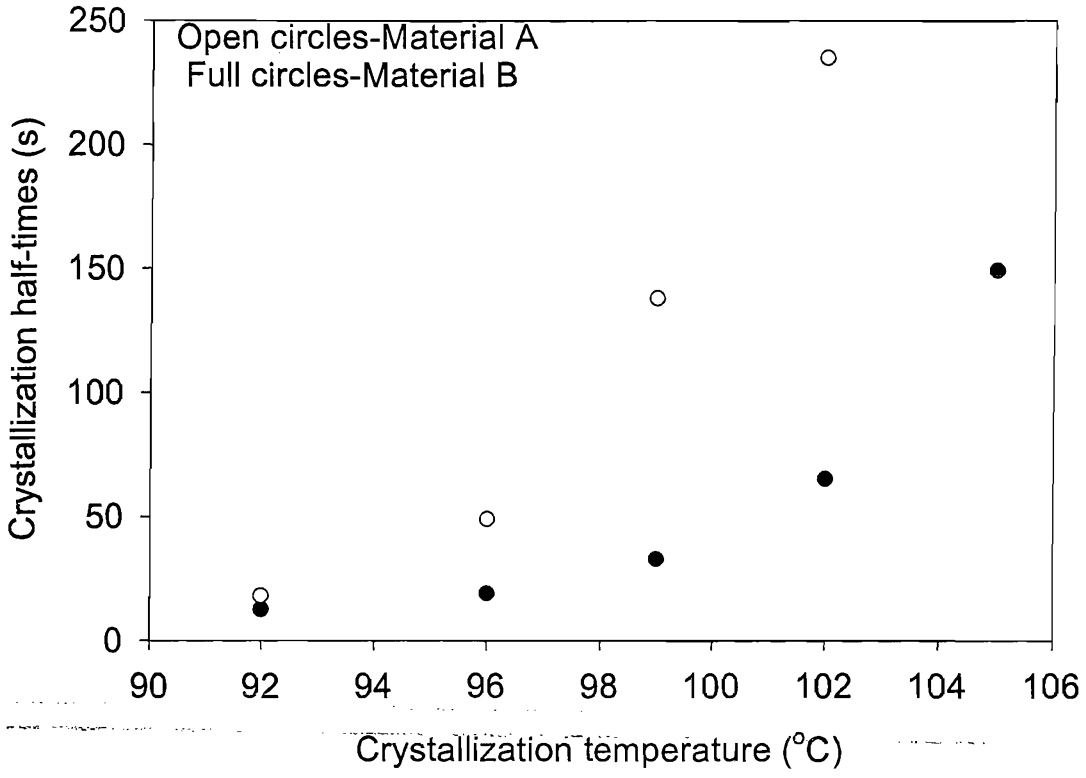

Figure 3.2: Representation of $t_{1/2}$ values versus isothermal crystallization temperatures. (Black dots stand for Material B's data points)

3.2.2 Effect of time and temperature on the activation of crosslinking reactions

This section exclusively deals with Material C's properties. Here, we were particularly interested in exploring DCP thermal activation, by following the effect of crosslinking on DSC melting traces. To examine the effect of chemical crosslinking, a thermo-chemical reaction presented in section 1.2.4.1.3, we undertook to vary the times and temperature at which DCP is activated; we then arbitrarily fixed the crystallization conditions for all of our samples[5]. Fig.3.3 shows melting traces obtained from equivalent (Mat.C/200/t/99) samples, t varying between 0.1 and 1 minute. In parallel, fig.3.4 exhibits melting traces obtained from equivalent (Mat.C/150/t/99) samples where the parameter t ranges from 1 to 60 minutes. In both cases, lengthened isothermal treatments eventually led to traces similar to those obtained from both (Mat.C/200/1/99) and (Mat.C/150/60/99) samples. From our two graphs, it is evident

[5] We will see further on that once crosslinking has taken place, isothermal crystallization treatments have lesser effect on Material C's melting traces.

that the fused melting peaks[6] situated at relatively higher temperatures are eventually displaced towards lower temperatures, but always remain somewhat above the isothermal crystallization temperature. Also, we noticed that the shortest treatment times leave the melting traces relatively unchanged, except for a small reduction in the relative amplitude of the melting peak situated at the highest temperature in each trace. From experimental results [27] and some material characteristics [69,70] employed by Yamazaki et al., it is evident that the half-life of DCP decreases as the activation temperature rises, as anticipated. Although DCP can be consumed both by proper crosslinking reactions and through reactions with antioxidants [2], we nevertheless attempted to estimate DCP's half-life from our data, in a very basic manner. Since no further changes in Material C's melting traces were seen for activation times exceeding that shown on our graphs, we assumed that the consumption of DCP molecules was merely involved in the thermo-chemical crosslinking reaction; moreover, we supposed that the crosslinking reaction reached values close enough to 100%. More precisely, if we consider that DCP consumption reached a level that falls between 95 and 99.9%, we find that DCP's half-life respectively correspond to values situated between 6 and 12 minutes and between 0.1 and 0.2 minutes at 150 and 200°C respectively. Data gathered by Yamazaki et al. [27,69,70] provide numerical values for DCP's half-time values of 600, 200, 5, 1 and 0.4 minutes; the latter are respectively associated with activation temperatures of 117, 120, 155, 171 and 180°C. Even though we crudely approximated values for DCP's half-time, we find that there is an excellent agreement between our data and those reported by these workers.

[6] Kao and Phillips report that the appearance of double melting peaks following isothermal crystallization stages are reported to be the norm for LDPE systems [62], let alone for the study of some gel fractions.

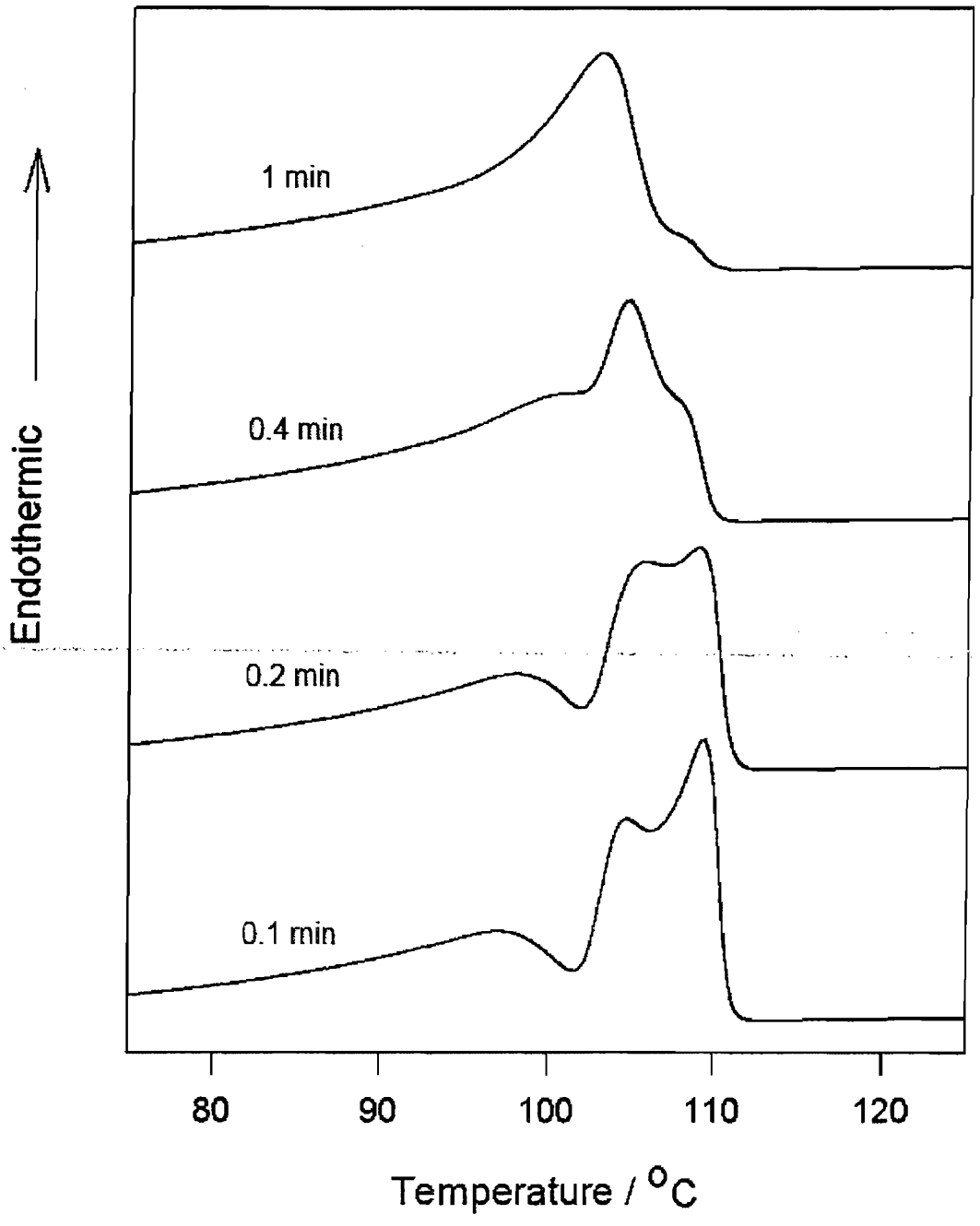

Figure 3.3: Melting traces obtained for a series of (Mat.C/200/t/99) samples-t ranges between 0.1 and 1 minute.

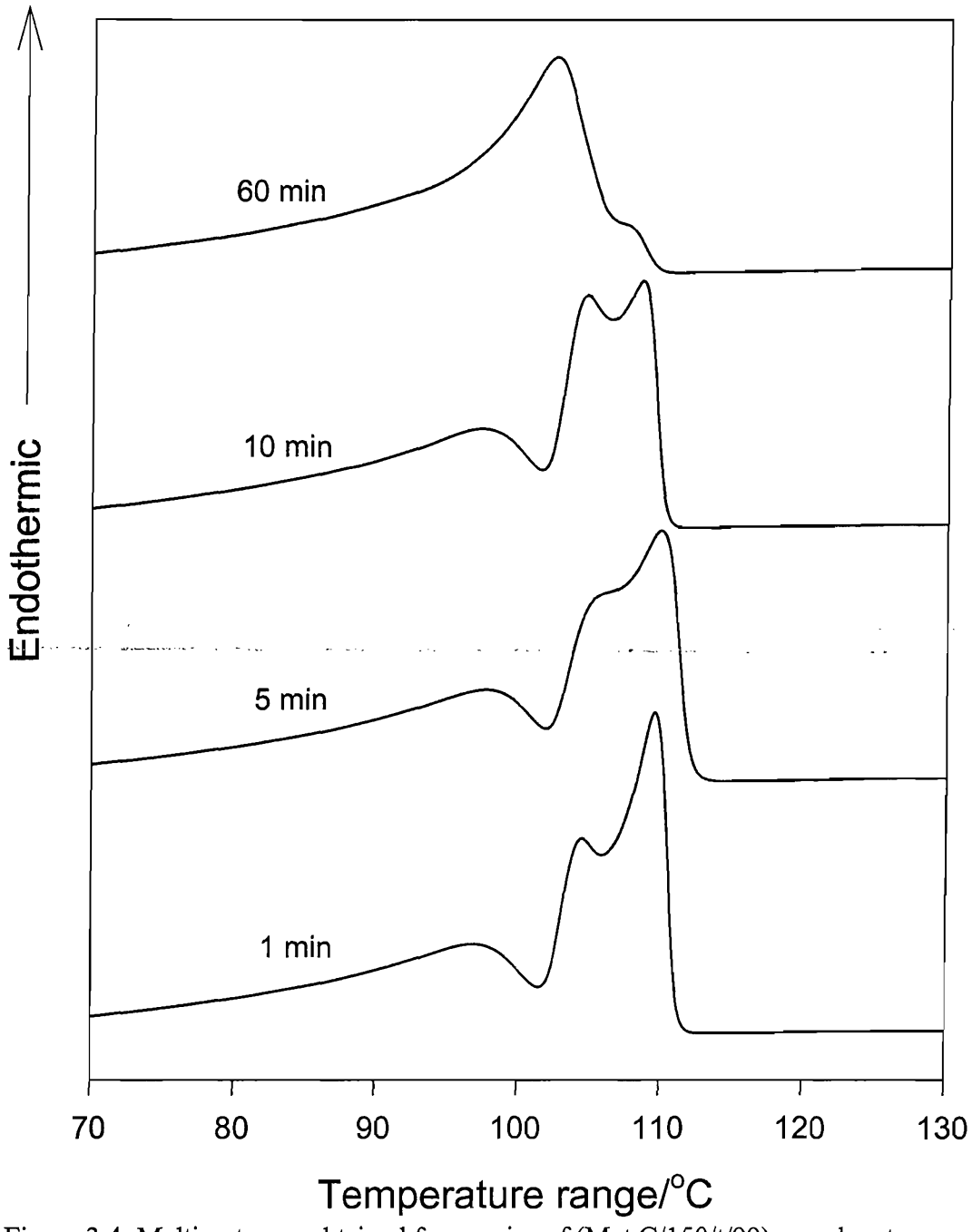

Figure 3.4: Melting traces obtained for a series of (Mat.C/150/t/99) samples- t ranges between 1 and 60 minutes.

3.2.3 Melting behaviour of Materials A, B and C

Since we now have a better perception of the roles played by each of the additives contained within our materials, we decided to compare their melting behaviour. We, therefore, obtained melting traces from the complete isothermal crystallization ranges accessible by our three materials. In this respect, fig.3.5 shows the different melting

traces obtained from (Mat.A/T) and (Mat.B/T) samples; their respective crystallization temperatures, T, are reported on the graph and Material B's melting traces are dashed. A similar graph, see fig.3.6, was obtained by overlaying melting traces using (Mat.C/X/T) and (Mat.C/T) samples; melting traces obtained from (Mat.C/T) samples are dashed. With the exception of the melting traces obtained from the crosslinked equivalent for Material C, we can systematically describe our melting traces thanks to the recurring formation of three distinct peaks. Close examination of our thermograms reveal that, in each trace, the peak which appears at the lowest temperature is always found at a temperature slightly below that of the isothermal crystallization treatment; hence, we cannot attribute the formation of this peak to isothermal crystallization stages and, therefore, this peak can only form during the subsequent cooling step. Conversely, the two overlapping peaks above the crystallization temperature are both related to isothermal crystallization. However, to ensure that this preliminary interpretation is correct, we need to check that none of the features present in each of our thermograms is the result of some kinetic artefact or, alternatively, originates from a dynamic reorganization of the system during the course of its melting. Thus, we studied the effect of the heating rate on the melting trace obtained from a (Mat.A/99) sample.

Fig.3.7 was generated by overlaying comparable melting traces obtained at different heating rates. From this figure, we can see that, unlike the peak formed at lower temperature, the fused peaks are displaced to some extent towards higher temperatures and tend to converge as when the heating rate increases. Despite this obvious kinetic effect, their overall appearance remains, nonetheless, comparable[7]. Consequently, we consider that the above melting traces are indicative of the presence of two distinct isothermal lamellar populations, both of which formed during the isothermal crystallization treatment. In a succession of publications, Phillips and co-workers [71-75] investigated the effect of DCP content on the crystallization, morphology and melting behaviour of the resulting XLPE systems. As in our results, their DSC's melting behaviour of uncrosslinked materials was described in terms of a quench

[7] Extrapolating peaks maximum to null heating rate is certainly feasible; without doing so, we can qualitatively observe that the relative displacement of the two overlapping peaks is indeed small. Importantly, dynamic reorganization effects have to be expected at extremely low heating rates, which were not investigated here.

peak[8], situated below the temperature of crystallization, and a double peak resulting from the melting of two distinct lamellar populations formed during isothermal treatments. If we return to fig.3.5 and fig.3.6, it is interesting to see how the choice of crystallization temperature affects the fraction of material able to crystallize isothermally. Fig.3.5 provides a qualitative view on how quench peaks grow in magnitude, to the detriment of the fused isothermal peaks, as the crystallization temperature increases; also, the melting temperatures of the two isothermal populations appear to get systematically closer as the crystallization temperature increases. More importantly, when isothermal crystallization occurs above 102°C, a drastic reduction is seen in the magnitude of the melting peak related to the isothermal component. This is also where Material B's additive reveals its nucleating capacity; the comparison between Material A and B's traces obtained at 108°C reveal that only Material B crystallizes to a significant degree at that temperature, given these identical crystallization times. If we then compare fig.3.5 and fig.3.6, we can also see how (Mat.B/T) and (Mat.C/T) melting traces relate to one another[9]. They are near identical in terms of peak distribution, appearance and magnitude. It is only when Material C is fully crosslinked that the overall appearances of the melting traces vary significantly. For Phillips and co-workers, obtaining XLPE melting traces comparable to those shown in fig.3.6 necessitates the addition of 6.8% DCP [73]. This amount seems unusually high, especially since maximum gel[10] contents are obtained through the activation of lower amounts of DCP. In addition to what was formerly discussed in section 1.2.4.1.2 (i.e. studies made by Bremner and Rudin [24] and Peacock [28] showing that the activation of 2 to 3% of DCP suffices to crosslink up to 90% of LDPE), Peacock also demonstrated that this value is unlikely to increase with higher DCP contents [28]. Despite that observation, Kao and Phillips' results are qualitatively in line with ours and the above discrepancy could simply arise from a difference in composition or DCP consumption mechanisms. For instance, we know that the amount and type of branching affect the ability of the system to form high-temperature melting

[8] The melting peak that corresponds to the fraction of material that crystallizes during cooling.

[9] Thermal treatments only differ in this that short annealing periods will activate DCP. Data shown in fig.3.4 indicates that its impact is in fact negligible on the melting trace.

[10] Uncrosslinked and crosslinked fractions extracted from XLPE samples are sometimes referred to as sol and gel phases.

lamellae, whilst the chemical nature and quantity of antioxidant will influence the effectiveness of the peroxide crosslinking process [2,26].

To summarize, Material B's antioxidant exhibits marked nucleation properties, and it systematically enhances crystallization in Material C, provided that the latter has not been crosslinked. Once crosslinked however, Material C's molecular configuration drastically hinders its ability to promote the formation of isothermal populations whose melting signature is found at lower temperatures.

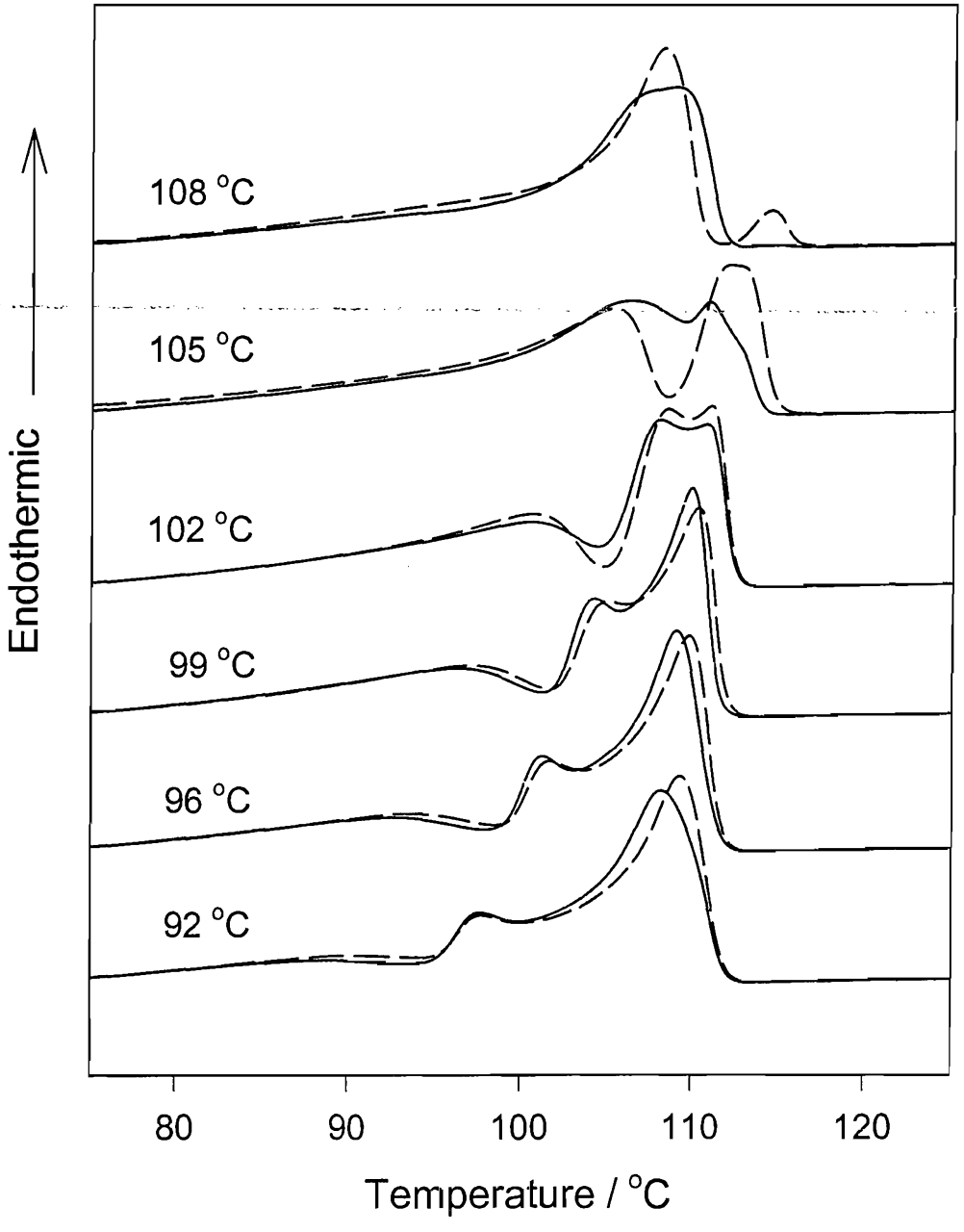

Figure 3.5: Overlaid melting traces obtained from Materials A (solid line) and B (dashed line) subjected to identical isothermal crystallization treatments.

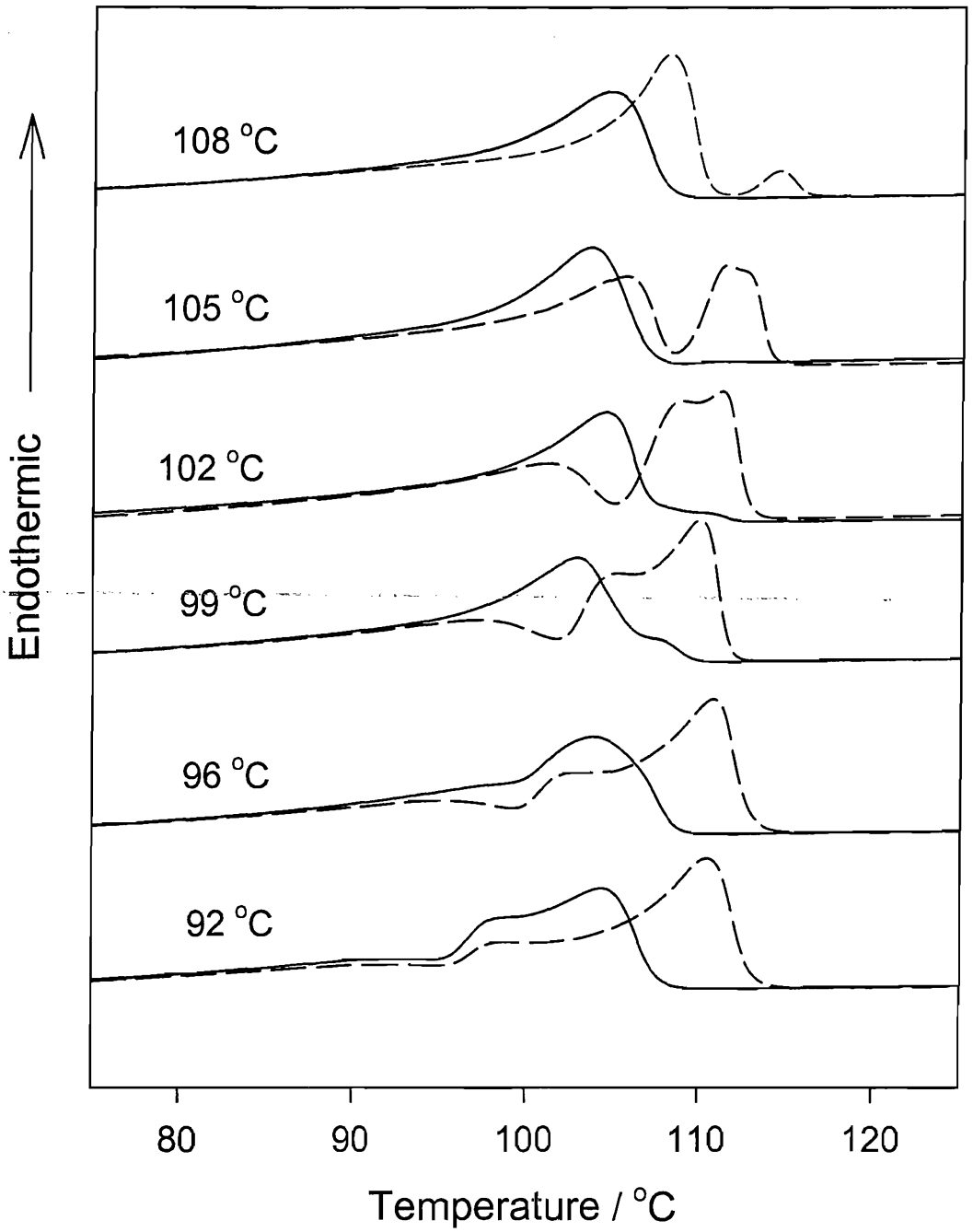

Figure 3.6: Melting traces displayed by Material C after isothermal crystallization treatments following two pre-activating DCP activation treatments (dashed:1min@ 150°C; solid:1min@200°C)

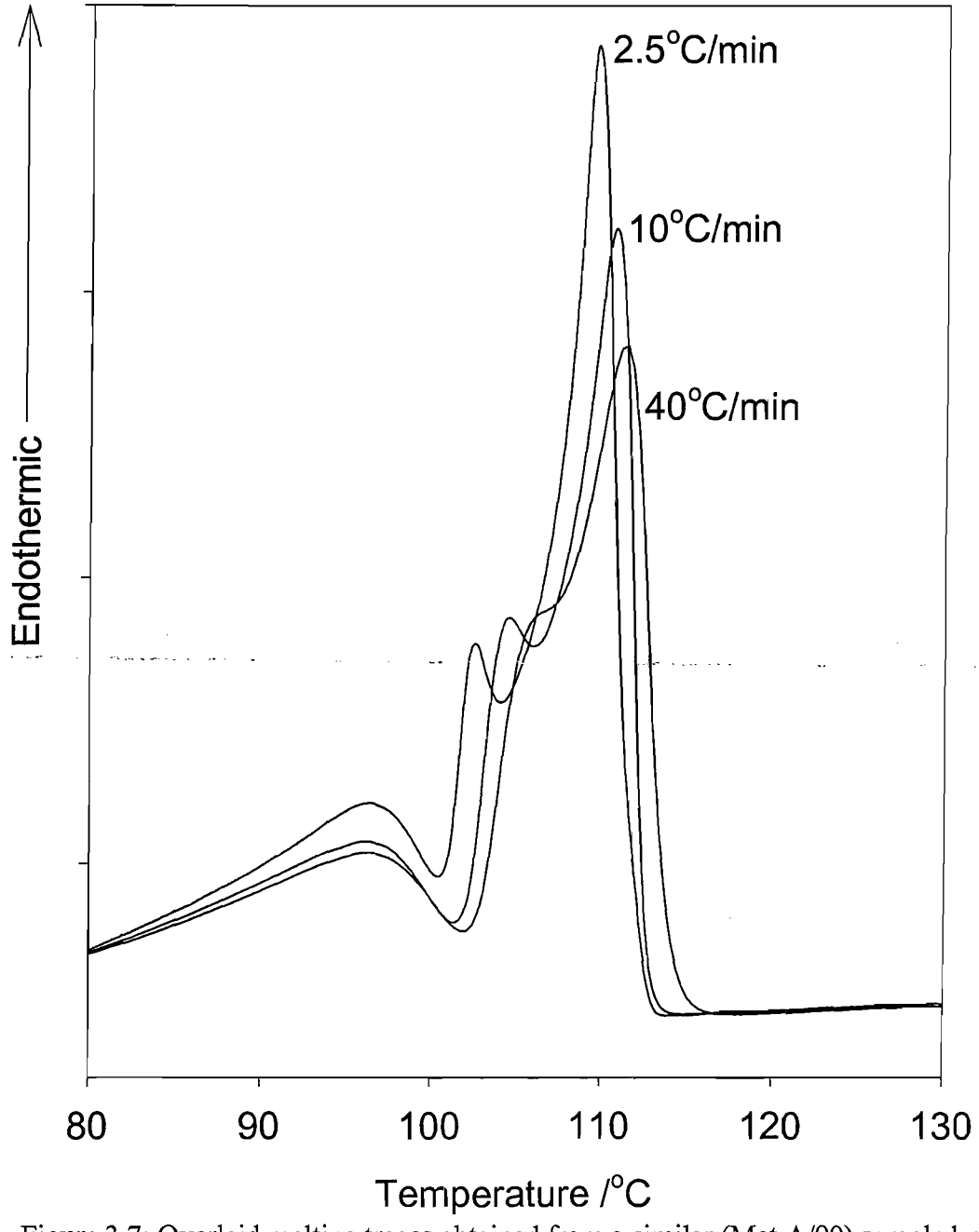

Figure 3.7: Overlaid melting traces obtained from a similar (Mat.A/99) sample but with a varying heating rate.

3.3 Dynamic mechanical testing of Materials A, B and C

Investigation of the mechanical properties for our model materials is primarily stimulated by the need to characterize molecular motions taking place within our model materials; the variety of morphologies encountered during the above DSC runs suggests that one can influence their morphological properties, and the latter may also

become important regarding water permeation processes. Here, we wanted to explore the effect of thermal conditioning and material composition on the appearance of one viscoelastic feature exhibited by all three of our materials. To summarize, LDPE generally exhibits three mechanical relaxation modes [76], among which one finds a primary relaxation mode situated above ambient temperature [77,78]. If we base our initial standpoint on the work done by Boyd on this subject [79,80], our interest in the α relaxation is directly linked to the active role played by the crystalline fraction in LDPE samples. Boyd's work implies that a mechanically active α process derives its magnitude from monomeric shear-slip mechanisms within lamellae, although the practical detection of this mechanism requires the presence of the amorphous phase. This molecular process was confirmed by more recent work carried out by Sirotkin and Brooks on polyethylene copolymers [77], who also showed that there exists a unique correlation between the positioning, in temperature, of the α peak (T_α), and lamellar thickness[11].

3.3.1 Effect of strain adjustments on mechanical testing

We initially studied how variations in oscillation amplitudes influence mechanical readings relating to the α-relaxation process. We believe that this is a crucial point to make, since we base our interpretations principally on the relative amplitude and displacements in temperature of the α peak; from a purely practical point of view, we wanted to separate and distinguish the role played by experimental and physical factors in the appearance of α peaks. Fig.3.8 was derived from repeated series of isothermal scans in frequency using a single (Mat.A/SQ) sample. For these experiments, we employed strain levels ranging from 1 to 90%[12]. As a result, fig.3.8 shows overlaid α peaks as a function of strain. As the strain level increases, the α peaks undergo an appreciable vertical shift. Conversely, there is no perceivable variation in T_α. We can also see that results obtained at lower strain levels, more precisely, strain levels ranging from 1 to 5%, do not provide reliable readings at higher testing frequencies. To reduce scattering in our data sets, all of our isothermal and isochronal scans were therefore acquired at a fixed strain level of 10%.

[11] They did so by correlating data derived by mechanical tests and small angle X-ray scattering.

[12] Strain levels depend on sample size and are calculated automatically by the software not to exceed the transducer's specifications; % strain is just a user input.

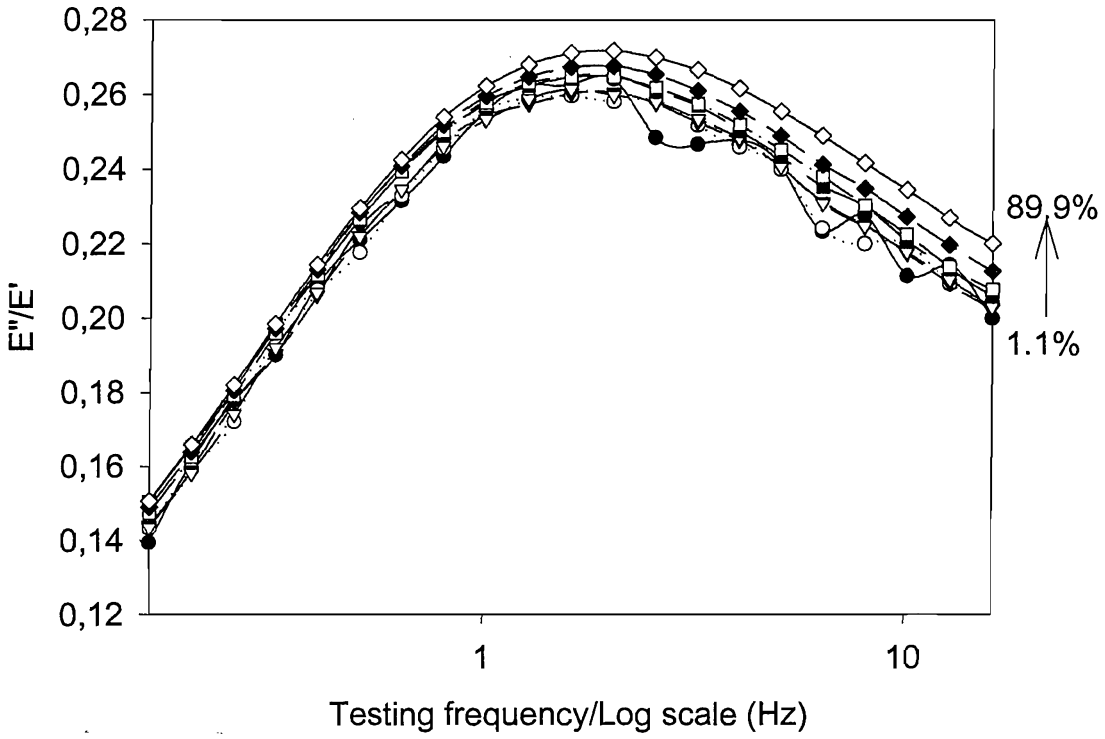

Figure 3.8: Effect of strain levels on the α peak. Isothermal testing performed at 67.5°C.

3.3.2 Comparison between isothermal and isochronal data acquisitions

Prior to investigating the effect of temperature and thermal treatment on the α peak, we attempted to compare the two testing methods available to us. Isothermal scans involve fixing the furnace's temperature and varying the frequency, whereas isochronal scans are performed by fixing the testing frequency and varying the temperature. We were particularly keen to investigate isochronal methods, since the latter are procedures that we thought would eliminate parasitic heating ramp effects. To probe both methods, we obtained comparable data sets from three identical samples, namely (Mat.A/SQ), (Mat.B/SQ) and (Mat.C/X/SQ). Fig.3.9 and fig.3.10 respectively contain data derived from isochronal and isothermal testing. Since the available range of testing frequencies is restricted, fig.3.10 shows a series of data obtained at 20, 50 and 70°C for each sample; continuous curves were simply obtained by shifting our data horizontally, considering that data acquired at 70°C serves as reference for the testing frequencies[13]. If we look at the amplitude of the α peak on both graphs, and consider this sole parameter for each sample type separately, we can see that both testing methods are in

[13] We made this choice since α peaks appear, most of the time, in this particular region of our data.

agreement; the lowest α peak being Material C's and then Material A's, but also, in both cases, (Mat.B/SQ)'s α peak falls outside our testing range[14]. There is, however, a slight difference between T_α for Materials A and B, since they do not exactly coincide in the case of the isochronal method. What systematically separates our two data sets though is the relative magnitude of the α peaks; For all three curves, the latter is constantly lower for data acquired under isothermal conditions.

On the basis of our results alone, we believe that there is no reason to prefer one procedure or the other; yet, it is important to gauge the effect of the testing method on the obtained results since, in the discussion that follows, we will employ both methods for different purposes. Thus, the two following sections contain data derived from isothermal measurements. We employ the latter to calculate activation energies needed for the α relaxation process to occur. We then present the result of isochronal experiments; from these, we examine the effect of crosslinking and crystallization treatments on the appearance of the α peaks. To have a better understanding of results derived using each methods, we attempted to compare results such as those shown in fig.3.9 to DSC results. What we can observe is that there exists a significant shift in the temperature scale which prevents us from reliably assigning α peaks to any feature previously shown in our melting traces. This is an important issue we have to consider, especially since mechanical tests could not be reliably extended towards higher testing temperatures. We must therefore envisage the possibility that other peaks could be situated above the investigated temperature range.

[14] Testing ranges could not be extended much further than 80°C because our samples were becoming too soft and the RSAII could no longer measure our samples' moduli.

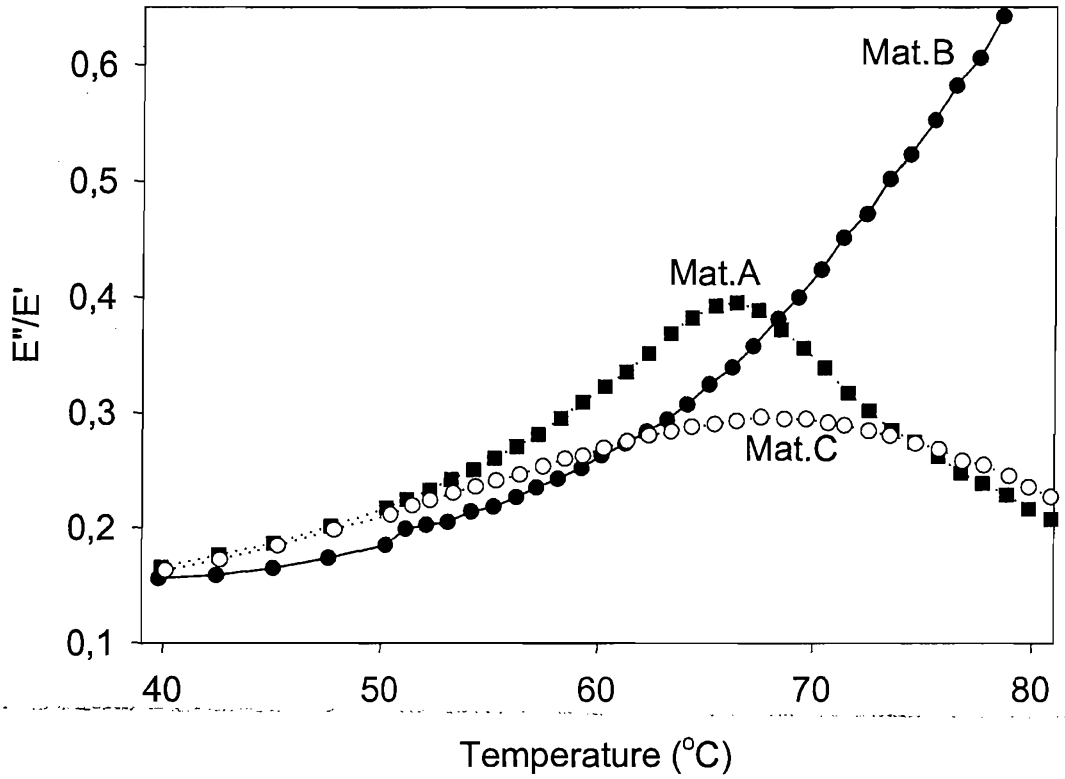

Figure 3.9: Typical series of isochronal data sets acquired for our three materials (1 Hz).

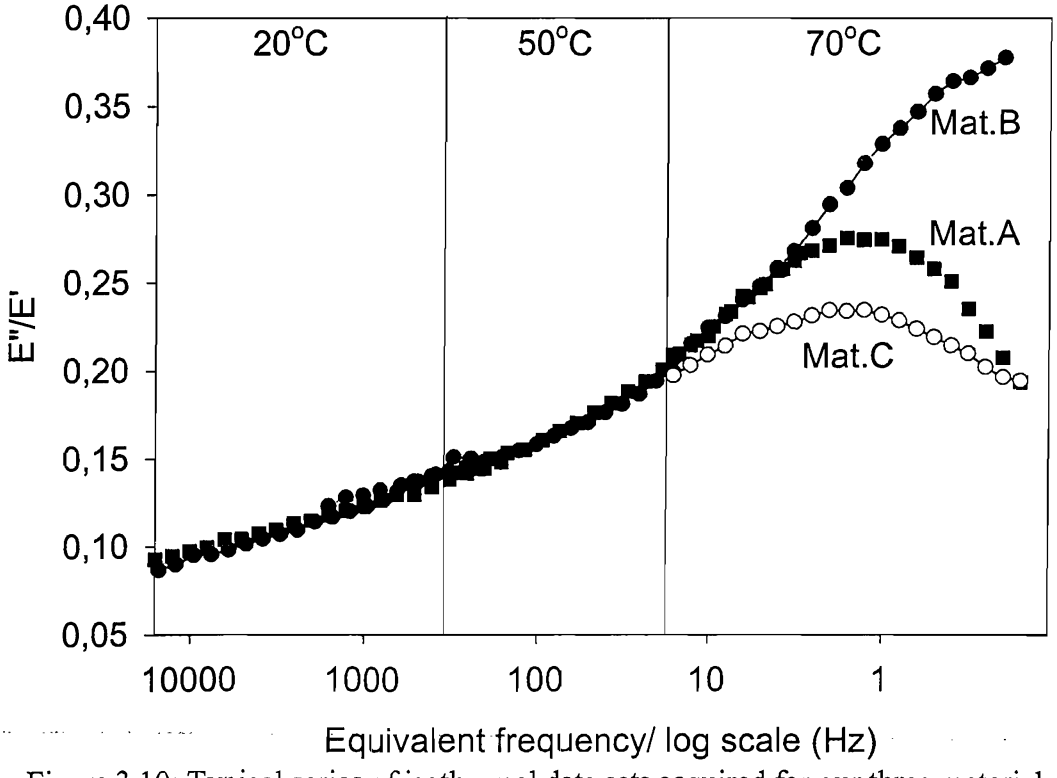

Figure 3.10: Typical series of isothermal data sets acquired for our three materials.

3.3.3 Isothermal data sets

Estimating values for the activation energies involved in physical processes is a classical way of evaluating the effect of temperature on molecular motions [81]. Unfortunately, such descriptions remain purely phenomenological in nature, in the sense that the process only provides the apparent thermal energies involved in processes such as the α relaxation. A simplified thermodynamic description for the frequency-temperature dependence which links both parameters is [81,82]:

$$\partial \ln \omega / \partial (1/T) = -\Delta H / R \qquad \text{(eq.3.1)}$$

Here, ω, T, ΔH and R respectively represent the testing frequency, the testing temperature, the activation energy and the gas constant. To employ this equation, we acquired isothermal data sets from (Mat.A/SQ), (Mat.B/SQ) and (Mat.C/X/SQ) samples. From these data, we generated fig.3.11, fig.3.12 and fig.3.13 respectively; the temperature at which each isothermal test was performed is reported on the graphs. From these, we can estimate the frequencies at which the α peak exhibits its maximum (f_{max}) and plot these as a function of the reciprocal temperature. As a result, fig.3.14 is a plot that collates the data extracted from the three previous figures; estimates for the activation energies were derived from individual linear regressions carried out on each plot in order to derive values for ΔH. Thus, we found activation energies of 102.1±2.8, 108.8±3.3 and 118.9±4.6 kJ/mol for Materials C, A and B in that order[15]. The same method has been employed by Danch et al. to characterize the α relaxation for commercial LDPE samples (Lupolen) [83], whose α peaks are found in the same temperature range as ours, typically 60 to 70°C. These authors found values for activation energies ranging from 101.6 to 122.4 kJ/mol and they specifically associated variations in activation energies to the restriction of the molecular motions required for the α process to occur. What they found was that annealed LDPE requires higher activation energies than some drawn and irradiated (crosslinked) LDPE samples. In view of our results, we can draw a strong parallel with the results obtained by Danch et al. [83], since the range for our activation energies agrees well with theirs and our crosslinked material also exhibits the lowest value for the activation energy. The regressions shown in fig.3.14 are well separated on the x-axis, and this simply reflects the temperature range at which our three materials exhibit their respective α relaxation process, see fig.3.11 to fig.3.13. Given that crystallization conditions were identical for

[15] The error values we indicate are simple standard deviation values.

Materials A, B and C, we suggest classifying the above materials according to our previous DSC results. In the most general configuration, Material B's melting peaks are found at temperatures being somewhat higher than Material A's and largely above Material C's. If we return to the above DSC investigations concerning the melting of isothermal lamellar populations, we can attempt to draw a more precise parallel between the present mechanical data and the melting data that involves the thermal program which provides the closest match to that of a mere cooling, i.e. the isothermal crystallization treatment performed at 108°C. Materials A, B and C are mostly characterized by the melting of material fractions crystallized on quenching. Also, fig.3.5 and fig.3.6 clearly demonstrate that Material C's quench peak is effectively situated well below those of Materials A and B, however, it appears more difficult to classify the latter materials on the sole basis of the location of their quench peaks, which fall within the same temperature range.

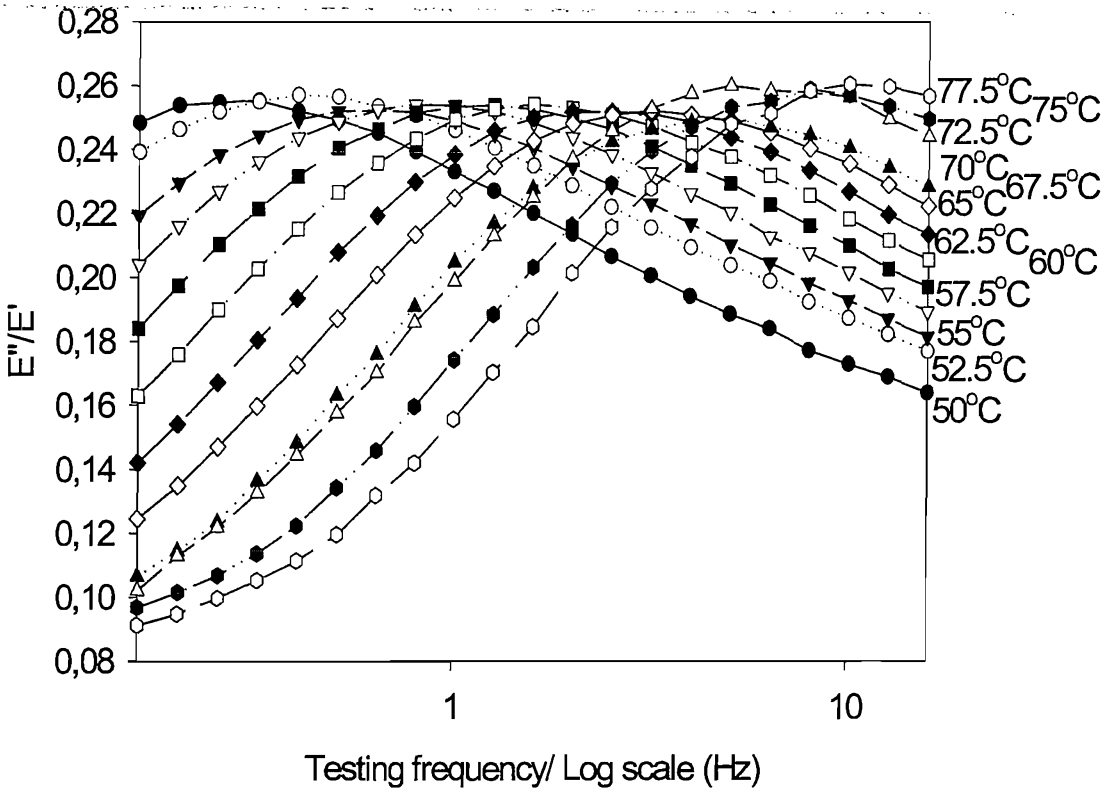

Figure 3.11: Series of isothermal data acquired from a (Mat.A/SQ) sample.

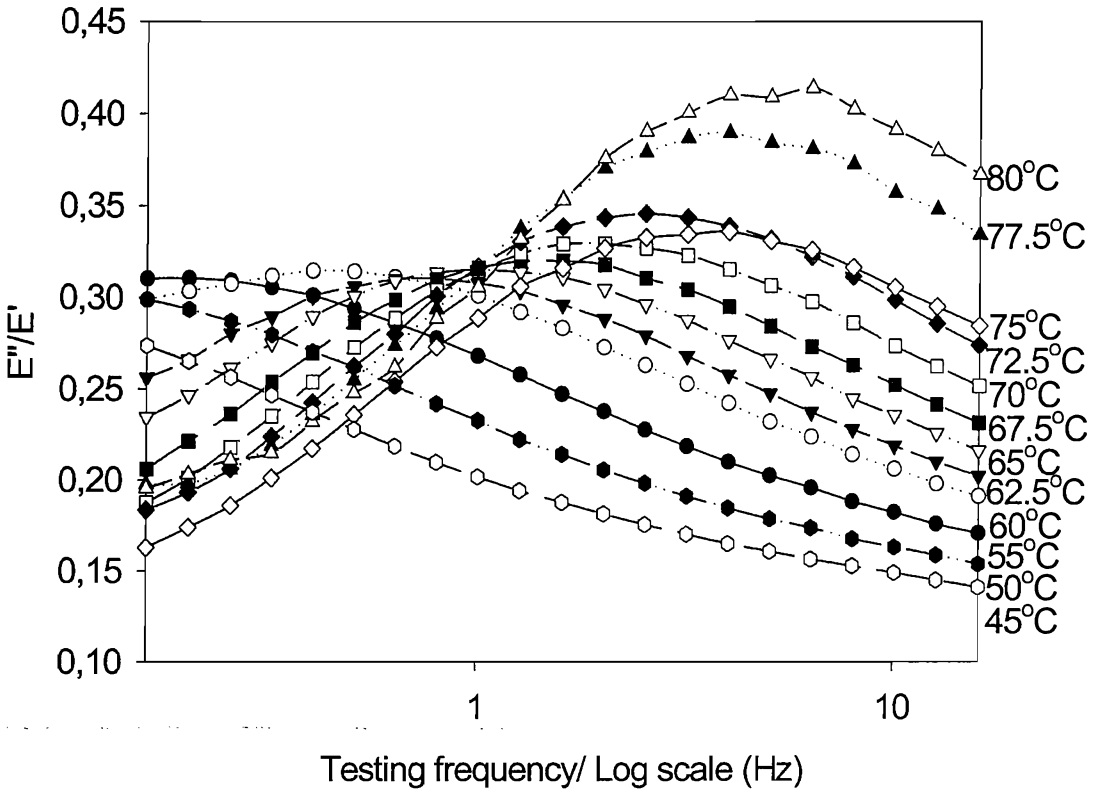

Figure 3.12: Series of isothermal data acquired from a (Mat.B/SQ) sample.

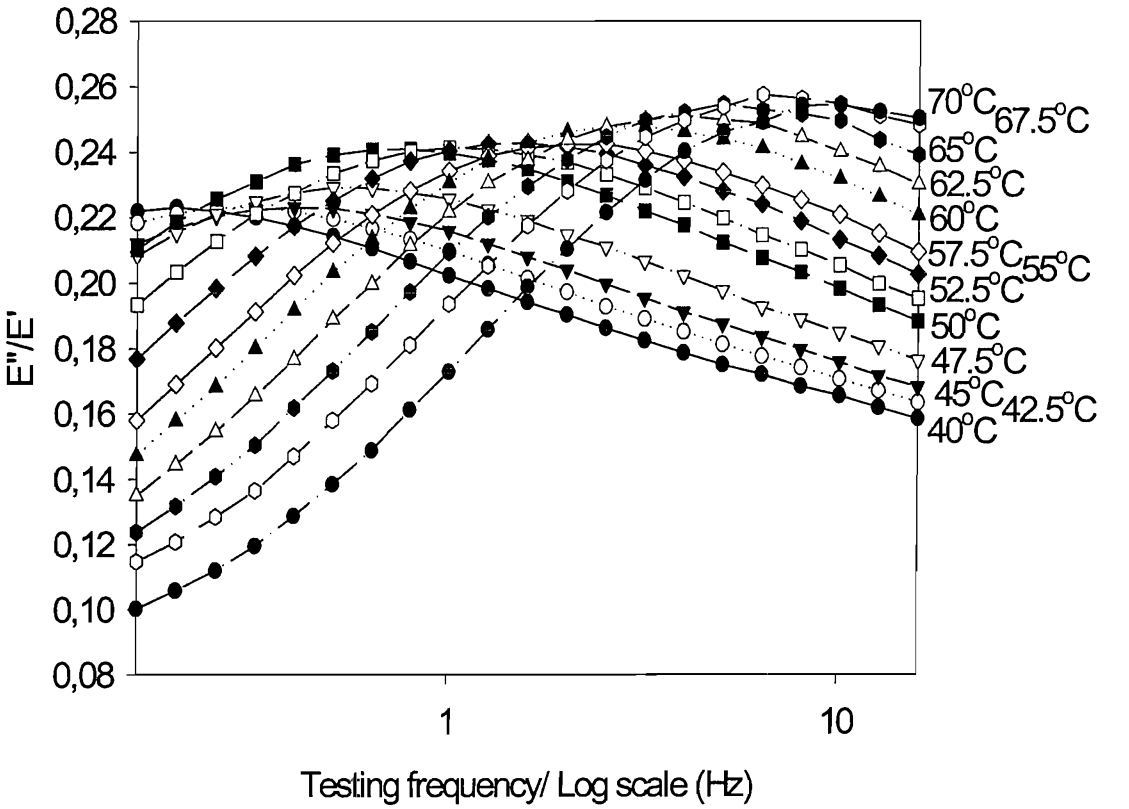

Figure 3.13: Series of isothermal data acquired from a (Mat.C/X/SQ) sample.

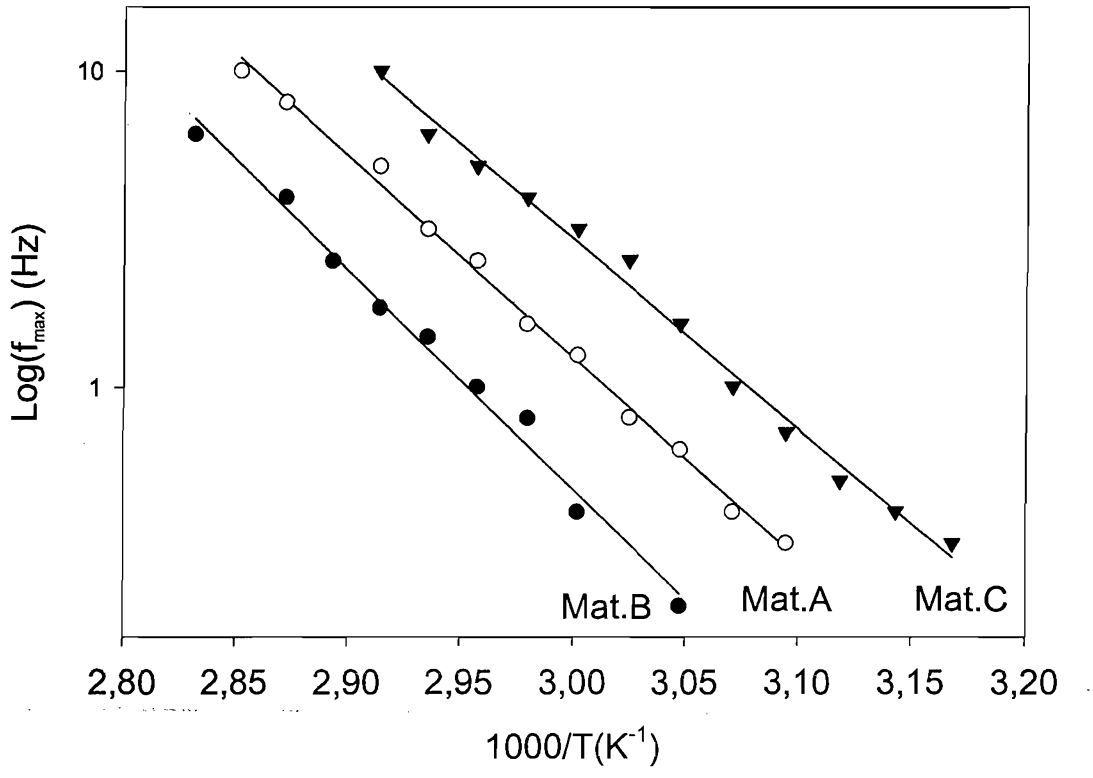

Fig.3.14: A plot of log f_{max} as a function of the reciprocal temperature-Values for f_{max} were taken from data that make up fig.3.15, fig.3.16 and fig.3.17.

3.3.4 Effects of crosslinking on the α relaxation

Here, we explored the effect of crosslinking on the formation of the α peak, by applying successive thermal treatments to a single sample formed from uncrosslinked Material C. Fig.3.15 contains several isochronal data sets; the latter were obtained from a (Mat.C/SQ) sample, named trace I, which was subsequently re-melted prior to activating DCP at 150°C for approximately 15 minutes, and reported as trace II. By doing so, we wished to acquire data from a partially crosslinked specimen. Then, traces numbered III and IV were then obtained from (Mat.C/X/SQ) and (Mat.C/X/FQ) samples, respectively. With the exception of trace IV, we can clearly see how the α peak behaves in response to the different crosslinking conditions. At first, the behaviour of the uncrosslinked sample is similar to Material B, in the sense that it resembles most closely the data obtained from (Mat.B/SQ), which is shown in fig.3.9. We think this result correlates well enough to the DSC melting behaviour of Materials B and C, when C is not crosslinked (cf. fig.3.5 and fig.3.6). Once initiated, crosslinking displaces the α peak towards lower temperatures without affecting its amplitude, see

trace II. Finally, trace III can be depicted in terms of a significant reduction in the peak's overall amplitude, which is not excessively affected in terms of positioning of T_α when compared to trace II. Since crosslinking is the only parameter that varies, we can suggest that it is crosslinking that displaces and, eventually, reduces the amplitude of the α peak.

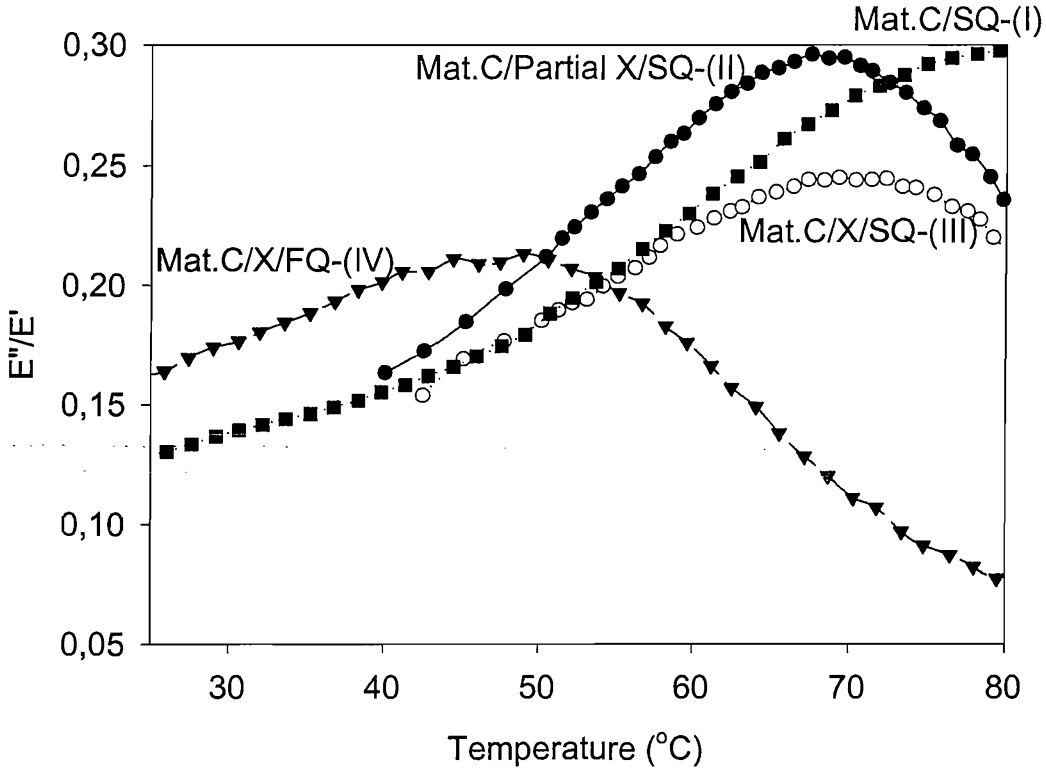

Figure 3.15: Changes in the α peak caused by the relative degree of crosslinking and quenching methods.

At this stage in our analysis, we can attempt to draw some conclusions about the molecular mechanisms behind the above phenomenon. Comparison of the Boyd [79] and Sirotkin [77] analysis with that given by Danch et al. [83] concerning the molecular interpretation of the α relaxation for PE, we see an apparent divergence of opinions regarding whether the α process originates from molecular motions taking place within the crystalline phase itself or in a some semi-ordered amorphous phase between lamellae. The latter point is precisely the one proposed by Danch et al., who support the idea that the α process arises from the "long-scale motion" of macromolecular segments situated in what they call a semi-ordered amorphous phase. They specifically claim that Boyd's interpretations were limited because the latter did not take into account the presence of a semi-ordered amorphous material. However,

Boyd clearly stated that the mechanical activity of the α relaxation is an "effect of crystal chain translation on the constrained amorphous phase", thereby explicitly differentiating the latter from a classical amorphous phase [79]. In both cases, it would therefore seem that it is molecular motions involving a constrained amorphous phase (i.e. a phase including tie molecules), from which mechanical methods detect the α relaxation. We specifically picture constrained chains as being part of the crosslinked network and suggest that this could lead to an overall reduction in molecular mobility, and, thus to a reduction in the magnitude of the α peak. However, to justify this viewpoint, we would also have to explain the fact that the amplitude of trace II is comparable to that of trace I. If we regard crosslinking as a gelation process, crosslinking must reach a certain point before exhibiting any consequent physical effect. Mandelkern points out that there is a threshold under which a developing network can not yet be considered as such [84], and we imagine this might be what differentiates partially and fully crosslinked networks. Fig.3.15 also shows that there is a major distinction to be made between trace III and trace IV, which must be related to the difference in the quenching method. Although crosslinking plays an obvious role in the reduction of the α peak, we certainly cannot ascribe this reduction uniquely to this parameter. Changing cooling kinetics might favour the rejection of the gel phase outside of the crosslinked network, but we can also hypothesize that any thermal step that permits chains to disentangle prior to crystallizing influences the mechanical relaxation we investigate.

3.3.5 Effects of thermal treatment on the α peak

Crystallization treatments developed from previous DSC examinations were now employed, prior to carrying out isochronal tests on the corresponding samples. Here, we restricted our testing to the study of three isothermal treatments, in addition to slow and fast quenching. Crystallization temperatures of 92, 102 and 108°C were considered here, in view of the marked differences between DSC melting traces obtained at these temperatures[16], if we except crosslinked Material C. Thus, fig.3.16, fig.3.17 and fig.3.18 were generated using equivalent data sets obtained from our three sample types. To categorize the effect of equivalent crystallization stages, we were particularly interested in identifying patterns that characterize the subsequent α peak, regardless of

[16] We considered that results obtained at 102°C represent a turning point in our DSC data.

sample type. To begin with, we point out that most α peaks fall outside our testing range in the case of Material B, in spite of having employed different crystallization treatments. If we now compare traces by pairs, it is interesting to see that T_α is the same for (Mat.A/SQ), (Mat.A/108) on one hand and (Mat.C/X/SQ) and (Mat.C/X/108) on the other hand. As mentioned above, we assume that this result originates from the fact that Materials A and C do not crystallize isothermally at 108°C[17], a result which follows directly DSC data. What differentiates the above pairs of data however, is the magnitude of the α peak, which is, in both cases, much higher when the sample is subjected to a straight quenching. We propose that this difference in behaviour originates from a variation in melt "pre-conditioning", that is, differences possibly occur in terms of molecular relaxation. We propose that molecular motions tend to change the distribution of macromolecular knots and topological constraints that are distinctive of any instant melt condition. Obviously, we cannot exclude the possibility that crystalline growth may then be influenced, to some extent, by this type of molecular relaxation and, possibly, by additional thermal fluctuation effects. The conceivable influence of such different factors certainly confers a greater complexity upon the ongoing analysis. Unfortunately, the only data we can reliably compare from our three graphs altogether are those obtained under fast quenching conditions. Employing these, we can attempt to extend the interpretation sketched out in the former section, since fast quenching conditions generate a drastic reduction in both T_α and the magnitude of the α peak. For all three materials, α peaks systematically form below values of T_α for data acquired with the same sample subjected to slow quenching. If we start by solely considering the variations in amplitude for such peaks as a function of thermal conditioning, we see that this parameter is strongly affected by crystallization treatments without the need for crosslinking reactions. If we then go back to the definition for the loss tangent, only a relative decrease in viscous dissipations can induce a decrease in the amplitude of the α peak. If we now attempt to rearrange the same data according to T_α's position, it is Material B which exhibits the highest temperature value, followed by Material C and, finally, Material A. Regrettably, because of experimental limitations, this type of classification cannot be extended to other crystallization conditions. We nonetheless suspect that extrinsic

[17] Slow quenching was the cooling method that was systematically employed after isothermal crystallization.

crystallization abilities may reveal themselves when cooling conditions are fast. By this, we mean that Material B's nucleation ability confers a direct advantage upon Material A, whose crystallization kinetics was shown to be slower. One could argue that Material C's crystallization ability is reduced due to crosslinking, when compared to Material A's when such materials are subjected to identical crystallization conditions; hence, we could expect Material A's T_α to be superior to that of Material C, especially since the melting of isothermal populations in Material A's case systematically takes place at higher temperatures than those of Material C. We do not, however, imagine that crosslinking reactions consume the entire amount of antioxidant originally present in Material C, therefore, we assume that such a remnant fraction could still enhance Material C's crystallization kinetics during fast cooling, yet, at this point, this remains to be shown. If we now compare data obtained from (Mat.A/SQ) and (Mat.C/X/SQ) samples, we observe that values for T_α fall in a much closer range than that observed for their FQ counterparts. In the latter configuration, Material A's T_α is only marginally lower than that of Material C.

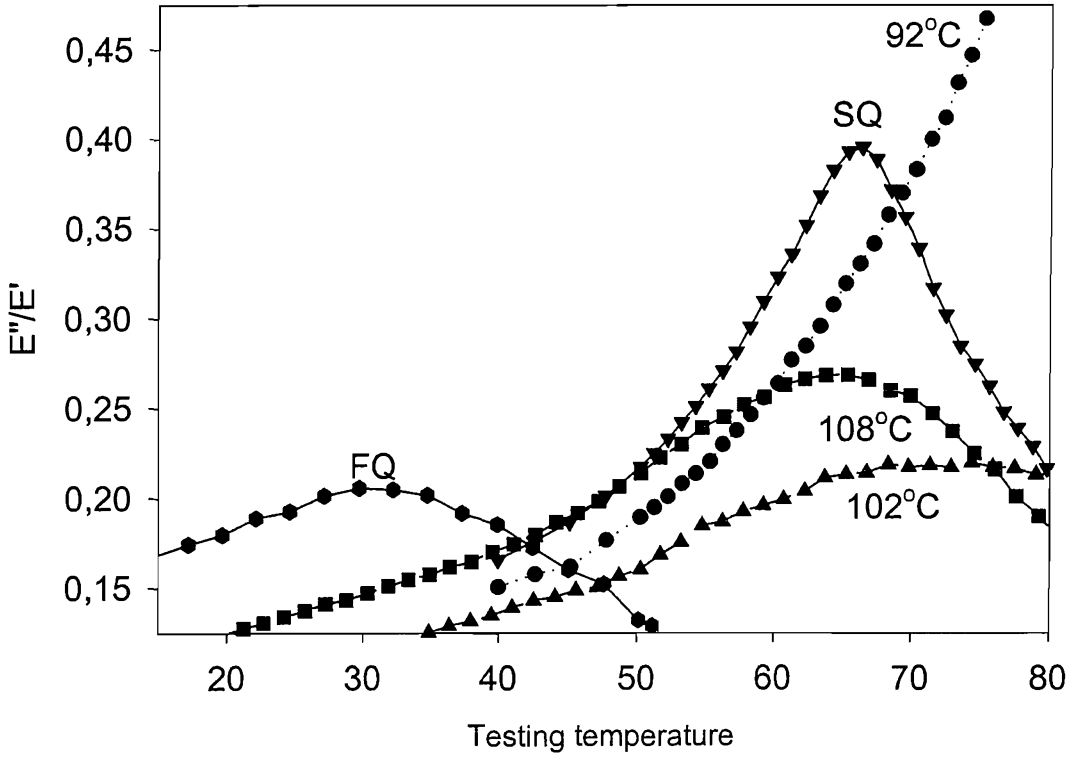

Figure 3.16: Isochronal data obtained from (Mat.A/T) samples; T reported on the graph.

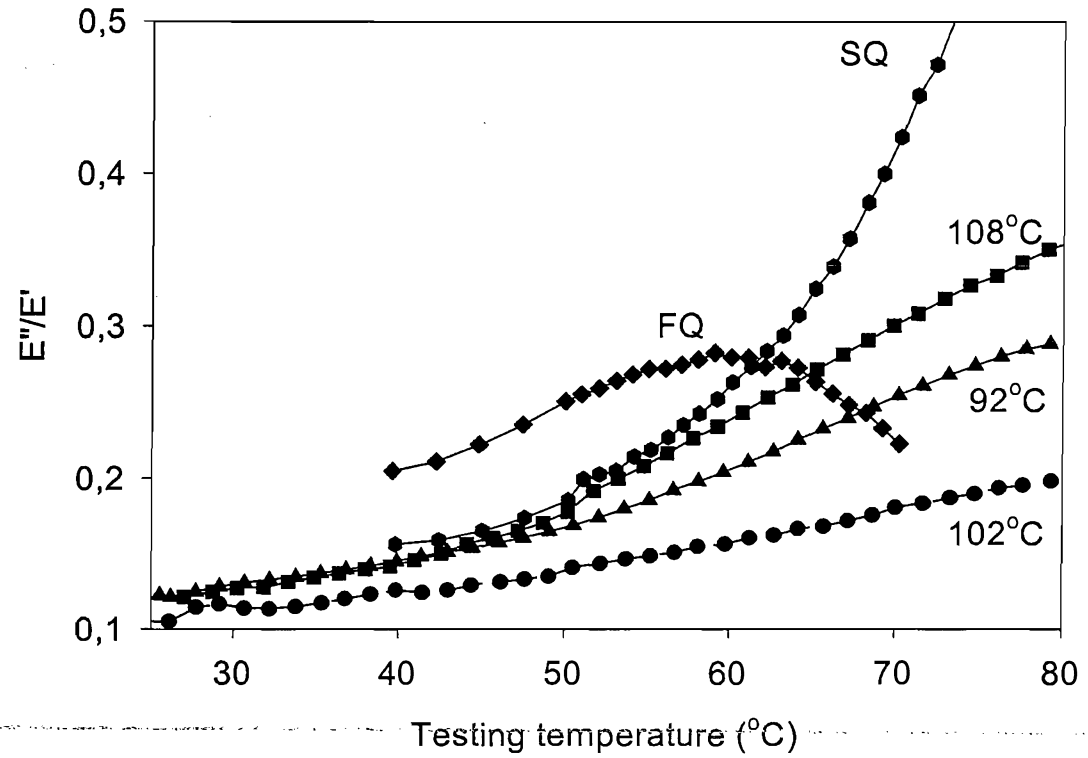

Figure 3.17: Isochronal data obtained from (Mat.B/T) samples; T reported in the graph.

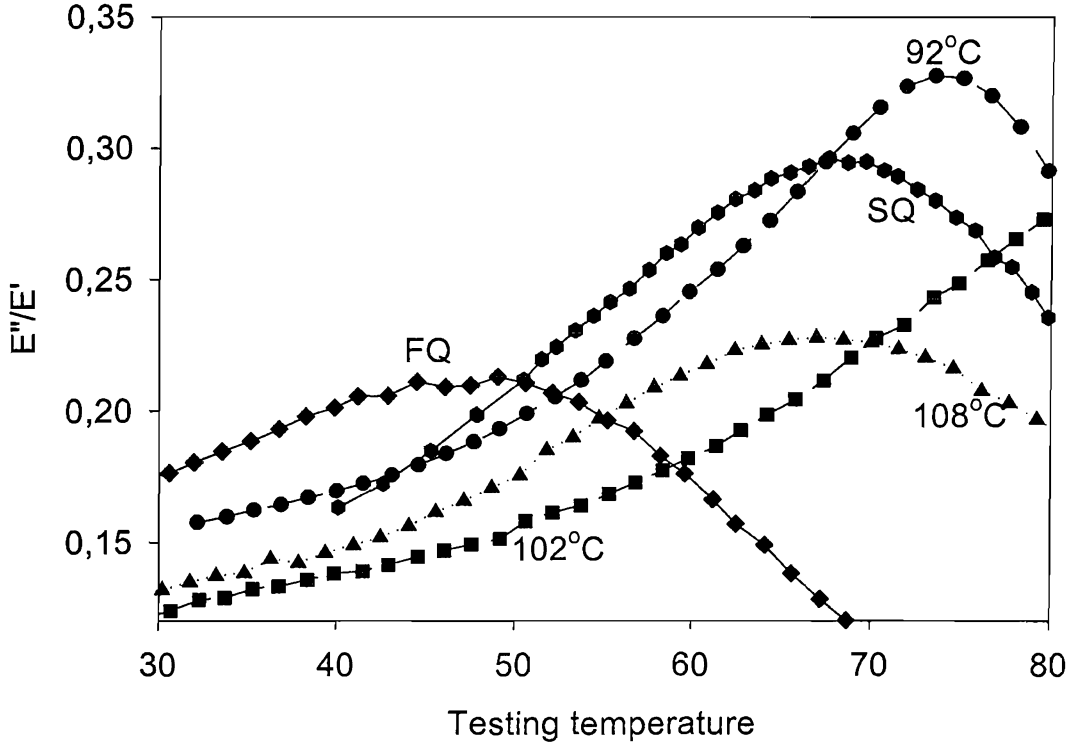

Figure 3.18: Isochronal data obtained from (Mat.C/X/T) samples; T reported in the graph.

We believe that the understanding of how the quantity *E"/E'* evolves with sample thermal history is essential; yet, it is the ensemble of molecular factors coupled to the respective magnitudes for *E'* and *E"* that are key to gaining a better understanding of the α process itself. Fig.3.19 is a histogram that displays values for the above moduli, obtained at different temperatures (30, 50 and 70°C), for a (Mat.C/X)[18] sample subjected to a range of crystallization conditions reported in fig.3.19. Table 3.1 also provides the numerical values used to build fig.3.19. From these data, we can see that values for the elastic modulus remain in a narrow range when the sample is crystallized isothermally, regardless of the crystallization temperature, however, we can classify our data on the basis of the magnitude of their loss modulus. Effectively, the higher the crystallization temperature, the lower dissipation they exhibit. This difference in behaviour tends to diminish when the testing temperature increases, to become elusive at 70°C. Otherwise, *E'* exhibits a significant reduction when the sample is quenched. More specifically, the (Mat.C/X/SQ) values for *E"* remain close enough to those for the (Mat.C/X/108) sample, however values for *E'* are lower here than for the latter sample. In addition, there is a significant reduction for both moduli which characterize the (Mat.C/X/FQ) sample relative to any other sample type. We assume the above variations indicate that changes in both moduli do arise in response to a thermal pre-conditioning coupled to crystallization conditions. It is certainly appealing to imagine that, as far as *E'* is concerned, a semi-crystalline polymer can be considered to be a composite material in which crystallites act as mechanical fillers; in such case, a higher elastic modulus potentially reflect the presence of a greater number of crystallites. In view of this, the (Mat.C/X/FQ) sample would be expected to be the least crystalline of all the presented samples. However, this explanation becomes questionable when comparing (Mat.C/X/SQ)'s elastic modulus to that of the (Mat.C/X/108) sample, since the magnitude of this modulus is likely to depend also on the presence of molecular entanglements.

[18] We only show values for Material C's moduli, the reason being that it is the only sample whose dimensions did not vary between annealing and crystallization treatments thanks to crosslinking.

Crystallization Temp. (/°C)	*E'*(Pa) @30°C	*E"*(Pa) @30°C	*E'*(Pa) @50°C	*E"*(Pa) @50°C	*E'*(Pa) @70°C	*E"*(Pa) @70°C
108	5.99e+08	7.90e+07	3.17e+08	5.57e+07	1.31e+08	2.96e+07
102	7.06e+08	8.75e+07	3.59e+08	5.68e+07	1.44e+08	3.28e+07
92	6.71e+08	1.14e+08	3.17e+08	6.30e+07	1.01e+08	3.18e+07
None/FQ	3.43e+08	6.05e+07	1.42e+08	2.99e+07	5.31e+07	5.89e+06
None/SQ	--	--	2.37e+08	5.02e+07	8.51e+07	2.48e+07

Table 3.1: Variations of sample C's moduli versus testing temperature.

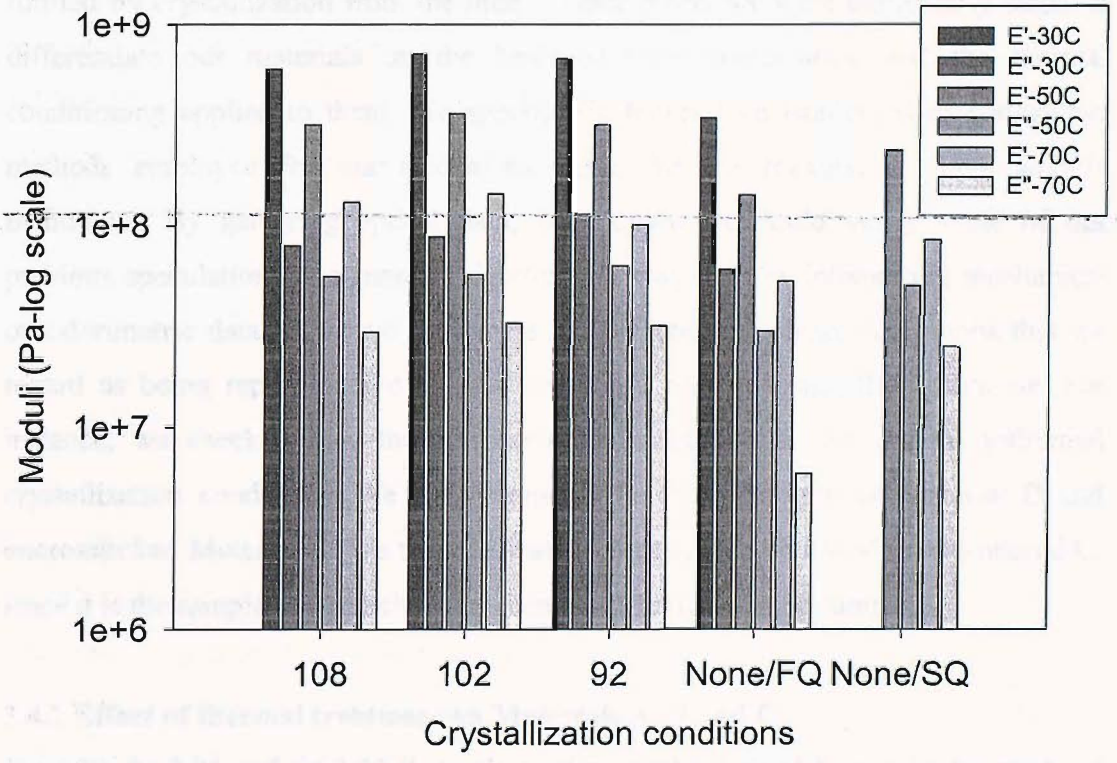

Figure 3.19: Variations of sample C's moduli versus testing temperature, as a function of the crystallization method-data were re-plotted from table 3.1.

To summarize, we believe that the mechanical data we have dealt with so far reflect the coupling that exists between different molecular processes that occur during the ensemble of thermal steps that make up complex crystallization treatments. Because of this, considering the sole crystallization temperature to explain how the α process occurs seems insufficient. Such process strongly depends on dissipative phenomena that are influenced, for instance, by factors such as crosslinking and molecular

relaxations taking place within the melt. Danch et al. [83] also speculated that the reorientation of crystallites in the amorphous matrix might have an additional role to play in LDPE's α relaxation. Since α relaxation features fall at temperatures significantly lower than those characteristic of the melting of isothermal populations observed using the DSC technique, we think that the α process could extend towards higher temperature and that the mechanical data dealt with thus far relate to fractions of quenched material.

3.4 Optical examination of thermally treated samples

In this section, we present several optical photomicrographs of crystalline entities formed by crystallization from the melt[19]. Once more, we were particularly eager to differentiate our materials on the basis of their composition and the thermal conditioning applied to them. We specifically focused on isothermal crystallization methods employed for our mechanical tests, for the reasons we have already mentioned. By gathering optical data, we thought we could verify some of our previous speculations in a more straightforward way than by interpreting mechanical or calorimetric data. What we show here is a selection of photomicrographs that we regard as being representative of what we could achieve using this technique. For instance, we checked how the morphology of Material A varies with isothermal crystallization conditions. We also compared the morphologies of Material B and uncrosslinked Material C. We then dedicate a short section to crosslinked Material C, since it is the sample whose behaviour seemed, at first, the most complex.

3.4.1 Effect of thermal treatment on Materials A, B and C

Fig.3.20, fig.3.21 and fig.3.22 show photomicrographs derived from samples made of Materials A, B and C respectively. More specifically, fig.3.20 shows the effect of isothermal crystallization on Material A; crystallization temperatures were 92, 102 and 108°C. What we can see from fig.3.20's micrographs are individual objects separated by clear, straight boundaries[20]. The objects seen in each micrograph exhibit radii that

[19] Some attempts were made to make our samples even thinner by adding a small amount of xylene prior to pressing them. This procedure affected the outcome of the crystallization stages and this method was therefore discarded.

[20] Purposely, our micrographs were captured slightly out of focus to accentuate the appearance of boundaries.

range from 20 to 40μm; more importantly, they all show extinction patterns that are characteristic of a spherulitic-like structure. Regardless of the crystallization treatment, there is no distinguishable variation between these three micrographs. Importantly, we must mention that the spherulites that formed in the (Mat.A/108) did not form at this crystallization temperature[21], but appeared during cooling. This can be observed in a direct manner, thus supporting the former DSC and mechanical analysis. There is nothing more to see from a (Mat.A/SQ) sample, therefore we did not include it here. Fig.3.21 shows the effect of the aforementioned crystallization treatments on Material B. In this material, no individual crystalline entities can be seen at all, even though our samples did crystallize under the imposed conditions; what we could see, however, is the fast formation of a granular structure, which is especially pronounced in the case of the (Mat.B/92) sample. A similar texture could also be seen for a (Mat.B/SQ) sample, therefore we do not include it here. Finally fig.3.22 contains micrographs obtained from a (Mat.C/SQ) and (Mat.C/102). Any thermal treatment applied to an uncrosslinked sample of Material C produced the same granular appearance as seen in Material B. We therefore conclude that the behaviour of uncrosslinked Material C is dominated by the presence of the antioxidant, just like Material B. It correlates with the fact that melting traces for Materials B and C coincide with each other.

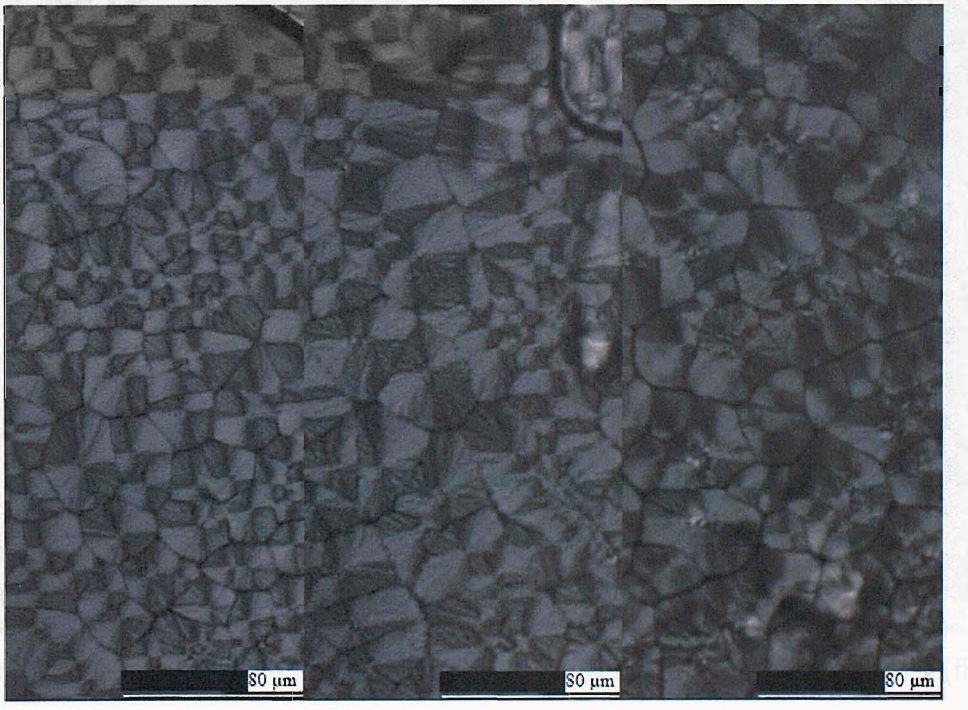

Figure 3.20: Micrographs obtained from (Mat.A/92), (Mat.A/102) and (Mat.A/108) samples (from left to right).

[21] Isolated birefringent objects do appear; they are extremely scarce.

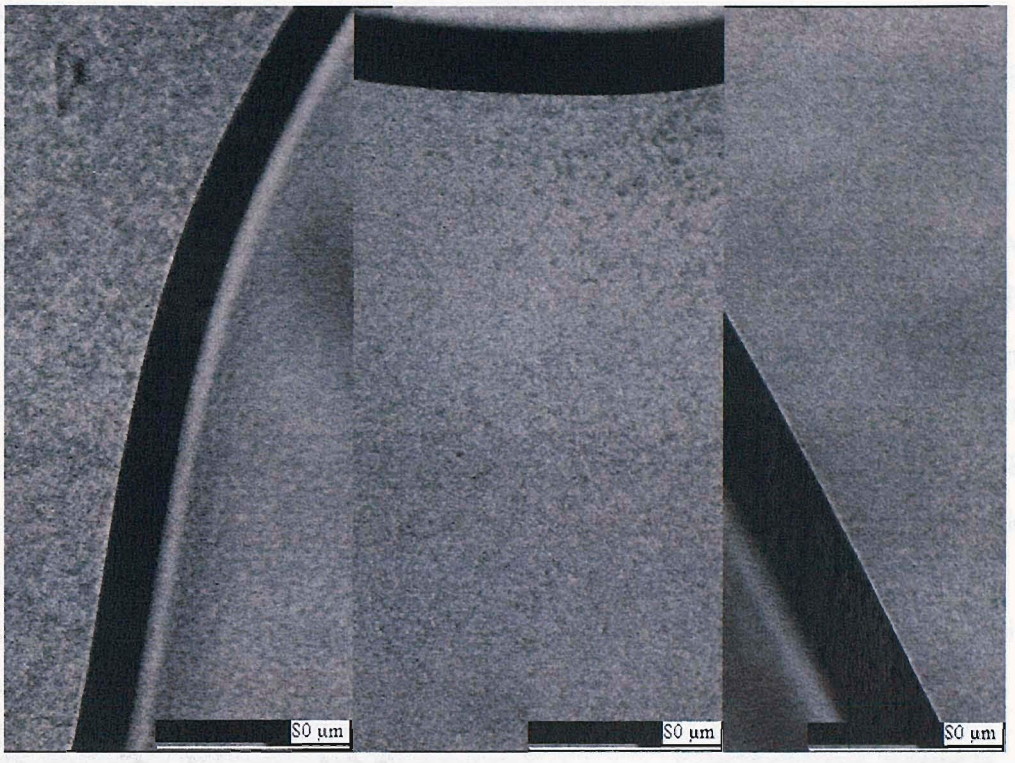

Figure 3.21: Micrographs obtained from (Mat.B/92), (Mat.B/102) and (Mat.B/108) samples (from left to right).

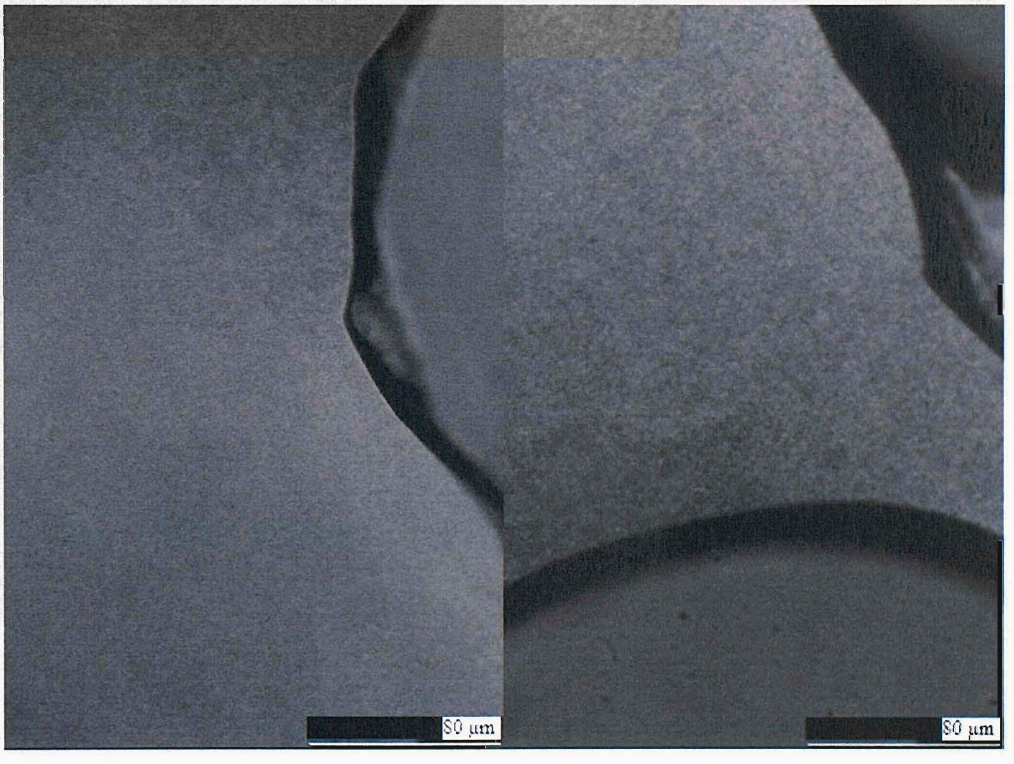

Figure 3.22: Micrographs obtained from (Mat.C/SQ) and (Mat.C/102) samples (from left to right).

3.4.2 Effect of crosslinking on the morphology of Material C

Material C's melt morphologies were largely varied, unfortunately, most examinations proved to be linked to the rejection of low molar mass LDPE chains out of the crosslinked material. The following figures, namely fig.3.23 to 3.26, illustrate this experimental artefact by differentiating bulk and edge morphologies. Fig.3.23 shows a spherulitic texture seen at the edge of a (Mat.C/X/SQ) sample, which exhibits individual entities whose size greatly exceeds that seen above for any micrograph obtained from Material A. Fig.3.24 illustrates the gradual passage from a spherulitic texture in (Mat.C/X/108) to a uniform granular texture that resembles Material B's. Finally, fig.3.25 and fig.3.26 display micrographs obtained from the edge and bulk of (Mat.C/X/92) and (Mat.C/X/102) samples. Fig.3.25 reveals a texture based upon the formation of banded spherulites[22], whereas fig.3.26 shows spherulite-like entities displaying thickness-related characteristics.

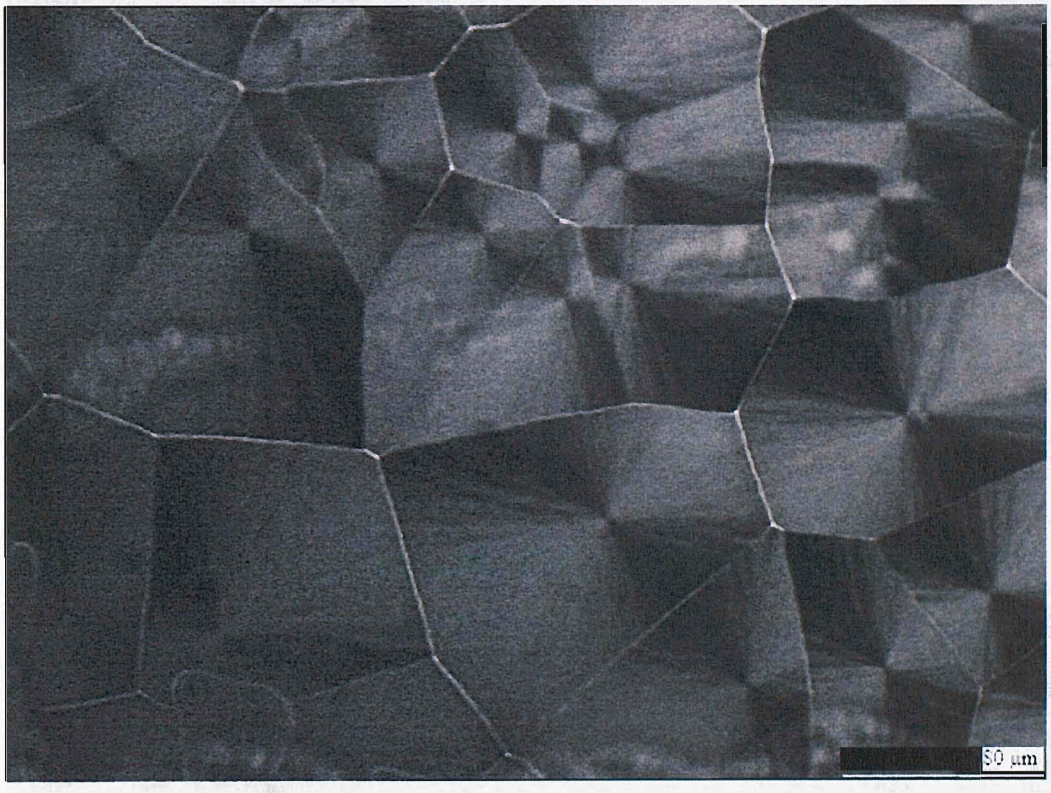

Figure 3.23: Micrograph obtained from the edge of a (Mat.C/X/SQ) sample.

[22] A banded spherulite derives its appearance from the regular reorientation of lamellae that are viewed edge-on in the bright ringed region.

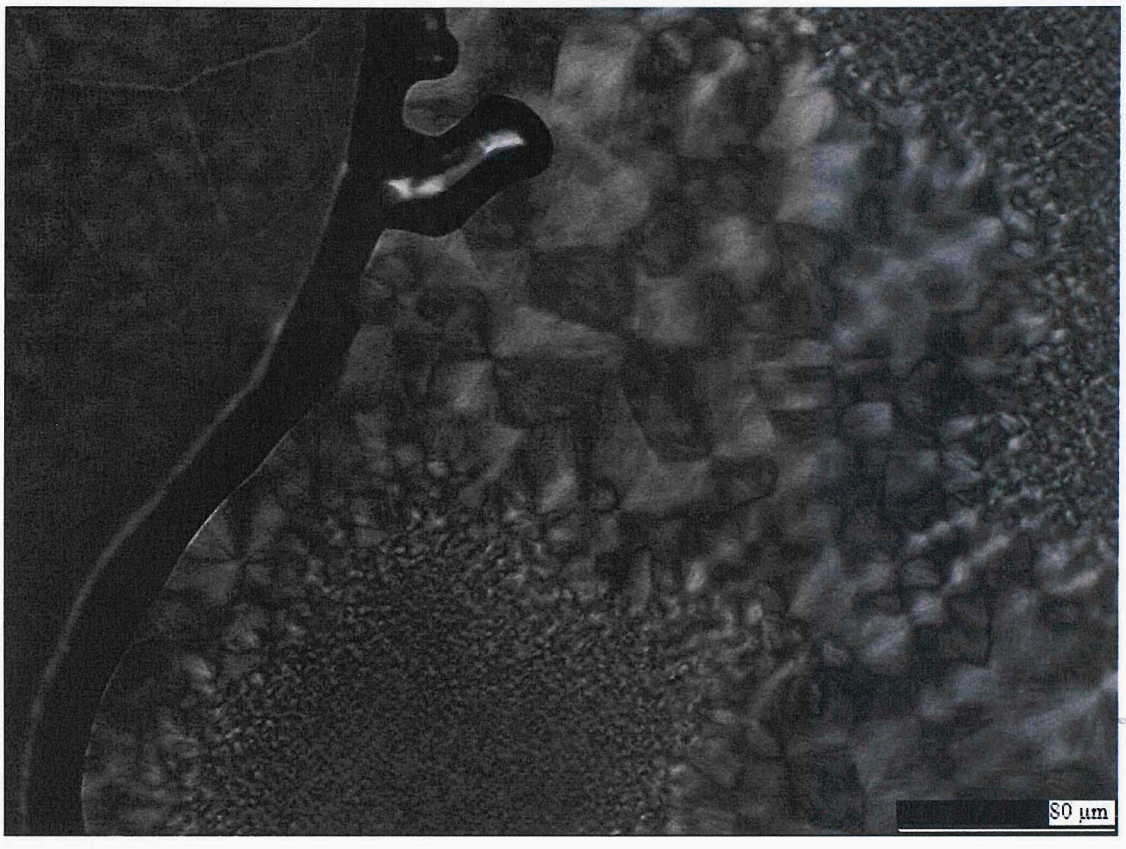

Figure 3.24: Micrograph obtained from a (Mat.C/X/108) sample.

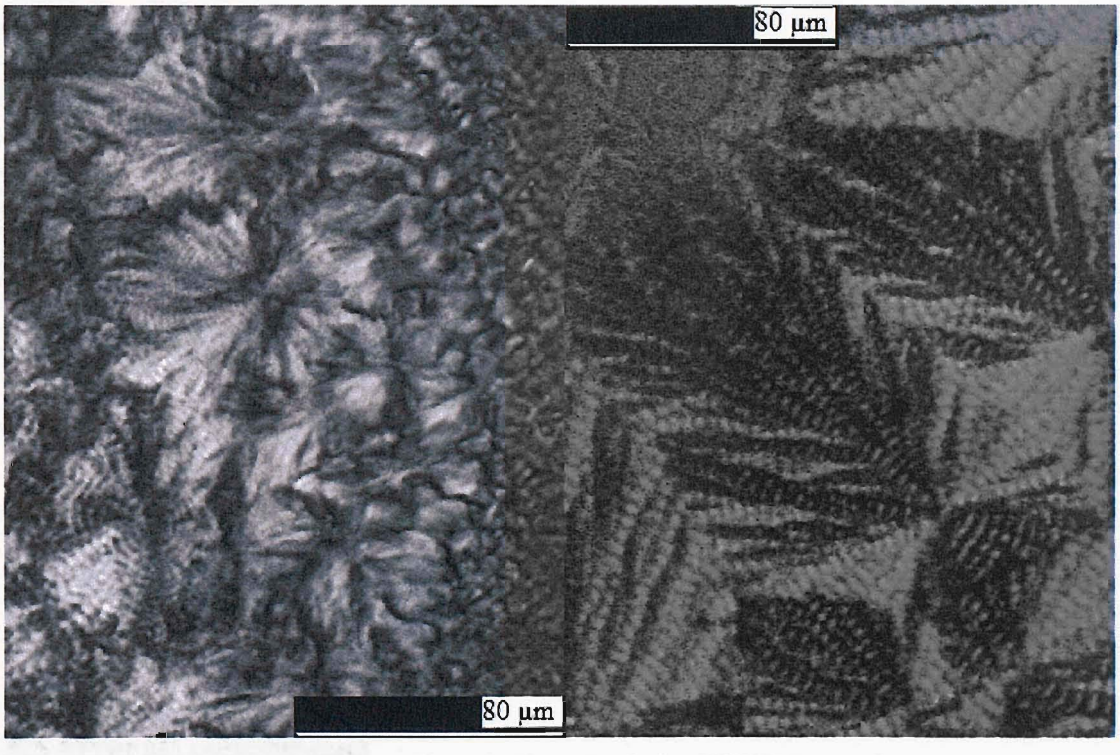

Figure 3.25: Bulk and edge of a (Mat.C/X/92) sample.

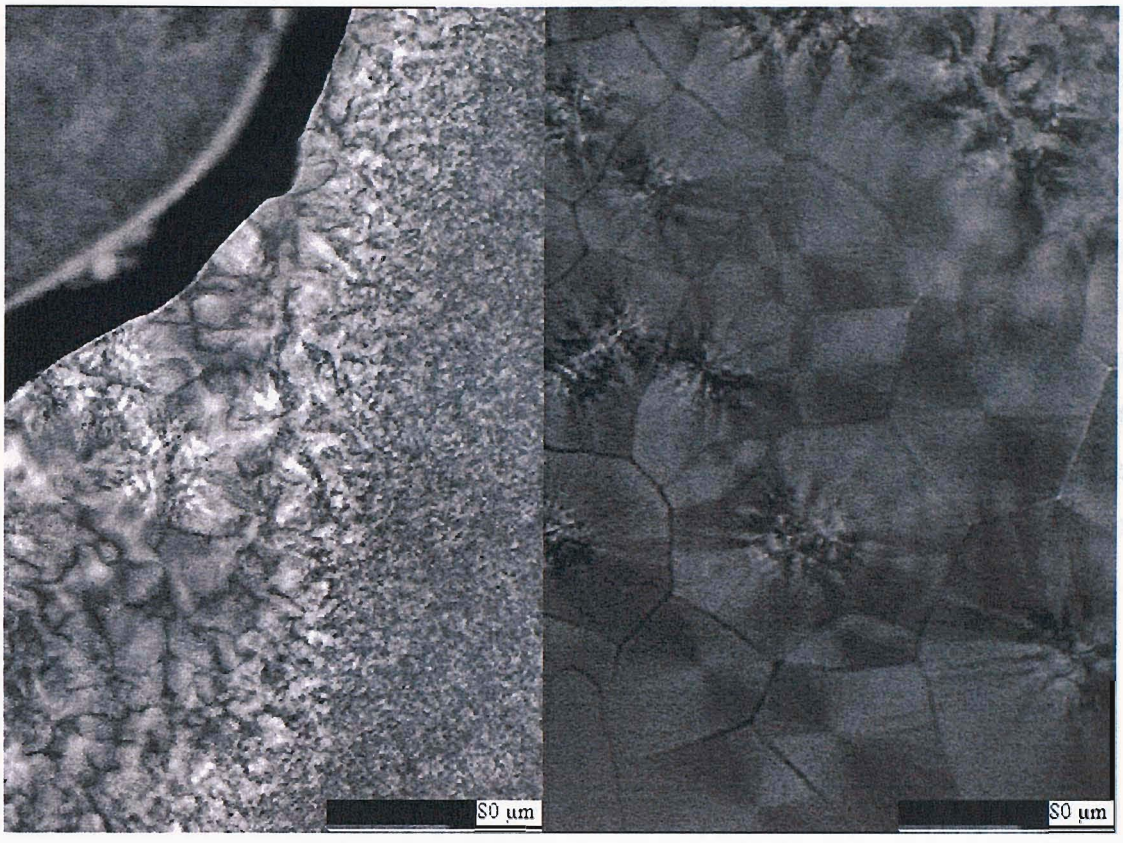

Figure 3.26: Bulk and edge of a (Mat.C/X/102) sample.

To summarize, the most meaningful results derived from our optical examinations is that uncrosslinked Material C behaves similarly to Material B, as soon as we examine bulk morphologies. This is due to the nucleating ability of the antioxidant, which provides a support to speculations discussed in section 3.3.5 regarding the classification of α peaks when materials are subjected to fast quenching. Also, we can confirm that Material A does not crystallize isothermally at 108°C, which is consistent with the corresponding melting trace obtained via DSC. Eventually, the discussion about a morphological "gradient" within samples made of crosslinked Material C proved to be no more than a sample preparation artefact. Still, the rejection of an uncrosslinked fraction may be a serious factor to take into account during the processing of power cables.

3.5 Overall conclusions

Throughout this chapter, we have described the main effects of sample composition and thermal processing on the structure of our model materials. Both DSC and mechanical measurements give insights into lamellar thickness and melting, whereas

optical examinations revealed more specifically how superstructures made of lamellae form under various thermal treatments. We place a strong emphasis to the fact that the interpretation of results derived via dynamic mechanical analysis is undermined by the temperature range accessible with our materials; we believe that we are dealing with a rather incomplete picture of LDPE's α relaxation, and that high-temperature features remain to be detected. Nevertheless, we demonstrated how complex the α process truly is, in the sense that a number of molecular processes are strongly coupled. What we can extract from the above collection of experiments is the unambiguous ability for Material B's additive to promote nucleation. This additive also determines the morphological properties of Material C, even when the latter is crosslinked prior to crystallizing.

Chapter 4

Water uptake kinetics in LDPE-based materials

4.1 Introduction

The topic of diffusion in polymers is relatively broad; see, for example, the overview presented by Crank and Park in the book, "Diffusion in polymers" [85]. In this, Barrie's work [48] specifically focused on the mechanism by which water diffuses in different polymers and reviewed the influence of a number of parameters on permeation characteristics. Barrie explains that the cross-sectional area for diffusion is reduced in the presence of crystallites, and shows that clustering is encouraged when vapour pressure is increased. As part of this study, we attempted to evaluate water diffusion characteristics in a range of LDPE-based samples but, in practice, this proved to be a challenging task since polyethylene's sorptive capacities are intrinsically low. Experimentally, it was easier to acquire data through desorption experiments, and, therefore, we will mainly discuss desorption results in this chapter. For comparison purposes, we will exploit several desorption data sets, which were acquired from different systems, including those studied in the preceding chapter. To enhance diffusion, additional desorption data sets were also collected from blended (EVA/LDPE) materials. The interpretation of our data is then performed both analytically and numerically; the latter method possesses significant advantages, since one can adjust the parameters in the simulation in order to reproduce experimental data.

4.2 Description of analytical and numerical methods

4.2.1 Analytical estimates for the diffusion coefficient

The basic equation that describes diffusion in isotropic substances is based upon Fick's laws of diffusion. The following equation is the most general form encountered for Fick's second law:

$$\partial C / \partial t = D div(grad C) \quad \text{(eq.4.1)}$$

Here, C, D and t respectively represent the concentration, diffusion coefficient and time.

Analytical estimates for D can be estimated from complex expressions such as:

$$M_t / M_\infty = 1 - (8/\pi^2) \sum_{n=0}^{\infty} (2n+1)^{-2} \exp[-D(2n+1)^2 L^{-2} \pi^2 t] \quad \text{(eq.4.2)}$$

In this equation, M_t and M_∞ stand for the masses of liquid sorbed at the instant t and the mass of liquid sorbed at infinite times; D again represents the diffusion coefficient and L the sample thickness. Eq.4.2 is introduced as a theoretical expression by Crank and Park [85] to describe sorption kinetics[1]. According to these authors, this equation also describes desorption in the case of membranes initially "conditioned to a uniform concentration and whose surface concentrations are instantaneously brought to zero at t=0" (sic). The diffusion coefficient can be estimated in several ways from a single plot, and simplified expressions can be utilized instead of the more complex eq.4.2 [85]:

- When $M_t/M_\infty<0.5$, $M_t / M_\infty = 4L^{-1}(Dt/\pi)^{1/2}$ (eq.4.3)
- When $M_t/M_\infty=0.5$, $D \sim 0.049/(t_{1/2}/L^2)$ (eq.4.4)
- When $M_t/M_\infty>0.5$, $M_t / M_\infty = 1 - (8/\pi^2)\exp(-DtL^{-2}\pi^2)$ (eq.4.5)

4.2.2 Implementation of the numerical method

Throughout this chapter, we also have recourse to a finite difference method (FDM) to derive numerical estimates for diffusion coefficients by reproducing experimental data acquired from several diffusion experiments. FDM is an interesting tool, which provides a simple mean of readily adjusting calculation parameters, such as boundary conditions and a numerical equivalent to the physical diffusion parameter. To perform numerical computations, the following method was implemented under MS Excel software.

To begin with, we discretized the Cartesian, unidirectional version of Fick's second law[2]:

$$\partial C / \partial t = D \partial^2 C / \partial x^2 \quad \text{(eq.4.6)}$$

---

[1] Sorption is a term which covers both sorption and desorption.

[2] We considered this approximation to be appropriate because our samples are membrane-like; therefore, sorption/desorption processes will take place along just a single axis.

Here, x stand for the position variable. Transforming this equation into its discrete formulation leads to the numerical scheme [86]:

$$(C_{x,t+dt} - C_{x,t})/\Delta t - D[\theta(C_{x+dx,t+dt} - 2C_{x,t+dt} + C_{x-dx,t+dt}) + (1-\theta)(C_{x+dx,t} - 2C_{x,t} + C_{x-dx,t})]/\Delta x^2 = 0 \quad \text{(eq.4.7)}$$

From eq.4.7, one can derive a fully explicit scheme[3] where θ is an adjustable numerical integration parameter as $\theta \in [0,1]$ (here $\theta=0$):-

$$C_{x,t+dt} = C_{x,t} + D(\Delta t/\Delta x^2)(C_{x-dx,t} - 2C_{x,t} + C_{x+dx,t}) \quad \text{(eq.4.8)}$$

where the parameter $C_{x,t+dt}$ remains the only unknown concentration value; the latter can then be directly evaluated from known quantities, $C_{x,t}$, $C_{x-dx,t}$, $C_{x+dx,t}$, D, Δt and Δx, which stand for the concentrations at the nodes of coordinates $(x,t),(x-dx,t),(x+dx,t)$ (see fig.4.1), a numerical diffusion coefficient, the time and position intervals in the FDM; x and t respectively represent the distance and time coordinates defining our interpolation grid, composed of interpolation nodes. A visual representation of this elementary interpolation grid is given in fig.4.1.

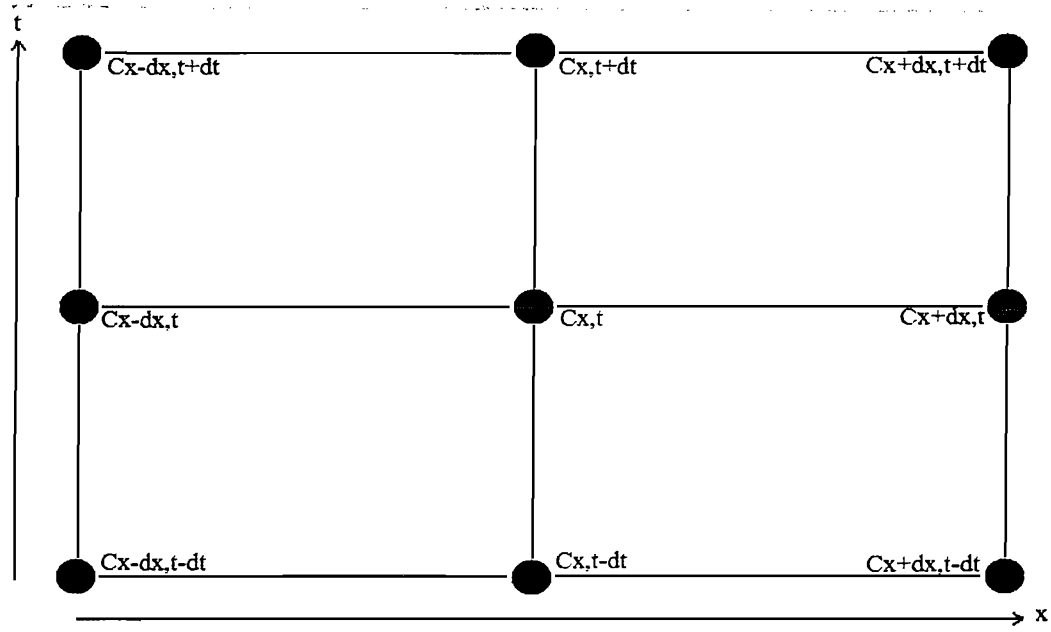

Figure 4.1: Elementary grid comprising interpolation nodes in x and t.

The correct utilization of the discrete formula provided by eq.4.8 requires conditions that link D, Δt and Δx. Hence, a necessary condition for numerical convergence is that [86]:

$$\Delta t/\Delta x^2 \leq 1/((2-4\theta)D) \quad \text{(eq.4.9)}$$

[3] When $\theta=0$, the formula which gives the quantity $C_{x,t+dt}$ relies uniquely on employing data "from the past".

Eq.4.8 holds for θ values that are strictly less than *1/2*. Thus, a condition of numerical convergence is obtained thanks to the following inequality, when $\theta=0$:

$$0 < (\Delta t / \Delta x^2) \leq (2D)^{-1} \qquad \text{(eq.4.10)}$$

Eq.4.10 expresses the necessary balance for calculations to converge. The choice of an adequate mesh gives access to a range of numerical diffusion coefficients, when the latter is treated as an adjustable input. At this point, one must address the choice of boundary and initial conditions. Such parameters are chosen to represent physical variables, such as the initial concentration gradients present at the interface of the numerical specimen. In sorption, both boundary and initial conditions remain simple, since internal concentration gradients are nil and only an external gradient applies. Basic conditions for desorption are given as examples here. Provided that concentration equilibrium is reached after a given sorption time, we first assumed that the overall concentration in the swollen material is likely to appear constant; albeit with an internal interface effect accompanied by a sharp drop in penetrant concentration. We chose to represent this condition by using an exponential drop which normalizes concentration levels to unity:

$$C(x, t = 0) = 1 - \exp(-ax) \qquad \text{(eq.4.11)}$$

Here, the parameter a influences the sharpness of the drop in concentration found at the interface, and discrete values for C extracted from that model served as starting data points for the calculations. Then, we chose an expression for the chosen boundary condition:

$$C(x = 0, t) = k \qquad \text{(eq.4.12)}$$

Here, k is a constant that can be adjusted. A visual representation of the initial condition is given in fig.4.2, which shows a typical interpolation mesh, comprising ten interpolation nodes along the x-axis. Fig.4.2 also contains a graphical representation of eq.4.11, with a value of $a=100$. Fig.4.2 illustrates the fact that only the values found at the intercept between the continuous concentration profile and the node at which calculations are performed have an effect on the subsequent computations. Therefore, the rate at which the real concentration profile drops in the vicinity of the interface cannot be rendered using these calculations; obviously, we could have arbitrarily assigned a constant value of 1 to all nodes, except the one that corresponds to the interface, which would make perfect sense with the analytical treatment previously described. We nonetheless believe that eq.4.11 constitutes a more realistic

representation of the underlying physics, even though the latter is lost somewhat when passing to the discrete case.

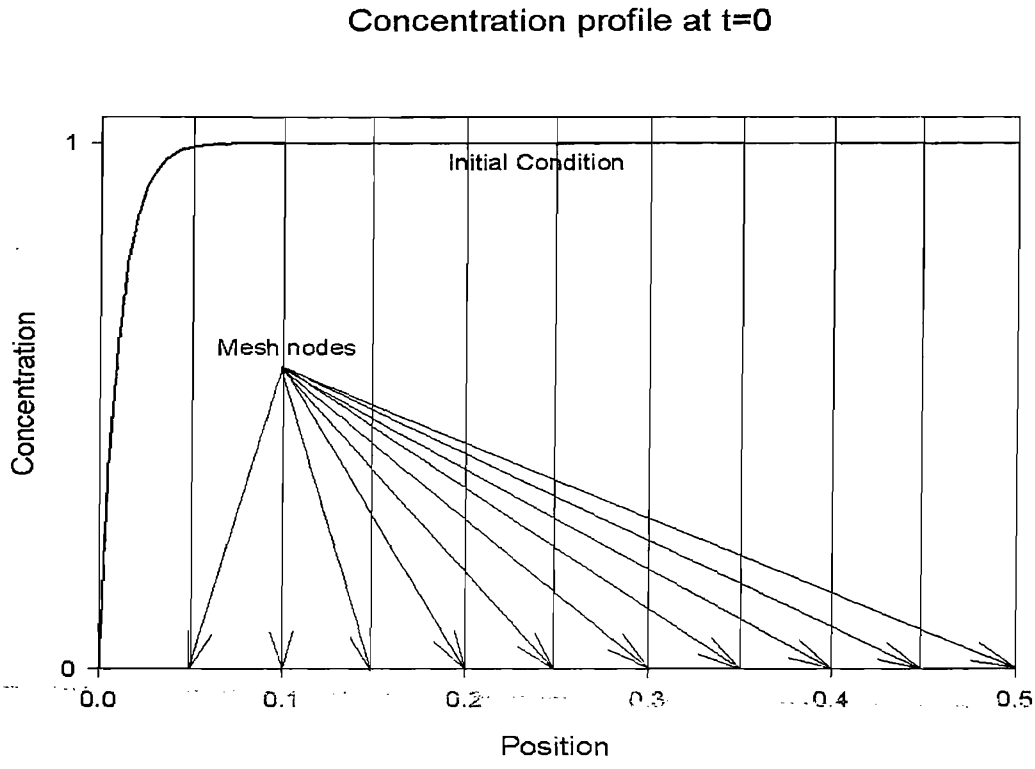

Figure 4.2: Initial condition reported on the mesh nodes (*a=100*).

To illustrate the kind of numerical results we obtain using this FDM method, we generated fig.4.3, which shows a series of numerical concentration desorption profiles computed for different values of t (1, 30, 300 and 1800 seconds respectively[4]). This figure shows how the concentration profiles varies from the interface to the symmetry axis of the sample. By doing so, we implicitly considered that diffusion occurs equivalently through both sample sides.

When dealing with experimental data, our aim was to obtain numerical estimates for D by reproducing experimental profiles. More precisely, if a sample loses or gains a certain mass of water after a given amount of time, we need only reproduce this behaviour numerically to obtain an estimate for D, provided that the other conditions under which our computations are carried out are also well-defined. To get from data of the form shown in fig.4.3 to estimates for D, we included an additional MS Excel routine. In this, an average absorbed mass is derived by summing up elementary

[4] To carry out calculations, an arbitrary value of 10^{-10} m^2/s was chosen for D.

rectangular areas whose length and width are respectively provided by nodal values and the fixed quantity, Δx.

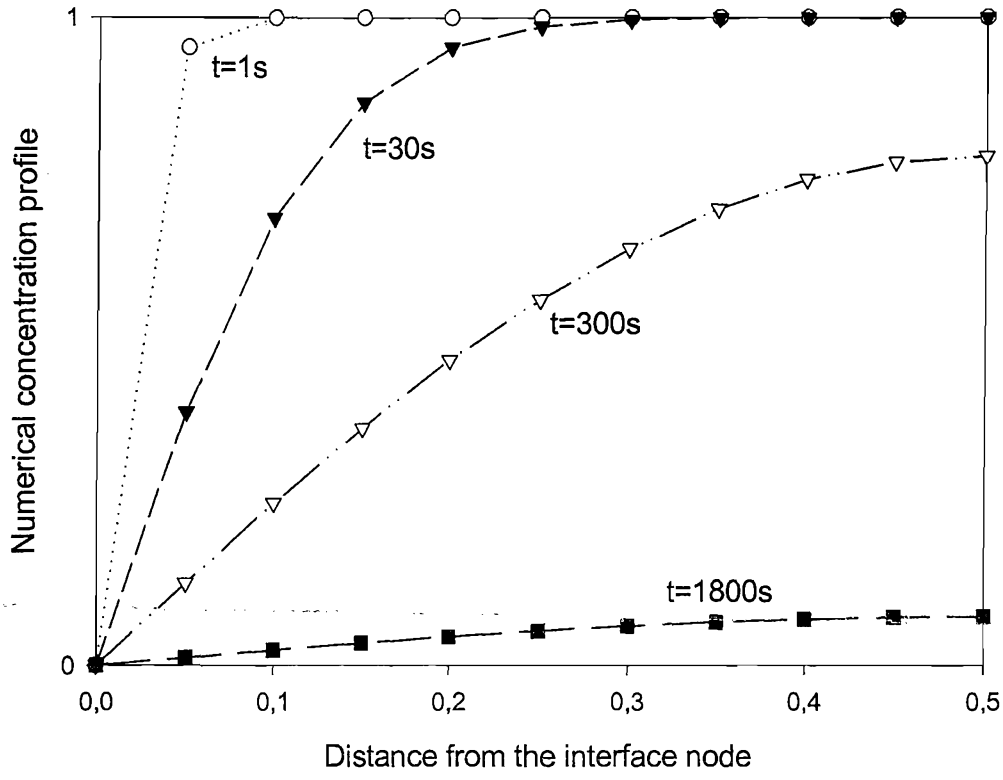

Figure 4.3: Numerical concentration profiles computed for desorption (*a=100*; $D=10^{-10}$ m^2/s; Δt=1 s; Δx=0.05 mm; k=0).

4.3 Diffusion experiments carried out on Materials A, B and C and (EVA/LDPE) blends

In this section, we will introduce our experimental results and then interpret them using the aforementioned techniques.

4.3.1 Presentation of raw absorption data

The decision to follow, in real time, water desorption in LDPE-based materials rather than absorption processes, stems from the fact that the very act of following absorption could, in itself, disrupt the process. This is because our measurement method relies on weighing samples immersed in water, hence samples need to be dried and weighed as rapidly as possible. Consequently, the sampling rate at which measurements were carried out had to be carefully considered, since the measurement times would appear to the sample, as a sequence of short desorption periods. In fig.4.4, we provide

several absorption data sets acquired from Materials A, B and C. The data points shown in this figure correspond to ratios of the sample mass at time t (m_t) divided by the original sample mass (m_o); this provides a straightforward mean of comparing water uptake levels between our different samples. Individual data points shown in fig.4.4 were acquired sequentially from samples re-immersed in water once weighing had been performed; the morphological structure of the considered samples is that of slow-quenched materials[5], and most data were acquired from samples immersed in tap water.

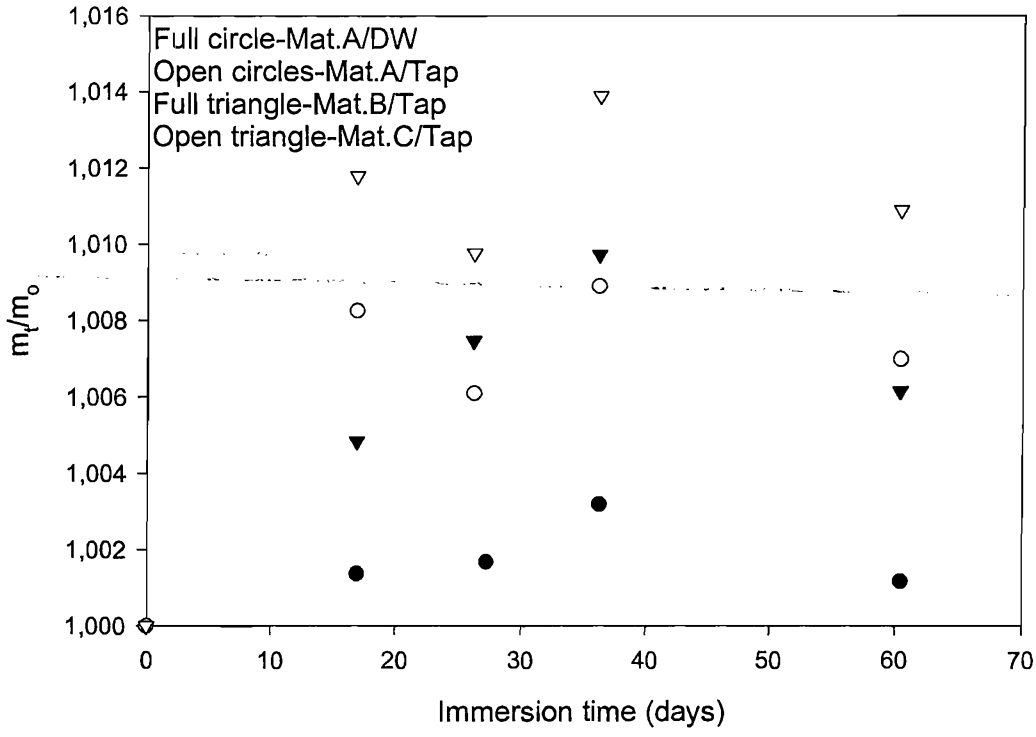

Figure 4.4: Several water uptake data sets acquired from slow-quenched LDPE-based samples.

Fig.4.4 clearly shows that all individual plots reveal marked water uptake after an immersion time of 15 days, regardless of sample type and solvent quality. It is not clear that these samples continue to absorb additional water quantities when re-immersed in water, since, from these results, we cannot exclude the possibility that the totality of water diffusion occurs during the earliest absorption stage, to remain constant afterwards. In their book, Raff and Allison [87] present data sets concerning the

[5] DSC material provided as Appendix IV-1 demonstrates that, due to sample thickness, one cannot have a complete control over sample morphology.

absorption of water in PE, obtained by an immersion method of sheets in water at 70°C and room temperature, with a constant sampling rate of 6 months, for a total time of 2 years. Interestingly, their data show that an increase in weight does not appear systematic, even though both sets exhibit a global increase up to 2 years immersion time. Fig.4.4 raises an additional issue, which is, the effect of solvent quality on diffusion characteristics. It is obvious that the magnitude of tap water's absorption is significantly higher than that of DW's. We think one can mainly ascribe this effect to the likely presence of a range of polar substances in tap water. Since water absorption levels are always small in PE, we decided to accept any factor which significantly increases water uptake, even though uncertainties due to water composition may complicate the interpretation of our data. Consequently, we principally employed tap water for our desorption experiments. Additionally, we believe that this option could provide a realistic contamination aspect to our work.

The same method was adopted to study desorption kinetics in some blended samples, namely (20/80), (40/60), (60/40) samples[6]. In such systems, saturation times were typically reached after about 48 hours.

4.3.2 Presentation of processed desorption data

Desorption plots presented in this section were all generated by representing the quantity M_t/M_∞, as a percentage, versus the quantity $t^{1/2}$, which is the square root of desorption time; M_t and M_∞ are quantities that were previously introduced in connection with eq.4.2. Desorption data were all acquired at room temperature. The following figures, namely fig.4.5 and fig.4.6 respectively display plots obtained from Materials A, B and C, and the aforementioned blends. Independent of sample type, we observe that within experimental uncertainty, all of our plots exhibit a dominant linear decrease, albeit with a slight misalignment with the starting point; we highlighted these linear parts by adding straight lines to individual plots. Linear parts are systematically followed by a slower, non-linear decrease in mass loss, once the concentration in penetrant has fallen by 60 to 80%. We think that the initial deviation concerning the first data point is attributable, at least partly, to an experimental time-lag; that is, there may be a brief transient time during which water does not diffuse constantly, or

[6] A (80/20) sample was also prepared, however the latter became solubilized and, hence, could not be used any further.

alternatively, there might be a short time[7] during which the microbalance remains insensitive to weight variations. We will return to this in due course.

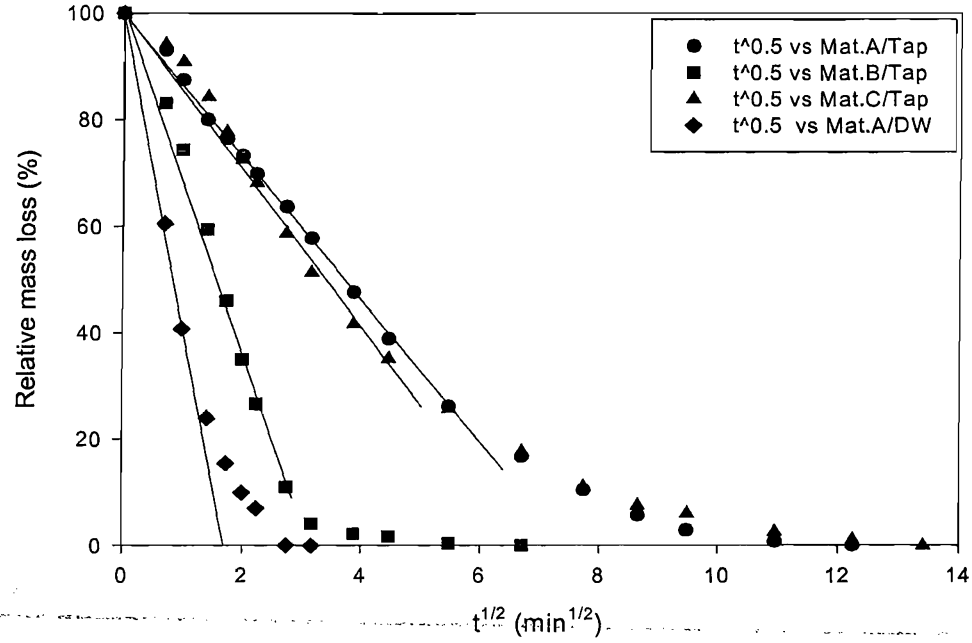

Figure 4.5: Desorption data acquired from Materials A, B and C, immersed in DW (only Mat.A) and tap water.

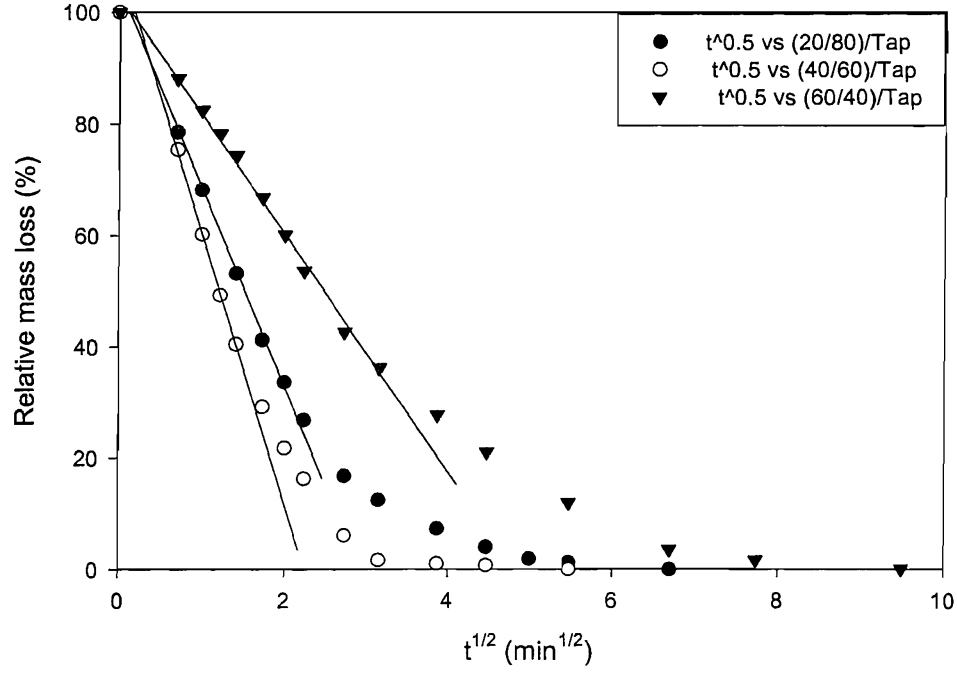

Figure 4.6: Desorption data obtained from the (20/80), (40/60) and (60/40) specimens, immersed in tap water.

[7] As specified in section 2.3.4, the balance stabilizes, on average, after ten seconds.

According to Fujita [88], several criteria must be met to ensure that sorption data truly conform to Fickian characteristics:

- First, sorption curves must be linear over the greater portion of the curve, typically 60% of the plot.
- Then, the observed curves must be concave to the abscissa axis.
- Additionally, reduced[8] sorption curves must be superimposable;

It is not possible to judge our plots according to all the above criteria, since we did not perform experiments on sheets of variable thickness; furthermore, it was difficult to acquire data to construct absorption curves, and fewer points were acquired, essentially to check whether diffusion processes were still ongoing or not. The above plots meet some of the requirements to be characterized as Fickian, yet we do not possess the appropriate data to ensure that this is absolutely the case.

4.3.3 Analytical estimates for the diffusion coefficient

According to Barrie [48], polyolefins are a class of materials in which the "solution of water in the polymer appears to be thermodynamically ideal and the mobility factor independent of concentration so that D is constant". Inversely, polar systems are more likely to exhibit a concentration-dependent value for D [48]. For such systems, a fraction of sorbed molecules can be trapped (immobilized) and follow a Langmuir-type sorption model [48].

To perform the following analysis, we employed eq.4.4 to derive analytical estimates for D; to do so, we had to locate the experimental point at which exactly 50% of the liquid had diffused out of the sample ($t_{1/2}$). Table 4.1 contains values acquired from the different graphs shown in both fig.4.5 and fig.4.6. In this table, we provide estimates for D and $t_{1/2}$, and we also include saturation concentrations measured for our different samples.

	A/Tap	B/Tap	C/Tap	A/DW	(20/80)/Tap	(40/60)/Tap	(60/40)/Tap
D ($x10^{10}$ m^2/s)	**0.61**	**3.20**	**0.73**	**11.24**	**3.61**	**4.60**	**1.36**
$t_{1/2}$ (s)	**821.5**	**155.5**	**681.5**	**44.4**	**138.6**	**89.3**	**366.1**
Saturation concentration ($mmol.cm^{-3}$)	**0.62**	**0.60**	**1.27**	**0.08**	**0.73**	**0.65**	**1.35**

Table 4.1: Analytical estimates acquired for D and $t_{1/2}$. Saturation concentrations are also included.

[8] Reduced sorption curves are plots whose x-axis is normalized thanks to sample thickness.

First, Table 4.1 quantifies the data presented in fig.4.4, and shows that the solvent type exerts a strong influence on the final quantity of water absorbed by a sample, in this case, Material A. Thus, the effect of water composition is to change saturation concentrations, by almost one order of magnitude in this case. Other saturation concentrations, including those obtained from blended materials, remain globally of the same order as that of Material A immersed in tap water. The highest amount of water are found both in Material C and the (60/40) sample, which exhibit a saturation concentration approximately twice that of other samples immersed in tap water. If we return to the mixing theory, one can derive saturation concentrations on the basis of the difference in solubility between both species. By employing an expression similar to eq.1.32, Iordanskii et al. [89] calculated that, for oligomeric hydrocarbon systems, the soluble fraction of water attains 0.01 mmol.cm^{-3} at 25°C; our saturation values exceed this theoretical solubility threshold by between one and three orders of magnitude. Obviously, the latter estimate is not readily applicable to our materials, since we are not dealing with an oligomer. In addition, our water diffusion experiments were performed at 50°C. Nevertheless, we believe that the above estimate provides a fair assessment of what is to be expected in terms of reciprocal solubility for this general class of systems. Also, Iordanskii et al. [89] state that water concentration is expected to be higher in hydrocarbon polymers than that of oligomers. We believe this partially explains the fact that the saturation concentration displayed by Material A immersed in tap water is effectively higher than the above estimate but, again, this experimental concentration was obtained at a temperature exceeding that employed to calculate the above estimate (50°C). Exclusively for XLPE samples, Ilstad [14] reports an experimental concentration value of 3.3 μmol/cm^3 at 50°C, a value much lower than ours. However, the latter author decided to stop his absorption experiments after just two hours of immersion. Saturation concentrations for water[9] in LDPE and EVA polymers were experimentally measured by Devallencourt et al. [90]; the values they report range between 0.02 mmol/cm^3 for LDPE and 0.83 mmol/cm^3 for EVA samples containing 70% of VA groups (in weight). Such values are in quite good agreement with those shown in the above table. Moreover, the latter authors report saturation concentrations for a range of EVA with increasing amount of VA groups (4.5 to 70%), and, for these, there is no obvious increase in saturation concentration with the amount of VA, except

[9] These authors do not specify the type of solvent they employ.

for the material with the most vinyl groups. If we go back to values for the diffusion coefficient, we can see that there is no easy way to find a correlation between the absorbed quantities of water and desorption kinetics. However, prior to discussing in more detail the figures presented in Table 4.1, we need to discuss the possible effect of some experimental conditions on these.

4.3.4 Reproduction of experimental data by numerical simulation

The principal reason for employing a numerical method is that certain experimental conditions may have affected data acquisition. Here, we will discuss the effect of relative humidity level on sorption profiles, and we will also attempt to provide an insight into the effect on numerical computations of the chosen boundary conditions. To begin with, we probe the method itself by looking at errors introduced by changing some computational parameters.

4.3.4.1 Position and time discretization effects on subsequent calculations

Before employing the numerical method to reproduce experimental data, we completed a series of model computations to determine the method's accuracy when discretization intervals, namely Δx and Δt, are changed. In doing this, all other calculation conditions were kept constant; here, the numerical diffusion coefficient was fixed at an arbitrary value of 10^{-10} m^2/s. To see whether time and distance intervals play a symmetric role in the computation, we generated two separate graphs, which investigate equivalent ranges for Δx and Δt, in terms of their implementation in eq.4.8. Fig.4.7 contains a series of numerical concentration profiles acquired by varying Δx between 0.01 and 0.1 mm (one order of magnitude); this graph contains series of plots acquired after different calculation times. In the other, namely fig.4.8, similar series of concentration profiles are presented, which were acquired by varying the quantity Δt between 0.01 and 1 s (two orders of magnitude). From fig.4.7, we see that nodal concentration values obtained with Δx=0.1 mm are systematically lower than those acquired with smaller values for Δx. This effect is especially pronounced at short computational times, when simulated concentration gradients are at their strongest. Such variations decline at longer computational times and numerical concentration profiles eventually tend to coincide. On the other hand, fig.4.8 shows how insignificant are the variations that exist between concentration profiles with different Δt values. Fig.4.8 does not enable the differences between the various data points calculated at nodal values to be

distinguished. Even though this is not evident from the latter figure, slightly more precision is gained when time intervals are reduced, even though such a gain in accuracy is marginal.

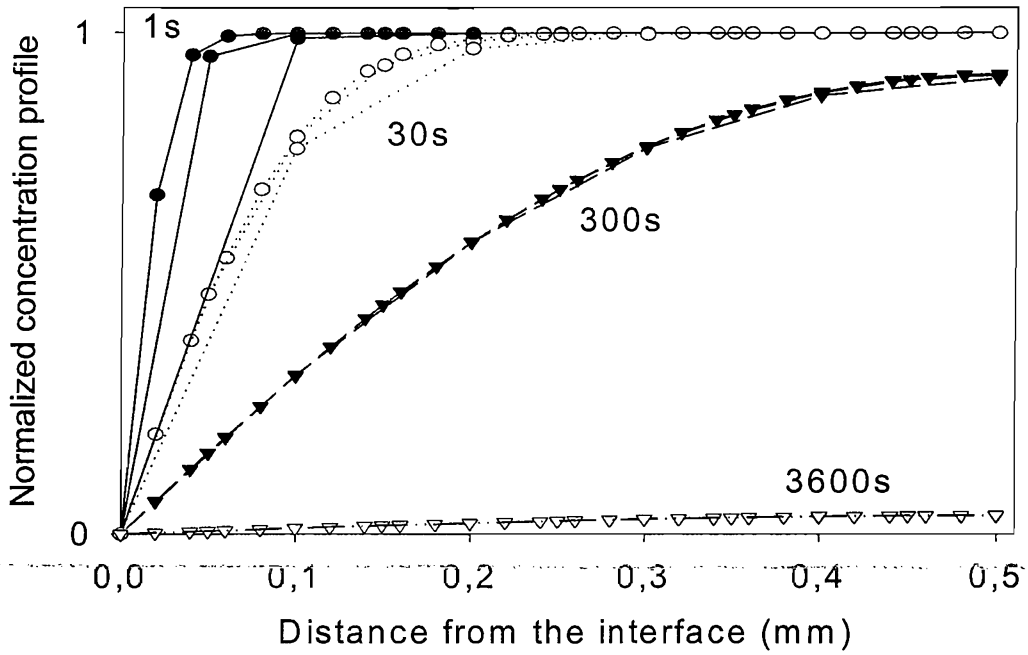

Figure 4.7: Desorption concentration profiles obtained after different computational times, and with different values of Δx (0.1, 0.05 and 0.01 mm).

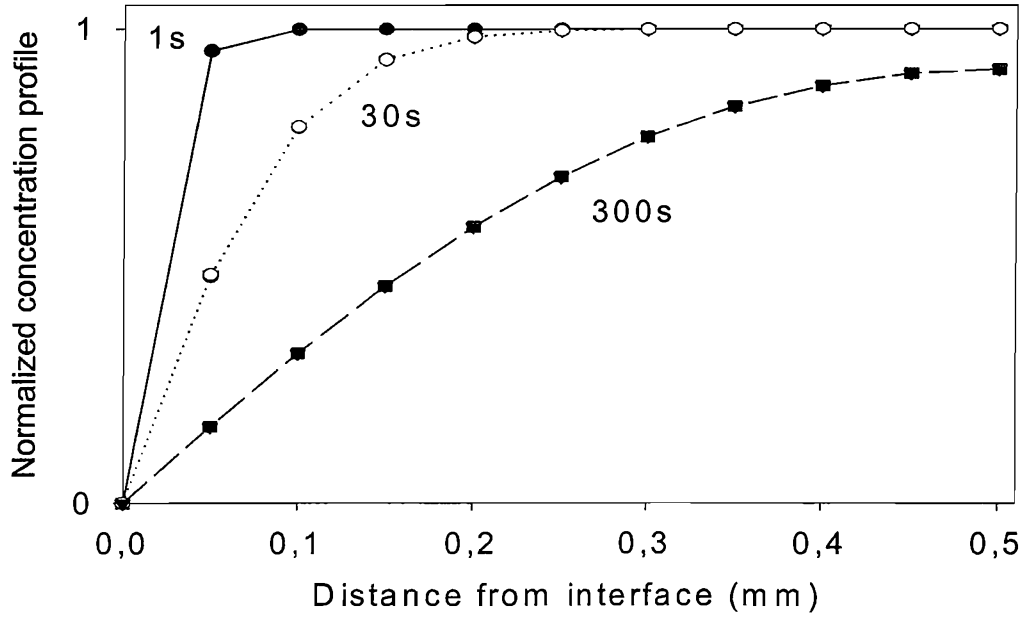

Figure 4.8: Desorption concentration profiles obtained after different computational times and with different values of Δt (0.01, 0.1, 0.25 and 1 s). The various data sets coincide almost perfectly and cannot be distinguished in this figure.

In view of the above results, the following computations were all carried out on nodes separated by a same Δx of 0.05 mm. Numerical concentration profiles also need to be integrated to derive figures equivalent to relative mass loss; hence, by fixing Δx, we also systematize the errors that characterize the estimates of the areas situated below each curve.

4.3.4.2 Are experimental and numerical data comparable?

It is crucial to see how experimental data match their numerical counterparts. To explore this, we attempted to reproduce a typical set of data acquired from Material A, following immersion in tap water. Computation conditions were determined by our analytical results, and thus, the chosen value for D was that reported in Table 4.1. Initial conditions are those originally presented in section 4.2.2, with boundary conditions corresponding to $k=0$, and Δt being fixed at 1 s. Fig.4.9 contains the experimental data previously shown in fig.4.5, in addition to two numerical profiles based upon the same numerical calculations. The first numerical desorption plot, reported as "rectangular" in the figure's legend, indicates that this profile was generated using a simple surface integration method we implemented within MS Excel. Conversely, the second plot, described as "trapezoidal", exploited a Sigma Plot macro command to integrate the same numerical data a second time. From fig.4.9, we can see that our numerical data match almost perfectly with our experimental data; moreover, the trapezoidal integration method draws nearer both experimental and numerical data, and we assume that the reason is that the latter method gives a better estimate of areas below each concentration profiles. We wish to point out that, in fig.4.9, both integration methods connect a first numerical point to an experimental one. Because of this, the rectangular method seems to exhibit an initial, non-linear characteristic. This is a mere effect regarding the visual connection between data points of different natures and, therefore, this apparent behaviour has no numerical justification.

At this point, we wish to readdress the experimental issue regarding the acquisition of initial data points. In practice, experiments were started as soon as mass variations were displayed by the balance. By doing so, we assumed that the latter had already stabilized and, in view of this, we started suspecting the existence of a short time lag characterizing the earliest desorption stage. It remains to be seen whether this transient stage is physical or experimental in nature. For instance, this process may originate from the initial drying procedure applied to the samples.

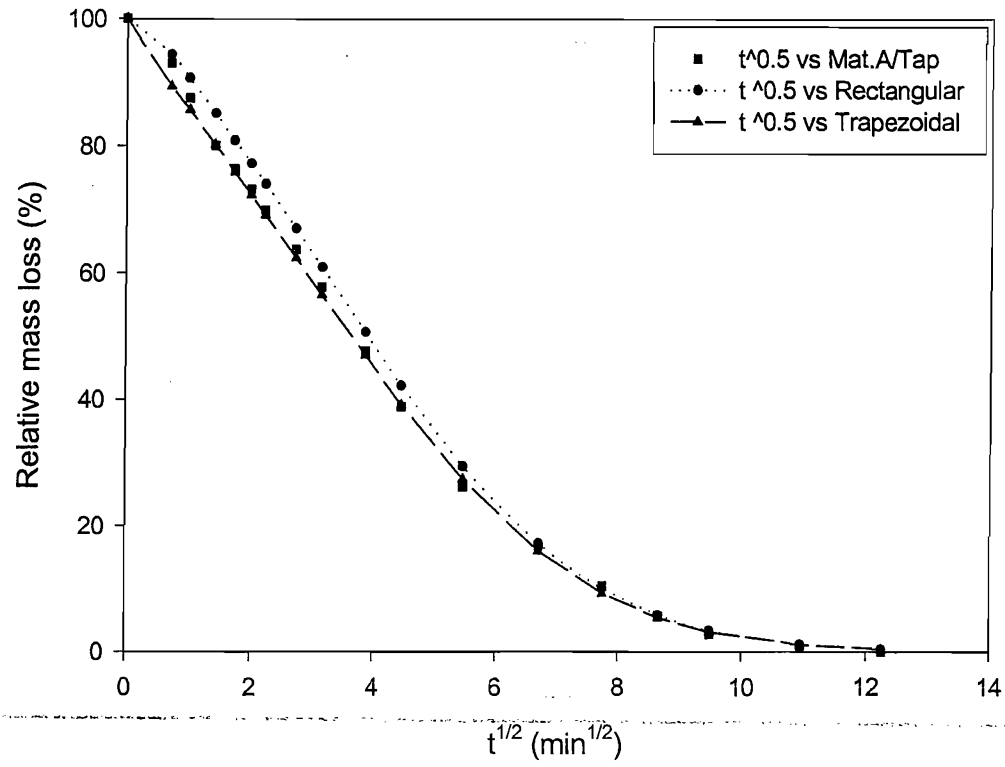

Figure 4.9: Overlaid experimental and numerical desorption profiles for Material A immersed in tap water (numerical conditions are detailed in the current paragraph).

4.3.4.3 Effects of relative humidity levels on desorption profiles

Fig.4.9 clearly illustrates the connection between Fickian processes and the experimental desorption profiles. Effectively, eq.4.6 assumes a diffusion coefficient which is not concentration-dependent, hence the previous results infer that our samples' desorption kinetics are Fickian. Here, we are interested in simulating the presence of relative humidity when performing a computation; this is simply done by fixing k to a constant value we determine. We originally omitted to evaluate relative humidity levels when acquiring our data, and this factor may prove of critical importance since the quantities of water dealt with in LDPE's case are extremely low. We estimated that air's saturation of water vapour occurs at a concentration of about 2 μmol/cm^3 (at 25°C), a value which is approximately 40 times smaller than water's saturation concentration of Material A immersed in DW[10]. Thanks to this estimate, we could implement a value of k which reproduces the presence of relative humidity. Obviously,

[10] We assumed that, at 25°C, water vapour saturation occurs when there are 12 kg of water per 454 kg of air.

the above concentration value in water vapour cannot be employed as such, since a 100% relative humidity level would not permit evaporation. To perform numerical computations, we simply assumed a 50% relative humidity level, and thus, adjusted the boundary condition as required. Fig.4.10 contains the result of numerical computations done for Material A immersed in both DW and tap water. This figure contains the two corresponding experimental plots, and it also contains two pairs of numerical desorption profiles. The latter profiles were respectively acquired by choosing relative humidity levels of 0 and 50%; moreover, the construction of those numerical profiles was made by employing only the trapezoidal method, which, as seen above, provides a better fit to experimental data. From fig.4.10, it is difficult to distinguish the outcome of varying the boundary condition on the appearance of the numerical data. This effect is even smaller in the case of Material A immersed in tap water, for which a plateau in relative mass loss is found at about 0.15%. A similar plateau can be found at about 1.25% for the numerical profile which corresponds to the data acquired from Material A immersed in DW. In both cases, the effect of this boundary condition does not, therefore, appear to greatly affect the numerical data. Thanks to this evaluation, we believe that relative humidity did not greatly affect our experimental readings.

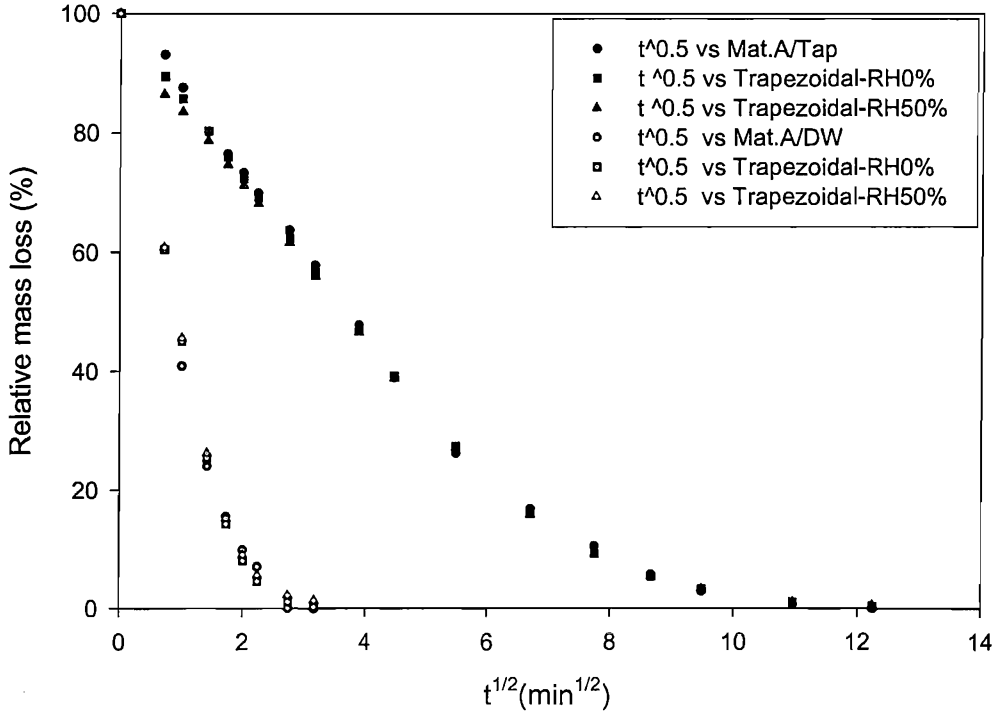

Figure 4.10: Superimposed concentration profiles evaluated numerically illustrating the effect of mesh refining and numerical gradient effects on nodal values.

4.3.4 Global interpretation of our data

Using our numerical method, we have demonstrated the validity of eq.4.6 with respect to our experimental desorption profiles throughout the complete desorption process. Hence, our results imply that D is a quantity which is not concentration-dependent and, under such circumstances, this rules out the experimental need to reach saturation concentration in studying sorption kinetics in LDPE-based and (EVA/LDPE) samples. We can now concentrate on the figures shown in Table 4.1 for D. The latter parameter was found to fall in a range between $6x10^{-11}$ and $1x10^{-9}$ m^2/s. If we first compare values for Material A immersed in tap water and DW, we can observe the extreme effect of solvent quantity on desorption kinetics, since DW diffused out of the sample at a rate which is approximately 20 times faster than for its counterpart. If we assume that tap water contains solubilized polar species, we can hypothesize that such polar species diffuse into a sample and, eventually, slow down the desorption process. The lowest diffusion rates are found for both Material A and Material C immersed in tap water, and we believe that the above effect may be attributable to variations in solvent quality. For XLPE, at 23°C, Ilstad [14] found a value for D of $4x10^{-11}$ m^2/s in absorption. For LDPE, Devallencourt et al. [90] report a value of $1.25x10^{-11}$ m^2/s for D, also in absorption. Such values are fairly close to that found for Materials A and C when immersed in tap water. Desorption kinetics for Material B appears significantly faster than that for Materials A and C. We can speculate that this variation originates either from a structural difference between our different samples or because of the presence of antioxidant in Material B, which may alter the sorption kinetics. We did not precisely determine the chemical nature of this antioxidant, but we can speculate that the latter produces a plasticizing effect, which could increase the frequency at which water molecules carry out elementary displacements. Also, Materials A and B are structurally very different.

If we now focus on data acquired from the blends, we can see that the range of values covered by D is relatively narrow, and the magnitude of D is close to that found for Material B. If water uptake increases with increasing fraction of EVA, the variations seen for D seem rather contradictory, in the sense that it appears difficult to state whether desorption kinetics become slower or faster as the quantity of EVA in the blend is increased. For EVA systems, Devallencourt et al. [90] report that D increases when EVA systems contain higher quantities of VA groups. The latter authors provide values for D of 1.4 to $3.9x10^{-11}$ m^2/s for EVA systems containing 33 and 50% VA

groups (in weight) respectively. Our own values differ from the above by one order of magnitude. This means that desorption kinetics measured from our blends is faster than that of pure EVA systems. One would expect water molecules to graft preferentially onto VA groups; however, blended systems may exhibit some complex composite behaviour relative to sorption kinetics, and this could explicate why our values for D differ from those of pure EVA materials, in particular, in the case of systems containing discrete EVA zones embedded within a continuous PE matrix.

4.4 Conclusions

Combined analytical and numerical analysis provided a better description of desorption kinetics for both LDPE and (EVA/LDPE) samples. Thanks to the numerical method, we could clearly determine that such processes are Fickian, and thus show that diffusion coefficients are not concentration-dependent quantities. The use of tap water as a penetrant showed its influence on water uptake, in the sense that absorbed quantities are considerably higher than with DW. Prior to carrying out sorption experiments, we expected blended materials to absorb the highest amount of water. Contrary to expectations, it is Material C which exhibited the highest saturation concentration. This may have further implications regarding the use of XLPE in power cables, especially because the contamination of water appears potentially to slow down desorption processes.

Chapter 5

Water-binding properties of guar gum

5.1 Introduction

To formulate a suitable water-trapping layer, it is necessary to understand the mechanisms by which water molecules can be retained by an active material that binds with such molecules. To be a successful water-trapping element, guar must also resist long-term effects, such as those generated by heat-producing elements found within power cables; we specifically refer to the conductors. This major consideration determined our choice of the most relevant accelerated ageing conditions to apply to unrefined guar samples; consequently, such conditions were chosen to reproduce an environmental state which is thought to correspond to that encountered in a warm and gas-free environment, as in an operating HV cable. We also employed alternative ageing conditions by preparing series of samples in air, as well as in nitrogen gas, so that potential oxidative reactions could also be considered. In the most general cases, guar molecules appear sensitive to oxidative and thermal depolymerisation processes [35], chemical and enzymatic cleavage [91], shear flow degradation [92] and ultrasonic irradiation processes [93]. In the context of this study though, we exclusively focused on the outcome produced by the ageing conditions mentioned above. In practice, the result was tested on refined, dilute solutions of guar, and, more precisely, the effect of thermo-oxidative degradation was explored using a viscometry technique. This type of measurement has been widely used to provide estimates of intrinsic viscosity [32,36,38,91,92,94,95]; it is also a useful means of deriving numerical estimates for the Flory-Huggins interaction parameter[1] [32,36,91,92,94] which is of great significance in understanding guar's binding with water.

In the first part of this chapter, we briefly explain the type of tests that were initially performed to determine the true nature of our material. Then, we demonstrate the need

[1] The Flory-Huggins interaction parameter is alternatively referred to as the Huggins' constant, or simply as the interaction parameter, in the literature.

for sample preparation; this is done, principally, by reviewing the different preparation methods encountered in the literature and by discussing some of our own results. Only then do we commence the analysis of our results. First, we comment on the effect of solvent quality, which determines the appearance of raw data, prior to discussing the methods for post-processing the latter. Afterwards, we introduce the main part of our results, which were extrapolated from data obtained from our different series of aged samples. Finally, we discuss, separately, the evolution of intrinsic viscosity and the interaction parameter with ageing conditions.

5.1.1 Overview of the preliminary work done to identify guar

Although this overview is not essential in understanding the following work, here, we provide a summary of several experiments which were initially performed to characterize our material:

- The earliest viscometry experiments we performed were intended to find which solvents exhibit the strongest affinity, and more specifically the closest solubility parameter, to that of our material. In practice, flow times were recorded several times with a given solution as soon as the latter was prepared. We carried out equivalent measurements on solutions prepared with different solvents, including n-hexane ($14.9MPa^{1/2}$), acetone ($20.3MPa^{1/2}$), methanol ($29.7MPa^{1/2}$), and water ($47.9MPa^{1/2}$). Efflux times tended towards that of the pure solvent for the first three solvents; this indicates that, in these, guar molecules precipitate in a finite time, so that they no longer contribute to solution viscosity. Conversely, the efflux times recorded from aqueous solutions of guar increased with time.
- Subsequently, we attempted to follow the evolution of efflux times over time since we thought they were linked to physical phenomena such as hydration kinetics, coil expansion and possibly hydrolysis kinetics. Series of measurements on diluted solutions were also performed; however, this ensemble of tests was invalidated principally by the fact that the viscometer could become obstructed by some clotted material. This led us systematically to refine dilute solutions prior to testing them.
- As indicated in Chapter 1, the most rigorous identification of guar was done by comparing its Raman fingerprint with that of related polysaccharides, e.g.

locust bean and xanthan gums. The next chapter covers, in detail, spectroscopy studies carried out after this initial forensic analysis.

5.1.2 Conditions for sample preparation

Raw guar can contain several components, including crude fibres, ashes and proteins [40,94] as well as other impurities[2]. As a result, a large range of refining procedures have been employed by different workers prior to testing guar. These procedures range from simple "top-taking" methods [32], which rely on natural precipitation of insoluble elements, to more sophisticated preparation procedures [34,36] which aim to obtain highly-refined samples, e.g. monodisperse ones. However, a number of refining procedures for polysaccharides rely, either partially or totally, on centrifugation [38,96,97] or alternatively on ultra-centrifugation [34,36,37]. We wish to point out that the initial preparation of guar solutions is rather delicate, since the quality of mixing with water depends on how the powder spreads onto the water's surface. Our solutions were prepared in a similar manner to that described by Cheng et al. [91]; that is, the powder was first sprinkled onto the solvent surface, then, an additional quantity of solvent was added, which enables residues formed on the walls of the flasks to be recovered. Contrary to the previous authors, we did not employ stirring to agitate the resultant mix[3]. Instead, we left individual solutions to stand for about 100 hours. We think this period of time is needed for guar to hydrate, if not completely, then, to at least a large extent[4]; from the work of Ross-Murphy et al. [98], we know that there is a relationship between the hydration time, the initial concentration and the molar mass of guar. These authors specifically studied hydration kinetics for guar and they showed that for unaged 0.4%[5] solutions, 80% of the material hydrates in about 3 hours. However, they employ a specific mixing device to obtain this result. Since we relied on mere diffusion mechanisms to reach maximal hydration, we also took into account the work reported by Chen et al. [99]. The latter authors give a relationship that links

[2] Fibres were found in the bulk of National Grid Transco's material.

[3] Not only is stirring totally ineffective at breaking aggregates, high shear-rate levels are also likely to break hydrated molecules.

[4] Some of our early viscometry experiments showed that efflux times exhibit a maximum after ~24 hours for solutions left at room temperature, a time which decreases when temperature increases.

[5] This is precisely the starting concentration of our unrefined guar/water mixtures.

characteristic swelling time, τ, to geometrical factors for individual, non-porous hydrogel particles.

$$\tau = L^2 / D \qquad \text{(eq.5.1)}$$

Here, L and D respectively stand for the typical size of a particle and a diffusion coefficient. Chen et al. [99] indicate that particles of ~1 mm in size become fully swollen in one day, assuming an average value for D of 10^{-7} cm^2/s. Our preliminary viscometry testing done on unrefined solutions concurs with this in that maximum viscosity is reached after about 24 hours at room temperature. Longer hydration times were subsequently allowed, since soluble material could then also diffuse out of large aggregates.

Pelleting conditions were studied by following the effect of centrifugal speed and time on pellet formation. We determined that the removal of insoluble, clotted material reaches a constant value under a centrifugal field of about 560g (1500rpm), in conjunction with centrifugal times exceeding 5 minutes. Eventually, all of our unrefined solutions were centrifuged under equivalent conditions, namely a centrifugal force of about 750g applied for a duration of 15 minutes. Similar refining conditions (700g, 10 minutes) were employed by Casas et al. to study guar solutions [96].

Fig.5.1 presents data concerning the effect of pelleting on our diverse series of aged samples. We can see that pelleting leads to the removal of a significant fraction of insoluble material from unrefined solutions, regardless of the employed ageing conditions. From this figure, it would seem that the amount of dissolved material increases when the ageing temperature is high enough; that is, both the ($G90/O_2$) and ($G90/N_2$) sample series exhibit a decrease of the insoluble fraction with ageing time; this behaviour is not obvious for the other series of samples, ($G50/O_2$) and ($G50/N_2$), whose pelleted fractions remain roughly constant, despite the ageing process. Still, fig.5.1 does not contain error bars because initial preparation conditions are difficult to replicate. We nonetheless propose that ageing can result in variations in the hydration process, and, therefore, we think that the trend seen for both (G90) sample series pertains to physical processes superimposed onto fluctuations due solely to sample preparation. At this early point in our analysis though, it is premature to judge the nature of such changes, yet it is pertinent to the overall goal of this study to note that ageing promotes the hydration of larger quantities of material. This suggests that the nature of what we term insoluble material could involve a fraction of non-dissolved material.

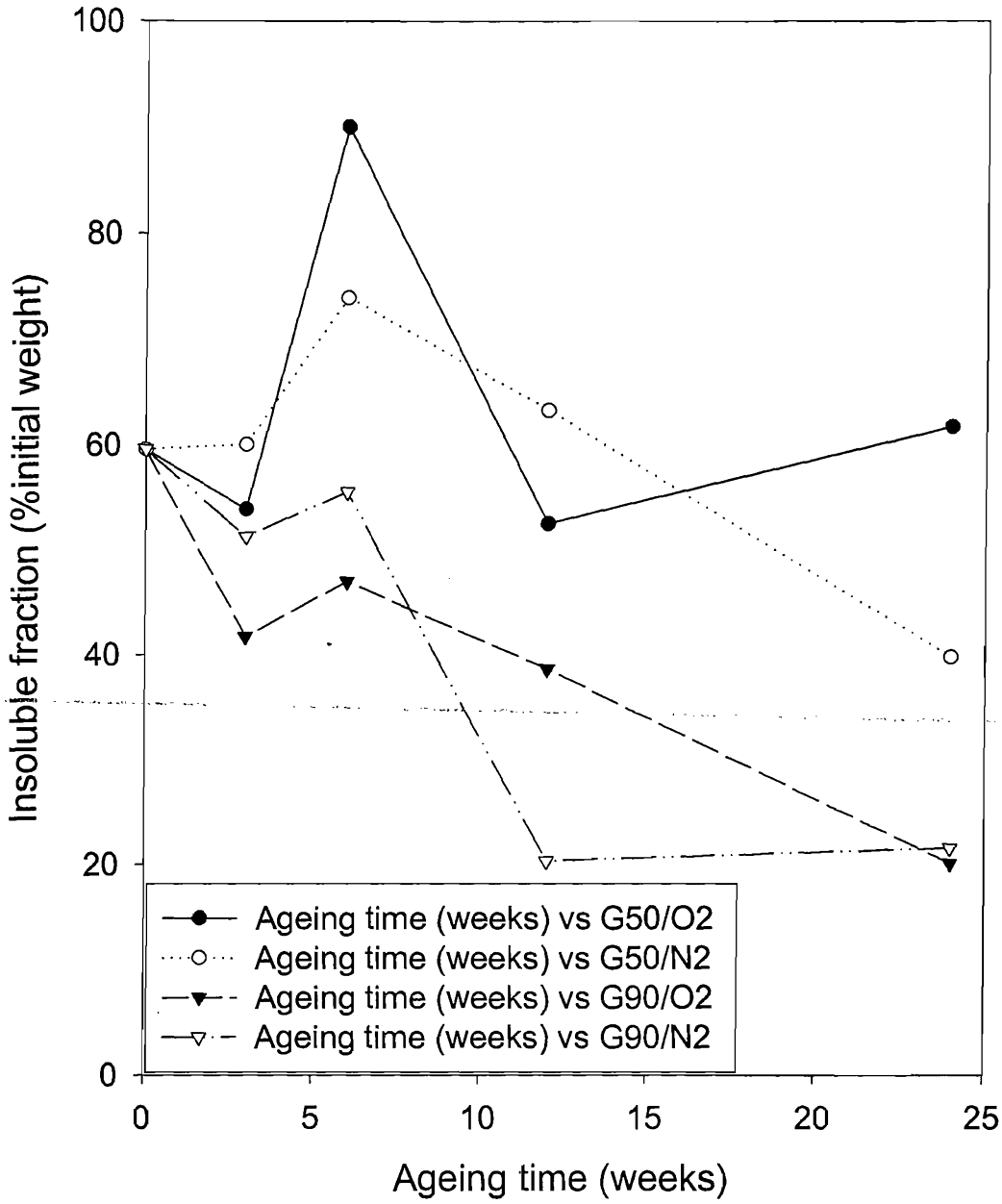

Figure 5.1: Effect of ageing conditions on the quantity of insoluble material removed from guar solutions during pelleting.

5.2 Viscometry testing of guar solutions

Dilute viscometry techniques are widely employed in the study of aqueous solutions of GG and LBG, when one needs to evaluate intrinsic viscosities [32,36,38,91,92,94,95]. This technique is also used to derive numerical values for the Flory-Huggins interaction parameter [32,36,91,92,94], whose theoretical implications were described in the introductory chapter. However, in spite of their apparent simplicity, viscometry testing experiments must be carefully planned and executed, as flow conditions in

capillaries can be influenced by many parameters. The nature of the flow in capillary viscometry is determined by factors including end effects, losses of kinetic energy, surface tension effects and drainage problems [100]. According to Hall and Fouss though [101], drainage issues dominate over variations attributable to kinetic energy losses. They also provide an empirical formula which provides an estimate of residual volumes of fluids, ΔV:

$$\Delta V = a\eta / \rho t \qquad \text{(eq.5.2)}$$

Here, a, η, ρ and t stand for a constant, the viscosity, density and efflux time of the tested fluid. Drainage issues were addressed practically in that we attempted systematically to reduce ΔV by employing a syringe to force remnant fluid out of the glassware.

Geometrical factors such as end effects cannot, for obvious reasons, be ruled out. Thus, the capillary's length to radius ratio should ideally exceed a value of 200 [100] to alleviate end effects totally. In our case, this ratio is only 90. Even though this value is somewhat lower than the ideal figure, it remains, nonetheless, of the same order of magnitude. Flow-induced effects also include shear-thinning [39], which makes viscosity values depart from their Newtonian counterparts. We will re-consider this issue later on. Results presented in the following sections presuppose the knowledge of efflux times for the employed solvents, which can also be seen as calibrating fluids[6]. Efflux times for the employed solvents were acquired several times and over the complete range of flow temperatures used to carry out our tests. They were then averaged, for each temperature, prior to being used in further processing formulae.

5.2.1 Effect of solvent quality on efflux times; a statistical description

To begin with, we will examine the effect of solvent quality on flow times for two equivalent dilute solutions of guar. One was prepared with DDW, the other with tap water[7]. Fig.5.2 provides a graphical representation which contains the corresponding series of data. Both data sets are characterized by significant scatter, especially at higher concentration levels. In this region, our two data sets do not coincide, but they gradually converge as we move towards the lower concentration regions. We tried to

[6] Water's viscosity at 25°C is 0.89mPa.s according to Ross-Murphy et al. [39].

[7] Two data sets were obtained under identical testing conditions, including starting concentrations and dilution steps; both solutions were tested at room temperature.

rule out experimental uncertainties, as far as possible, in making these measurements and, therefore, we suggest that the differences in behaviour must be due, at least partly, to changes in the solvent. In view of this, we wanted to decide objectively whether the two data sets that make up fig.5.2 are equivalent. Thus, prior to post-processing our data as part of further calculations, we wanted to determine whether both data sets are statistically comparable; we wanted to establish whether solvent quality is a key factor in influencing viscometry testing. To answer this, we attempted to evaluate whether statistical fluctuations prevail over experimental effects, including solvent quality, on the overall distribution of efflux times. To do so ,we employed a statistical criterion, namely a Wilcoxon matched pairs signed rank test [102], which was run automatically by the software Sigma Stat. The two series of efflux times shown in fig.5.1 served as direct inputs for the test, as the final result takes the form of a probability value (P); the latter indicates whether both sets are statistically equivalent or not. In this case, we found P=0.04. This lies below 0.05, which means that the differences between our two data sets exceed those which could be attributed purely to chance. If we look more closely at the overall distribution of points in fig.5.2, however, we can see that both data sets contain an initial efflux time (arrowed) which appears to be systematically lower than that of its closest neighbour. Since we carried out numerous experiments of the same nature during the course of this work, we began to suspect that such initial points are influenced by the fact that initial efflux times are obtained using glassware whose surfaces that have not yet "seen" the tested solutions. Because of this possible change in surface tension, we repeated the above statistical test on data sets exempt of these starting data points. The software then reports a value of P=0.065 in this case, which means that, from a purely statistical point of view, there is a possibility that the two sub-sets being considered are statistically equivalent, which leaves us to decide whether solvent quality is the origin of the differences seen in fig.5.2. Experimental errors cannot be entirely eliminated, and must, therefore, contribute to the scatter in our data sets. Thus, we see that statistical criteria are influenced by the careful choice of restricted data sets. Since efflux times exhibit narrower values in the low concentration region, we can speculate that DDW and tap water hydrate guar similarly in both cases, and that experimental deviations are more pronounced when the tested liquids are more concentrated.

Thanks to this preliminary investigation, we have an overview of the effect of solvent quality on the evaluation of efflux times. The employed statistical criterion tends to

indicate that variations in solvent quality could influence derived data to some degree and, therefore, our choice of DDW is principally linked to experimental reproducibility issues. We think that, for instance, gradual lime scale deposition could alter measurements and the composition of tap water is also likely to vary over time. In view of this, all the results presented in the following sections were performed using DDW, whose conductivity and purity levels could consistently be controlled. The utilization of DDW as an "inert" glassware filler and cleaning solvent also proved successful in terms of reproducing solvent efflux times between distinct series of measurements.

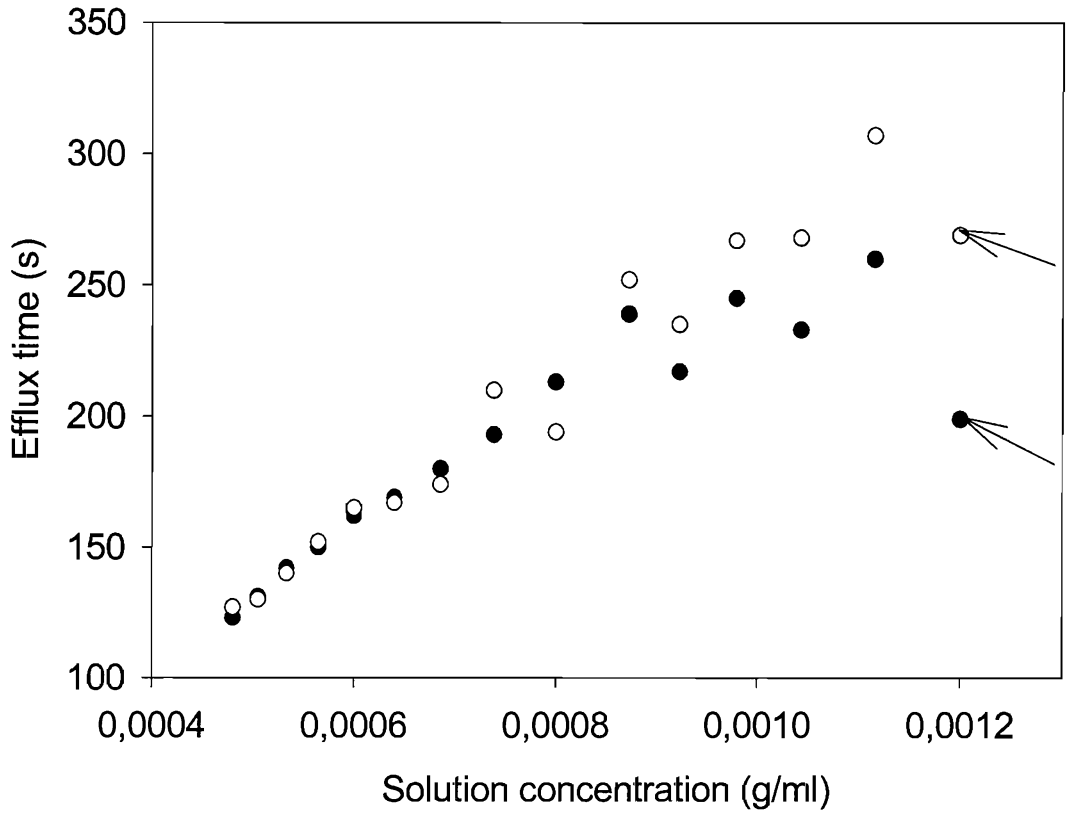

Figure 5.2: Compared efflux times for similar guar solutions; solvents employed are tap water (white dots) and DDW.

5.2.2 Comparison between extrapolation methods for dilute solutions

Here, we carry out further comparisons between the data sets introduced in the former section. Extrapolation methods encountered in the literature are still those originally developed by Kraemer and then by Huggins in the 1940's [59,60]. It has recently been

incorporated in generalized models for suspensions such as Sudduth's [103]. The following equations are individualized expressions for eq.2.8:

$$(\eta_{rel} - 1)/C = [\eta] + k'[\eta]^2 C \qquad \text{(eq.5.3)}$$

$$\ln(\eta_{rel})/C = [\eta] + k''[\eta]^2 C \qquad \text{(eq.5.4)}$$

From both of these relations, one can derive values for $[\eta]$, k' and k''. We reiterate (see section 2.2.4.1) that η_{rel}, $[\eta]$, k', k'' and C respectively stand for relative and intrinsic viscosities, Huggins' and Kraemer's constants and the solution concentration. Since automatic regressions provide access to standard errors computed for $[\eta]$ and $(d\eta/dC)$, the regression's slope, we can use error propagation formulae [104] to determine uncertainties in derived quantities such as $k'$and k''. Estimates for both constants involve determining the quantity $(d\eta/dC)/[\eta]^2$, which is done by dividing the slope of a linear regression by the squared value of the corresponding intercept on the y-axis[8]. Sudduth transformed eq.5.3 and eq.5.4 to highlight the mathematical link between k' and k'' [103], thus showing that Kraemer interpolation routines can be related to Huggins':

$$k' = 0.5 + k'' \qquad \text{(eq.5.5)}$$

Fig.5.2a and fig.5.2b contain data sets processed with both Huggins' and Kraemer's extrapolation methods; these figures respectively contain plots for the data sets obtained with tap water and DDW. More specifically, each figure comprises two distinct plots obtained by employing successively eq.5.3 and eq.5.4; for each individual plot, we also include the resultant linear regressions and 95% confidence intervals. From both figures, we see that regressions carried out using the Huggins and Kremer extrapolations do not result in absolutely identical intercepts on the y-axis; this behaviour is more pronounced in fig.5.2b, where the confidence intervals do not cover a common section of the y-axis. In both figures, we can see that the Huggins type extrapolations are characterized by larger uncertainties for $d[\eta]$ and $d(d\eta/dC)$ than for their Kraemer counterparts. This is merely an effect of the extrapolation itself since Kraemer's is based upon a logarithmic term. This mathematical function drastically reduces the uncertainties in the regression, even though the overall point distribution remains similar to that which characterizes the initial distribution of points seen for efflux times. Table 5.1 contains numerical data extracted from our different plots; values for $[\eta]$ and k' were obtained from automated regression results and error

[8] To obtain k'', one must simply add 0.5 to this quantity.

percentages are also reported for these quantities. For both solvent types, we can see that *k'* values lie within a narrow range, typically between 0.29 and 0.39, that is, if we exclude values for $[\eta]$ and *k'* derived from the Huggins' plot shown in fig.5.2b, since both of these are significantly different. This is a reflection of the initial scatter in the raw data set shown in fig.5.1. We consider, therefore, that the different plots shown in fig.5.2a and fig.5.2b convey the same quantitative information as each other, since results processed using Kraemer's method indicates that these data are equivalent; it is also true that the Kraemer representation reduces the effects of scatter present in the raw data, thus globally reducing uncertainties. In view of this, we decided to employ only the Kraemer extrapolation method for the following parts of our analysis.

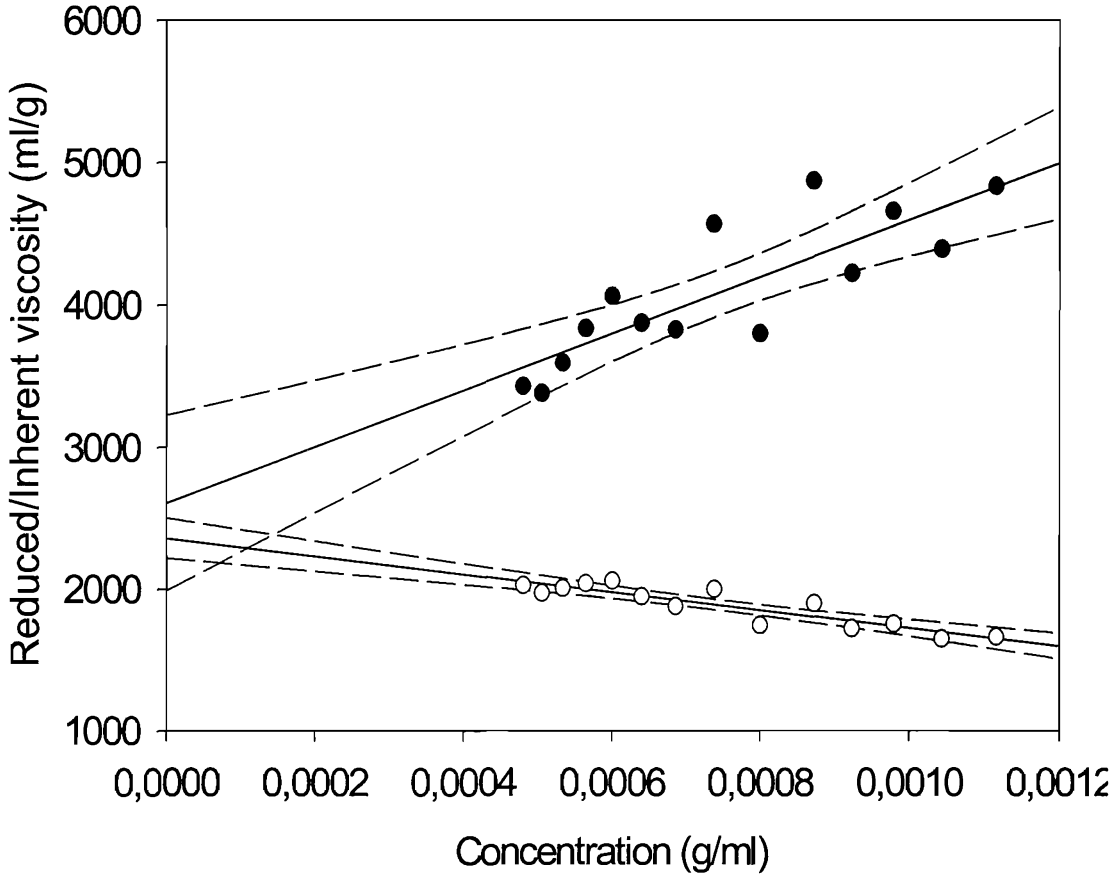

Figure 5.2a: Linear regressions carried out using Huggins (black dots) and Kraemer extrapolation methods; solvent: tap water.

UNIVERSITY OF SOUTHAMPTON LIBRARY

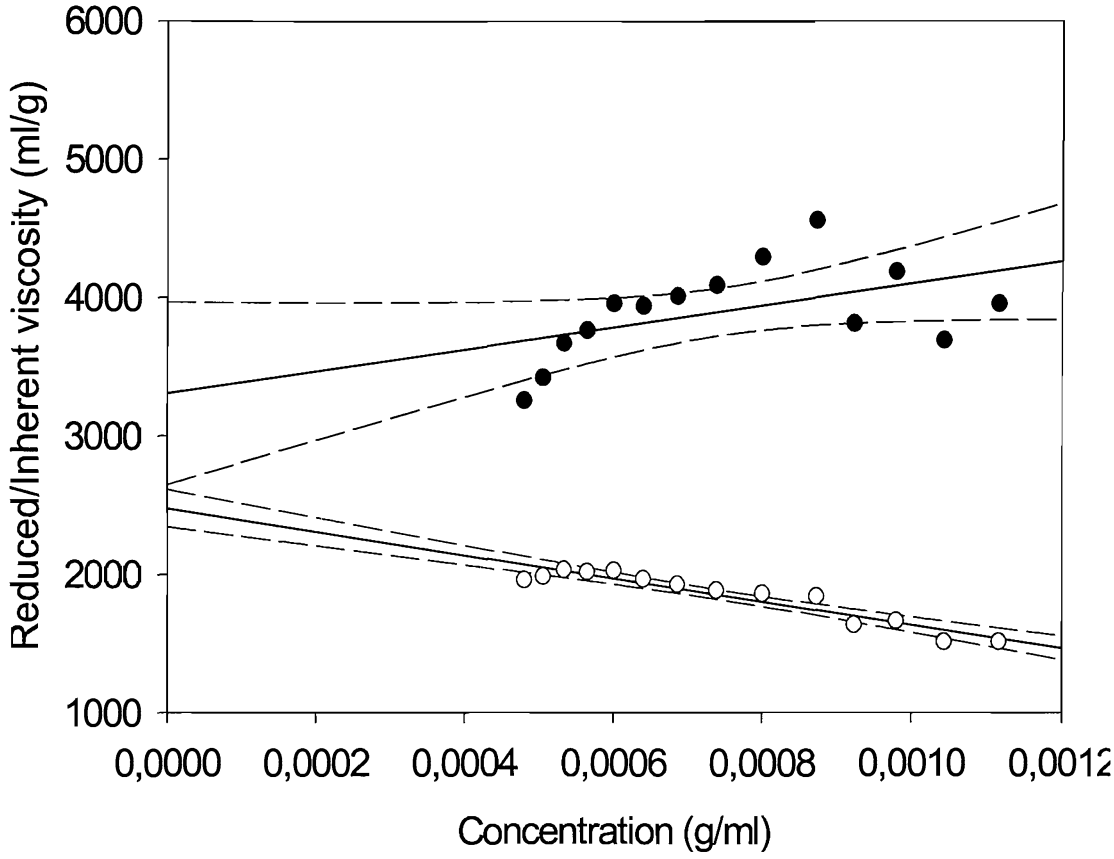

Figure 5.2b: Linear regressions carried out on Huggins (black dots) and Kraemer interpolations; solvent: DDW.

Interpolation	Solvent	$[\eta]$ (g/ml)	$d[\eta]$ (%)	$d[\eta]/dC$ $(ml/g)^2$	$d(d[\eta]/dC)$ (%)	k'/0.5+k"
Huggins	DDW	3306	~10	7.95E+05	~50	0.072±0.050
Kraemer	DDW	2474	~2.5	-8.40E+05	~10	0.363±0.021
Huggins	Tap	2607	~10	1.99E+06	~30	0.293±0.147
Kraemer	Tap	2358	~2.5	-6.35E+05	~10	0.386±0.017

Table 5.1: Numerical values derived from the linear regressions shown in fig.5.2a and 5.2b.

5.2.3 Presentation of processed data for our four series of aged samples

Here, we present processed data sets derived for an ensemble of samples prepared under accelerated ageing conditions. In total, 17 different samples were tested; each of them was tested at least at five flow temperatures. The following figures contain Kraemer extrapolations to which we applied linear regressions[9]. These groups of

[9] The corresponding 95% confidence intervals are also included.

figures are classified by sample type, in the following order: data for a reference (unaged) sample makes up fig.5.3; (G50/N2) data were used for fig.5.4a to fig.5.4d; (G50/O2) for fig.5.5a to fig.5.5d; (G90/N2) for fig.5.6a to fig.5.6d; (G90/O2) for fig.5.7a to fig.5.7d. Regardless of the chosen figure, individual data sets are characterized both by the numerical value for their intercept and the slope of the regression line, which is linked to a numerical value for the interaction parameter. Also, the concentration ranges under which extrapolations were carried out reflect the original concentration of the refined solution; therefore, variations in testing concentrations are determined by the initial amount of material removed by pelleting, see fig.5.1, and thus, by the viscosity of the parent solutions. One way to look at the data presented in the following figures is to consider variations in the slope of the regression lines. Effectively, positive slopes indicate values for k' exceeding 0.5, whereas negative slopes signify values for k' that lie below 0.5. We initially attempted to explore variations in k' and $[\eta]$ with flow temperature. However, this point is not discussed at that point, for reasons that will be made apparent later in the analysis. It is especially difficult to comment on the distribution of negative and positive slopes appearing on each graph, and no clear trend emerges either by looking at individual graphs or groups of graphs. Fig.5.3 also includes an evaluation of a threshold concentration, C^*, representing the transition between the dilute and the semi-dilute regime; that is, the point at which the solutions are not sufficiently diluted to consider that molecules do not interact. We can define this threshold by the vertical line at $1.7.10^{-3}$ g/ml in fig.5.3. This quantity corresponds to the condition where intermolecular interactions are likely to take place and disrupt the validity of eq.5.3 and eq.5.4. Ross-Murphy et al. [39] provide a mathematical relationship to separate the two domains, and it is the one we employed to derive the above estimate:

$$C^* \approx \frac{4}{[\eta]} \qquad \text{(eq.5.6)}$$

However, as will be shown below, $[\eta]$ decreases with ageing such that the above value of C^* represents an upper-limiting case for all the Kraemer plots shown in this section. Therefore, we do not include further values for C^* within the 16 other figures.

Eventually, 87 estimates of intrinsic viscosities were derived together with 87 values for the interaction parameter. We will separately discuss the variation of these two parameters with testing and ageing conditions, in the following sections.

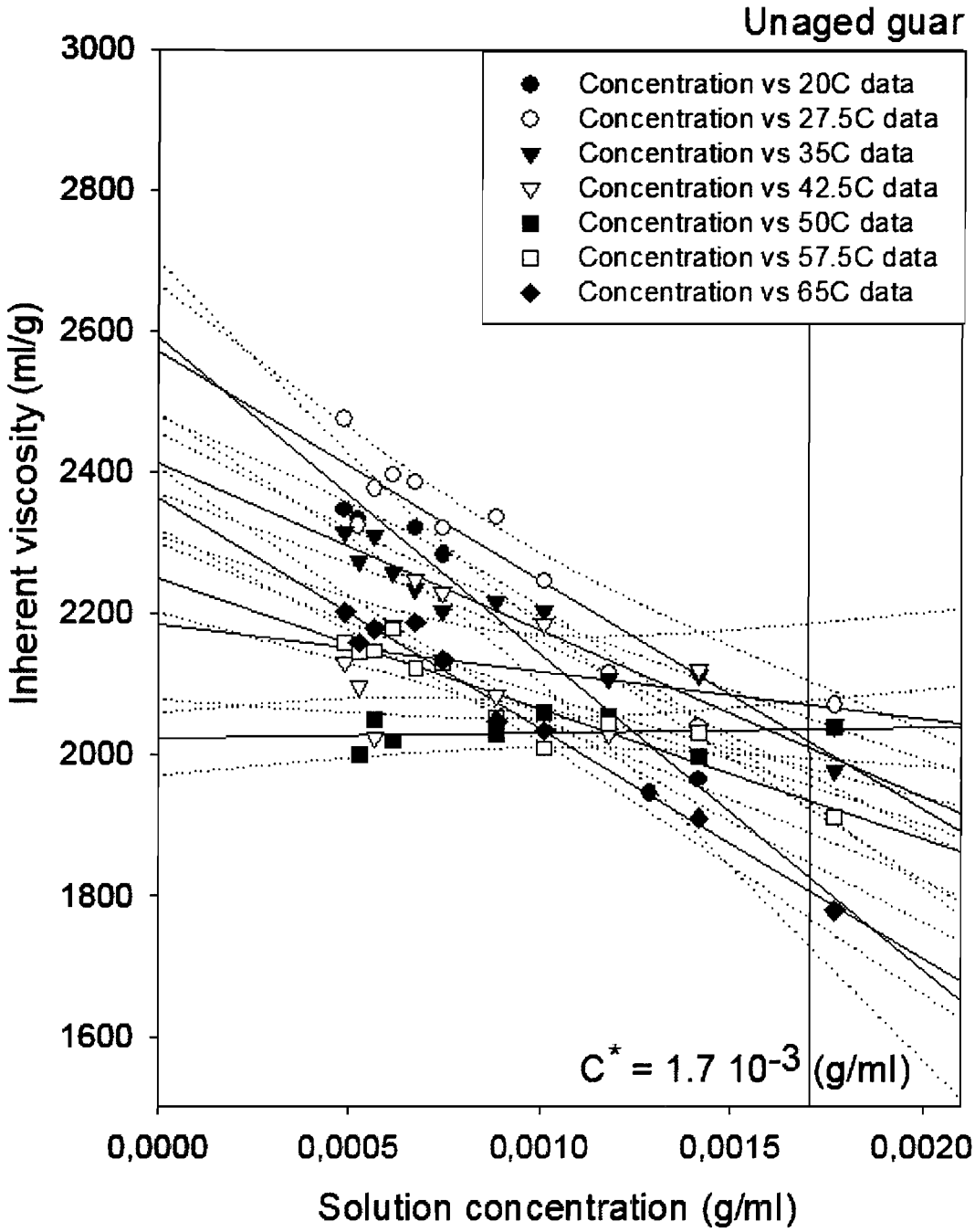

Figure 5.3: Kraemer plots obtained from an unaged guar solution tested @ seven flow temperatures (20°C, 27.5°C, 35°C, 42.5°C, 50°C, 57.5°C and 65°C).

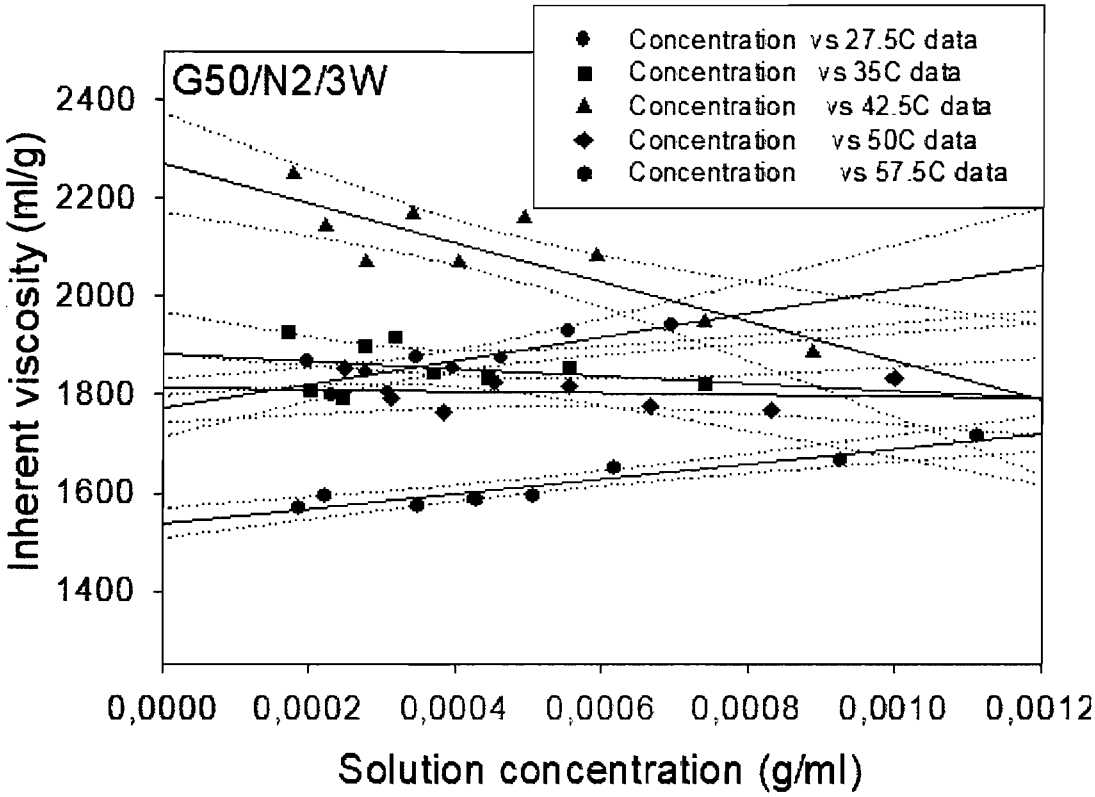

Figure 5.4a: Kraemer plots obtained from solutions made of (G50/N_2/3W) samples. Tests were made @ five flow temperatures (27.5°C, 35°C, 42.5°C, 50°C, 57.5°C).

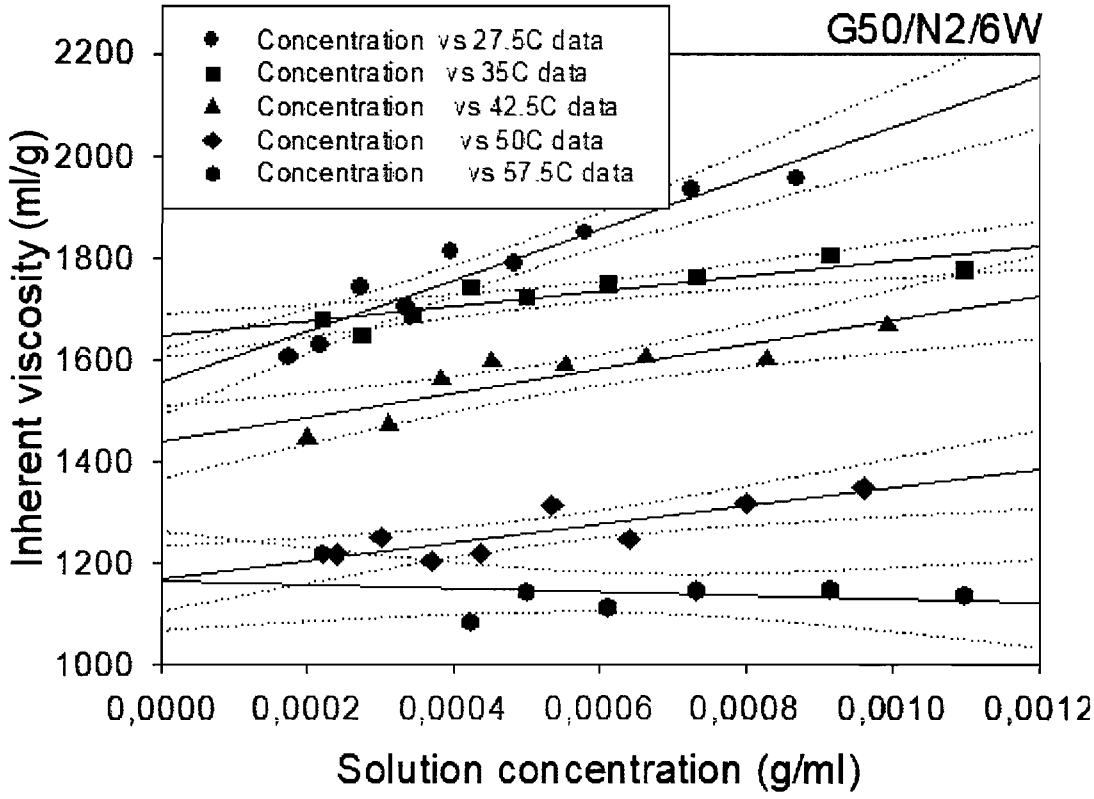

Figure 5.4b: Kraemer plots obtained from solutions made of (G50/N_2/6W) samples. Tests were made @ five flow temperatures (27.5°C, 35°C, 42.5°C, 50°C, 57.5°C).

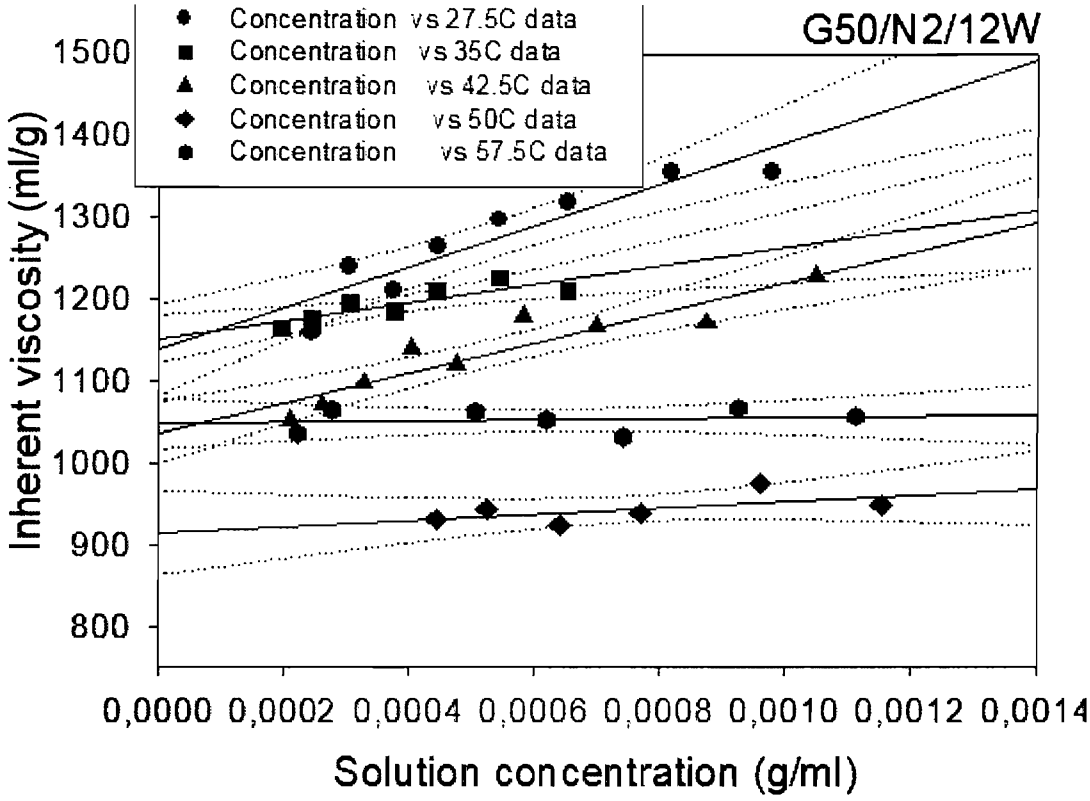

Figure 5.4c: Kraemer plots obtained from solutions made of (G50/N_2/12W) samples. Tests were made @ five flow temperatures (27.5°C, 35°C, 42.5°C, 50°C, 57.5°C).

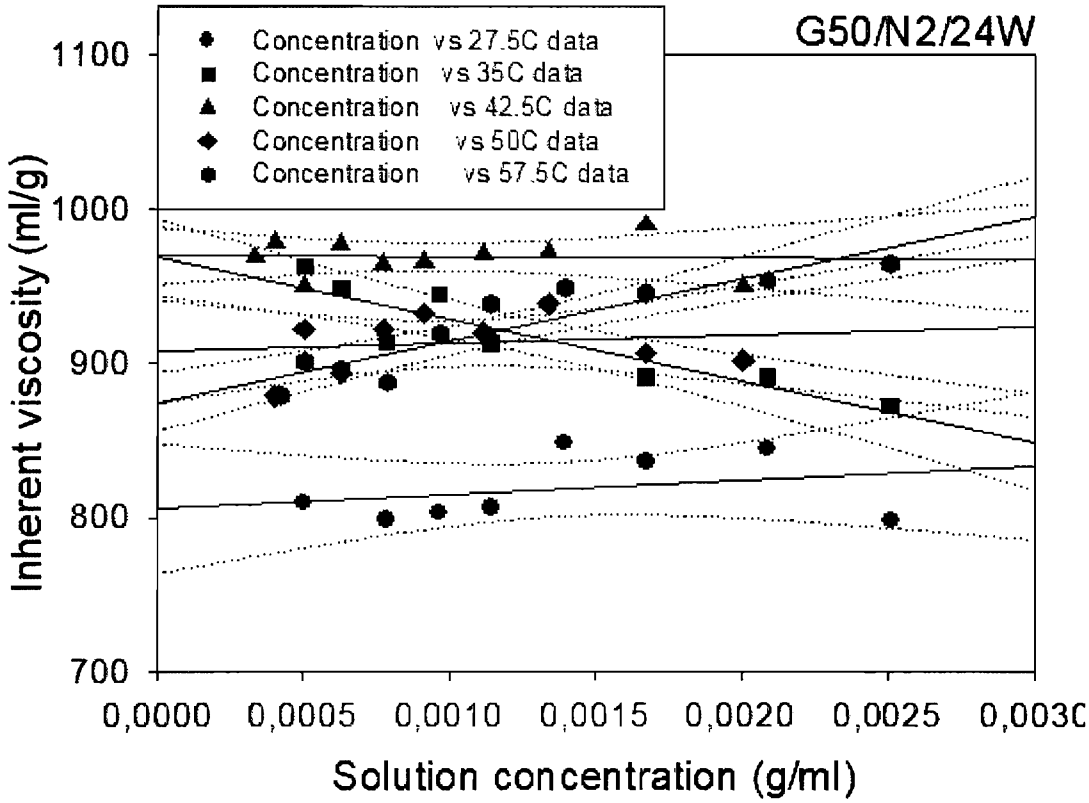

Figure 5.4d: Kraemer plots obtained from solutions made of (G50/N_2/24W) samples. Tests were made @ five flow temperatures (27.5°C, 35°C, 42.5°C, 50°C, 57.5°C).

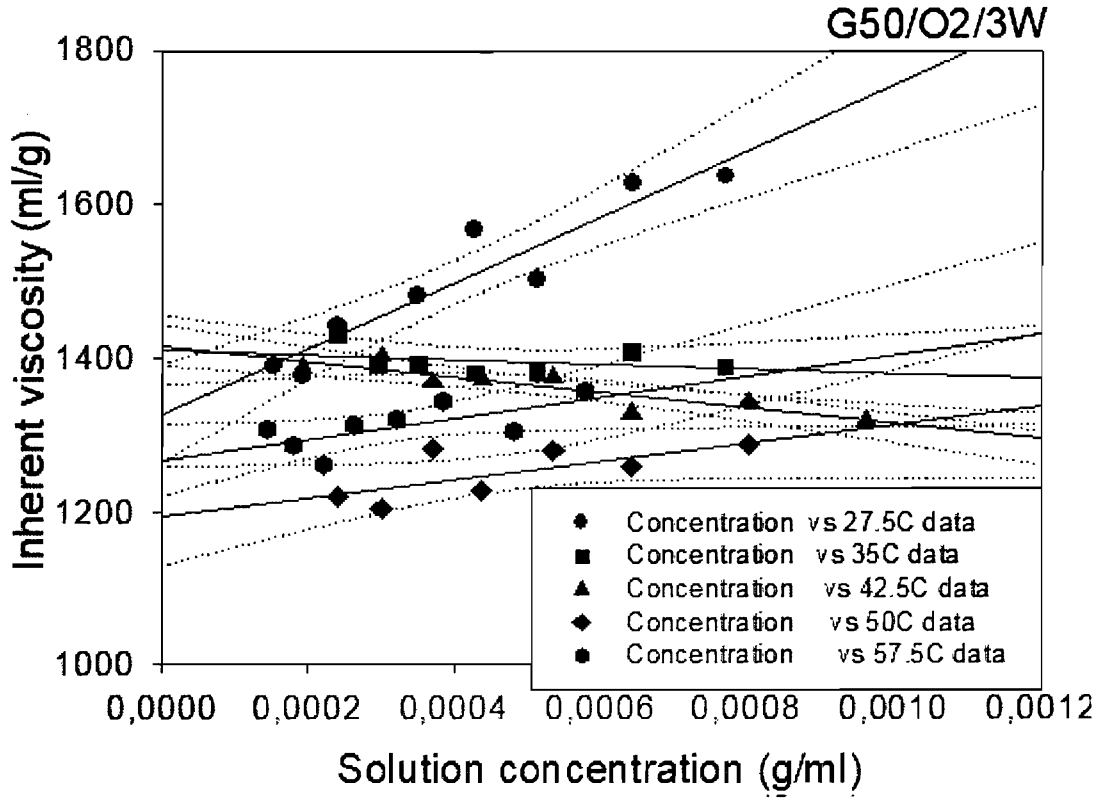

Figure 5.5a: Kraemer plots obtained from solutions made of ($G50/O_2/3W$) samples. Tests were made @ five flow temperatures (27.5°C, 35°C, 42.5°C, 50°C, 57.5°C).

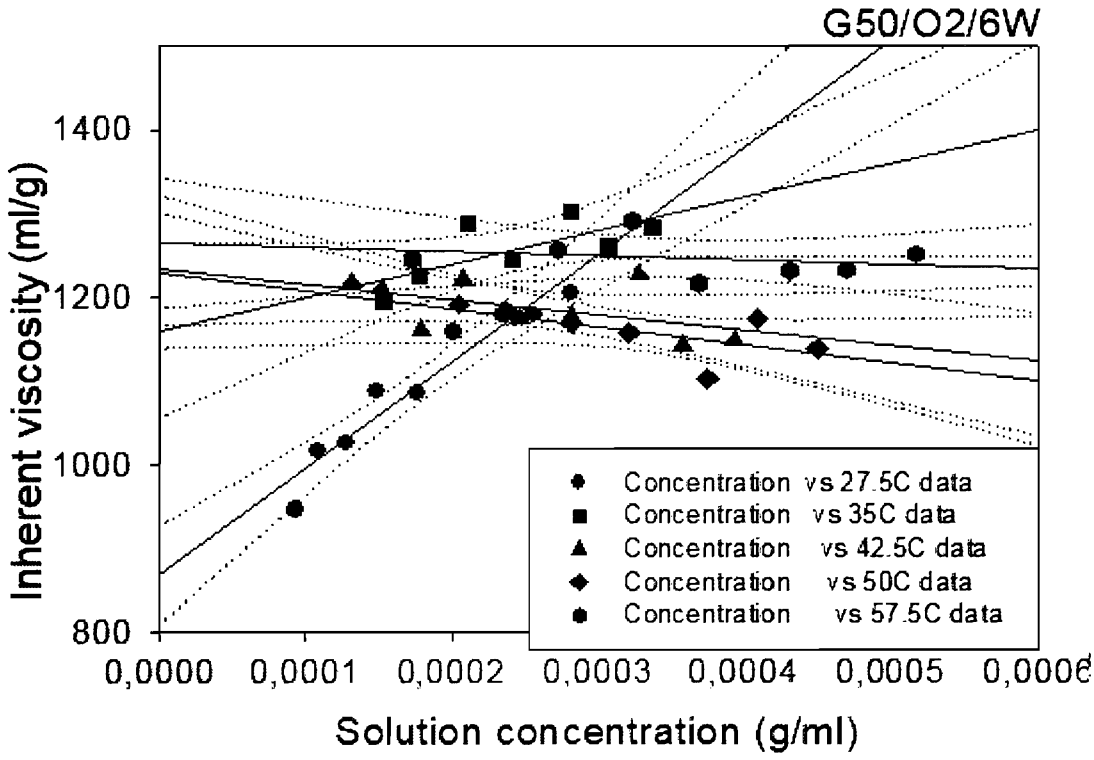

Figure 5.5b: Kraemer plots obtained from solutions made of ($G50/O_2/6W$) samples. Tests were made @ five flow temperatures (27.5°C, 35°C, 42.5°C, 50°C, 57.5°C).

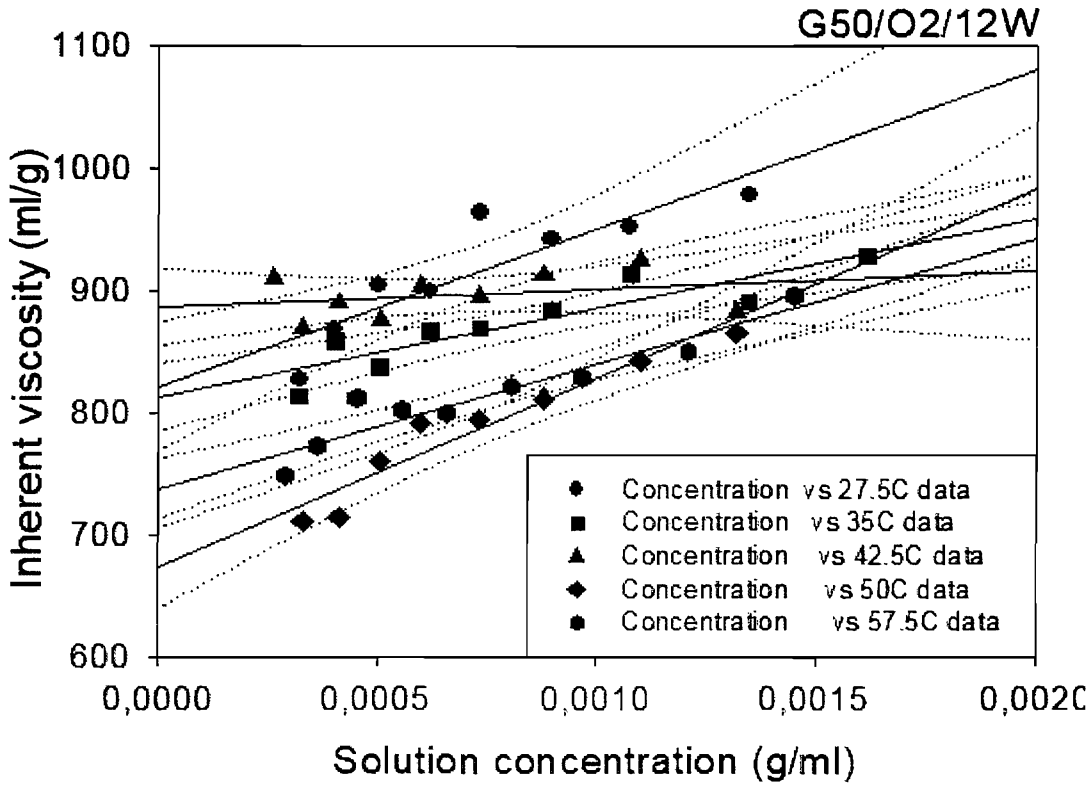

Figure 5.5c: Kraemer plots obtained from solutions made of ($G50/O_2/12W$) samples. Tests were made @ five flow temperatures (27.5°C, 35°C, 42.5°C, 50°C, 57.5°C).

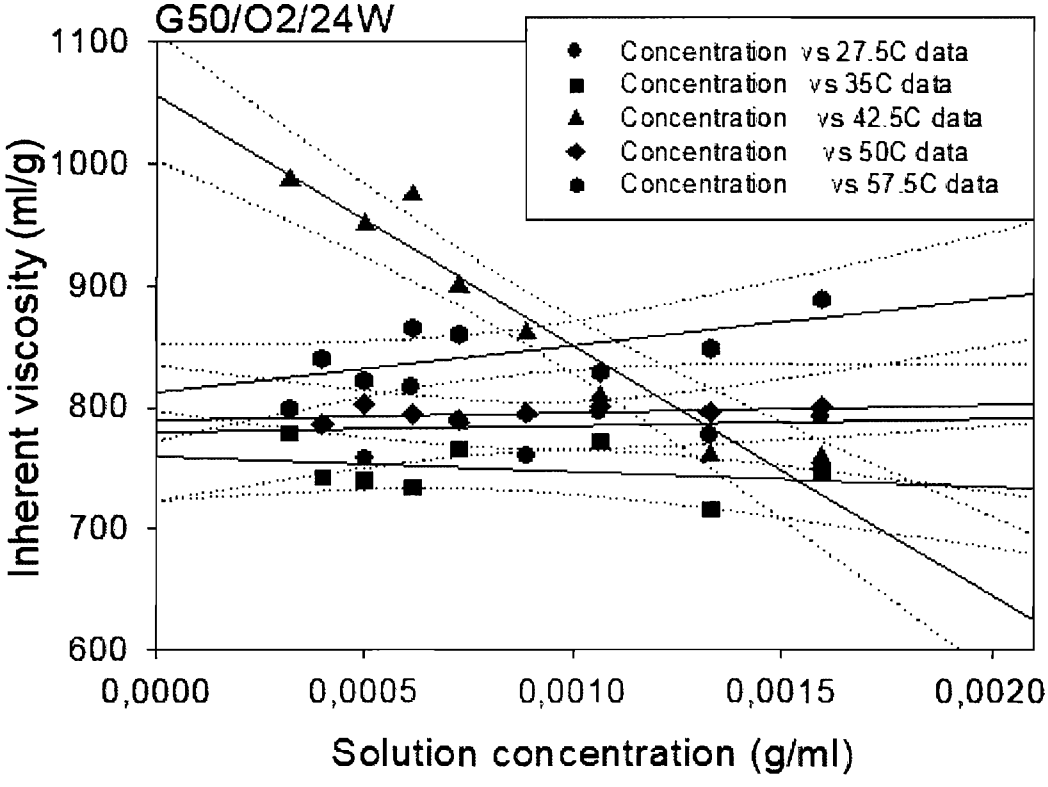

Figure 5.5d: Kraemer plots obtained from solutions made of ($G50/O_2/24W$) samples. Tests were made @ five flow temperatures (27.5°C, 35°C, 42.5°C, 50°C, 57.5°C).

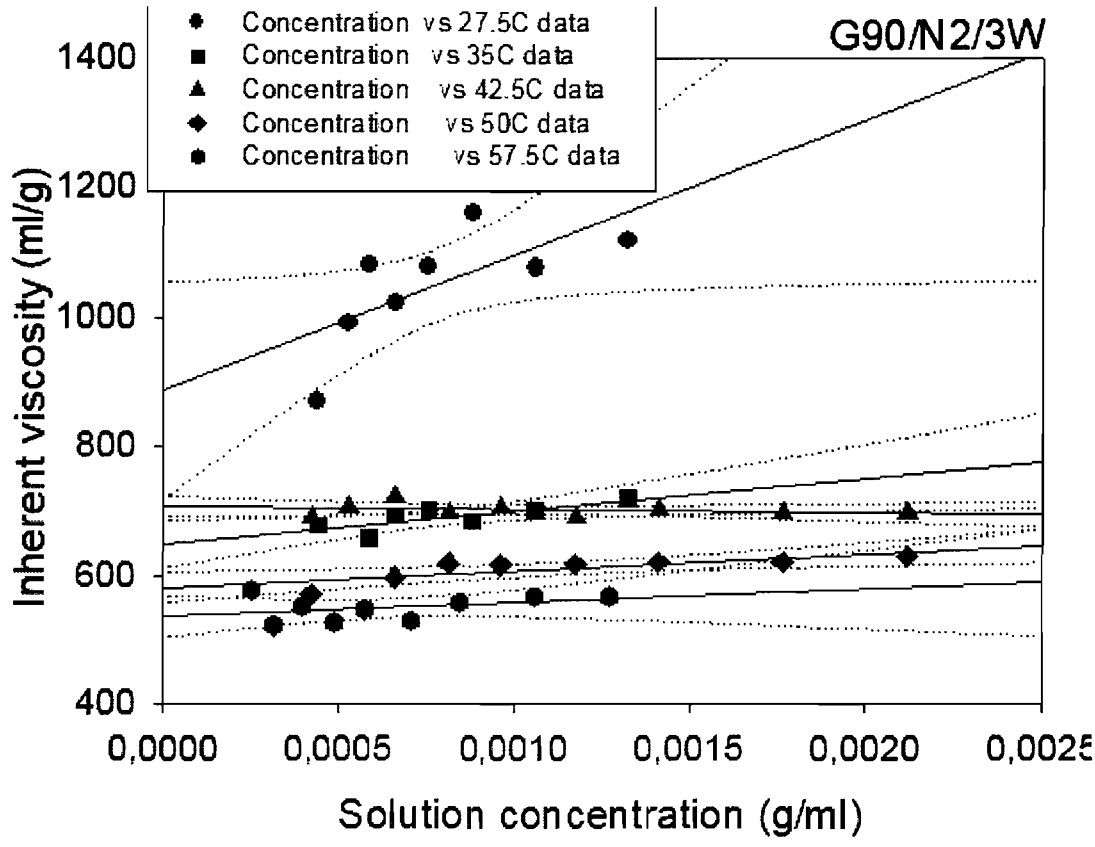

Figure 5.6a: Kraemer plots obtained from solutions made of (G90/N_2/3W) samples. Tests were made @ five flow temperatures (27.5°C, 35°C, 42.5°C, 50°C, 57.5°C).

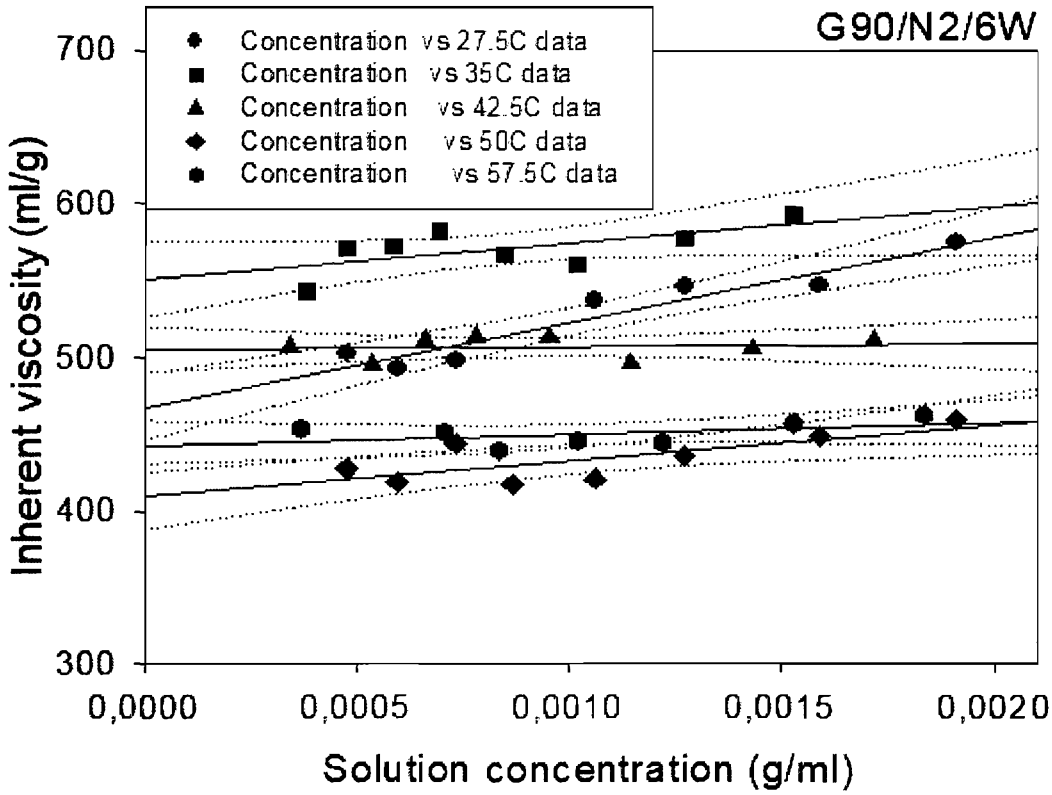

Figure 5.6b: Kraemer plots obtained from solutions made of (G90/N_2/6W) samples. Tests were made @ five flow temperatures (27.5°C, 35°C, 42.5°C, 50°C, 57.5°C).

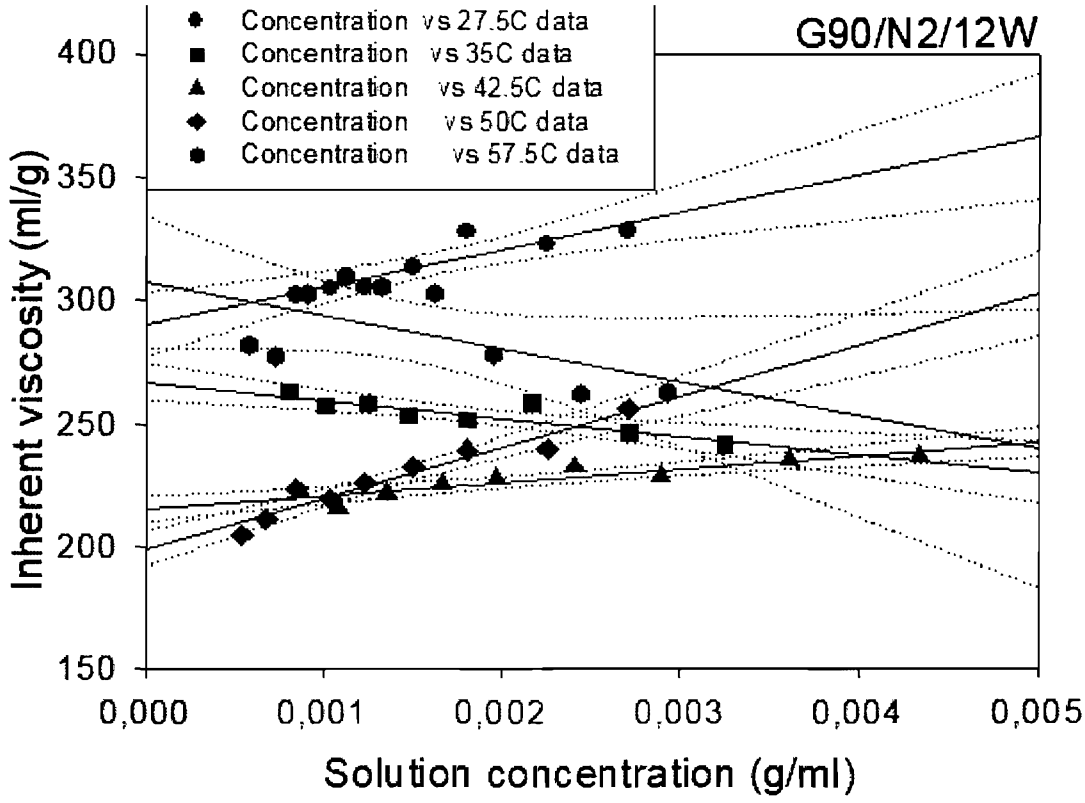

Figure 5.6c: Kraemer plots obtained from solutions made of (G90/N_2/12W) samples. Tests were made @ five flow temperatures (27.5°C, 35°C, 42.5°C, 50°C, 57.5°C).

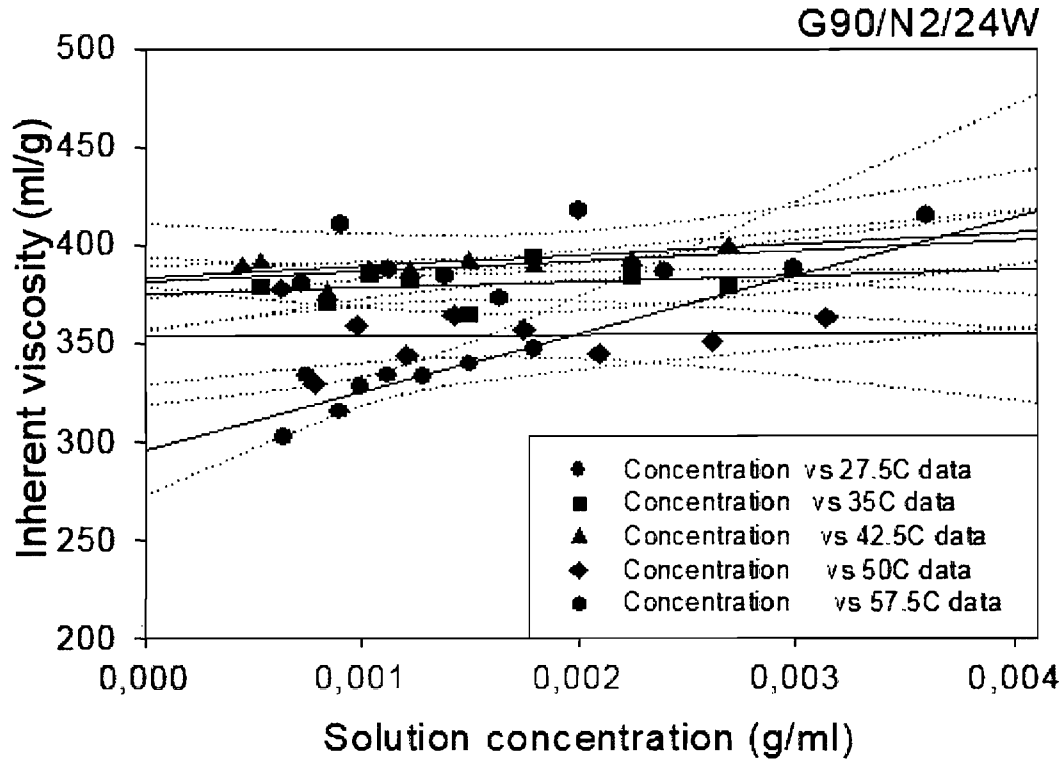

Figure 5.6d: Kraemer plots obtained from solutions made of (G90/N_2/24W) samples. Tests were made @ five flow temperatures (27.5°C, 35°C, 42.5°C, 50°C, 57.5°C).

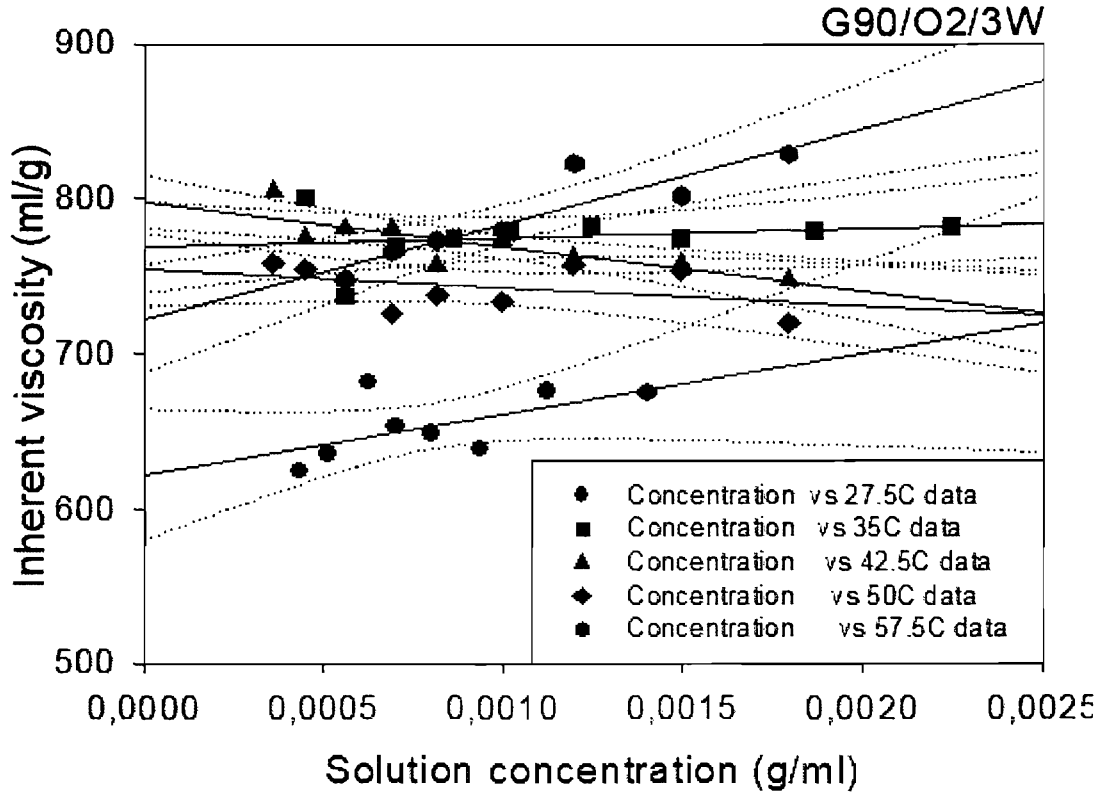

Figure 5.7a: Kraemer plots obtained from solutions made of (G90/O_2/3W) samples. Tests were made @ five flow temperatures (27.5°C, 35°C, 42.5°C, 50°C, 57.5°C).

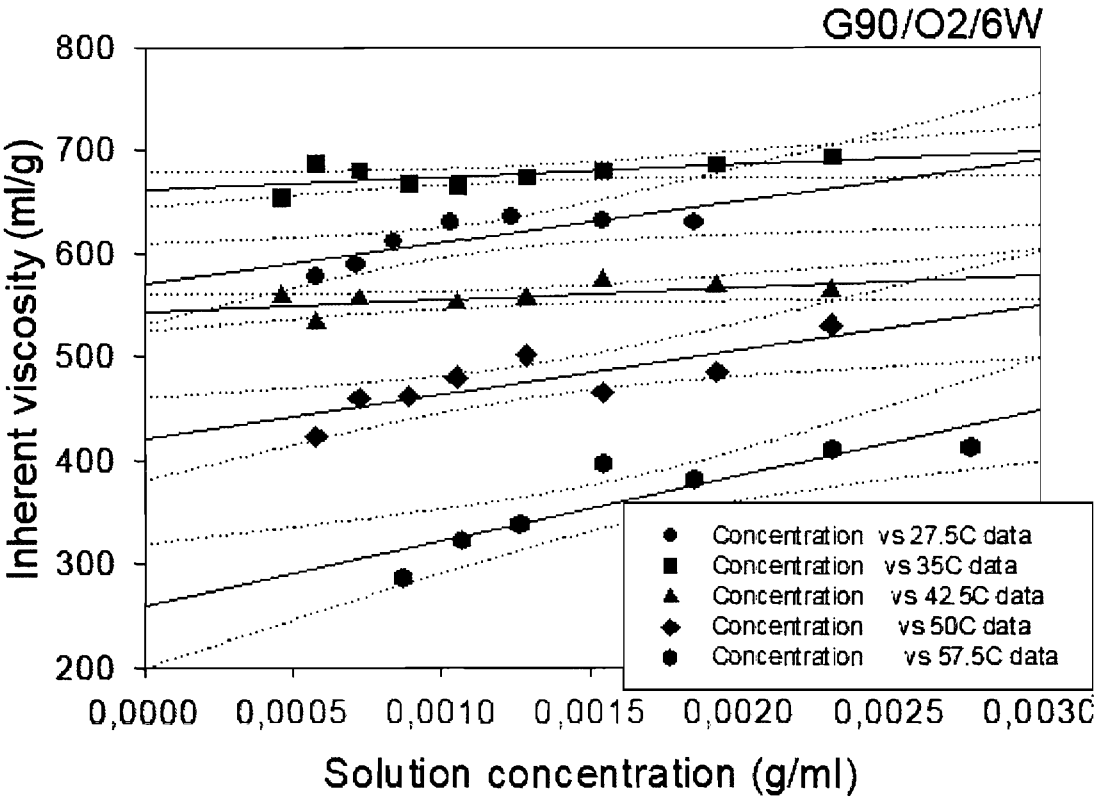

Figure 5.7b: Kraemer plots obtained from solutions made of (G90/O_2/6W) samples. Tests were made @ five flow temperatures (27.5°C, 35°C, 42.5°C, 50°C, 57.5°C).

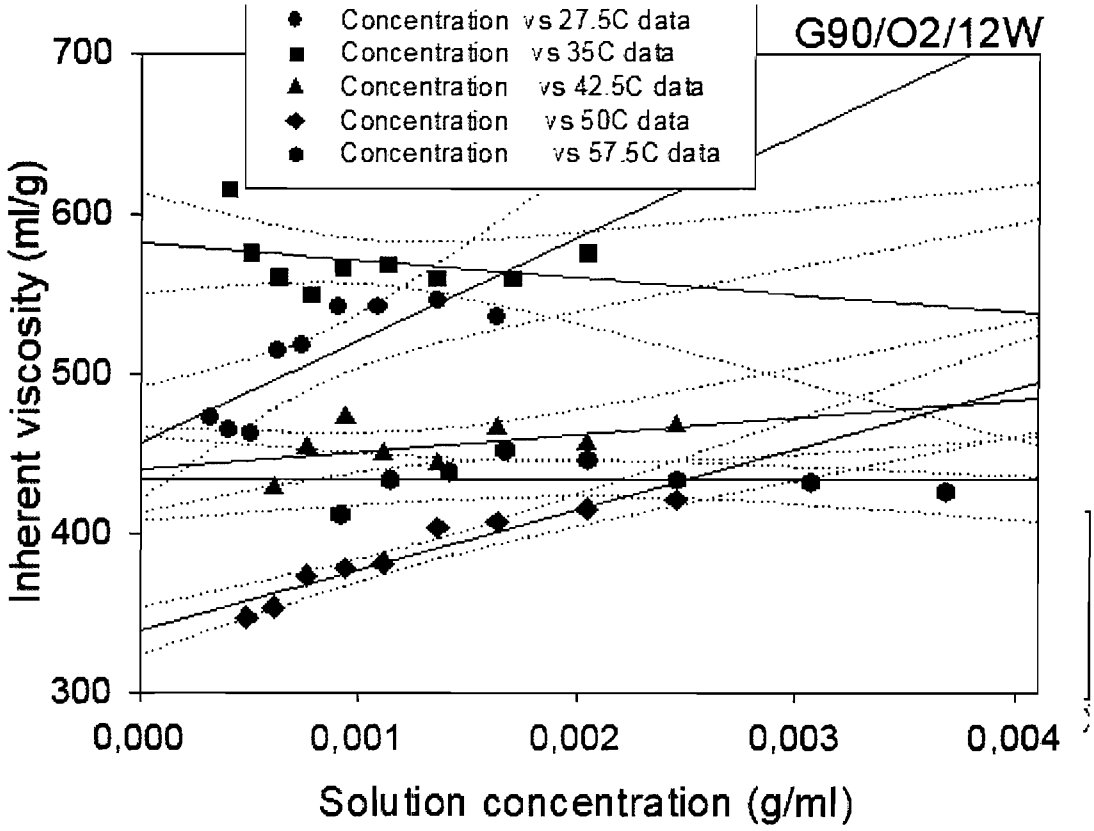

Figure 5.7c: Kraemer plots obtained from solutions made of (G90/O_2/12W) samples. Tests were made @ five flow temperatures (27.5°C, 35°C, 42.5°C, 50°C, 57.5°C).

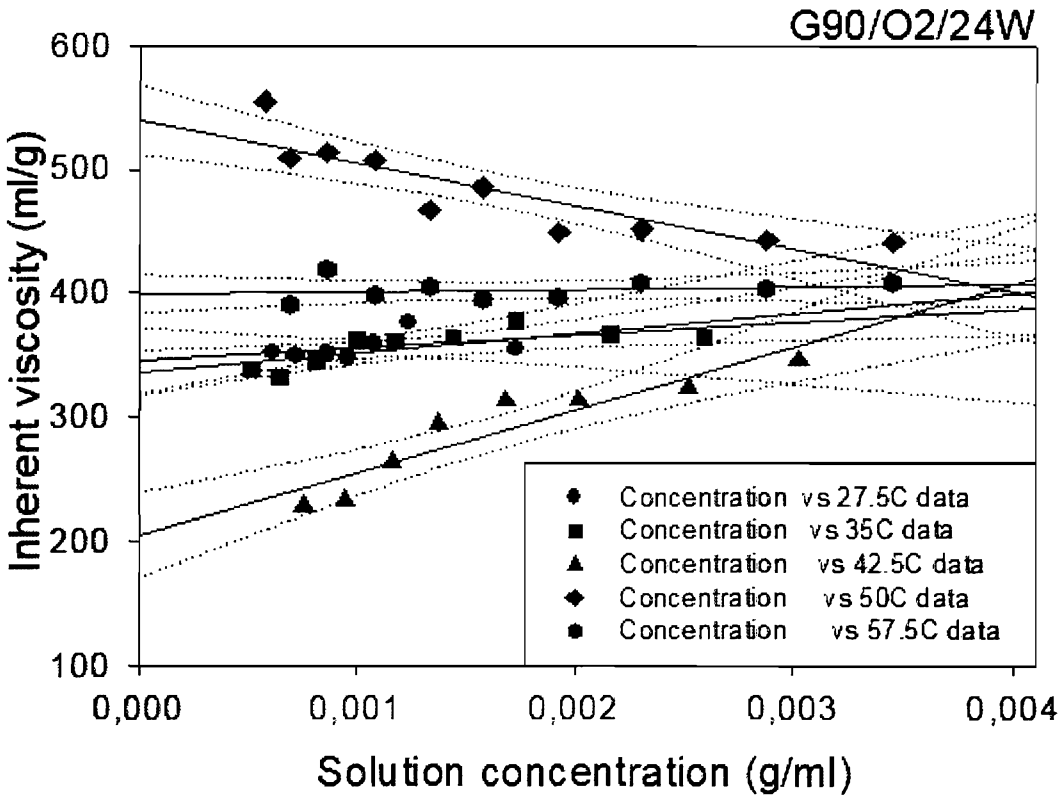

Figure 5.7d: Kraemer plots obtained from solutions made of (G90/O_2/24W) samples. Tests were made @ five flow temperatures (27.5°C, 35°C, 42.5°C, 50°C, 57.5°C).

5.2.4 Intrinsic viscosities, a link to molar masses

Intrinsic viscosity values can be used to provide average molar masses for macromolecular species in solution; hence, values extracted from Kraemer plots can be post-processed using the Mark-Houwink-Sakurada (MHS) equation, which is widely used for that purpose [35,36,38,39,91,92,95,97]:

$$[\eta] = K\overline{M}_w^{\,a} \qquad \text{(eq.5.7)}$$

In this equation, K and a are a pair of constants that are unique to every solute/solvent combination. Such constants pertain to the stiffness of a macromolecule in solution, and chain stiffness varies when the solvent's solubility parameter changes. In this case, a recent pair of values for solutions of water/guar is $K = 5.13x10^{-4}$ *dl/g* and $a=0.72$. We derived these values from the work of Beer et al. on such systems [97]; the latter authors acquired these using size exclusion chromatography. Although the two constants measured by Beer et al. coincide with earlier estimates of these parameters [39], some discrepancies do appear in the literature [36] regarding MHS constants for identical mixtures.

Before processing our data using the above MHS relationship, we will first discuss the appearance of plots of intrinsic viscosity versus testing temperatures; two figures, namely fig.5.8a and fig.5.8b, were produced using the results shown in fig.5.3 and the ensemble of data from fig.5.4a, fig.5.5a, fig.5.6a and 5.7a respectively. Since thermal effects are likely to favour depolymerisation reactions, it is evident that we have to address the effect of flow temperature on intrinsic viscosity. Fig.5.8a shows the effect of temperature on such a plot, for the unaged material. From this figure, we can see that the intrinsic viscosity decreases as the testing temperature is increased; this behaviour is evident up to 50°C, whereas, at higher temperatures, there is an apparent reverse to this trend. Fig.5.8b displays the different profiles for the intrinsic viscosity of all the samples that had been aged for a total duration of 3 weeks. From this, the ordering of series of data points and, more specifically, a systematic decrease of intrinsic viscosity with the testing temperature cannot be observed[10]. We think that unaged guar is particularly vulnerable to scission processes, whereas molecules that were already subjected to ageing conditions are far less subjected to flow-induced degradation modes.

[10] We did not generate figures for the other 12 samples since intrinsic viscosities do not systematically decrease when the testing temperature is increased.

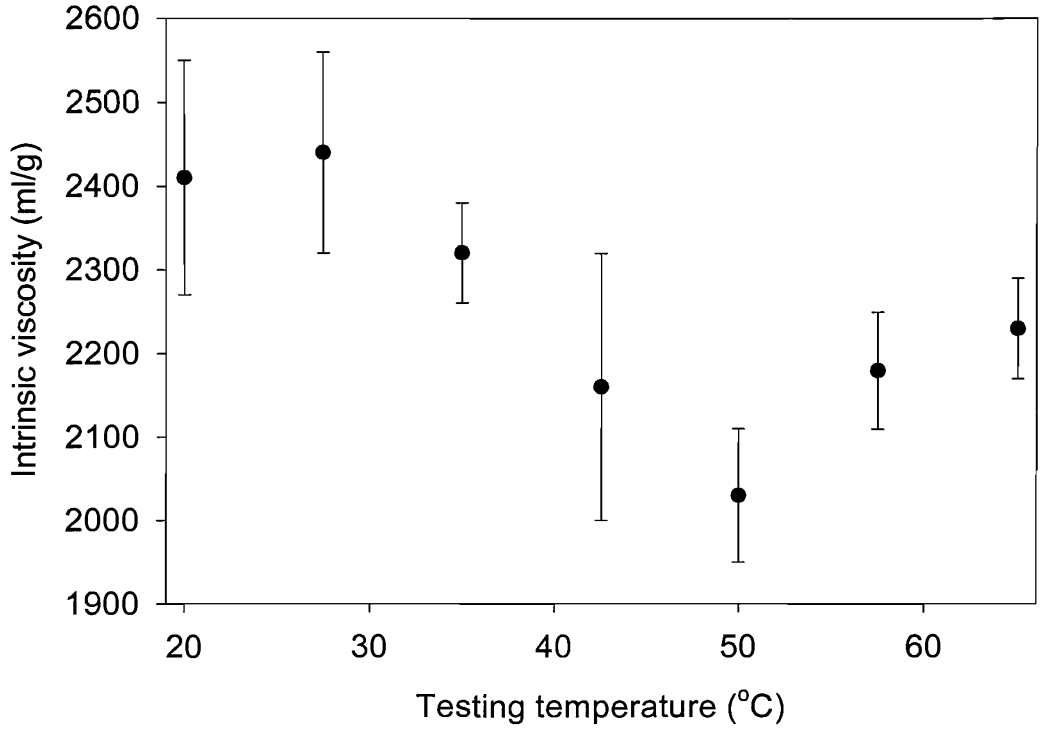

Figure 5.8a: Variations of intrinsic viscosity with flow temperatures-Data points were taken from linear regressions seen in fig.5.3, i.e. for unaged guar solutions.

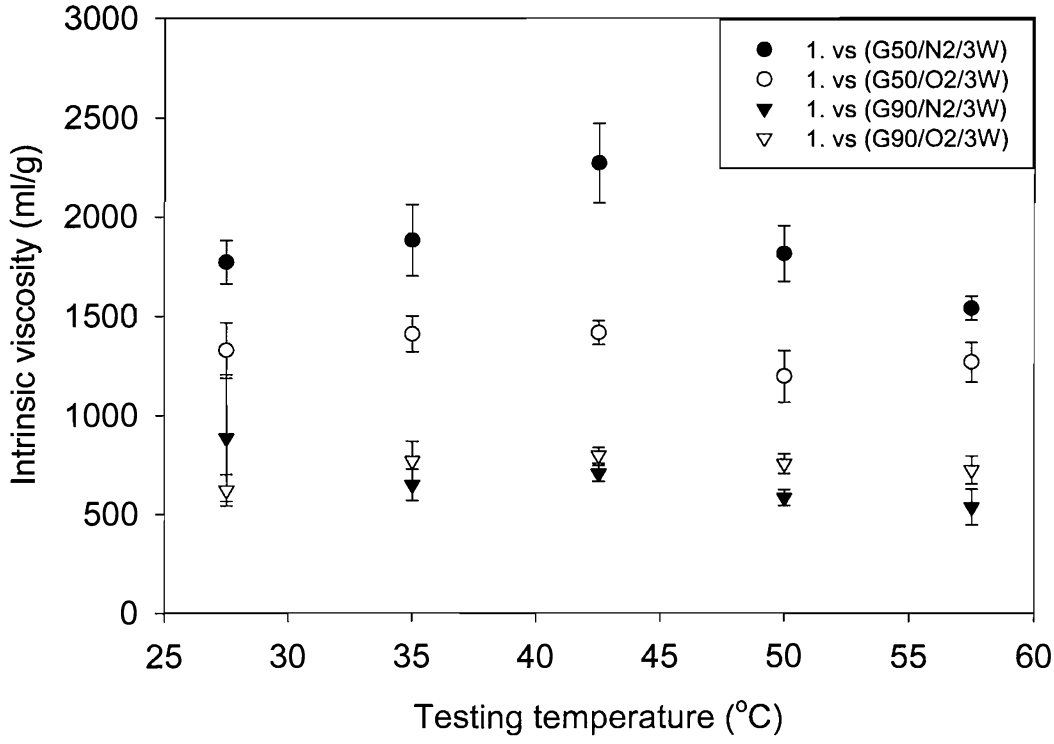

Figure 5.8b: Variations of the intrinsic viscosity with flowing temperatures-Data points were taken from linear regressions seen in fig.5.4a, fig.5.5a, fig.5.6a and fig.5.7a.

In view of the previous results, we decided not to differentiate the various estimates for intrinsic viscosities obtained for a single sample at different flow temperatures. Furthermore, we calculated averages for each sample type; these were subsequently processed to give average molar masses via eq.5.7, even though, strictly, zero-shear intrinsic viscosity values should be utilized for this purpose [39]. Shear-thinning effects intrinsically relate to flow conditions in the testing capillary, therefore we must be aware that the data we term average molar masses are artificially decreased if we compare them to the values that would be obtained under "no-flow" conditions[11]. Our non-zero shear intrinsic viscosities were nonetheless employed to generate fig.5.9. This figure contains plots of average molar masses as a function of ageing time for the four different sets of samples. The initial data point is common to all four plots and corresponds to a value of $3.0x10^6 \pm 5.10^5$ g.mol^{-1}; the error bars indicated on each data point were derived from standard deviation values computed together with averages for intrinsic viscosities. Consequently, the error bars appear rather large, since they each reflect the distribution of several intercept values extracted from different series of Kraemer plots. Typically, viscosity-based estimates of the average molar mass of guar fall in the range of $1.7x10^6$ [40] to $2.0x10^6$ g.mol^{-1} [91,92], whereas Beer et al. [97] report a value for guar's molar mass of $1.5x10^6$ g.mol^{-1}. From these estimates, we can see the effect of our testing method, since the molar mass we report for unaged guar is somewhat higher than values reported by other workers.

If we now concentrate on the appearance of the data shown in fig.5.9, the different plots clearly demonstrate the non-linear decay of molar masses with ageing time. Given the size of individual error bars, we can consider that data obtained for the ($G50/O_2$) and ($G50/N_2$) samples and the ($G90/O_2$) and ($G90/N_2$) samples are comparable. By this, we mean that additional depolymerisation effects catalysed by the presence of oxygen may not be as important as thermally-based depolymerisation processes; in other words, oxidation effects can easily be masked because of the magnitude of our error bars. At this point of our analysis though, it is particularly important to consider the mechanisms by which chain scission processes occur. Tayal and Khan [93] report on three statistical cleavage models that they subsequently employed for numerical computations aimed at understanding depolymerisation

[11] To carry out such measurements, one needs to control the pressure level applied onto the tested fluids, so that shear levels become adjustable and zero-shear viscosity extrapolated from series of data sets.

processes induced by ultrasonic degradation. To summarize, these models consist of a random scission model, a central scission model and, finally, a Gaussian-distributed probabilistic scission model.

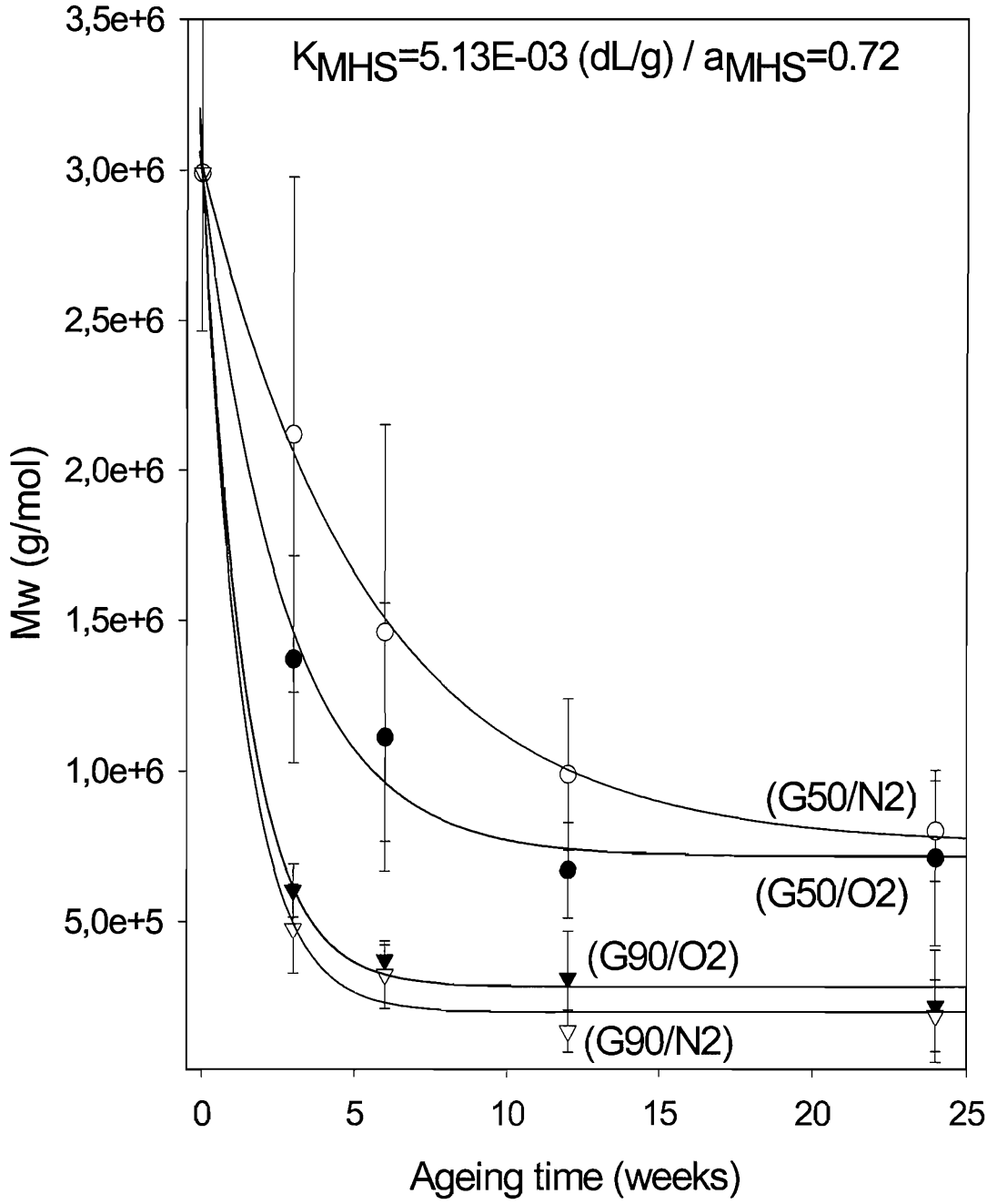

Figure 5.9: Variations of molar masses versus ageing, for our four sample types.

Several workers who employ viscometry techniques, namely Kők et al. [32], Cheng et al. [34] and Bradley and Mitchell [105,106] determined that guar macromolecules are in fact subjected to random cleavage mechanisms; consequently, the mentioned

authors resorted to a first-order degradation model to describe their data. Additionally, depolymerisation kinetics of several other polysaccharides studied by Lai and al. [95] also follow first order depolymerisation models. To fit the plots seen in fig.5.9, we therefore considered the following first-order model [34,35,95,105]:

$$\frac{1}{\overline{M}_t} - \frac{1}{\overline{M}_0} = \frac{k_d t}{m} \qquad \text{(eq.5.8)}$$

where, M_o, M_t, t and m respectively stand for the initial molar mass, the mean molar mass of the degraded chain after an elapsed ageing time t and the molar mass of the repeat unit; finally, k_d is a depolymerisation constant. Eq.5.8 can be integrated to give the following exponential form:

$$\overline{M}_t = A\exp(-Bt) + C \qquad \text{(eq.5.9)}$$

where A, B and C are constants. Eq.5.9 was then employed to fit the four sets of data shown in fig.5.9; regression results, which were obtained using the Sigma Plot software, are summarized in Table 5.2.

Sample Type	**(G50/N2)**	**(G50/O2)**	**(G90/O2)**	**(G90/N2)**
A / 10^{-6} ($g.mol^{-1}$)	**2.26 ± 0.08**	**2.26 ± 0.16**	**2.71 ± 0.71**	**2.79 ± 0.95**
B * 10^{7} (s^{-1})	**3.02 ± 0.26**	**6.12 ± 1.13**	**11.6 ± 1.19**	**12.37 ± 1.79**
C / 10^{-5} ($g.mol^{-1}$)	**7.53 ± 0.61**	**7.15 ± 0.98**	**2.83 ± 0.38**	**2.00 ± 0.50**
Determ. coefficient R^2	**0.998**	**0.990**	**0.999**	**0.998**

Table 5.2: Regressions results for the four sets of data shown in fig.5.9.

In this table, the sum of the parameters A and C give the initial molar mass of the virgin guar ($A+C=M_o$), whereas B provides a measure of the depolymerisation rate. Table 5.2 also provides a value for the determination coefficient, R^2, which indicates the goodness of the fit to a particular set of data; the lowest determination coefficient logically corresponds to the ($G50/O_2$) sample, which is characterized by the highest scatter around its regression line (see fig.5.9). From Table 5.2, it is evident that the

depolymerisation rate becomes higher when the ageing temperature passes from 50 to 90°C. Also, we can comment that the constant B is not quite the same for regressions that relate to ($G50/O_2$) and ($G50/N_2$) samples. It is possible to redefine k_d so that an activation energy (E_d) for degradation can be calculated, although, with just two ageing temperatures, this is of limited significance. Nevertheless, we will use the following equation, which comes from the work of Kők et al. [35] (a similar approach was also employed by Bradley and Mitchell [105] and Lai et al. [95] for other systems):

$$k_d = k_{do} \exp(-E_d / RT) \qquad \text{(eq.5.10)}$$

Here, k_{do}, R and T stand for a constant, the gas constant and testing temperature. Using this equation, eq.5.8 can be rewritten:

$$1/M_t - 1/M_o = (k_{do} t / 2m) \exp(-E_d / RT) \qquad \text{(eq.5.11)}$$

Using the latter formula, data that make up fig.5.9 were employed to construct fig.5.10. Regression lines reported in this figure were then employed, by pairs, to derive values for k_{do} and E_d. Two distinct pairs of constants could be calculated; one for samples aged in nitrogen, and the other for samples aged in air. Numerical estimates for such constants are (E_d=30 kJ/mol;k_{do}=1.6x10^{-5} s^{-1}) and (E_d=61 kJ/mol;k_{do}=0.65 s^{-1}), respectively. Equivalent pairs of constants can be found in the work of Kők et al. [35] (E_d=63 kJ/mol;k_{do}=18 s^{-1}) and Bradley et al. [106] (E_d=56 kJ/mol;k_{do}=0.51 s^{-1}). In both cases, such values quantify thermal degradation processes imposed on guar solutions via high temperature viscosity measurements. Such values are fairly close to our pair of constants derived for guar samples aged in air, however, they differ significantly from those derived for guar samples aged in nitrogen. This difference, we propose, is linked to the mechanisms through which guar molecules are degraded. In our case, thermally-based scission processes occur in guar's solid state, whereas Kők et al. [35] and Bradley et al. [106] follow thermally-based degradation processes of guar solutions, in which hydrolysis depolymerisation processes are dominant experimental factors. Bradley et al. [106] also report that depolymerisation kinetics is concentration-dependent, and the above pair of constants was obtained for solutions whose concentration was 0.5%. For information, Kők et al. [35] studied guar solutions whose concentration did not exceed 1%.

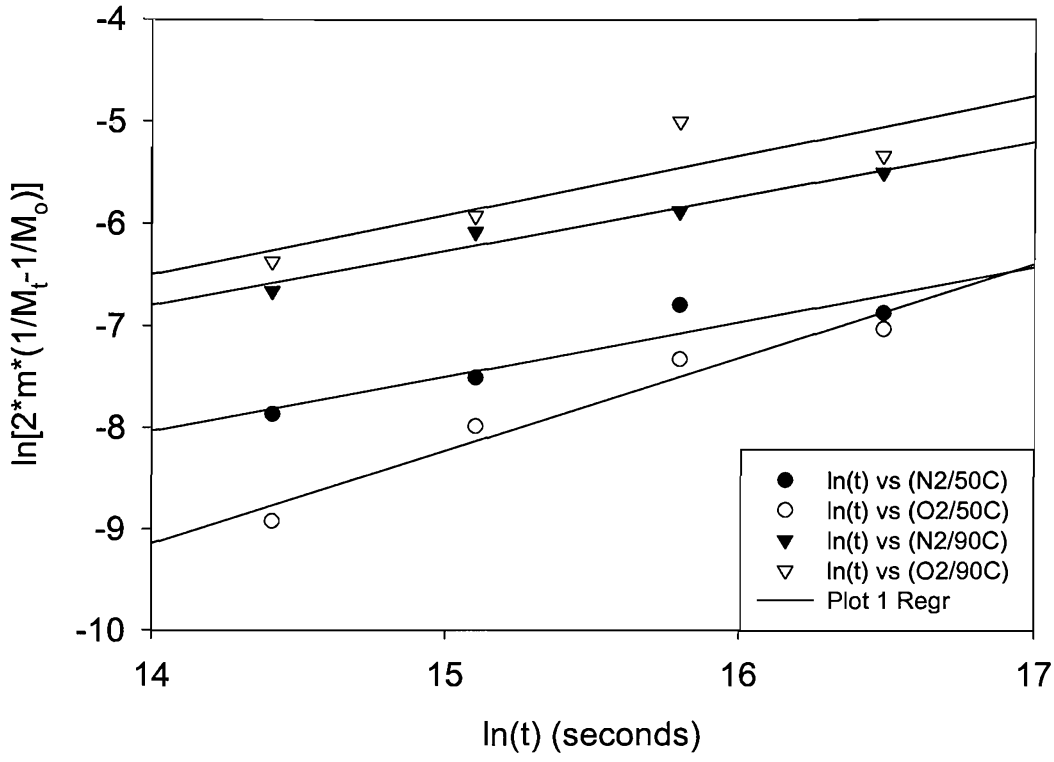

Figure 5.10: Graphical representation of quantities derived from eq.5.11-Molar masses are identical to those reported in fig.5.9. (m=486g/mol).

Thanks to eq.5.11, we could investigate, via a numerical route, depolymerisation processes by adjusting values for both constants in the range mentioned above. To illustrate this, we constructed a numerical data set, which is plotted in fig.5.11. To create this graph, we employed values for E_d and k_{do} of 61 kJ/mol and 0.65 s^{-1}. This 3D representation encompasses the time-temperature domain which was explored experimentally, and we are fairly confident that data interpolated within this domain truly reflects molar mass reductions that would occur at intermediate temperatures. Importantly, the ageing conditions employed to degrade guar rule out the need for studying concentration-dependent degradation kinetics. The latter point may become crucial if guar, employed as a water-trapping material, were subjected to water penetration; in such case, hydrolysis processes could change degradation kinetics.

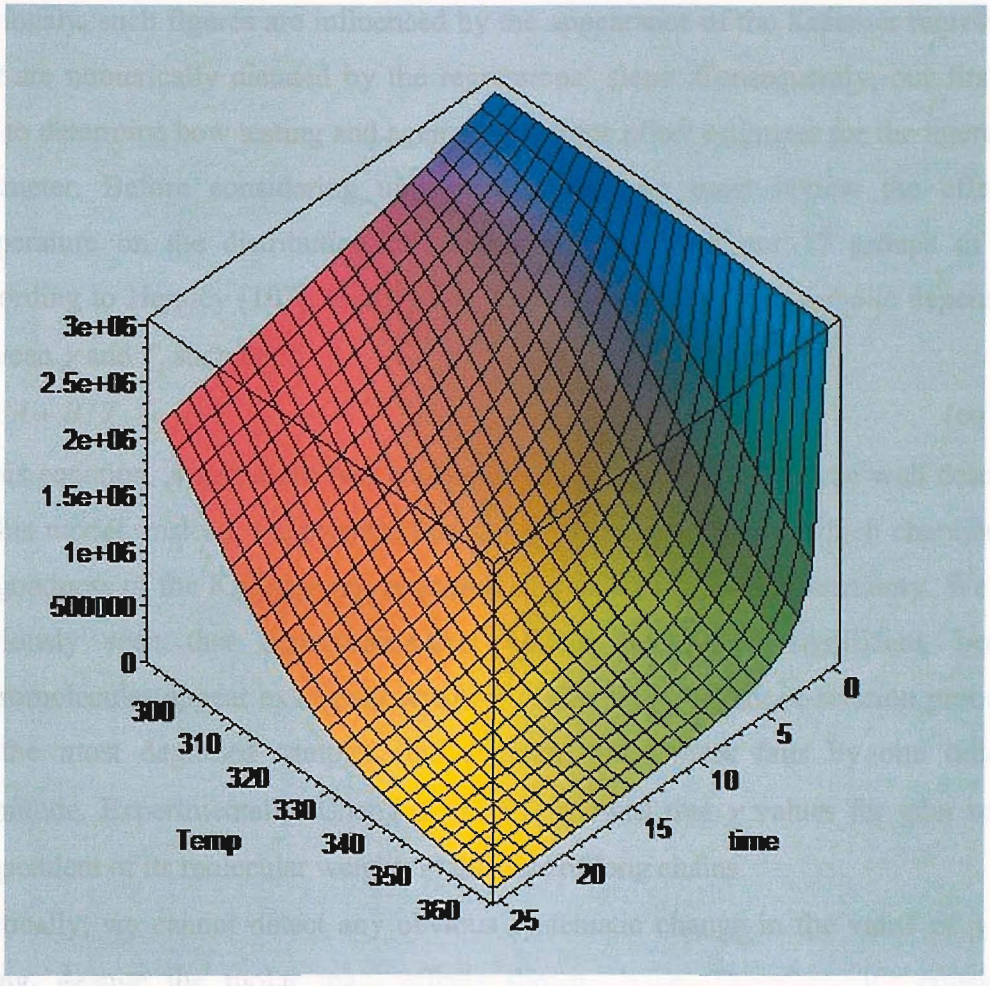

Figure 5.11: 3D map constructed from eq.5.11-Temp. (K), ageing time (weeks), z-axis-M_w (g.mol^{-1}), M_{wo}=3.10^6 g.mol^{-1}; E_d=61 kJ/mol; k_{do}=0.65 s^{-1}.

5.2.5 Effect of ageing on the interaction parameter between guar and water

The second parameter extracted from the above Kraemer plots, *k''*, leads to values for *k'*, whose physical interpretation is the interaction parameter χ presented in the introduction chapter. From a theoretical prospective, the model used throughout the latter chapter is not, in the strictest sense, applicable to our system, since the interactions that occur between guar and water are polar ones. Despite this fact, such theoretical concepts have nonetheless been adopted by many different workers [36,37,40,91,92], who discuss the meaning of this interaction parameter in the context of the theory.

Within the context of this study, our interest in accumulating many estimates for the interaction parameter is to provide an insight into the binding capacity of our material during ageing. In total, 87 individual estimates for χ were acquired, each of which corresponds to a unique combination of ageing conditions and flow temperature.

Obviously, such figures are influenced by the appearance of the Kraemer regressions; they are numerically dictated by the regressions' slope. Consequently, our first task was to determine how testing and ageing conditions affect estimates for the interaction parameter. Before considering numerical values, we must review the effect of temperature on the distribution of points extracted from our 17 groups of data. According to Hamley [107], there exists, for some systems, a hyperbolic dependence between χ and T, such that:

$$\chi = A + B/T \qquad \text{(eq.5.12)}$$

In this equation, A and B are two constants. Our data, however are not well described by this model; instead, we propose that the apparent randomness which characterizes the goodness of the Kraemer regressions is due to experimental uncertainty. We have previously seen that depolymerisation effects are indeed significant, because macromolecules appear extremely sensitive to thermally-enhanced scission processes; for the most degraded samples, the average molar mass falls by one order of magnitude. Experimentally, Cheng et al. [91] showed that χ values for guar remain independent of its molecular weight, in the case of long chains.

Practically, we cannot detect any obvious systematic change in the value of χ with ageing, despite the molar mass effects shown above. Therefore, we considered averaging our data in a number of ways, thinking that trends could possibly emerge as a result; Table 5.3 lists data obtained via several averaging methods. The first approach is similar to that employed with intrinsic viscosities, in which, different averages for χ were obtained by distinguishing the 17 samples characterized by different ageing histories[12]. The resultant data demonstrates that while different samples exhibit different averages for χ, we cannot classify our data in this way according to a regular scheme. For example, χ neither increases, nor decreases systematically with ageing time. We also computed χ values for groups of samples that belong to the same category, e.g., (G50/N_2/all), and, alternatively, according to the nominal temperature and ageing time, e.g. (G50/all/3W), and finally, according to just the ageing time, e.g. (G_{all}/All/3W). Again, no clear trends emerge, since the grouping by sample category leads to similar results for the (G50/N_2/all) and (G50/O_2/all) samples on one hand, and for the (G90/N_2/all) and (G90/O_2/all) samples on the other hand. This grouping method does, however, appear to show that (G50/O_2-N_2/all) samples are characterized by a

[12] This groups data acquired at different flow temperatures for each material type.

slightly lower interaction parameter (~0.552) than their (G90/O_2-N_2/all) counterpart (~0.575). This may indicate a slight differentiation between these two groups of materials.

Sample type	Interaction coefficient	Standard deviation
Unaged	**0,4624**	**0,0242**
(G50/N2/3W)	**0,5076**	**0,0638**
(G50/N2/6W)	**0,5954**	**0,0871**
(G50/N2/12W)	**0,6006**	**0,0802**
(G50/N2/24W)	**0,5060**	**0,0339**
(G50/O2/3W)	**0,5691**	**0,1144**
(G50/O2/6W)	**0,4991**	**0,2013**
(G50/O2/12W)	**0,6703**	**0,1196**
(G50/O2/24W)	**0,4744**	**0,0933**
(G90/N2/3W)	**0,6059**	**0,1017**
(G90/N2/6W)	**0,6029**	**0,0968**
(G90/N2/12W)	**0,5124**	**0,1595**
(G90/N2/24W)	**0,5874**	**0,1419**
(G90/O2/3W)	**0,5322**	**0,0727**
(G90/O2/6W)	**0,6089**	**0,0988**
(G90/O2/12W)	**0,6322**	**0,1731**
(G90/O2/24W)	**0,5297**	**0,1120**
(G50/N2/all)	**0,5524**	**0,0527**
(G50/O2/all)	**0,5532**	**0,0877**
(G90/N2/all)	**0,5772**	**0,0439**
(G90/O2/all)	**0,5758**	**0,0526**
(G50/all/3W)	**0,5384**	**0,0435**
(G50/all/6W)	**0,5473**	**0,0681**
(G50/all/12W)	**0,6355**	**0,0492**
(G50/all/24W)	**0,4902**	**0,0223**
(G90/all/3W)	**0,5691**	**0,0521**
(G90/all/6W)	**0,6059**	**0,0042**
(G90/all/12W)	**0,5723**	**0,0847**
(G90/all/24W)	**0,5586**	**0,0407**
(Gall/all/3W)	**0,5537**	**0,0430**
(Gall/all/6W)	**0,5766**	**0,0519**
(Gall/all/12W)	**0,6039**	**0,0673**
(Gall/all/24W)	**0,5244**	**0,0477**

Table 5.3: Different grouping methods lead to a number of averaged values for the interaction parameter.

Despite this final result, we believe that the data shown in Table 5.3 demonstrate that there is little to differentiate the various averages for χ considered here. In view of this, we decided to return to the hypothesis that the 87 individual values for χ are, in truth,

equivalent. Fig.5.12 was therefore constructed without assigning individual χ values to any particular data set. We simply applied a standard statistical treatment to that large data set, and the overall average and standard deviation values (σ) are reported in fig.5.12.

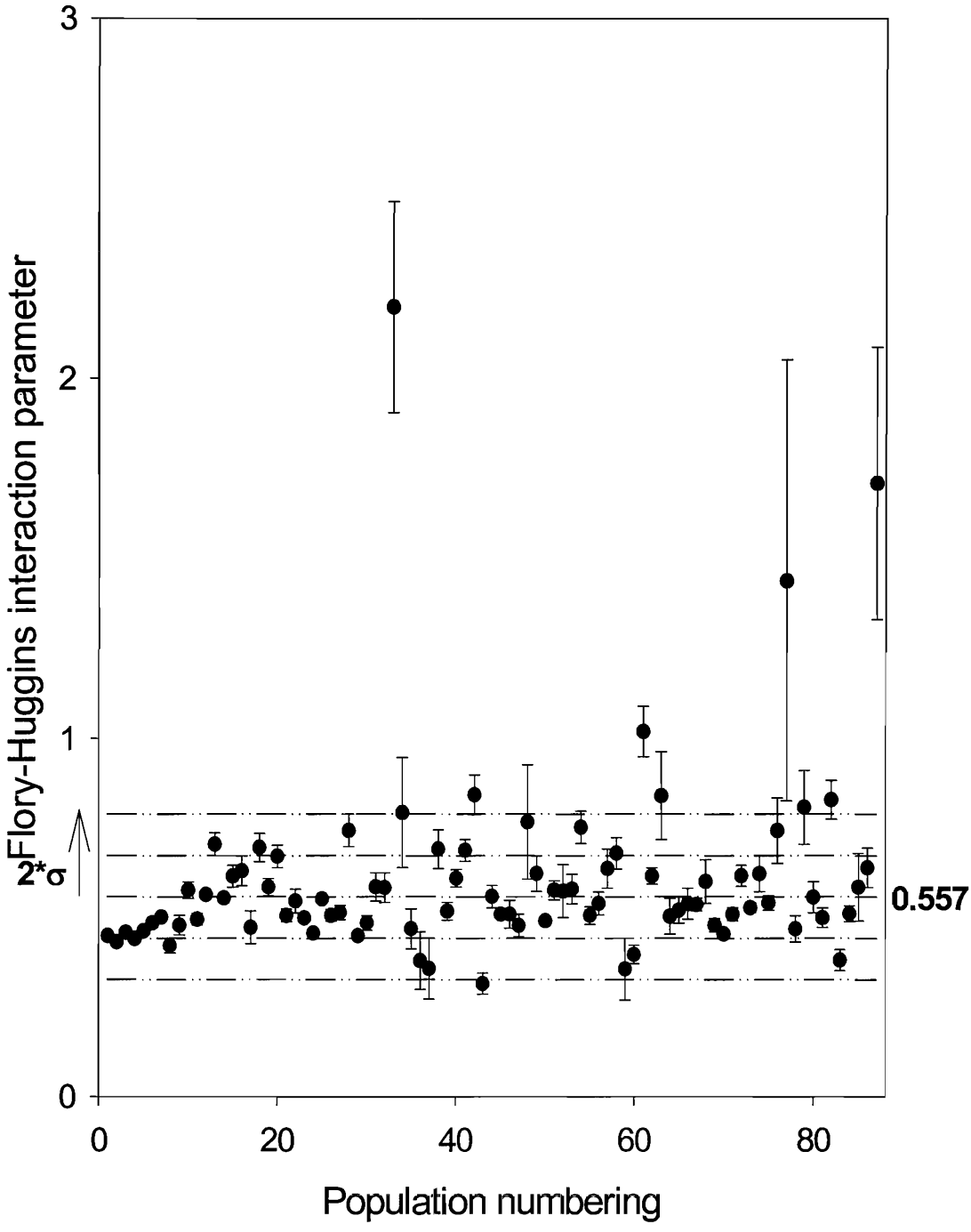

Figure 5.12: Full population of the Flory-Huggins interaction parameter.

From this figure, it can be seen that several data points values are situated well outside the indicated 2σ interval; more precisely, four points are found outside a 3σ interval (not reported), which corresponds to a 99% confidence interval. Although these four points were not removed from the figure, the reported average and standard deviation values were calculated using a truncated data set of 83 data points. The principal reason for not entirely ignoring this apparently anomalous collection of data points is linked to the appearance of their Kraemer regressions. These, we cannot consider as being anomalous, although they do exhibit an unusually high, positive slope. For instance, one of the five plots shown in fig.5.6b led to one of the uncharacteristic χ values, but the linear regression carried out on this plot is no worse than any other; yet, it is characterized by a low value for $[\eta]$ whose magnitude strongly determines that of χ. If we now consider the entire data set shown in fig.5.12, we find an average χ value of 0.61±0.21, whereas our restricted data set of 83 data points give an average of 0.56±0.12.

Before concluding, it is necessary to compare the data that make up fig.5.12 with those presented in the literature, to address one important issue: are our data numerically reasonable? Wientjes et al. [36] studied water-guar interactions and derived χ values of 0.55 ± 0.05 using only the Huggins extrapolation method and guar mixtures whose molecular weights vary approximately by one order of magnitude. Alternatively, Cheng et al. [91,92] reported values of χ of 0.7-0.8 for unaged guar, a value that drops to 0.2-0.3 with molar mass reduction [91]; these workers explain the occurrence of higher values for χ because of aggregation processes that only occur when guar molecules are not degraded; this is a result which resembles particularly that of locust bean gum which gives χ values as high as 0.8-0.9 according to the work of Fernandes [40]. In the context of the Flory-Krigbaum theory, we know that values exceeding 0.5 are due to aggregation phenomena. For locust bean molecules, aggregation is due to hyperentanglements [40,108]; that is, inter and intramolecular associations which lead to aggregation. Returning to guar, both Huggins and Kraemer equations were used by Azero et al. [94], to give a χ value of 0.59 for guar solutions; these workers also remarked that some values derived from their Huggins and Kraemer interpolations varied with the solution preparation method, including their centrifugation and filtering procedures. Using a different experimental route, Simonet et al. [37] reported a value for χ of 0.48, which falls below 0.5. However, these authors derived this using light

scattering data, which was processed using a set of equations that relate to the Flory-Huggins theory. These equations do not permit χ values in excess of 0.5. Thanks to this review, we can see that the literature provides strong evidence that the χ parameter should lie in the vicinity of 0.5. However, it has long been appreciated that this critical value of 0.5 can indeed be exceeded, but, as we have just seen, this depends on the experimental method. Sudduth [103] indicates that the experimental range of χ values for good solvency lies between 0.5 and 0.7; whereas Cheng et al. [91] state that the good solvency domain is found for values situated between 0.4 and 0.5 and that θ-solvency[13] would be attained for values situated between 0.5 and 0.8.

From the above literature review, it would appear that our range of χ values, and the mentioned average of 0.56±0.12 for χ is in perfect agreement with equivalent values measured by several workers for unaged guar. Importantly, we stress that our values for the interaction parameter are not altered by ageing conditions, and we believe that this result is far from obvious. This contrasts rather strongly with the fact that a strong decay in molar mass is induced by thermal scission processes, and this decay is unlikely to alter, in itself, the values for the interaction parameter. One way to interpret our result is to hypothesize that, quantitatively, the binding process between water and guar molecules does not change; we therefore propose that the subjacent mechanism by which χ remains a constant is linked to the fact that guar's characteristic mannose to galactose ratio remains unaltered. This will be explored later.

5.3 Conclusions

This investigation provides useful practical information concerning the outcome of accelerated ageing on the binding process between guar and water molecules. Obviously, the viscometry technique we employed has to be considered cautiously, since numerous experimental factors are likely to influence measurements acquired via this route. We also addressed the problem of choosing an appropriate extrapolation technique, and, in our case, we chose to employ Kraemer's, because its mathematical form greatly reduces experimental scatter in our data. The complete treatment of our data thanks to this technique eventually revealed how sensitive guar molecules are towards thermally-based depolymerisation processes, yet the superimposition of

[13] A θ-solvent is a solvent in which molecular attractions exactly cancel out steric repulsion effects. This happens at the temperature θ.

oxidative effects to the latter could not be termed dominant because of the original averaging method employed method to derive molar masses. In this precise context, we addressed the key issue of interpolating our results to other temperatures and ageing times. It gave us the opportunity of reproducing experimental data concerning molar mass variations thanks to a numerical method. Then, the close examination of ageing effects on the interaction parameter describing our system revealed that, independently of scission mechanisms, guar's M:G ratio does not vary, or at least, not in a noticeable way. Applicability of theories such as that of Flory-Huggins is restricted by the very nature of our solute/solvent system, but our results are well supported by the results of other workers.

Chapter 6

Vibrational spectroscopy of guar and locust bean gum

6.1 Introduction

We employed spectroscopic techniques to test the above viscometry results and their interpretations. More precisely, we cannot infer from our previous experiments the behaviour of less soluble guar molecules, and, more specifically those molecules that make up GG's insoluble fraction. It is not evident that they will bind with water molecules in a similar way to that of their soluble counterpart and, therefore, we must take into account the fact that we have a limited knowledge of what differentiates those two fractions. We can speculate that guar's insolubility, potentially, originates from structural irregularities such as physical entanglements or the presence of a crosslinked network, from unreported chemical variations, or even both[1]. Viscometry is especially sensitive to changes in molar mass; our results implied that the mechanism by which guar molecules hydrate remains unchanged during ageing. From a quantitative point of view, this can only be explained by the fact that the distribution of galactose groups on a guar chain stays constant. This is a crucial point we intended to test since it is also the factor that most strongly correlates to guar's water-binding capacity. To paraphrase Bayerlein [30], a mannan chain is essentially insoluble in water as such, and locust bean molecules (LBG) can only be solubilized in hot water [40]. This behaviour is characteristic of a lower substitution degree in galactose and this relative lack of substitution leads both to inter and intra-molecular associations, which are specifically referred to as hyper-entanglements by Goycoolea et al. [108][2]. We did not eliminate

[1] We do not ignore that sample preparation might be a complicating factor, since clotting is somewhat reduced by increasing the contact surface between guar particles and the solvent.

[2] Goycoolea et al. [108] also report that at least seven consecutive, unsubstituted mannose groups are necessary for hyper-entanglements to appear. This aggregation effect renders LBG molecules insoluble in cold water.

the possibility that guar molecules might undergo chemical changes during ageing. From the work conducted by Ferguson et al. on guar fermentation [109], it becomes apparent that guar can degrade and generate different types of by-products including acids, although Ferguson et al. worked specifically on a degradation mode triggered by the presence of particular bacteria. Interestingly though, indirect clues concerning the inherent stability of polysaccharides such as GG and LBG can be found in the work of Colombani et al. [110], who successfully identified carbohydrates many hundreds of years old in wall paintings. However, the same authors forewarn that the positive identification of GG and LBG samples via spectral routes is difficult, since these two polysaccharides show "strict similarities between spectra of different gums" (sic). To make matters worse, the composition of GG and LBG will also vary, depending upon their respective provenance [31,110]. We, nonetheless, know from the work performed by Mrozek and Weaver [111] on aqueous monosaccharides, that Raman spectroscopy enables mannose to be distinguished from galactose. Even though they share the same chemical formula along with glucose, and more generally, hexoses, they can nevertheless be distinguished in specific regions of their Raman spectra [111,112]. Thus, we undertook to utilize FTIR and Raman spectroscopy techniques to see how suited they are to revealing differences between our various samples. We will begin by discussing the occurrence of spectral features, and by presenting FTIR and Raman spectra derived from reference GG samples. Afterwards, we will attempt to follow systematic changes due to sample type and ageing conditions.

An original aspect of the work presented in this chapter relates to the way we attempted to interpret the meaning of spectral features encountered in both IR and Raman spectra. Since we could not find references specifically dealing directly with the spectral response of GG or LBG systems, we undertook to carry out our spectral analysis by incorporating some elements of analysis inspired by the work of several workers on biomolecules that present similarities to our polysaccharides.

6.2 FTIR spectroscopy

In this study, we employed FTIR, primarily, as a comparative tool to test the different ideas proposed in the introduction. Initially, we will review the vibrational modes in a reference spectrum of GG. Then, we will attempt to differentiate GG and LBG's spectra, to facilitate further comparisons between reference and other GG spectra.

After that, we will examine, in detail, a series of aged guar samples, with the objective of following the effect of ageing on the appearance of the FTIR spectra. Eventually, we will also attempt to derive some information from samples made from guar's insoluble fraction.

6.2.1 Band assignment for a reference GG spectrum

The most straightforward means of understanding the following FTIR spectra involves splitting the latter into different regions similarly to a reference spectrum and, then, reviewing and attributing specific vibrational modes to the features present in each of the resultant spectral sub-regions. Thus, aided by literature reviews dealing specifically with spectral data obtained from materials that are chemically similar to guar, we initially undertook to separate and decode information contained in the regions that make up our reference GG spectrum[3]. We interpreted the presence of the different peaks present in the latter spectrum by reviewing the specific interpretations of spectral features given by different workers on cellulose[4] [113,114], starches[5] [115] and other summaries regarding vibrational frequencies for galactose [116].

Our first three figures cover the 400-1500 cm^{-1} region, which contains most of the features related to vibrational modes of atoms or molecules linked by single covalent bonds. Proniewicz et al. [113,114] clearly state that it is impossible to identify precisely all the spectral features exhibited by carbohydrates[6]; from our three first figures, it is evident that many overlapping peaks are present in the 400-1500 cm^{-1} region. Concerning cellulose, the latter authors report that one can attribute vibrational modes involving deformation and torsion of CCC, CCO, COC, OCO and COH groups in the region below 900 cm^{-1}; this is the vibrational zone encompassed by fig.6.1a. Infrared band assignment for starches by Kizil [115] include C-C stretching at 764 cm^{-1} and C1-H/CH_2 deformation at 860 cm^{-1}; we think that peaks respectively situated at 770 cm^{-1} and 871 cm^{-1} (see fig.6.1a) may correspond to these vibrational

---

[3] The latter was obtained by drying a dilute solution equivalent to that used previously as a reference in viscometry testing.

[4] The backbone for cellulose only differs from guar's at C-2 [39]. Cellulose is not comprised of lateral galactose groups though [39,116].

[5] Starches are principally made of glucose groups attached by α-1,4 glycosidic linkages [115].

[6] They emphasize this point by pointing out that a single α-anomer of D-glucose exhibits 18 vibrational modes in just the 1200-1500cm^{-1} region.

modes, even though both peaks are shifted somewhat towards higher wavenumbers. Since we do not know whether mannose and galactose groups contribute separately or jointly to the spectral features seen in this region of our spectrum, we attempted to locate peaks that might be attributed solely to vibrational modes for α-D galactose. To do this, we examined the entire list of vibrational frequencies given by Zbankhov et al. [102] for this moiety, but we could not find any matching wavenumbers. The most likely explanation for this is that spectra for polysaccharides are not simple combinations of the spectra of the monosaccharides of which they are composed. Fig.6.1b covers the 900-1200 cm^{-1} region; this is the zone where cellulose [116] exhibits CO and CH stretching, antisymmetric ring stretching, antisymmetric bridge COC, CCH and OCH deformation vibrations. Some work carried out by Shingel on dextran and pullulan[7] [117] has identified the same vibrational modes in this region, except that CH stretching was reported instead of CC stretching. In this region of the spectrum, we could find possible matches between galactose [116], which exhibits peaks at 1074 cm^{-1} and 1147 cm^{-1} and features located at 1076 cm^{-1} and 1149 cm^{-1} in fig.6.1b; the closest match for starches (1067 cm^{-1} and 1163 cm^{-1}) relate to COH bending on one hand, and CC and CO stretching modes on the other hand. Fig.6.1c encompasses the 1200-1500 cm^{-1} region; for cellulose, this region includes COH planar bending, CCH, OCH and CCH stretching as well as HCH bending and wagging modes [113]. The vibrations of starch at 1344 cm^{-1} and 1415 cm^{-1}, closely match some of our highly fused features found at 1345 cm^{-1} and 1414.5 cm^{-1} and, potentially, indicate COH bending and CH_2 twisting on one hand, and CH_2 bending and COO stretching on the other hand.

Above the 400-1500 cm^{-1} region, there is a change in the general appearance of our spectrum, since it contains only a limited number of features. These are, nevertheless, of great interest. Fig.6.1d shows the 1500-2200 cm^{-1} region, where a single peak situated at 1650 cm^{-1} can be seen. The latter is unanimously reported to relate to bending modes of adsorbed water molecules in the case of both cellulose and starches [113,115]. Thus, this peak has more to do with the sample's surface than its bulk composition. However, we believe that a close examination of this region is required, since 1715±100 cm^{-1} also corresponds to the region where C=O stretching appears

[7] Dextran and pullulan are made of α-D glucose respectively linked by C1-C6 and C1-C4/C1-C6 bonds [118].

[61,114]. Importantly, the features present in the 1800-2600 cm^{-1} region only relate to background variations; hence, we pay no particular attention to this part of our spectrum. Fig.6.1e covers the 2200-3000 cm^{-1} region, where the 2900±100 cm^{-1} region relates to CH_2 deformation modes [115]. Finally, the 3400 cm^{-1} band, see fig.6.1f, is attributed to OH stretching modes for cellulose [114].

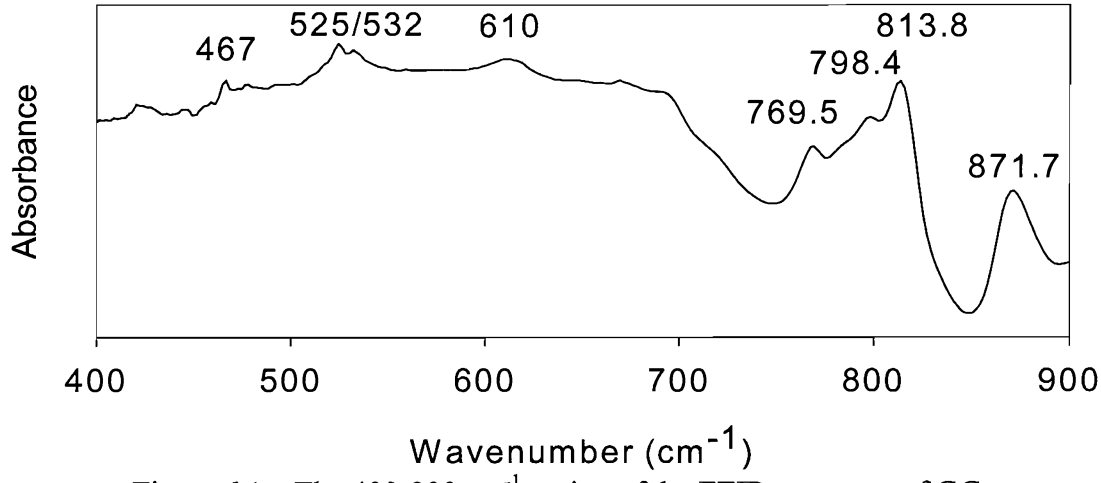

Figure 6.1a: The 400-900 cm^{-1} region of the FTIR spectrum of GG.

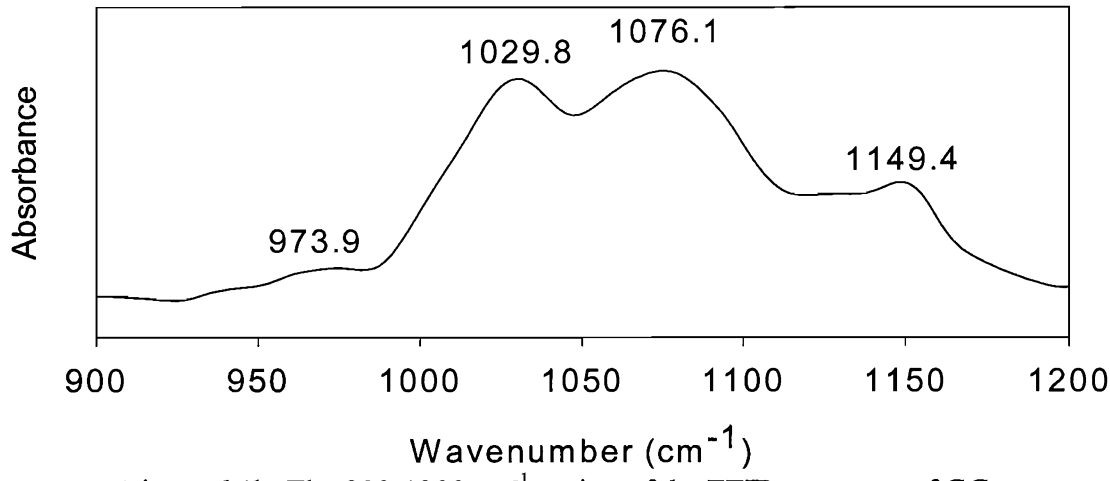

Figure 6.1b: The 900-1200 cm^{-1} region of the FTIR spectrum of GG.

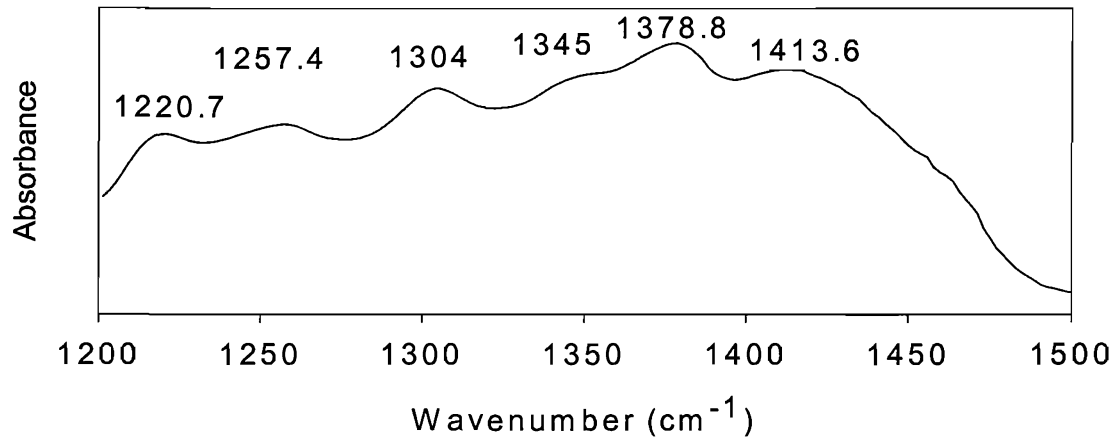

Figure 6.1c: The 1200-1500 cm^{-1} region of the FTIR spectrum of GG.

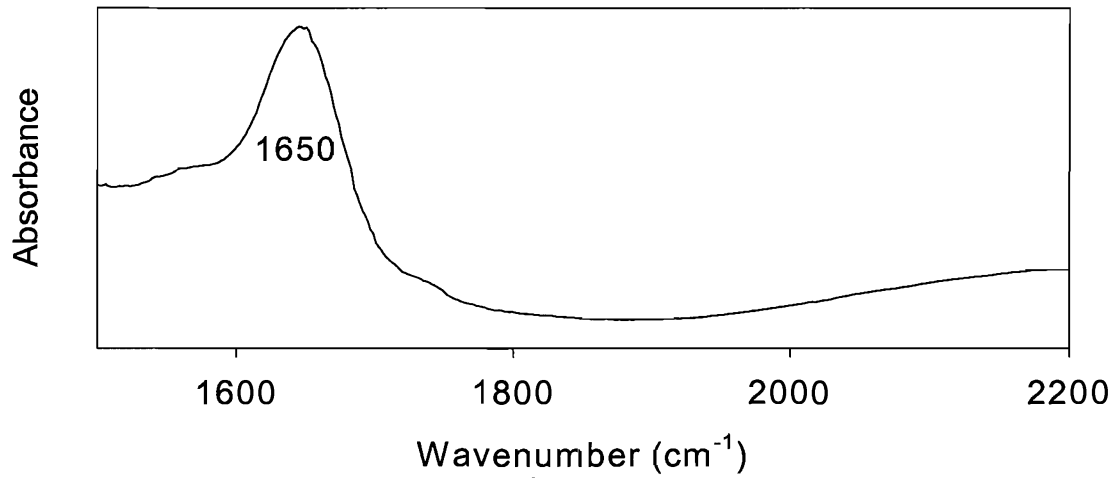

Figure 6.1d: The 1200-2200 cm^{-1} region of the FTIR spectrum of GG.

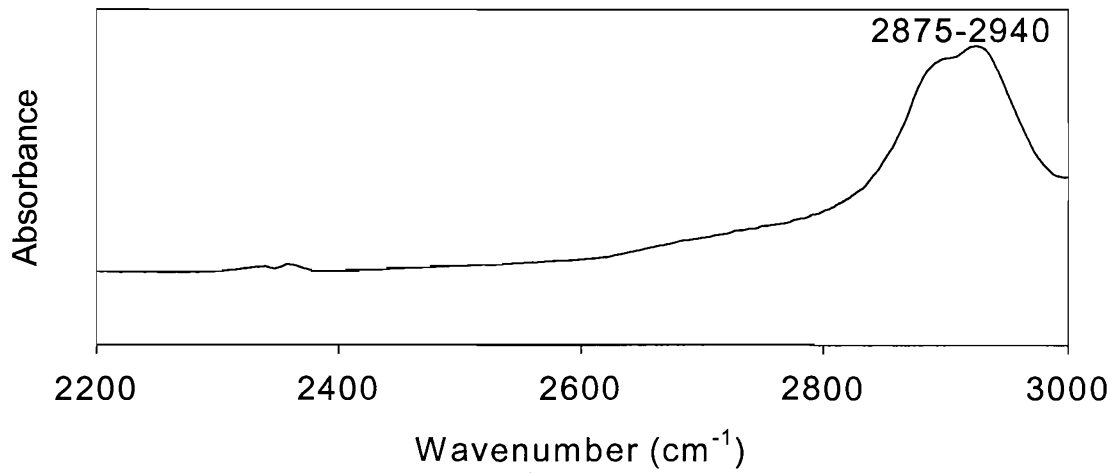

Figure 6.1e: The 2200-3000 cm^{-1} region of the FTIR spectrum of GG.

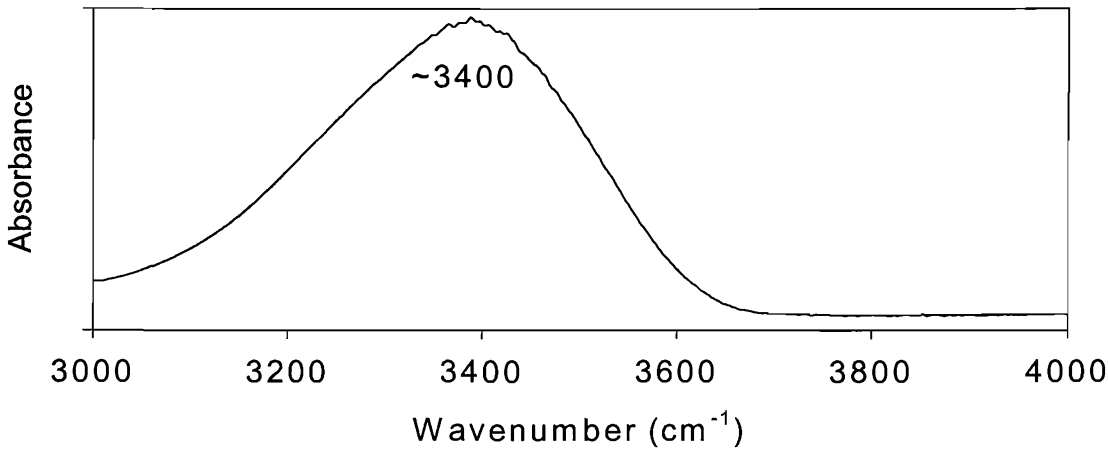

Figure 6.1f: The 3000-4000 cm^{-1} region of the FTIR spectrum of GG.

6.2.2 Comparison between reference spectra for GG and LBG

Fig.6.2 contains the complete GG reference spectrum used to construct the above series of figures and, in addition, compares this with another spectrum similarly derived from unaged LBG[8]. From this figure, it is evident just how similar these two reference spectra are. Almost all of the peaks present in the reference spectrum for GG are also present in LBG's. However, a closer examination of both spectra reveals that, in general, the LBG absorbance peaks appear more clearly defined and protrude further above the absorbance background; this is especially visible in the 400-900 and 1200-1500 cm^{-1} regions. While this effect is partly due to the fact that we did not rescale our spectra[9], such that the relative amplitude of the LBG peaks is consistently higher than in GG's, small differences can nonetheless be identified; GG's 1650 cm^{-1} peak, for example, is preceded by a shoulder, which is not present in the LBG spectrum. Since there is no reference to any feature in this region as far as our literature review is concerned, we can hypothesise that this shoulder is either a lower-energy extension of the following 1650 cm^{-1} peak or an experimental artefact. In addition, the

[8] At first, we attempted to hydrate LBG samples in a similar manner to GG samples, prior to centrifuging, casting and desiccating a fraction of the corresponding dilute solution. Repeated attempts demonstrated that no fraction of LBG is soluble at room temperature, as one would logically expect. Fernandes states that a nominal temperature of 90°C is necessary to attain complete dissolution for LBG [40]. Therefore, we successfully prepared a thin film out of LBG powder by boiling a locust bean gum solution for 30 minutes. It was then cooled down and dried to form a suitable sample.

[9] We did not rescale or process any spectrum presented in the following sections.

overlapping peaks found in the 2900 cm^{-1} region are of a similar height in LBG, whereas the 2875 cm^{-1} peak is slightly smaller than the 2940 cm^{-1} peak in the GG spectrum. At this stage, it would however be premature to ascribe this difference to genuine differences in CH_2 deformation modes, variations in sample preparation or spectrum acquisition conditions.

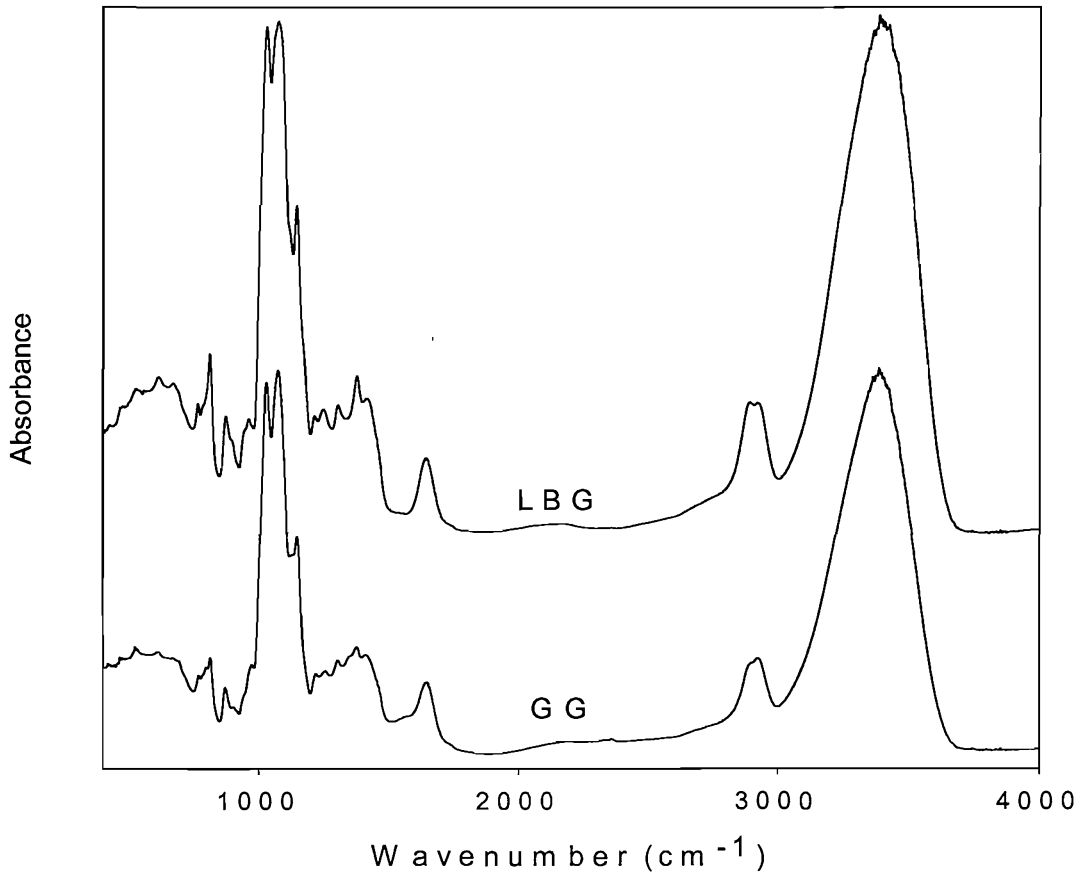

Figure 6.2: Overlaid spectra of GG and LBG.

6.2.3 The influence of ageing on the appearance of FTIR spectra

Fig.6.3a was generated using overlaid spectra derived from our ($G90/O_2$) series of samples; ageing times are as indicated in fig.6.3a. We wish to emphasise the fact that another spectrum acquired in a nominally equivalent manner to the former reference spectrum of GG, has been used as a new reference spectrum for this series of data. From fig.6.3, we see that the shoulder preceding the 1650 cm^{-1} peak mentioned above is no longer present in this new reference spectrum but that, otherwise, this new spectrum is totally consistent with the former. In fig.6.3a, this is the only spectrum devoid of noise. For some reason, the 1500-1800 and 3600-4000 cm^{-1} regions are

particularly affected by the superimposition of incoherent data points; it is difficult to identify a clear origin for this effect, since all samples were rigorously prepared and tested under equivalent conditions. Nevertheless, given that this specifically appears in the 1500-1800 cm^{-1} region of our spectra, it might be associated with some unknown variation in the samples' surfaces, i.e. changes in adsorption processes.

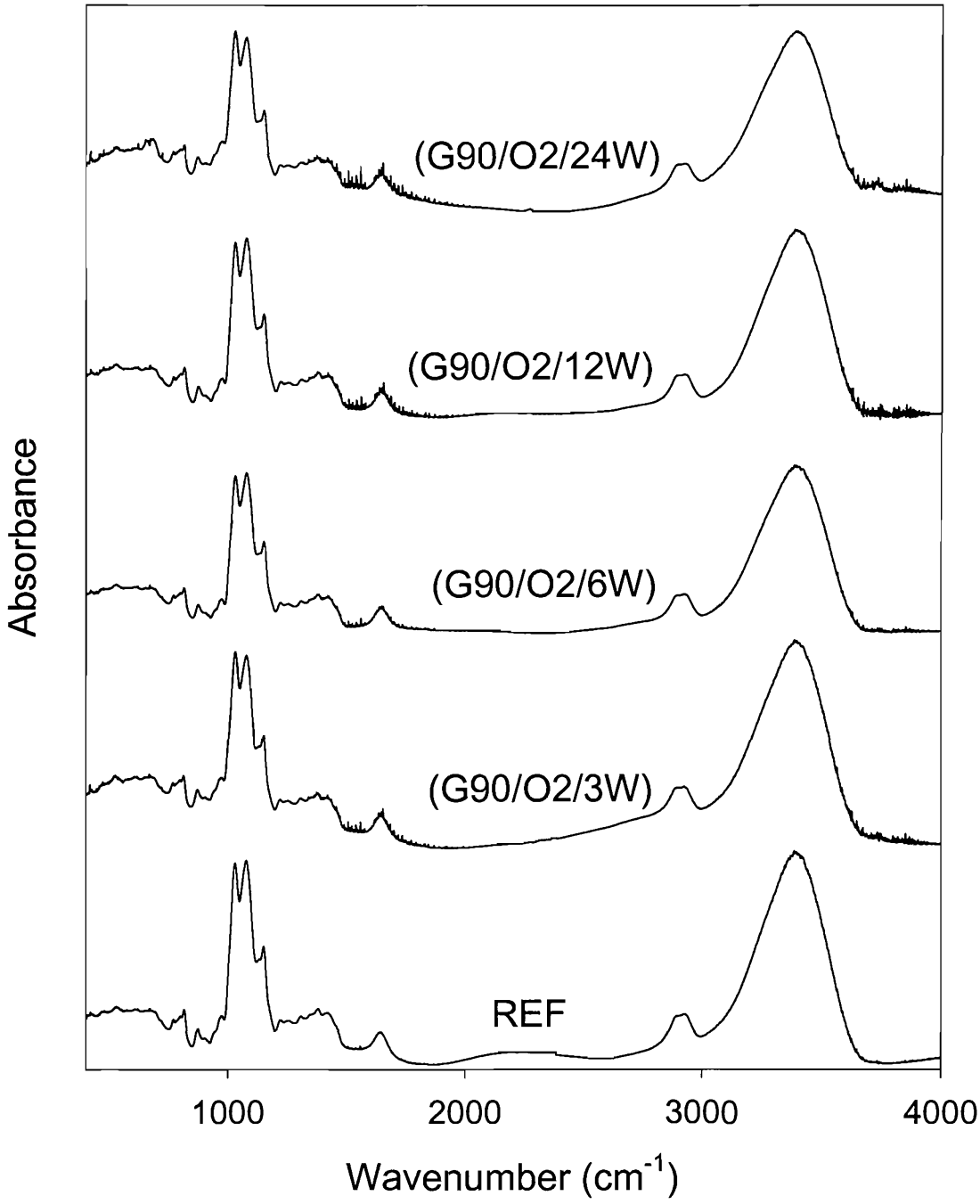

Figure 6.3a: Overlaid FTIR spectra of GG samples that belong to the ($G90/O_2$) series of samples.

Except for the noise in our data, the significant element of this figure is the astonishing similarity between all of the spectra that are shown. To have a better insight into what might differentiate our samples, fig.6.3b and fig.6.3c were generated using two sub-sets of data taken from those displayed in fig.6.3a. What we did was simply to smooth the 1600-1800 cm^{-1} region for each spectrum, and then overlay the results[10]. Conversely, the spectral sub-sets used to produce fig.6.3c were not processed in any way.

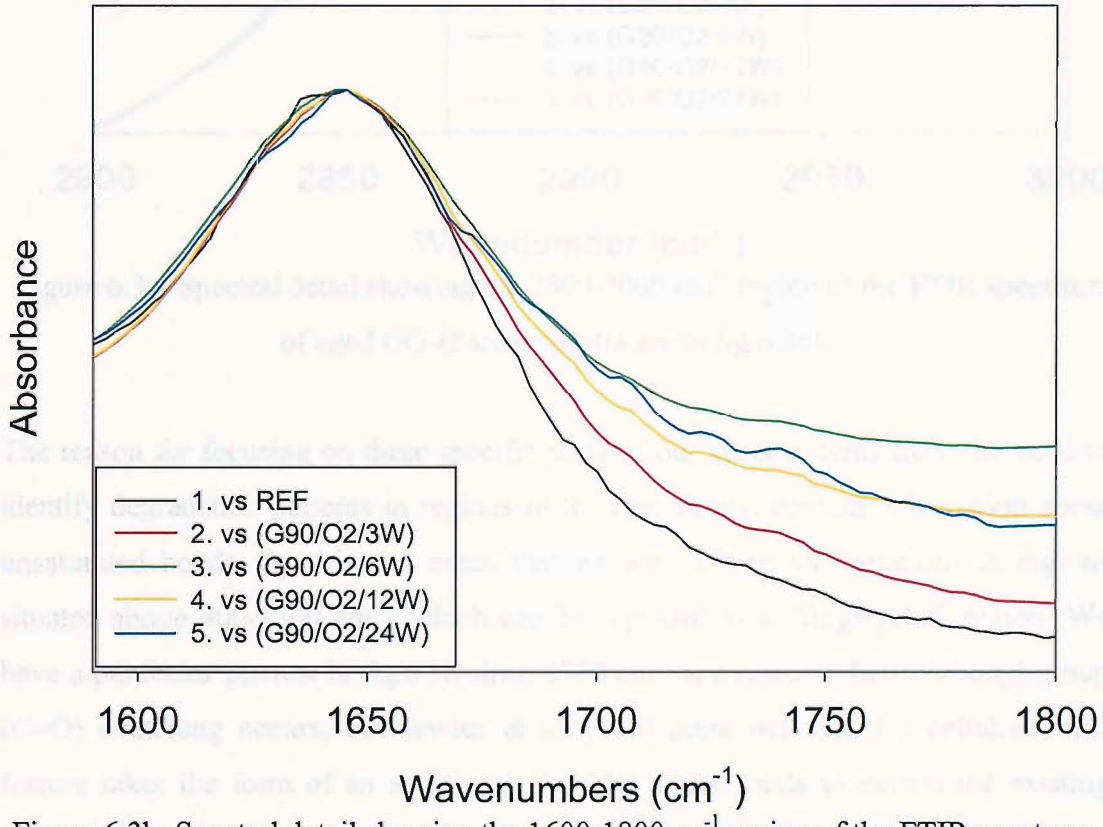

Figure 6.3b: Spectral detail showing the 1600-1800cm^{-1} region of the FTIR spectrum of aged GG-(Parent spectra are in fig.6.3a).

[10] We carefully adapted the smoothing method so that the visual appearance of the processed data remained true to the original data sets. This region of the spectrum contains no sharp spectral peaks that would have been adversely affected by this process.

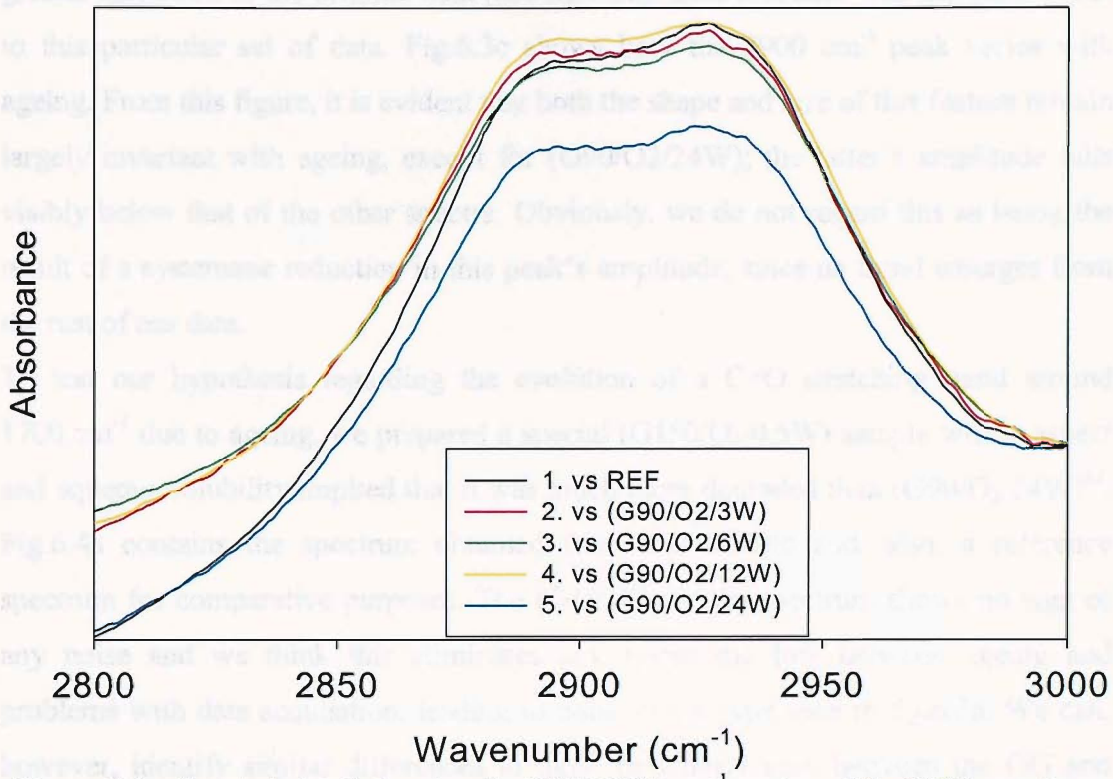

Figure 6.3c: Spectral detail showing the 2800-3000 cm^{-1} region of the FTIR spectrum of aged GG-(Parent spectra are in fig.6.3a).

The reason for focusing on these specific parts of our spectra stems from the need to identify degradation patterns in regions of the spectra that contain information about unsaturated bonds. By this, we mean that we are looking for variations in regions situated above 400-1500 cm^{-1}, which can be regarded as a "fingerprint" region. We have a particular interest in fig.6.3b since 1730 cm^{-1} is a region where carbonyl group (C=O) stretching occurs; Proniewicz et al. [113] point out that, for cellulose, this feature takes the form of an additional shoulder which tends to extend the existing 1650 cm^{-1} peak to higher wavenumbers. The data presented in fig.6.3b were manually adjusted so that the maximum in each 1650 cm^{-1} peak aligns with that of the reference spectrum[11]. We then examined the variation in absorbance above the 1650 cm^{-1} region as a function of ageing. From fig.6.3b, it appears that the absorbance level increases perceptibly with ageing time; unfortunately, this general trend is somewhat undermined by the fact that the data for (G90/O2/6W) sample has a lower amplitude than that of (G90/O2/12W). Also, we believe that the quality of the smoothed data for

[11] Data alignment was rather marginal and was only needed for two sub-sets of data.

the (G90/O2/24W) is poorer than that obtained from the other samples due to the greater distortion of the original data (see fig.6.3a). Less credence was therefore given to this particular set of data. Fig.6.3c shows how the 2900 cm^{-1} peak varies with ageing. From this figure, it is evident that both the shape and size of this feature remain largely invariant with ageing, except for (G90/O2/24W); the latter's amplitude falls visibly below that of the other spectra. Obviously, we do not regard this as being the result of a systematic reduction in this peak's amplitude, since no trend emerges from the rest of our data.

To test our hypothesis regarding the evolution of a C=O stretching band around 1700 cm^{-1} due to ageing, we prepared a special (G150/O_2/0.5W) sample whose aspect and aqueous solubility implied that it was much more degraded than (G90/O_2/24W)[12]. Fig.6.4a contains the spectrum obtained from this sample and, also, a reference spectrum for comparative purposes. The (G150/O_2/0.5W) spectrum shows no sign of any noise and we think this eliminates any systematic link between ageing and problems with data acquisition, leading to noise of the type seen in fig.6.3a. We can, however, identify similar differences to those previously seen between the GG and LBG reference spectra, in the sense that the spectrum for (G150/O_2/0.5W) exhibits peaks that are relatively higher than those of the reference spectrum. Again, this is partly due to the fact that the overall amplitudes of our two spectra do not exactly match. However, we can see, for instance, that the relative amplitude of the peak situated at 814 cm^{-1} in the (G150/O_2/0.5W) trace exceeds, somewhat, the amplitude of the collection of overlapping peaks found at lower wavenumbers, as in the reference spectrum of LBG. In addition, the fused peaks situated at 2875 and 2940 cm^{-1} exhibit similar amplitudes, unlike in the GG reference spectrum. Fig.6.4b was then produced using sub-sets of the data that make up fig.6.4a and corresponds to the spectral region previously shown in fig.6.3b; this time, the data were neither smoothed nor rescaled. Fig.6.4b unambiguously shows that absorbance levels for the (G150/O_2/0.5W) in the 1730 cm^{-1} region exceeds that of the reference spectrum, thus reinforcing the idea that an increase in C=O stretching mode genuinely appears as a consequence of ageing.

[12] This was confirmed experimentally by the fact that we could not test this sample via viscometry. Our samples were too fluid and numerous and long filamentary aggregates formed even after pelleting.

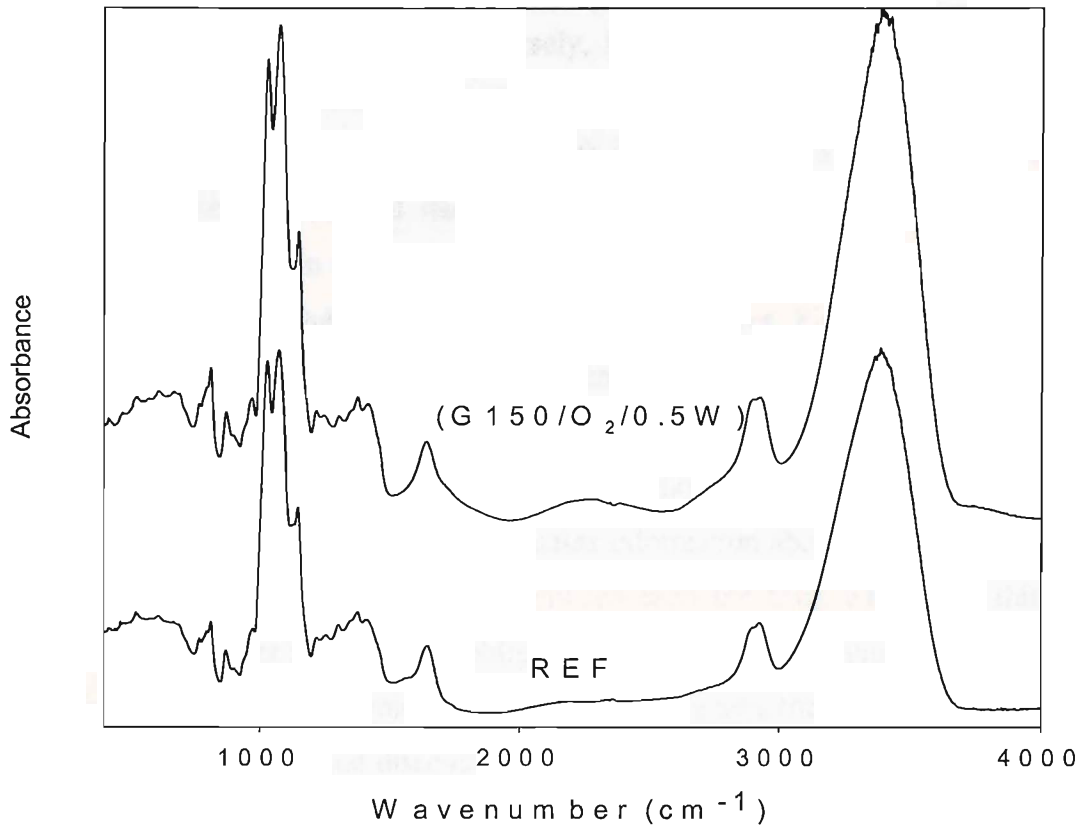

Figure 6.4a: Comparison of the FTIR spectra of aged and unaged GG.

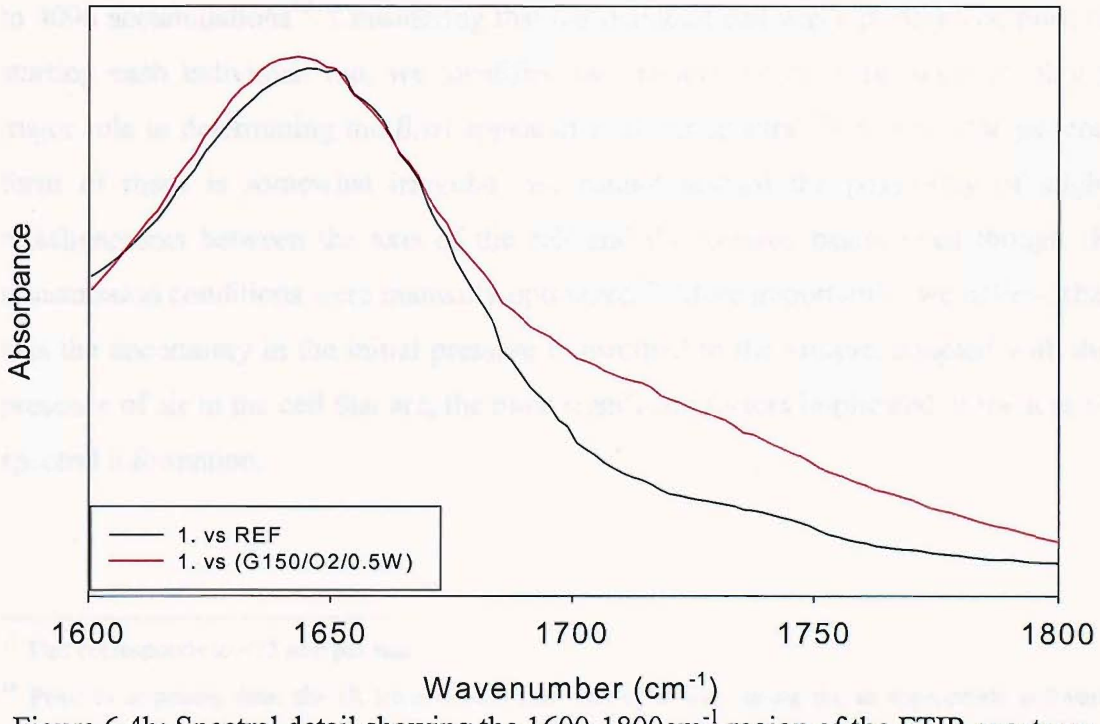

Figure 6.4b: Spectral detail showing the 1600-1800cm^{-1} region of the FTIR spectrum of GG samples-(Parent spectra are in fig.6.4a).

6.2.4 FTIR spectra obtained with a diamond compression cell

Due to the nature of our samples, it was relatively easy to produce thin film samples from solubilized guar fractions. Conversely, insoluble guar residues could not be employed as such and, therefore, we attempted to use a diamond compression cell to analyze dry guar residues. Before attempting to extract data from insoluble specimens, we first evaluated the method itself, by employing the same pieces of thin film previously used to obtain data such as those shown in fig.6.3a. Thus, fig.6.5 contains spectra derived from soluble samples in the ($G90/O_2$) series. Fig.6.5 should therefore contain the same information as fig.6.3a; evidently, this is not so. Specifically, there is a great deal of information which is lost in different parts of the spectra, and most of the fine details that were present in fig.6.3a cannot now be distinguished. If we specifically consider the region which contains information about the background, we can see that marked variations appear between each spectrum which, we think, is largely due to the fact that we were obliged to employ extended runs to acquire these data. Since the aperture by which the infra-red beam enters the cell is reduced to the diamond's diameter, we first discovered that we had to compensate for this reduction in size by accumulating many more acquisitions than was required with the standard sample holder. Thus, instead of generating spectra by integrating, typically, 256 accumulations, we determined that averaging effects could visibly smooth our data up to 4096 accumulations[13]. Considering that our diamond cell was a priori clean prior to starting each individual run, we identified two factors which were likely to play a major role in determining the final appearance of our spectra. First, since the general form of these is somewhat irregular, we cannot discard the possibility of slight misalignments between the axis of the cell and the infrared beam, even though IR transmission conditions were manually optimized[14]. More importantly, we believe that it is the uncertainty in the initial pressure transmitted to the sample, coupled with the presence of air in the cell that are, the most significant factors implicated in the loss of spectral information.

[13] This corresponds to ~75 min per run.

[14] Prior to acquiring data, the IR transmission rate was optimized, using the to appropriate software function. This permits the unprocessed signal to be observed, and, more specifically, the centerburst amplitude; the latter was maximized prior to each run.

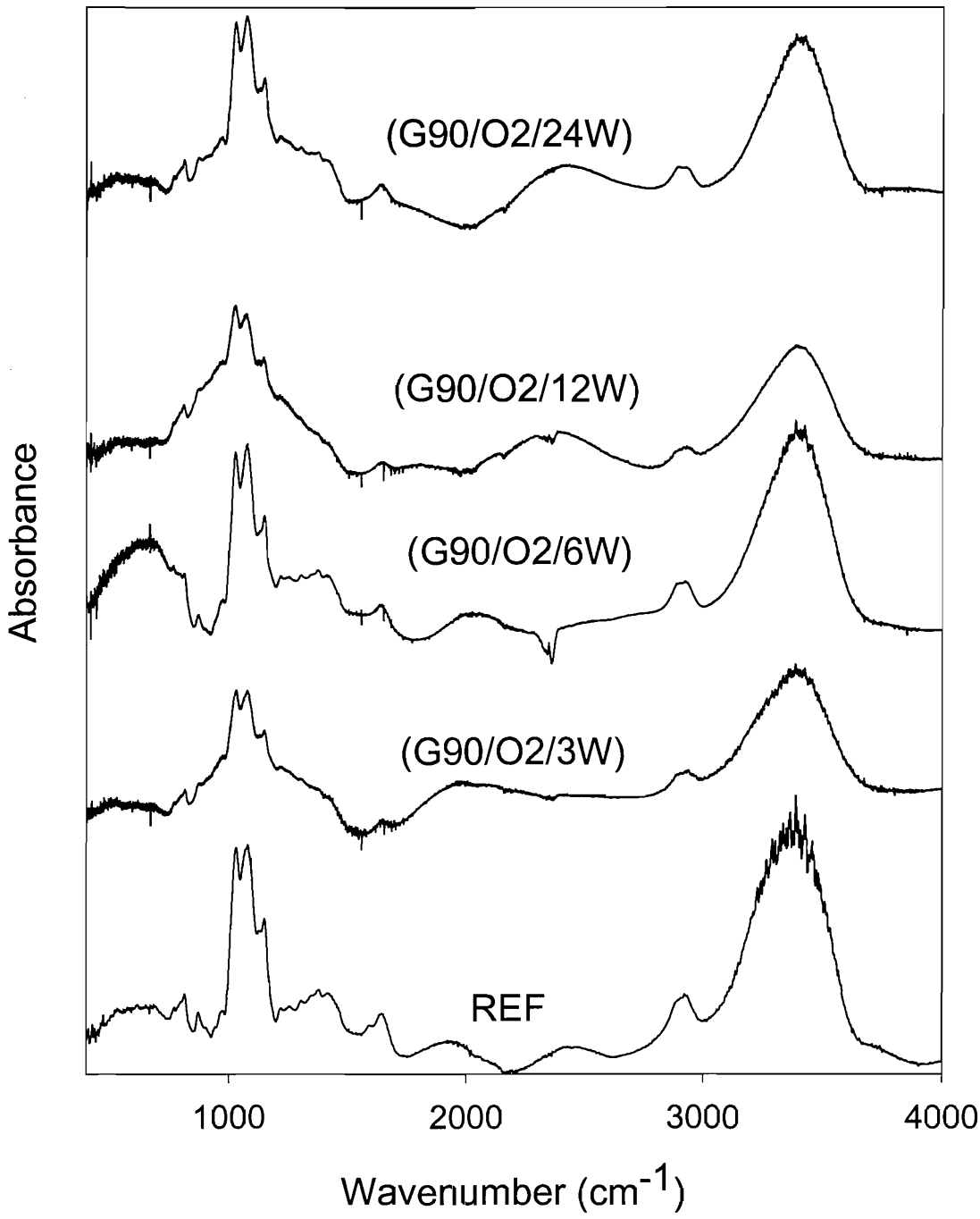

Figure 6.5: Spectral data to be compared to that of fig.6.3a; in this figure, data were acquired with a diamond compression cell.

Since obtaining spectral data for insoluble guar residues was our initial goal, fig.6.6 shows one spectrum for the insoluble fraction of a reference sample. We can see from this that most of the characteristic features of GG are present in this spectrum, albeit with a high level of distortion. As in the spectra shown in fig.6.5, it is the low

wavenumber region which contains the most uncertainties; such that, it is difficult to distinguish individual features within this part of the spectrum. We especially note the apparent broadening of the peak situated around 3400 cm^{-1}. We think that this feature could reasonably relate to sample type, because equivalent peaks located in this region in fig.6.5 are not broadened by the testing technique. Hence, this may potentially indicate that there is a significantly broader distribution in energy for vibrational modes, including OH-based ones that make up this particular feature. A few other spectra were obtained from insoluble residues. They also display this characteristic enlargement in the 3400 cm^{-1} region.

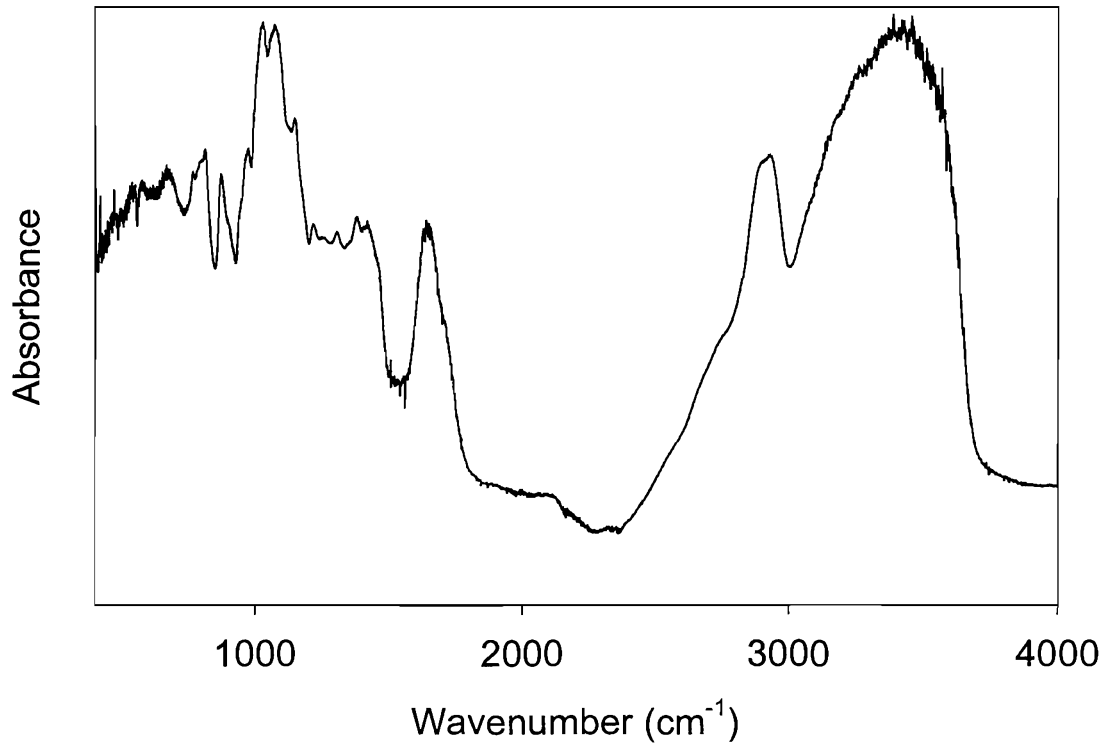

Figure 6.6: FTIR spectrum obtained from the insoluble fraction of a reference sample of GG.

6.3 Raman spectroscopy

Initially, we employed Raman spectroscopy simply as a material identification tool. However, it was subsequently used for similar reasons to the FTIR technique described above; therefore, this section is organized in a similar way to the previous one. Consequently, we begin with a review of features present in one particular region of the GG Raman spectrum. Then, we establish the differences between the spectra of

GG and LBG. At this point, however, the following sections diverge somewhat from the structure employed above, because of the increased versatility of Raman spectroscopy as an analytical tool. Here, this specifically relates to the effect of sample preparation on spectral data. However, we were somewhat constrained by the time required to obtain an individual spectrum; acquisition times were much longer than those required for FTIR, such that we could only examine what we considered to be the most important samples within the overall context of our study. Specifically, we investigated the effect of sample packing, sample type and ageing on final spectral data. Additionally, we attempted to conduct a quantitative study of a particular feature in Raman spectra, which is not presented in the following section.

6.3.1 Band assignment for Raman spectra in the fingerprint region

No attempt was made to address the theoretical issues concerning IR and Raman activity but, rather, we approached Raman spectroscopy in a simple, practical way. This means that we did not specifically attempt to discover which spectral features are common to both techniques, but, instead we began by attempting to distinguishing specific features relating to galactose and mannose groups separately. To begin with, we know that Raman spectroscopy is a technique which is very sensitive to sample conformation; indeed, it was recently utilized as a characterization tool by Mrozek et al. [111] who successfully differentiated aqueous, monosaccharidic solutions of D-glucose, D-mannose and D-galactose, as well as other monosaccharides. A more specific study of D-glucose was carried out by Bell et al. [112], and it is from these two studies that we were most inspired in terms of analyzing our reference Raman spectrum. For the purpose of their studies, the latter authors restricted themselves to a specific area of their Raman spectra; we will do likewise here because nearly all the information concerning the Raman spectra of polysaccharides is contained in the 100-1500 cm^{-1} Raman shift area[15]. Consequently, the following figures were generated from a reference spectrum[16], which was divided into five distinct regions, and labelled according to the work of Bell et al. [112]. By analogy with the vibrational response of carbohydrates [111], the most precise example being that of D-glucose [112], we refer

[15] Early experiments aimed at identifying guar showed that this is effectively the case for the considered polysaccharides.

[16] Our reference spectrum was obtained from a compacted, powdery guar sample.

to the 100-500 and 500-750 cm^{-1} Raman shift regions respectively as the endocyclic and exocyclic deformation regions (skeletal modes) (see fig.6.7a and 6.7b). Then, the 750-950 cm^{-1} region is referred to as the anomeric region, (see fig.6.7c), since the information found in this region relates to the presence of α and β conformers. Fig.6.7d is termed the fingerprint region [111,112]. Finally, it is the 950-1200 cm^{-1} Raman shift region which leads to the identification of a particular hexose, since the features present here relate to hydroxyl position [111]. Finally, fig.6.7e covers the 1200-1500 cm^{-1} region, which is related to CH_2/COH deformations. In the section that follows, we will compare the GG and LBG's spectra, in an attempt to relate the presence of specific features to sample composition.

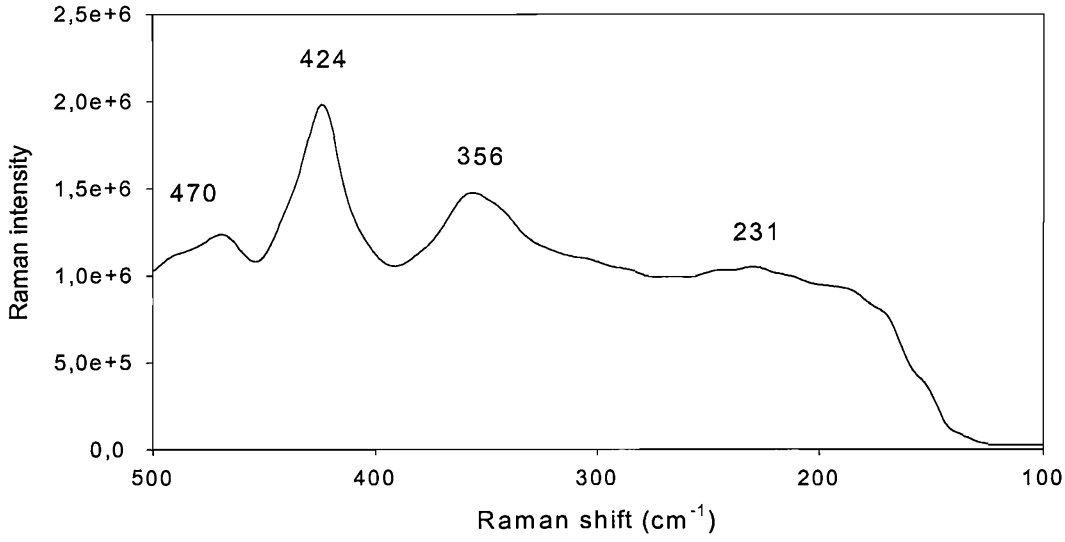

Figure 6.7a: Endocyclic deformation region of the Raman spectrum of GG.

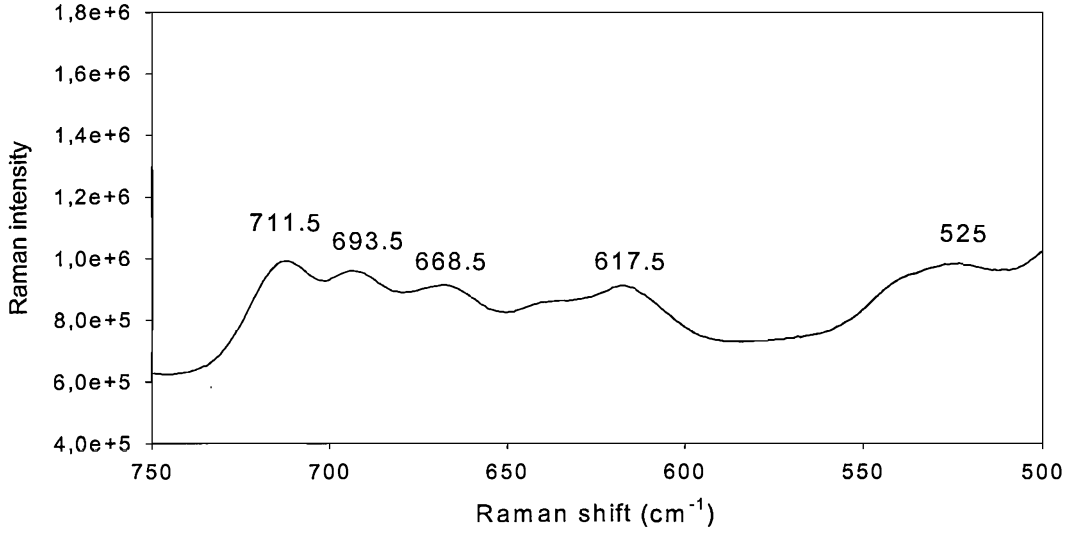

Figure 6.7b: Exocyclic deformation region of the Raman spectrum of GG.

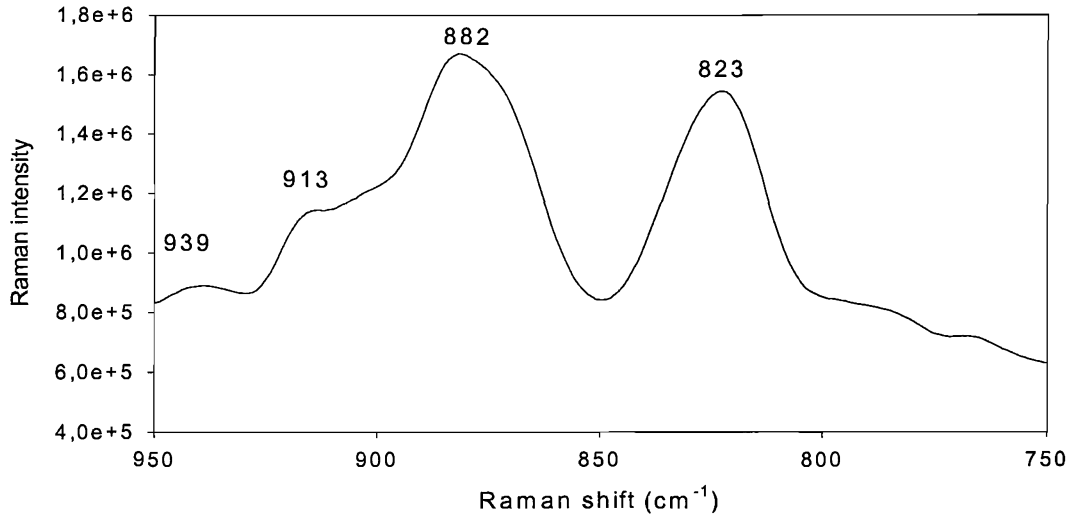

Figure 6.7c: Anomeric region of the Raman spectrum of GG.

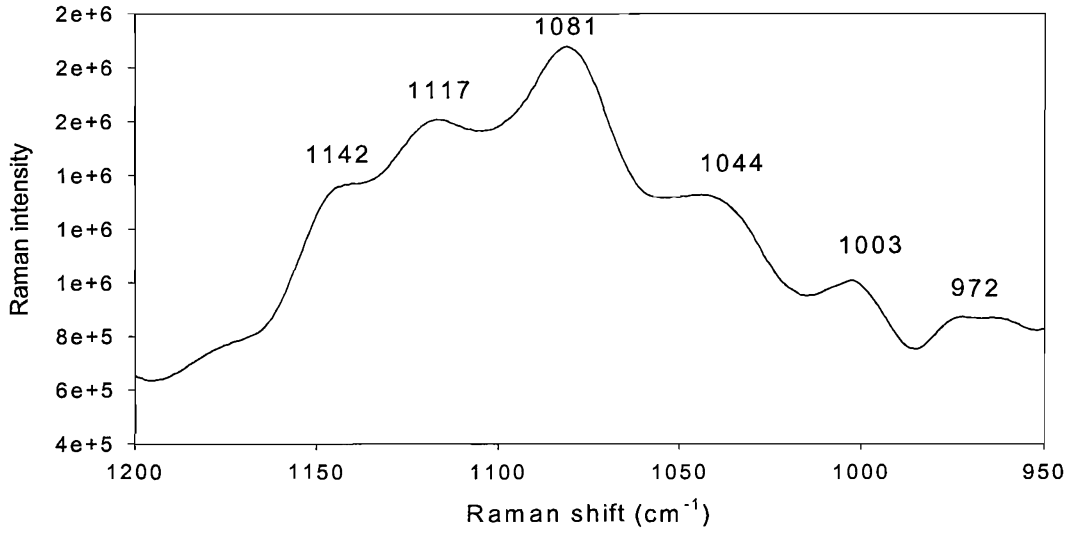

Figure 6.7d: "Fingerprint" region (CO stretching region) of the Raman spectrum of GG.

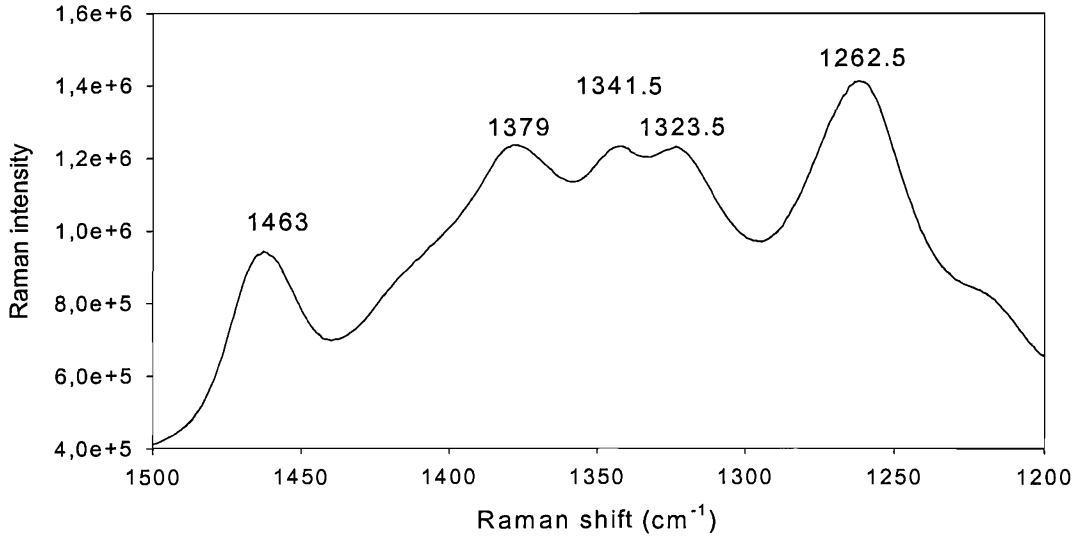

Figure 6.7e: The CH_2/COH deformation region of the Raman spectrum of GG.

6.3.2 Comparison between reference spectra for GG and LBG

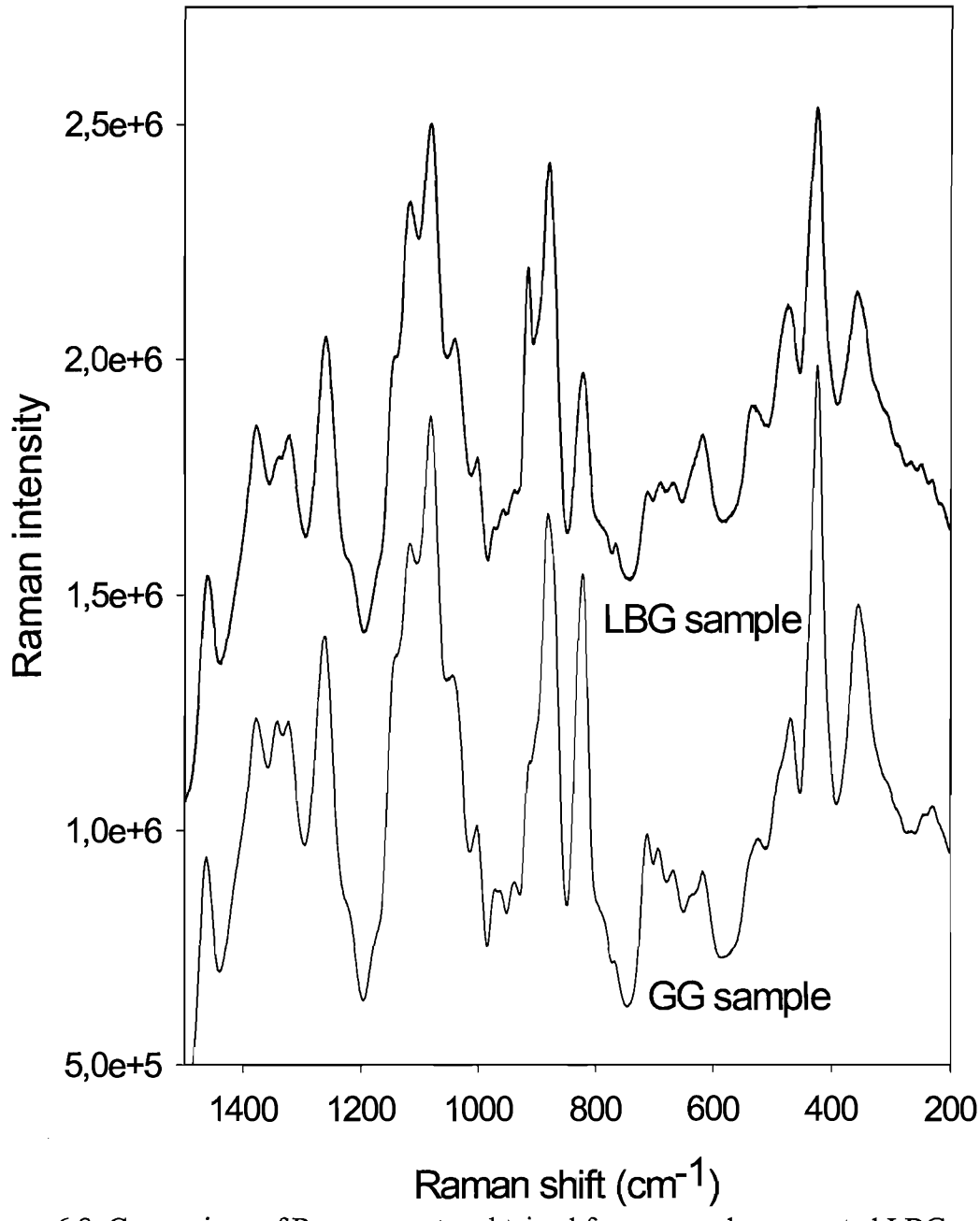

Figure 6.8: Comparison of Raman spectra obtained from unaged, compacted LBG and GG samples.

Fig.6.8 contains two spectra derived from GG and LBG using equivalent testing conditions. Straightforward comparison of the two spectra reveals that they exhibit noticeable differences in each of the regions identified in the previous figures. If we first consider the endocyclic deformation region, we can see that the amplitude of the peaks situated at 231, 356 and 424 cm^{-1} is greater in the case of the GG sample; here, by amplitude, we specifically mean the difference in Raman intensity between a peak's maximum and the local background intensity of the spectrum. From the LBG spectrum, we can also see that weak peaks might be concealed by the dominant peak located around 230 cm^{-1} in GG's spectrum. Thus, we checked the frequencies for molecular vibrations of D-galactose given by Zbankhov et al. [116] and those of D-mannose and D-galactose according to Mrozek et al. [111]. From these sources, the closest matches for the first two peaks listed above are the vibrational modes of galactose situated at 238 [116], 342 [111] and 345 cm^{-1} [116]. We can speculate that there might be significant variations in the vibrational frequencies of linked mannose and galactose groups in this particular region of the spectrum, since, as in FTIR spectroscopy, the Raman spectra of polysaccharides are certainly more complex than those of their constituent units. Conversely, we cannot reject the possibility that some shift in frequency could be related to calibration effects, even though applying a systematic shift in the above frequencies would not move our peak frequencies nearer to that found in the literature. In the data gathered by Mrozek et al. [111], we could not find evidence of a peak situated around 424 cm^{-1} for mannose or galactose, nor could we identify any comparable feature in the vibrational modes of galactose listed by Zbankhov et al. [116]. This reinforces the idea that distinctive peaks appear when mannose and galactose groups are assembled to form a repeating structure such as guar's.

If we now consider the exocyclic region of our spectra, we can identify five peaks; the first one, which is seen at 525 cm^{-1}, is followed by four narrow peaks located at 617.5, 668.5, 693.5 and 711.5 cm^{-1}. In LBG, the last three peaks are of lower intensity than the first, whereas the opposite is true in the case of GG. In this region, spectral data gathered by Mrozek et al. [111] show that the dominant peak for galactose is located at 524 cm^{-1}, with a weaker counterpart for mannose at lower frequencies (520 cm^{-1}). We can also point out that Zbankhov et al. [116] and Mrozek et al. [111] specifically indicate the presence of vibrational modes of galactose at 625 and 694 cm^{-1} and 614 and 696 cm^{-1}; one mannose peak being found at 660 cm^{-1} by Mrozek et al. [111]. To

sum up, it appears difficult to discuss the occurrence of Raman peaks in GG and LBG solely in terms of the vibrational modes of isolated mannose or galactose groups in the 100-750 cm^{-1} region. It is explicable if we consider that this region of the spectrum deals specifically with the relative positioning of lateral atoms on a carbon cycle.

If we now focus on the anomeric region, this is the region where the most pronounced differences occur between our spectra. Mrozek et al. [111] identified vibrational modes for mannose and galactose, respectively, at 830 and 868 cm^{-1} then 825 and 872 cm^{-1}. We suppose, therefore, that both mannose and galactose contribute to the peaks we see at 823 and 882 cm^{-1}. Indeed, the work carried out by Bell et al. [112] revealed that, in glucose, equivalent features relate solely to conformational differences[17]. By comparing our data to those derived from glucose, we can propose that the peak located at 823 cm^{-1} is related to the α-anomers of mannose and galactose; the other peak being related to their β forms. Additionally, the peak situated at 913 cm^{-1}, which is highly visible in LBG's spectrum, remains barely visible in the case of GG. A precise match in vibrational frequency for glucose was also indicated by Bell et al. [112]. They specifically relate this vibrational frequency to α-anomers coupled to "C-O stretches around the ring with contributions from C1H and CH_2 motions". Since α forms possibly contribute to peaks at 823 and 913 cm^{-1}, it is appealing to hypothesize that the formation of one type of α-anomer is detrimental to the other. This could relate to the solid-state properties of our materials, which will be influenced by local constraints such as hyper-entanglements and general chain conformation effects. Then, the two small peaks located at 939 and 972 cm^{-1}, which sit astride the boundary between the anomeric and fingerprint regions, could be ascribed to galactose groups; the vibrational modes of this are listed by Zbankhov et al. [116] and include peaks at 945 and 978 cm^{-1}. The relative shift for those two peaks would be more consistent with an overall shift in frequency for the overall spectrum. Also, since these peaks are extremely small in the LBG spectrum, we believe they could relate to the amount of galactose groups present in the sample. There might also be some contribution from vibrations of glycosidic linkages in the peak located at 939 cm^{-1}, since such features are present at 936 cm^{-1} in starch's Raman spectra [115].

If we now concentrate on the fingerprint region, we can see how close the appearance of the spectral data for GG and LBG is. More precisely, this region contains an

[17] For glucose, these two peaks are situated at 840 and 890cm^{-1}.

ensemble of five, highly overlapped peaks. This particular feature includes peaks found at 1003, 1044, 1081, 1117 and 1142 cm^{-1}. Zbankhov et al. [116] specifically report vibrational modes for galactose located at 1044, 1074, 1118 and 1139 cm^{-1}; however, the data gathered by Mrozek et al. [111] does not contain all these peaks, which is probably linked to the fact that the latter were acquired using extremely short sampling times. From fig.6.8, we can see that in the GG spectrum, the 1044 and 1117 cm^{-1} peaks appear to exhibit marginally less prominent intensities than in the LBG counterpart. However, on the basis of this part of the spectrum alone, there seems to be little to differentiate the two gums. It appears to be the same situation for the 1200-1500 cm^{-1} region, where just a minor difference in relative intensity is seen in the peak located at 1342 cm^{-1}. This peak is, relatively, lower in the LBG spectrum, in comparison to that seen in the GG spectrum. This particular peak is present in Mrozek et al.'s spectrum of galactose [111] but almost absent for mannose. In the case of starch [115], this peak relates to COH bending and CH_2 bending. The latter author also discussed the occurrence of peaks for starch, and some vibrational modes might correspond to peaks seen at 1262.5, 1379 and 1463 cm^{-1}; for starch, Kizil [115] reports CH_2OH vibrational modes in the 1260-1280 cm^{-1} region, then CH_2 scissoring, CH and COH deformations at 1382 cm^{-1} and finally CH_2 bending at 1460 cm^{-1}. We can also report that a peak for glucose [111] located at 1260 cm^{-1} relates to CH_2 and COH deformations, whereas another peak at 1316 cm^{-1} relates to C1H deformation; the latter vibrational mode could explain the presence of the peak located at 1323 cm^{-1}.

To summarize, we believe that the most marked difference between GG and LBG is to be found in the anomeric region of their spectra, even though other less pronounced differences are also detectable by the Raman technique. Aided by this preliminary work on reference spectra, we will now consider the effect of different parameters on the appearance of our data.

6.3.3 Effect of sample form on the acquired Raman spectra

The reason for systematically compacting samples prior to testing them was, principally, as a mean of ensuring better reproducibility and maximizing signal output. Thus, we decided to check whether this parameter has only the effect we hoped for, thereby ruling out artefacts that might originate from this specific sample preparation method. Consequently, fig.6.9 was produced to compare the previous spectrum of GG

with one acquired from an equivalent, but non-compacted sample (designated as "in bulk" in fig.6.9).

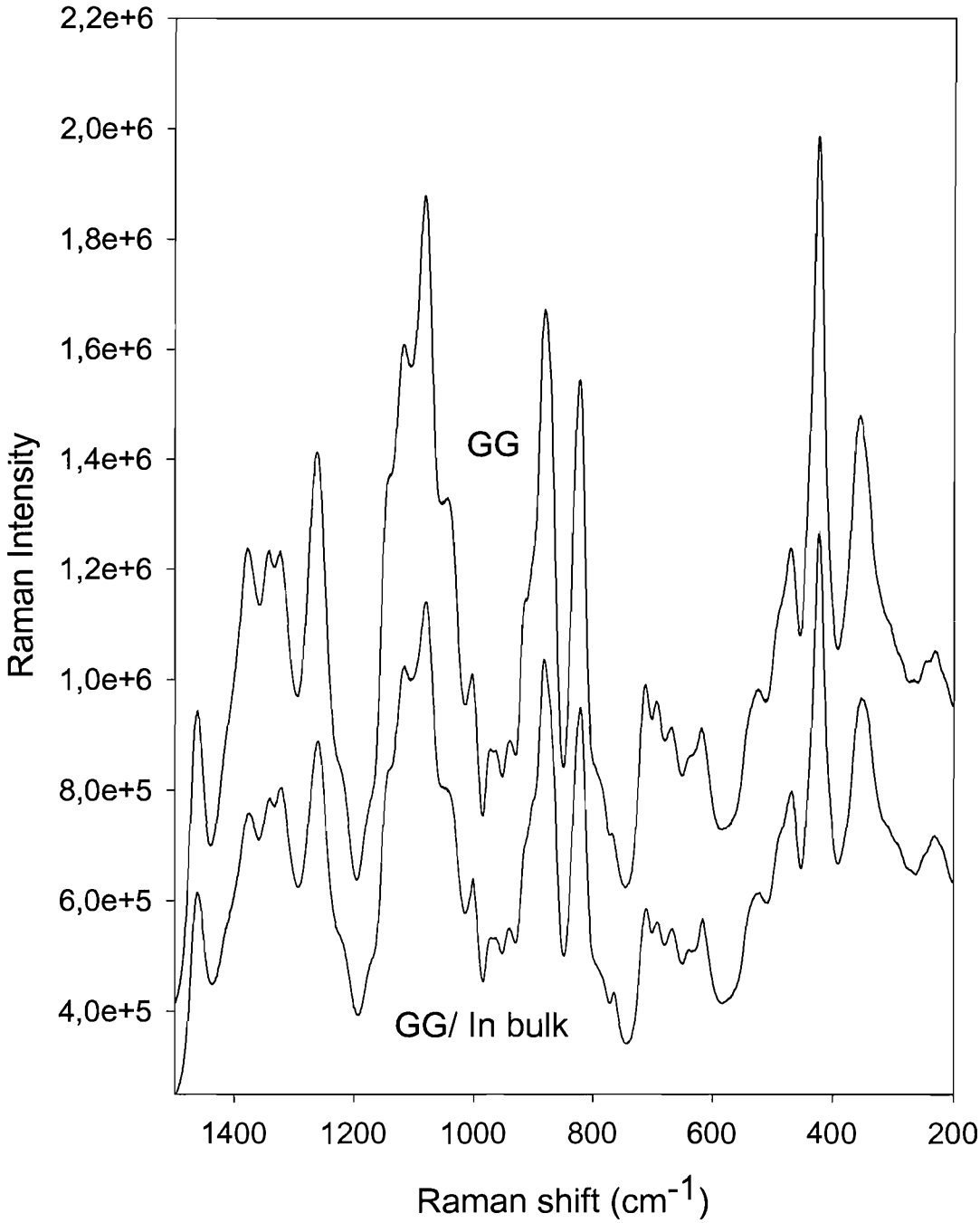

Figure 6.9: Comparison of Raman spectra for compressed and uncompressed GG powder samples.

From the above data, we can conclude that both spectra contain equivalent features, but with a global offset in Raman intensity, such that peak intensities are more prominent in the case of the compacted sample. However, some differences in relative

intensities do exist for peaks situated in the 500-750 cm^{-1} and 1200-1500 cm^{-1} regions. For example, the three narrow peaks located at 1323.5, 1341.5 and 1379 cm^{-1} exhibit comparable intensities in the compacted guar sample; this is not the case for their counterparts seen in the case of the "in bulk" GG spectrum. A similar variation is also detectable for the four main peaks found in the endocyclic region. We propose, therefore, that there could be an additional effect of pressure on the solid-state properties of our materials which, in some way, alters the relative intensity of some vibrational bands. To sum up, we demonstrate that sample compaction increases the detected intensity for the ensemble of peaks present in a spectrum; by this, we mean the difference in Raman intensity between a peak's maximum and the corresponding background intensity. However, there may be a slight superimposed molecular effect attributable to the initial compaction procedure, which may affect some vibrational modes more than others. Whether this effect genuinely relates to compaction or not, it nevertheless reinforces the general point that we cannot neglect factors linked to sample preparation when considering small differences between Raman spectra.

6.3.4 Ageing effects and Raman spectra

Unlike during FTIR investigations, we did not examine a complete series of samples as a function of ageing time. This is partly due to the fact that the Raman technique allows data to be acquired from a broader range of sample types and, hence, we were not restricted to using thin films obtained from soluble guar fractions. It is also linked to the fact that we expected to see variations in another part of the Raman spectrum which will be presented later on. Here, we decided to explore the effects of ageing by comparing spectra acquired using (G90/O_2/24W) and (G90/N_2/24W) samples. Fig.6.10 compares these two data sets, from which it is evident that both Raman spectra are extremely similar; they both contain the same basic features and both spectra are also similar to our reference spectrum for guar (see fig.6.8); the distribution and relative amplitude for the peaks situated in the anomeric region are entirely analogous to that of our reference sample. What seems to differentiate our aged samples from unaged guar though, is the background intensity which decreases with increasing Raman shift. Also, the overall Raman intensity for the (G90/O_2/24W) sample is higher than that of the (G90/N_2/24W). However, we think that this feature might not be exclusively related to ageing, since reference spectra for guar and locust bean also exhibit a strong offset in Raman intensity. More importantly, the intensity of some peaks appear

augmented, while others are diminished relatively to other peaks contained in the same region of the spectrum. If we consider peaks found in the exocyclic region, for instance, it is evident that the three peaks at 668.5, 693.5 and 711.5 cm^{-1} display intensities lower than that of the peak at 617.5 cm^{-1}. In this respect, the apparent distribution in peak amplitudes resembles that for LBG more than GG. To explain this behaviour, we propose that the latter is mainly due to the gradient in background intensity, which tends to offset these peaks to different degrees.

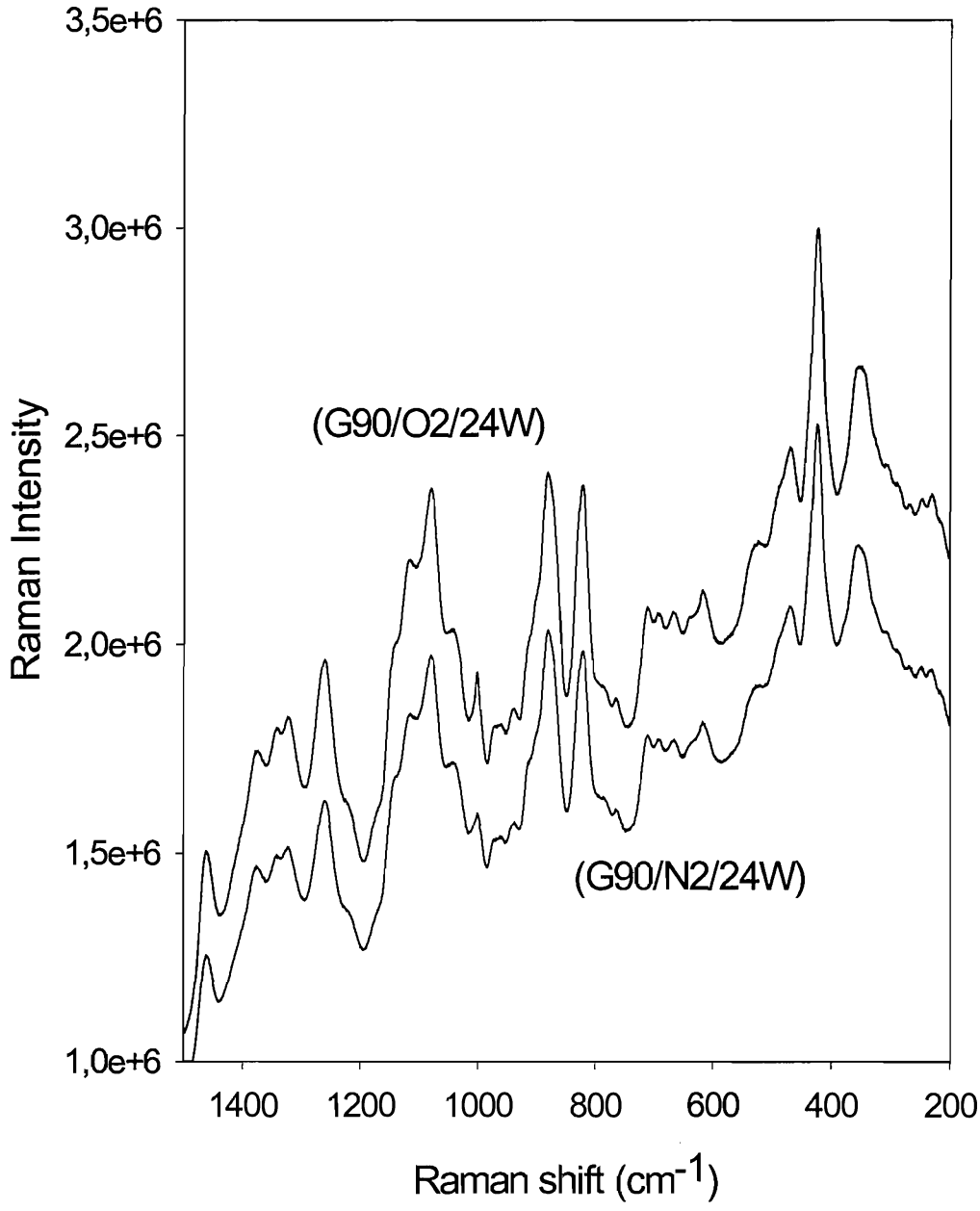

Figure 6.10: Comparison of spectra obtained from (G90/O_2/24W) and (G90/N_2/24W) samples.

To follow the effect of ageing even further, we also attempted to use the ($G150/O_2/0.5W$), sample which was previously employed for FTIR study. Unfortunately, this sample was so degraded that no information could be obtained from it. Specifically, we had to reduce individual acquisition times so that the CCD detector did not saturate; furthermore, even prolonged acquisition times, (i.e. 3 days of continuous testing) only revealed a fluorescent background with absolutely no superimposed remnants of the characteristic Raman bands of guar.

6.3.5 Effect of sample type on the resultant Raman spectra

We also wanted to investigate the effect of sample type on the acquired Raman spectra; by this we specifically refer to guar's soluble and insoluble fractions. Consequently, we first acquired two Raman spectra from soluble fractions of GG and LBG[18]; the resultant spectra are respectively presented in fig.6.11a and fig.6.11b. If we first consider fig.6.11a, we can see that the spectrum does not exactly match the reference shown in fig.6.8. It differs from the latter in that the background intensity is inclined, as in our former figure. Therefore care must be taken when ascribing apparent spectral changes to ageing processes. Since, as in the case of data acquired from aged samples, a differential shift in Raman intensity might explain apparent alterations in relative peaks amplitudes. However, variations in background intensity cannot explain the amplitude of the 1003 cm^{-1} peak which differentiates itself from the surrounding peaks. According to the above literature review, this peak could relate to a vibrational mode for mannose, or bonds linking adjacent rings; however, such an isolated change in peak intensity in the fingerprint region appears rather non-standard in comparison to the ensemble of our spectral data. Fig.6.11b contains the spectrum of the solubilized fraction of LBG; this spectrum differs significantly from the previous one, in the sense that it exhibits a closer appearance than that seen for the spectrum of LBG shown in fig.6.8. The background intensity remains horizontal in this case, and this permits a more direct comparison between the present spectrum and the reference spectrum of LBG. Specifically, we note that some peaks located in the 1200-1500 cm^{-1} region are truncated, whereas the peak located at 1379 cm^{-1} certainly exhibits a high amplitude;

[18] Soluble samples were prepared in a similar manner to those used for FTIR spectroscopy. Thin films were then folded and compacted using the same conditions as for powdery samples.

this apparent truncation concerns the peaks located at 1323.5 and 1341.5 cm^{-1}. We can speculate that this behaviour may originate from the sample preparation route, which necessitated boiling the initial LBG solution.

Finally, we acquired a spectrum from an insoluble residue of guar. Once more, we observe that the features that make up fig.6.12 are the same as those seen in the reference spectrum shown for GG in fig.6.8. Yet, the spectrum's overall intensity is far higher than that of either spectra of the reference or GG's soluble component. However, it is interesting to note that if we were simply to add the spectra for the soluble and insoluble fractions of guar (fig.6.11a and fig.6.12), we would not reconstruct the GG reference spectrum. Once more, we can propose that some spectral variations might be related to structural and conformational differences that occur when guar is initially hydrated. We know, for instance, that a fraction of galactose groups adopts open forms under aqueous conditions; thus, we suppose the kinetics of solvent evaporation might play a role in the eventual conformation of the macromolecules.

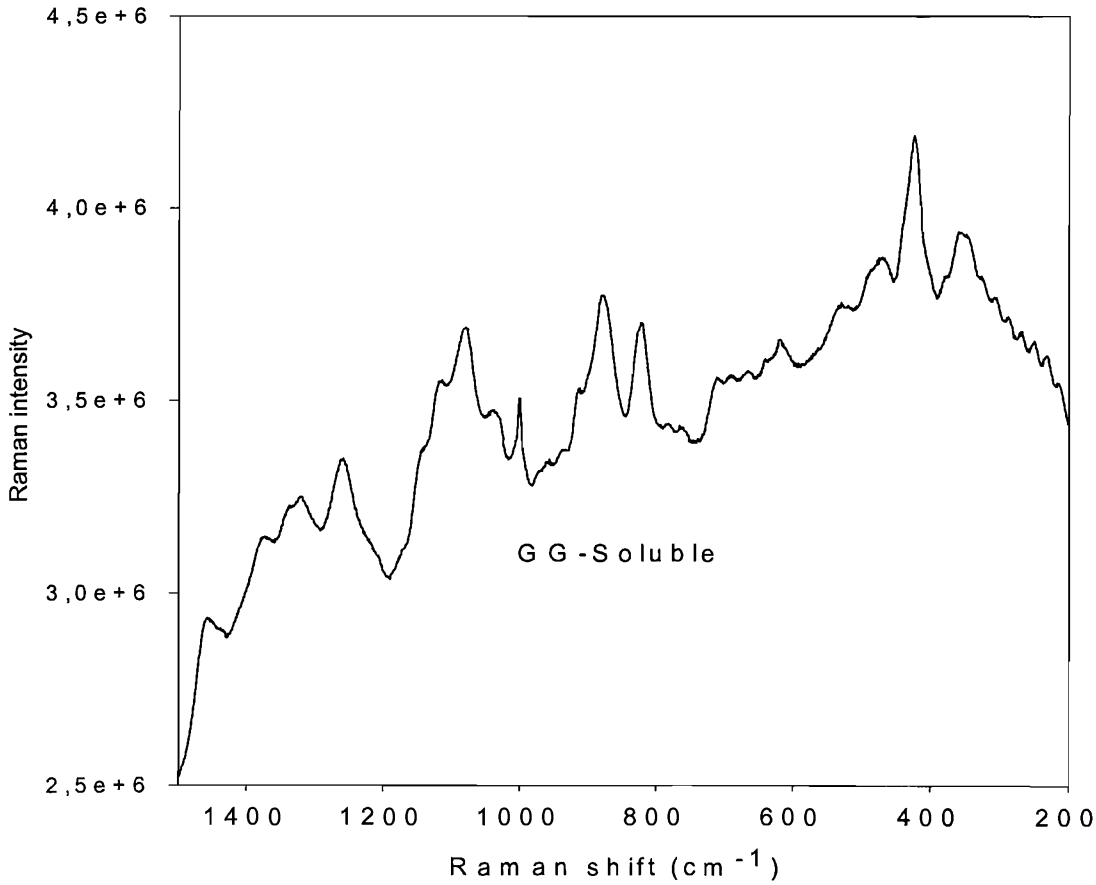

Figure 6.11a: Raman spectrum obtained from a dry, soluble fraction of GG.

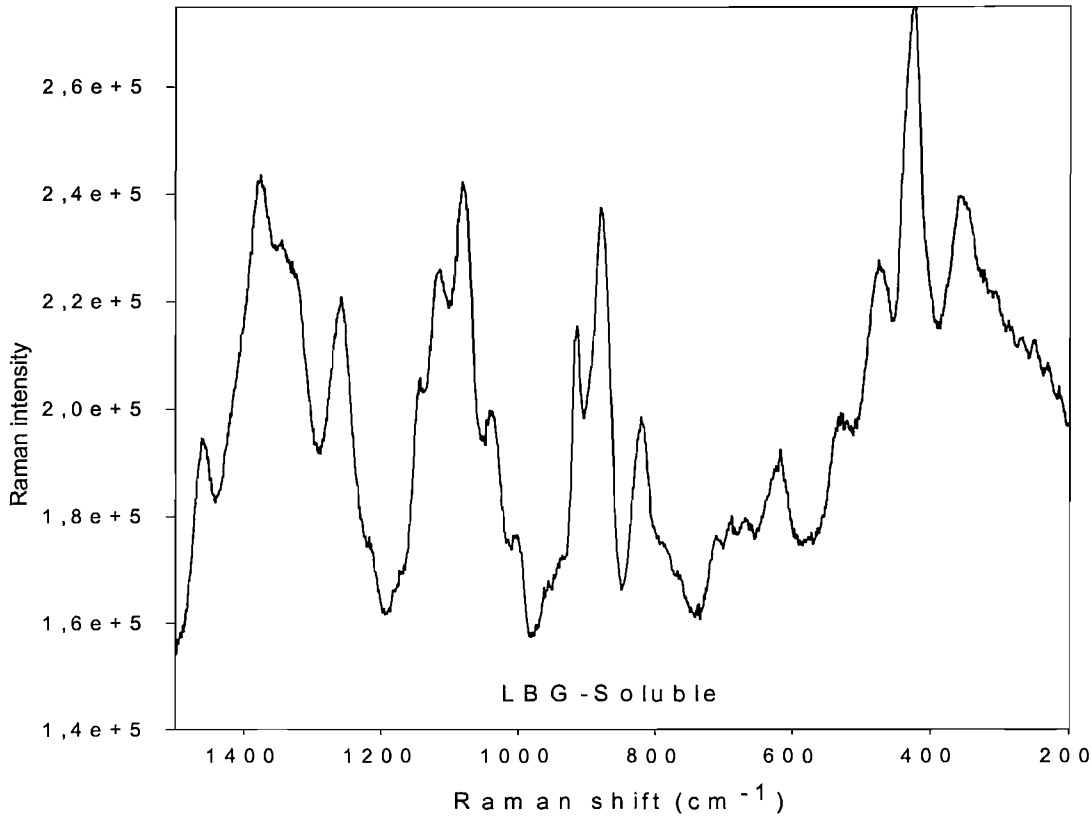

Figure 6.11b: Raman spectrum obtained from a dry, soluble fraction of LBG.

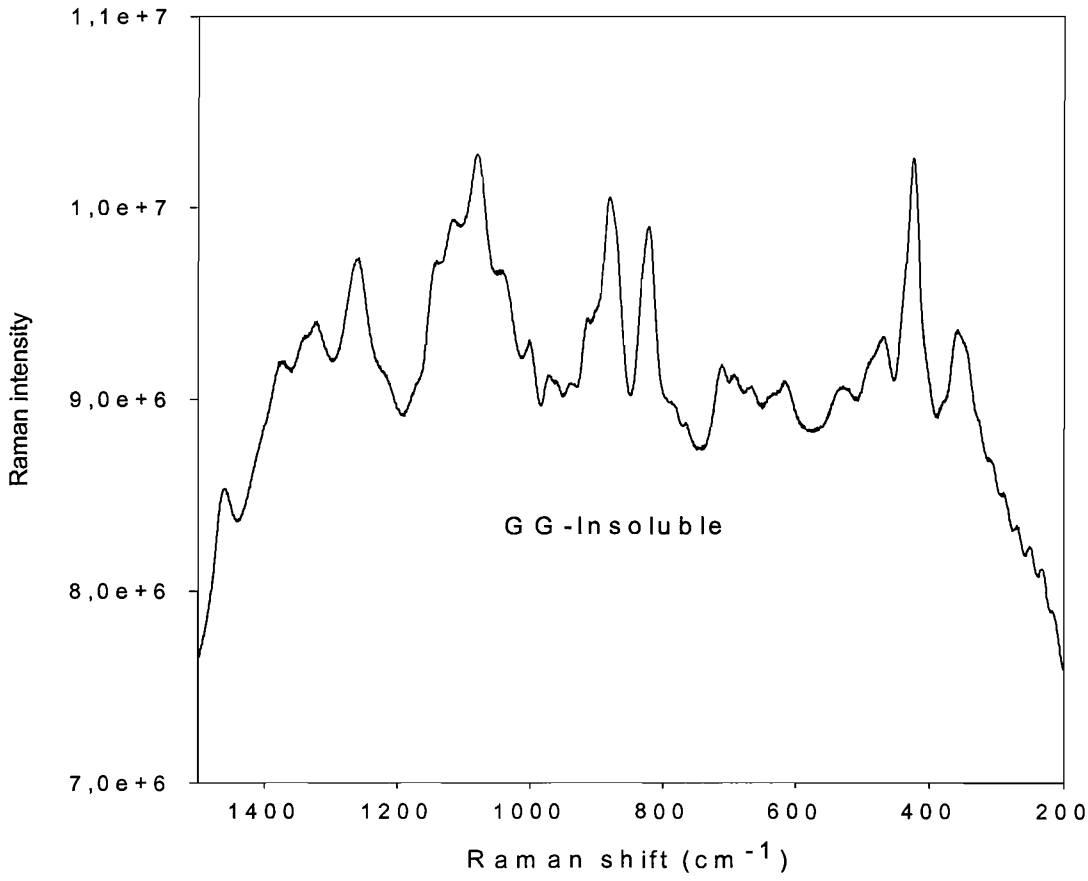

Figure 6.12: Raman spectrum obtained from an insoluble, GG residue.

6.3.6 The 2900 cm^{-1} Raman shift region, a possible indication of molar mass reduction

At the beginning of this section, we deliberately restricted ourselves to detailing the features present in the 200-1500 cm^{-1} Raman shift region. By doing so, we ignored the presence of a peak located at 2900 cm^{-1}, thereby markedly reducing acquisition times. Subsequently, we decided to dedicate some time to the study of this particular peak, principally, because of the work carried out by Zbankhov et al. [118] concerning the Raman spectra of dextran and pullulan. By studying the Raman response of monodisperse[19] samples, these workers related the magnitude of the 2900 cm^{-1} peak to the molar mass of their samples[20]. Hence, we were particularly interested in examining variations in this peak, to see whether it is possible to correlate spectral data to the molar mass decay predicted by viscometry. Our principal problems were then mainly linked to selecting the most appropriate series of samples and adopting a coherent methodology to evaluate variations in peak amplitudes as a function of ageing. Given the possibilities offered by the Raman spectrometer for testing different sample types, we particularly concentrated our efforts on the ($G90/O_2$) series of samples. The tested samples were either derived from unrefined, compacted guar powder or from thin films cast from their corresponding soluble fractions. For the following series of measurements, acquisition times were systematically reduced so that individual data sets could be obtained rapidly, typically after a few minutes.

6.3.6.1 Evaluations of Raman intensities for powder samples

Fig.6.13a contains an illustrative set of raw data obtained from a series of powder samples; the latter figure shows how the relative intensity for 2900 cm^{-1} peak changes with ageing time. However, we must emphasise, that while fig.6.13a is coherent, this kind of data appeared irreproducible. To illustrate this point, fig.6.13b contains numerical data which show the variation in maximum Raman intensity as a function of ageing time. To create this, we simply plotted the maximum peak intensity as a function of ageing time; the latter contains data from two sets of samples obtained

[19] Truly monodisperse samples are required for medical sciences to meet literally stringent when employed as blood's plasma substituents.

[20] For starches, this peak relates to CH stretching [116].

under equivalent testing conditions[21]. We believe this figure demonstrates well that data acquired from what we considered, a priori, as equivalent samples, do not provide coinciding spectral intensities. We then attempted to resolve this discrepancy by eliminating offset effects; to do this, we simply subtracted the estimated background intensity from the maximum peak value. To do this, we generated straight baselines by joining the flat, external tails surrounding the main peak. We then estimated the difference in Raman counts between each peak maximum and the point vertically below it on the baseline. We termed the resultant datum the relative peak amplitude, since it provides a systematic correction to the maximum Raman intensity by subtracting a corresponding value for background intensity. Thus, fig.6.13c displays the values for the relative peak amplitude as a function of ageing time. Although this procedure did not fully correct the data, it did, with the exception of the unaged specimen indicated by the open circle, produce some improvement. Finally, we derived numerical values for the peak areas; we integrated surfaces above the background, and normalized the resulting figures, dividing them by the value obtained for the unaged specimen. Fig.6.13d contains the processed results; the latter figure shows that this method did not alter the ordering for the first set of points (black dots), still it shows a drastic effect on the second set of points.

Despite our different approaches, the methods developed above fail to rearrange our data in a systematic manner. The samples tested here are raw powder-based ones, which mean they contain potentially both soluble and insoluble fractions of the material. In view of this, we reiterated similar tests with thin films derived from the soluble part of our materials.

[21] We generally repeated such runs using the same samples, but since we did not specifically target the same points, we consider that this is equivalent to testing another set of samples.

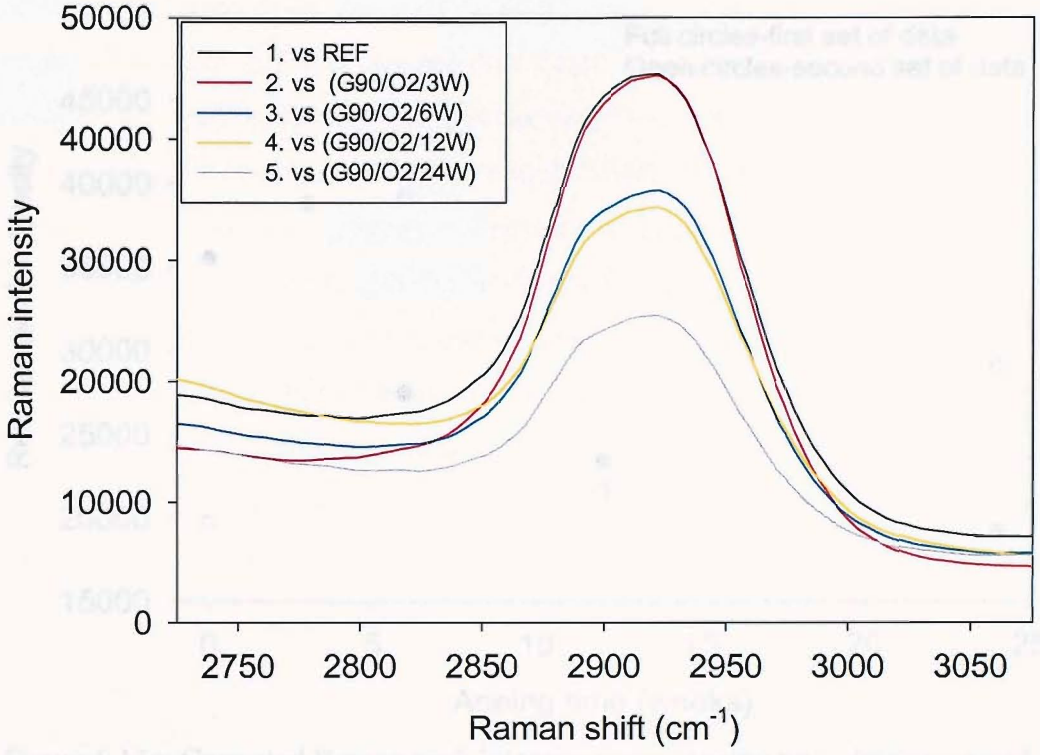

Figure 6.13a: Set of centred Raman acquisition at 2900 cm^{-1} obtained for the ($G90/O_2$) series of samples.

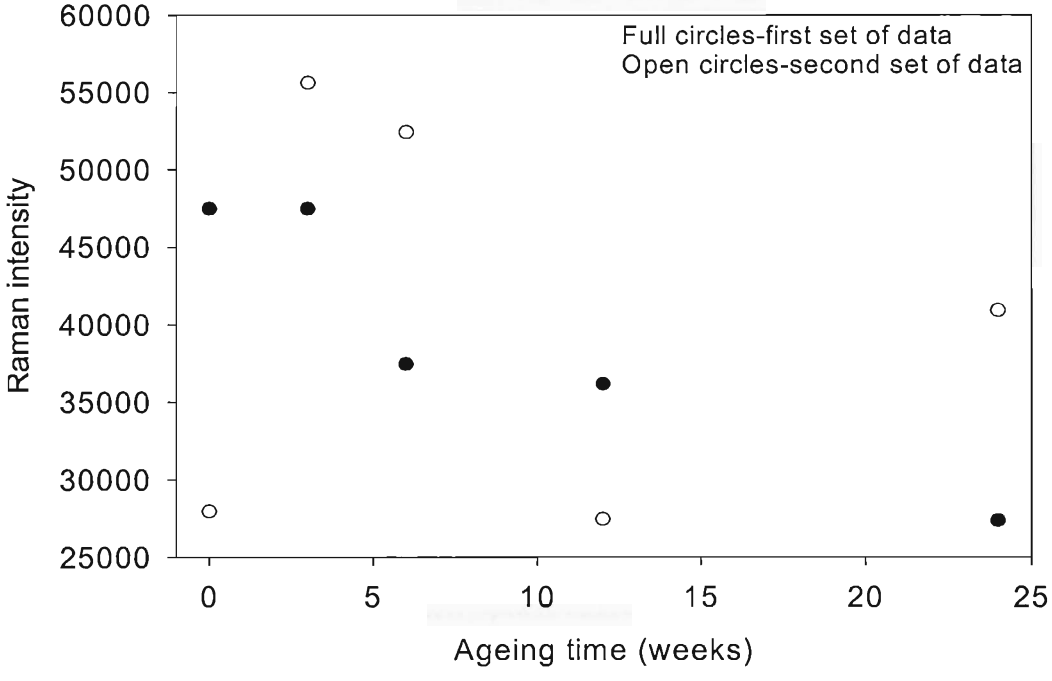

Figure 6.13b: Raman peak intensity versus ageing time-data processed from fig.6.13a.

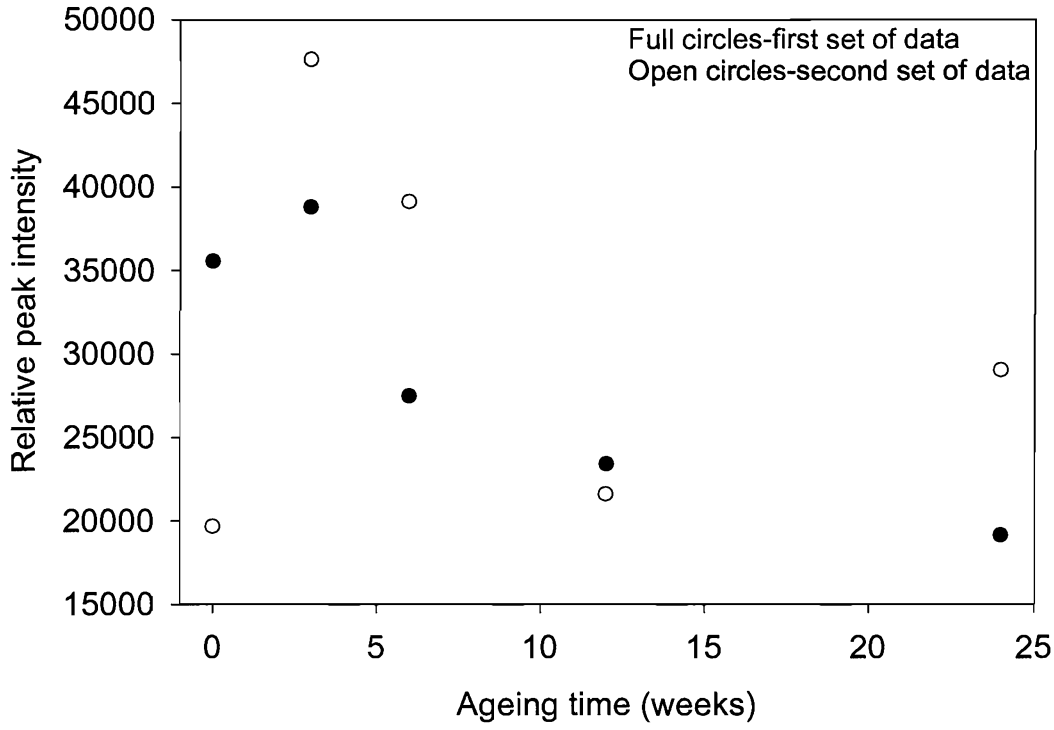

Figure 6.13c: Corrected Raman peak intensity versus ageing time-data processed from fig.6.13a.

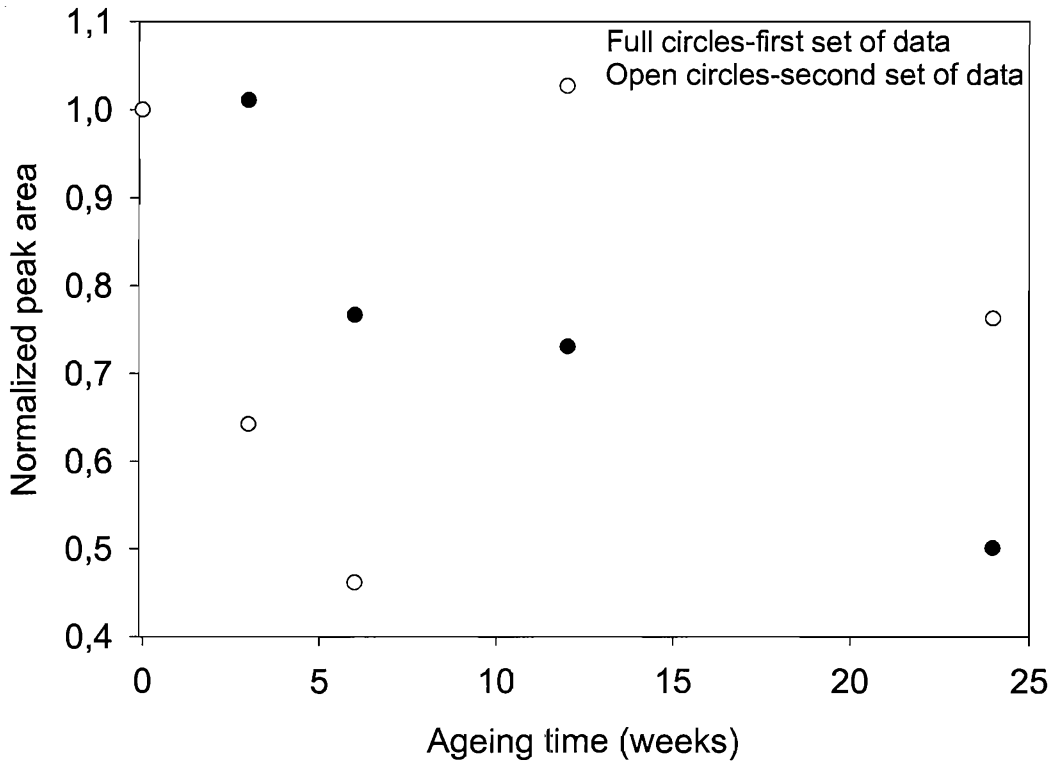

Figure 6.13d: Corrected Raman peak intensity versus ageing time-data processed from fig.6.13a.

6.3.6.2 Evaluations of Raman intensity for soluble fraction-based samples

Applying the same direct methods as above, we also attempted to derive quantitative information from series of soluble thin films[22]; the reason for testing this series of samples is linked to the fact that powder samples might not be ideal if the acquired spectral information pertains to sample molar mass. Fig.6.14a shows a set of raw data acquired in an equivalent manner to those shown in fig.6.13a, and two separate sets of data were also processed to give fig.6.14b and fig.6.14c. Again, the acquired data were not reproducible, see fig.6.14b, and the correction that takes background intensity into account does not rectify this behaviour, see fig.6.14c. From fig.6.14a, we can tell that the integration of peak intensities would not alter the ordering of data points constituted by black dots in the present series of figures; in view of this, it was not necessary to generate any supplementary plot.

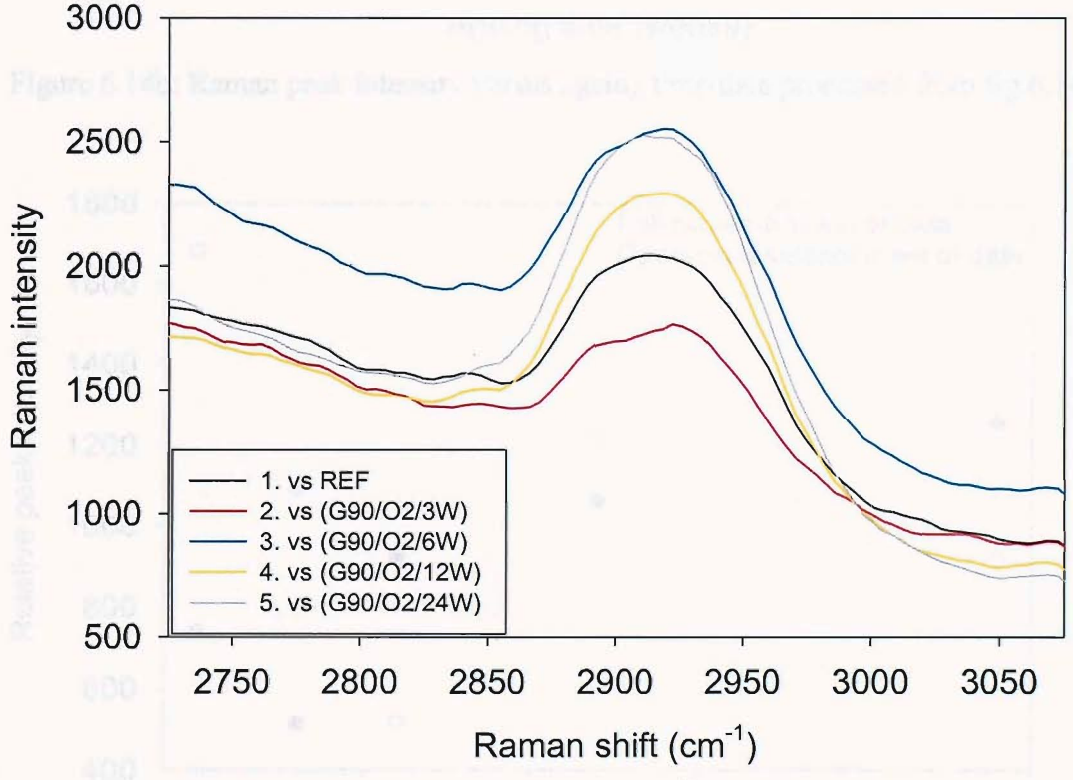

Figure 6.14a: Centred Raman acquisition at 2900 cm^{-1} obtained for the ($G90/O_2$) series of samples (soluble fractions).

[22] The latter were folded and compacted like powder samples.

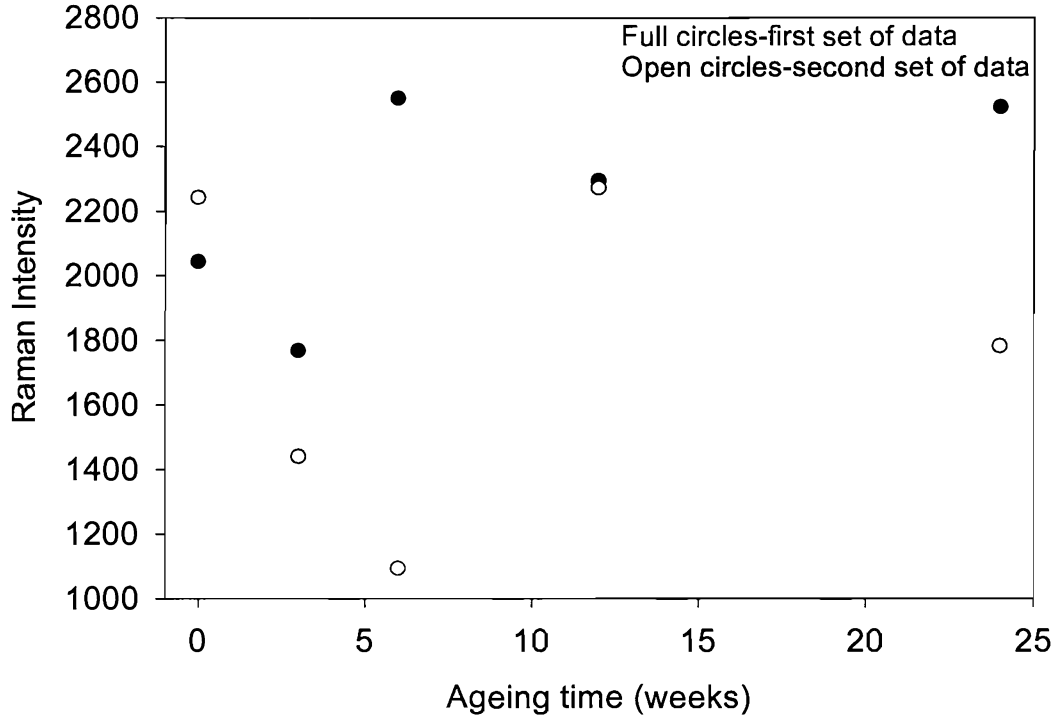

Figure 6.14b: Raman peak intensity versus ageing time-data processed from fig.6.14a.

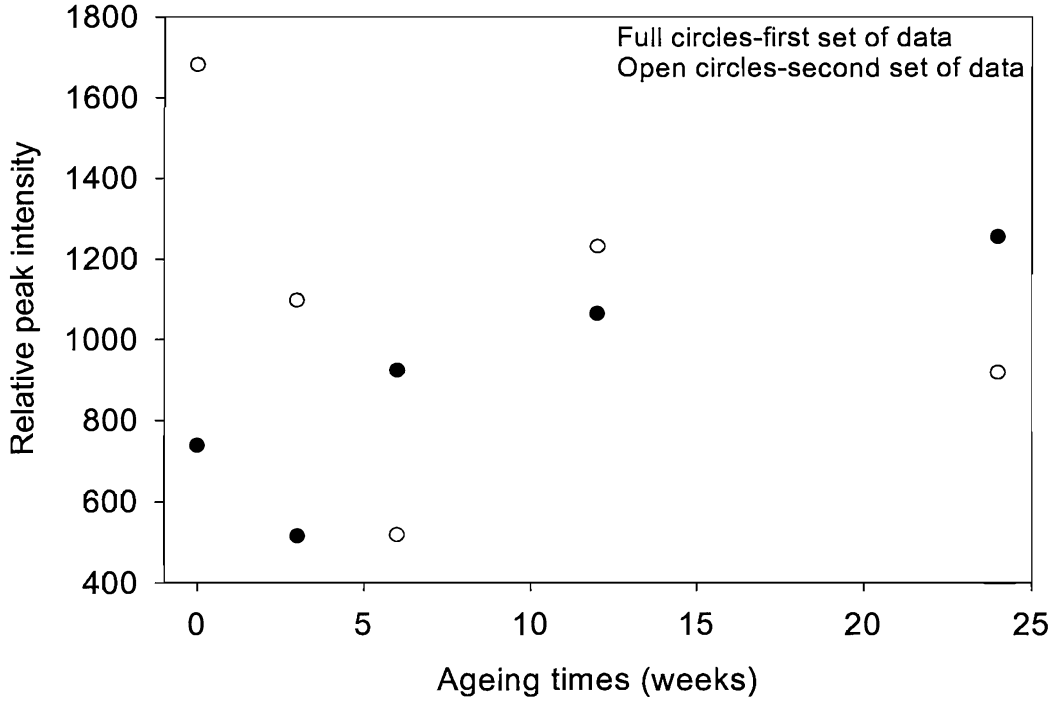

Figure 6.14c: Corrected Raman peak intensity versus ageing time-data processed from fig.6.14a.

6.4 Conclusions

During the course of this investigation, we explored the potential of both FTIR and Raman spectroscopy for the characterization of our different samples. We found that the FTIR technique is ineffective at differentiating guar and locust bean gum; however, this technique might be well suited to the detection of unsaturated bonds associated with the formation of carbonyl groups during ageing. A look back at fig.1.6 shows that carbonyl groups can either form between mannose groups as a result of depolymerisation processes, or between galactose groups as a result of the extraction of the latter groups from the mannan chain. It is also appealing to see that we could clearly identify aged samples that Raman spectroscopy could not characterize. Thus, the FTIR technique seems particularly useful when samples can be produced in the form of thin films and the stability of its response renders the technique interesting as an identification tool. Obviously, sample preparation is a crucial aspect for both techniques; we specifically demonstrated that the diamond compression is of limited utility in the case of the present specimens. Conversely, Raman spectroscopy is much more versatile when it comes to sample form; spectral data can be acquired from any sample type. With this technique, we could easily see conformational differences between guar and locust bean, especially in the anomeric region of our spectra. We additionally highlighted other less significant changes, which may possibly be due to changes in solid-state properties; the issue of reviewing an ensemble of experimental parameters is rather intricate, and we think that the full understanding of Raman spectra proposed here involves much more detailed work than could be performed within this study. Finally, our diverse attempts to quantify a molar mass decay by normalizing the intensity for the 2900 cm^{-1} peak were not as straightforward as the literature would suggest. Although some general trends were detected, these were not unambiguous. The origin of this may be the polydispersity inherent in our samples, and even the careful selection of soluble samples did not give results of the form we hoped for.

Chapter 7

Water-binding properties of a synthetic superabsorbent polymer

7.1 Introduction

This section is derived from the use of a synthetic water-blocking material within a high-voltage cable, which provides a technological alternative to a biomaterial such as guar. In this respect, we wanted to investigate the hydrophilic behaviour of this system in a similar way to that used for GG. Although the mechanisms and testing methods relevant to this chapter are unlike those utilized for the latter material, we will nonetheless attempt to provide parallels between our two studies, by employing similar ageing conditions to those utilized for GG. However, unlike the latter, the nature of our synthetic material is not precisely known; therefore, this section also includes forensic elements, along with the ageing study of this material. To achieve our goal, preliminary tests were therefore performed to explore the material's nature. The work that followed consequently assumed that the material belongs to a specific category of charged colloids. Certain experiments could therefore be seen as forensic analysis, null hypothesis testing or material analysis. The initial sub-section introduces the qualitative results of our early analysis, whereas the following sub-sections introduce swelling and conductivity measurements for such systems. We conclude this chapter with a global analysis based on the ensemble of our results.

7.1.1 Clues concerning the material's nature

Preliminary tests were carried out to explore the nature of our water-trapping material. Its surprisingly fast swelling response, of the order of a minute, was originally observed by simply plunging pieces of water-blocking tape into water. The superabsorbent particles, which were supplied sandwiched between layers of backing fabrics, were seen to expand to macroscopic dimensions in a matter of seconds, before becoming detached from their backing and moving freely in the liquid. Swollen

spherical particles could be seen suspended in water, with just the naked eye. Consequently, we initially attempted to quantify swelling kinetics via optical microscopy, by recording the growth of a single particle, after removal from its backing tape. Unfortunately, the enlargement of an individual particle was such that it could not be easily followed, since its centre and edges could not reliably be visualized throughout the experiment; even using lowest magnification lenses, visualization of the swelling particle in its entirety during the whole process was not possible[1]. In spite of this difficulty, we attempted to modify the swelling kinetics by varying the temperature, prior to adding water to isolated dry particles. Regardless of the temperature, rapid swelling was still observed prior to the collapse of the swollen particle due to water evaporation. Once desiccated, the particles did not regain their original shape, but rather collapsed onto the supporting slide. The further addition of water onto the collapsed particles led to renewed swelling. The following conclusions could, therefore, be drawn from our preliminary tests:

- Given the apparent size of individual swelling particles, see section 1.2.4.2.1, and their fast swelling time, simple water diffusion does not appear to be the dominant mechanism (cf. guar's hydration kinetics [98,99], section 5.1.2).
- The swelling/collapse cycles imposed on individual particles lead to a radical change of shape, implying that capillary based swelling mechanisms are also unlikely to be at work.
- Observation of dilute aqueous suspensions of particles, (e.g. at concentrations of 10^{-3} g/g) showed that swollen particles tend to collapse after a few days spent at room temperature. The precipitation and shrinkage of initially swollen particles, added to their inability to swell once more, implied that some active substance required for swelling had diffused out of the particles.

In view of such clues, a methodical search in the literature was carried out by crosschecking and categorizing key material properties, according to the above conclusions. The form of behaviour that most closely matched that described above was found to correspond to insoluble, collapsing polyelectrolytic gels [119], which can be classified as being charged colloidal suspensions [107]. In such systems, swelling rates vary with preparation parameters, including polymerization process and

[1] Examination of particles such as that shown in fig.1.4 combined with observation of differential swelling, indicates that such particles are aggregates of smaller objects.

monomer composition [120]. Such polyelectrolytic substances are able to lose mobile counterions to the external solvent, when placed in a dilute state, thanks to ionic dissociation mechanisms. The energy required for dissociation is reduced in pure water, in comparison to air, since the force of attraction between associated ions is modified because of water's relative permittivity. The latter is 81 times lower in water [121] than it is in air[2]. Individual particles eventually appear as isolated charged networks, which exhibit an electrical double layer, or "atmosphere of counterions" [107]. The phenomenon of particle collapse can then be depicted according to theoretical models such as Kuhn's [122], which is based upon a combination of Flory's theory and electrostatic interactions. In essence, this model advocates the existence of three main conformational regimes, which are determined mostly by temperature. At elevated temperatures, electrostatic forces have a negligible influence and charged macromolecules are reported to behave similarly to their neutral equivalents. At intermediate temperatures, electrostatic repulsion between charges expands the molecular structure whereas, at even lower temperatures, a counterion condensation phenomenon occurs, which leads to chain contraction.

7.1.2 Foreword concerning our testing methods

A number of different factors influenced our choice of testing methods:

- In the context of this study, our primary interest in swelling stability concerns the conditions under which such a system would behave as a durable water-trapping layer in an operational high-voltage cable. As in the case of GG, accelerated ageing conditions were chosen to correspond to conditions similar to those in a power cable. Swelling measurements are the most direct tests to apply to a superabsorbent material.
- The lack of knowledge concerning the composition of our material led us to the subjacent idea that our tests could also disprove or reinforce the above

[2] The relative permittivity of a substance arises from alterations in its atoms and molecules. The negatively charged electrons and positively charged nucleus of each atom are shifted in opposite directions by a tiny amount, a fraction of the diameter of an atom. The atoms as a whole move slightly, as well. The effect of these movements is to reduce the electric field passing through the material. The value of the permittivity depends on the amount by which the charges can move. Water has a high permittivity, because charges are highly separated in its molecules, and the molecules can rotate, producing a large effect on the electric field. Source: Microsoft Encarta.

polyelectrolyte hypothesis. Hence, conductivity tests were envisaged as a way of exploring the electrolytic nature of our material.

7.2 Ageing and other effects on swelling

Obtaining estimates of the swelling ratio is common practice when it comes to quantifying the swelling behaviour of absorbent materials. Swelling methods are commonly based upon measuring the variation of sample weight when immersed in a certain type of solvent [120,123-128], sometimes as a function of time [120,124-126]. Swelling ratio is simply obtained via the following equation:

$$S = (W_s - W_d)/W_d \qquad \text{(eq.7.1)}$$

In eq.7.1, W_s and W_d respectively stand for the weight of swollen and dry material. Other absorbent systems exhibit a maximum swelling ratio which is not necessarily found at neutral pH [123,124]. In view of this, we explored the swelling response of our material under different conditions by testing it alternatively with a strong base and a strong acid. We then investigated the effect of ageing conditions on the swelling ratio of our material.

7.2.1 Effect of pH on the swelling ratio

Fig.7.1 was generated by measuring the maximum swelling ratio for unaged square pieces of absorbent material at different values of pH; the materials were tested by using solutions of either NaOH or HCl. Apart from the additional data point located at neutral pH (the square point in fig.7.1), which was obtained by a method described in the following section, all the values for the swelling ratio were obtained as follows. A syringe was used to hydrate the sample plus backing fabric and the total number of droplets required for it to become entirely swollen[3] was counted. Thus, each point placed on the graph originates from one measurement carried out on an unaged sample; the corresponding error bar was computed from the value for the standard error obtained by studying droplet reproducibility (see Appendix VII-1); in essence, we considered that doubling the number of droplets increases the error bars by a factor of 2.

[3] An average of 200 droplets was required to swell each sample. Visual clues, such as the disappearance of individual boundaries between swollen particles added to excess solvent escape, were taken to indicate the stage at which particles were fully swollen.

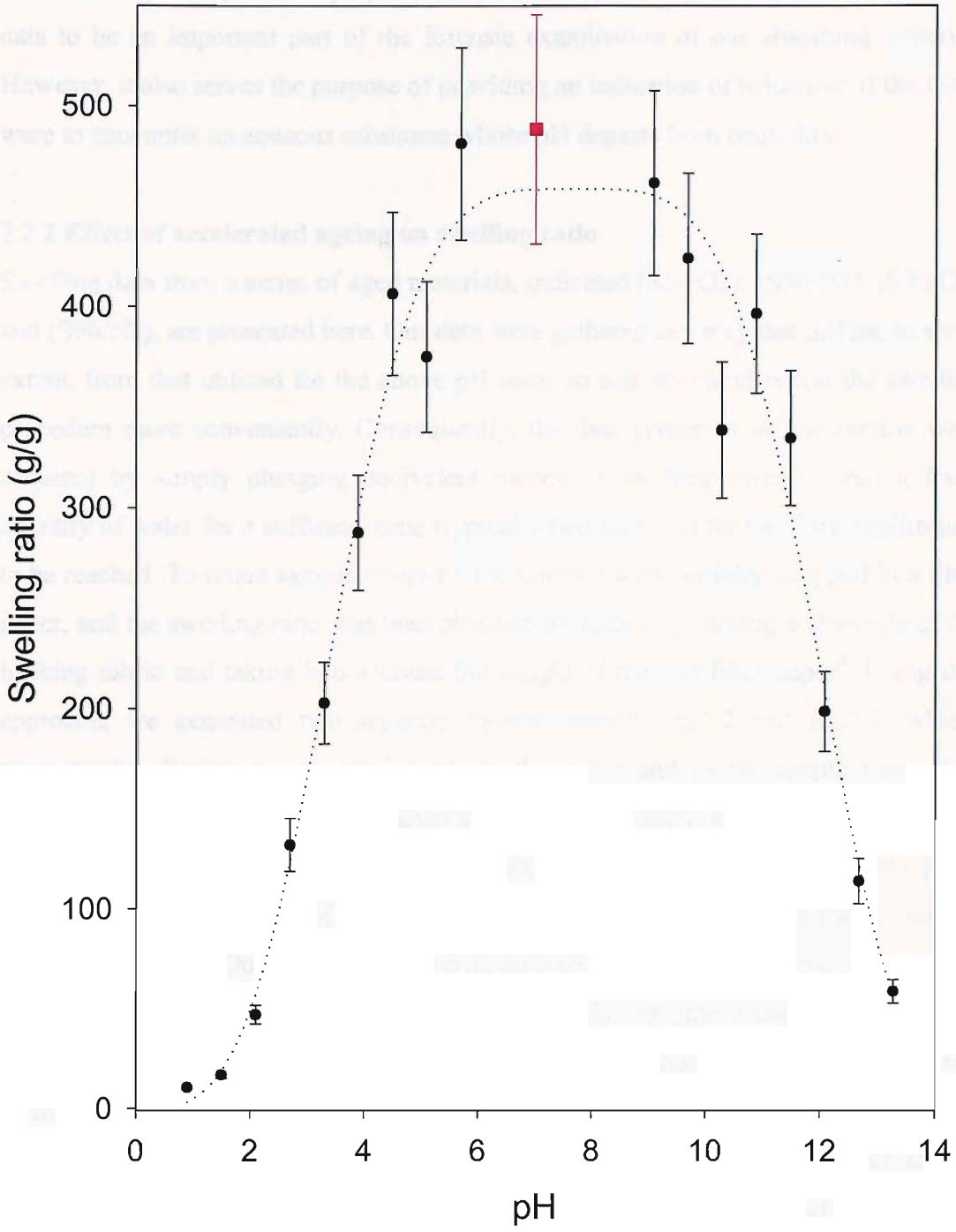

Figure 7.1: Swelling ratio profile for the superabsorbent material over a complete range of pH values.

Fig.7.1 clearly shows that the highest swelling ratios for our material are to be found in the vicinity of neutral pH, and the overall distribution of the data appears symmetric around this point. In addition, the data points placed on fig.7.1 were fitted to a Gaussian model, to highlight the bell-shaped form of swelling ratio's pH dependence.

In view of the symmetry of our results, it would appear that our superabsorbent material is not likely to be a polyacid and, therefore, we consider this particular set of data to be an important part of the forensic examination of our absorbing material. However, it also serves the purpose of providing an indication of behaviour if the latter were to encounter an aqueous substance whose pH departs from neutrality.

7.2.2 Effect of accelerated ageing on swelling ratio

Swelling data from a series of aged materials, indicated (S50/O2), (S50/N2), (S90/O2) and (S90/N2), are presented here. Our data were gathered in a way that differs, to some extent, from that utilized for the above pH tests, so that we could repeat the swelling procedure more conveniently. Consequently, the data presented in this section were acquired by simply plunging equivalent pieces of swelling material into a fixed quantity of water for a sufficient time (typically two minutes) for swelling equilibrium to be reached. To retain sample integrity, the samples were initially wrapped in a filter paper, and the swelling ratio was then obtained by removing, drying and weighing the backing fabric and taking into account the weight of the wet filter paper[4]. Using this approach, we generated two separate figures, namely fig.7.2 and fig.7.3, which, respectively, display results obtained from the (S50) and (S90) sample types. For clarity, we have separated data obtained at 50 and 90°C; additionally, dotted lines were added to both graphs to serve as guides for the eye. Each individual data point corresponds to an average of four values, while the error bars indicate the associated standard deviation. Our graphs include data derived from swelling experiments carried out at room temperature. In each set of data, we also include a common data point acquired from unaged samples, having repeated the procedure ten times, in an attempt to minimize uncertainty. It is this datum that was also reported in fig.7.1, both to demonstrate that our two swelling methods are consistent with one another and to complete the former data set. From fig.7.2 and fig.7.3, one can see the effects induced by thermal treatments on the swelling ratio. From both graphs, the swelling ratio appears to increase during the early stages of accelerated ageing, regardless of the ageing gas and temperature, and then stabilize. Globally, swelling ratios measured for samples aged at 90°C tend towards slightly higher values than those obtained at 50°C, although error bars in both data sets are significant.

[4] We also ruled out evaporation effects, which were found to be negligible given the duration of individual tests.

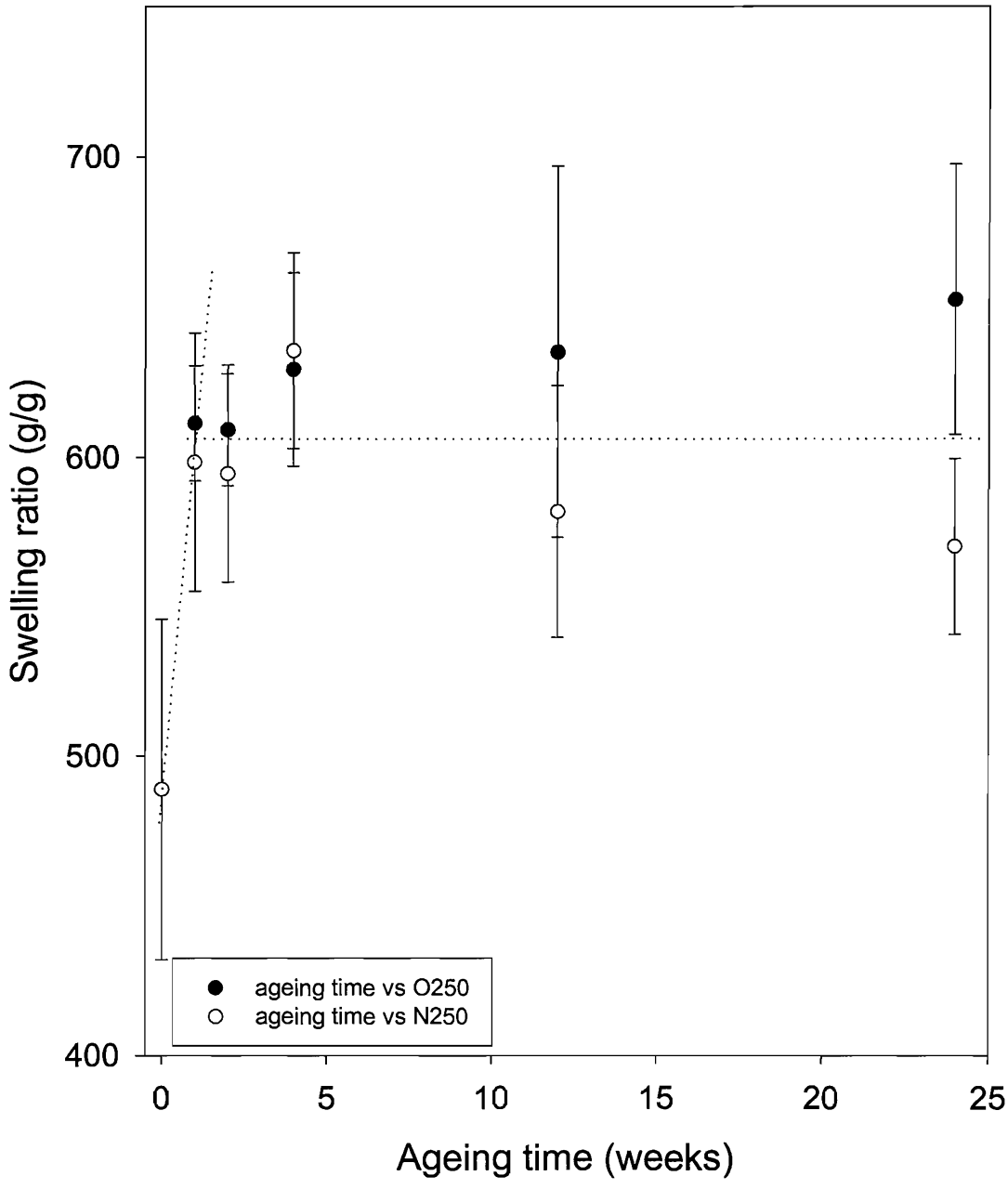

Figure 7.2: Swelling ratio obtained with DDW for aged (S50/O2) and (S50/N2) sample series.

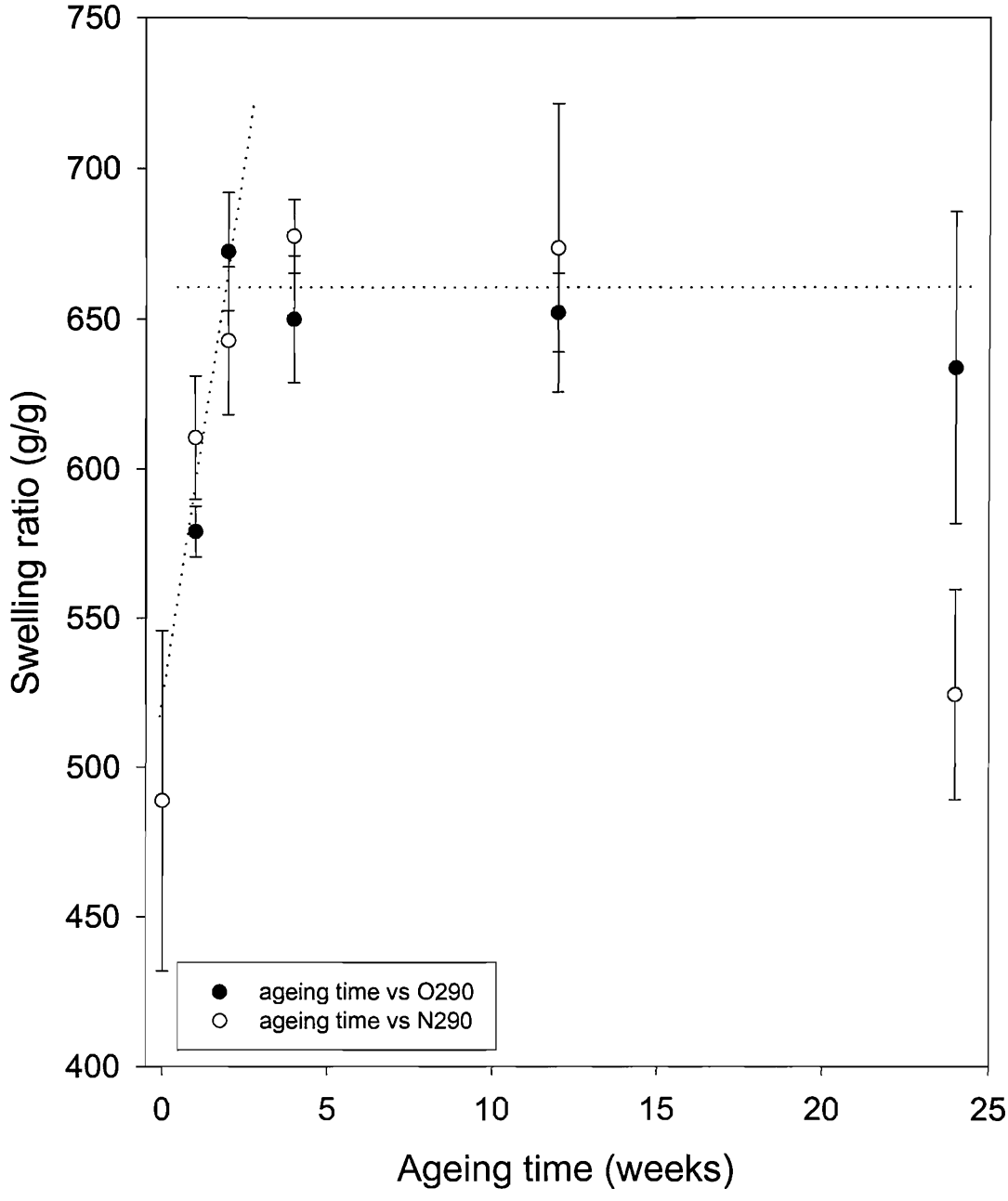

Figure 7.3: Swelling ratio obtained with DDW for aged (S90/O2) and (S90/N2) sample series.

From both figures, it appears tempting to conclude that ageing in air promotes swelling; this tendency is clearly visible in fig.7.2, but it is not a systematic trend in fig.7.3. Also, the behaviour of the ($G90/N_2/24W$) sample appears somewhat inconsistent. A closer examination of the individual measurements that were used to generate this point did not, however, revealed anything that appeared incongruous,

which could indicate a decrease in the swelling ratio on prolonged ageing[5]. We think, however, that this is unlikely given the behaviour of the ($G90/O_2$) sample series, and the swelling behaviour of the ($G90/O_2/24W$) sample remains marginal. Since polyelectrolytic absorbents are charged polymeric networks [127-130], we can speculate that the process involved in ageing is likely to be chain scission; this would certainly explain the observed increase in swelling ratio. However, this interpretation cannot be defended on the basis of these swelling results alone.

7.3 Conductivity testing

The irreversible collapse of individual superabsorbent particles in dilute suspension was visually observed in our preliminary experiments, as described above. Consequently, we undertook to explore the early stages of that process by performing conductivity measurements, since an increase in the value of the solvent conductivity as a function of time should occur if particle deswelling were indeed associated with counterions escaping from the sample. Although this idea appears simple, the electrical study of polyelectrolytic gels by Gong et al. [130] reveals a number of potential problems. These workers chose to devise their own testing equipment to ensure an optimal contact between the electrodes and their sample, demonstrating that contact surfaces and pressure are determining parameters in the testing of such materials. This also suggests that experimental conditions can significantly influence results. Aware of these authors' approach to evaluating conductivity for a polyelectrolyte system, we chose to adopt a different testing route. Our approach takes account of the granular nature of our sample and the experimental options offered by the fixed geometry of our testing cell. In the following sub-section, we first attempt to explain and deal with possible sources of uncertainty. Subsequent sections contain results derived by varying different testing parameters, such as sample ageing and testing temperature.

7.3.1 Calibration of the test cell

Prior to carrying out the more complex tests involving the hydration of our samples, it was necessary to devise a systematic way of rinsing our glassware and capacitor, so that we could evaluate the cleanliness of our testing system and begin different

[5] Limited quantities of material were originally subjected to the considered ageing conditions. Unfortunately, we did not have enough material to repeat our measurements for this data point.

experiments under identical conditions. Initial cleaning was performed once on the dismantled capacitor using acetone, in particular, to remove contaminants from the spacing silica balls. Routinely, the testing system was cleaned several successive times between measurements, by employing solely the system's solvent, namely DDW. Values for the capacitance were routinely acquired; such values were found to fall in the range of 30.8 to 30.9 pF, values that we initially related to a geometrical factor (see section 2.2.7.2.) termed cell constant. This value is subsequently used to extract the required sample parameters. In practice, values for the capacitance of the cell immersed in DDW were then found to fall between 2.2 and 2.5 nF, which correspond to a capacitance range of 27.16 to 30.86 pF in air. Conductivity levels of DDW were consistently found to lie in the range of 0.3 to 0.5 mSm^{-1}. Such values are far from ideal, since one would expect conductivity values of the order of $pS.m^{-1}$ from ultra-pure insulating liquids [131]. However, polar liquids are known for their propensity to become contaminated, e.g. migration of impurities come from the glassware itself [131]. The fact that the measured capacitances obtained with DDW fluctuate in spite of our care probably indicates that contamination takes place prior to starting our experiments. Nevertheless, it was reassuring to find that our calibration values for DDW were not varying randomly, and that conductivity values settled to a constant value after a short while, typically a few minutes[6]. When conductivity levels fell outside the expected range, cleaning was repeated, as required.

7.3.2 Effect of temperature on the conductivity of DDW

The first experiments carried out on dilute suspensions of superabsorbent particles seemed to indicate a strong, non-linear increase in conductivity level as a function of time, which did not correspond to anything previously encountered when using just pure DDW. We wanted to examine the effect of time and temperature on conductivity levels, but, more specifically, we wanted to dissociate these two effects. The reason for this is that we particularly wanted to explore the effect of temperature on the conductivity levels produced by a series of similar samples. To begin with, we therefore investigated the effect of temperature on the apparent conductivity of DDW, see fig.7.4. Evidently, the system requires a significant time to approach equilibrium,

[6] This is also true for the measured capacitance, albeit with a lower sensitiveness at the scale employed to perform measurements.

and, therefore, we had to wait for the system to stabilize in temperature in order to obtain a value for the system's conductivity. Fig.7.4 contains one plot (marked DDW), which shows that there is a small linear increase of conductivity with temperature for DDW; see also Table 7.1 for the corresponding determination coefficient. The other plots included in fig.7.4 represent data sets obtained from similar experiments, but now, in the presence of a superabsorbent sample. For these experiments, we devised a procedure to minimize the surface exchange between DDW and the presence of the superabsorbent material since, in this case, conductivity levels can vary faster than times required to stabilize the mixture being subjected to temperature increments. In this, an unaged sample was placed below the lowest plaque of our testing cell and literally pinched between the latter and the bottom of the glassware[7], prior to adding DDW. Using this approach, there was no obvious time-dependent drift in conductivity throughout the time interval required to accomplish the experiment. What we present in fig.7.4 are the temperature-dependent profiles of conductivity for that "pinched" sample, and equivalent measurements were repeated after different immersion times[8]. The latter are indicated in fig.7.4, and regression results are also reported in Table 7.1. From fig.7.4, we can see that a linear temperature-dependence of solvent conductivity systematically describes our different plots. In a day, we can also see that the conductivity has risen by more than one order of magnitude, relative to DDW alone; and there is also a significant increase in the gradient of our plots. For now, we are not concerned with the mechanism which makes all of our data sets linear; rather we are interested in the similarity between changes in solvent conductivity, with and without a sample in place. We believe fig.7.4 demonstrates that the exchange surface between swollen particles and the surrounding medium is a central factor, and that our experiments give credence to the idea that the increase in conductivity with time is due to ionic diffusion from the swollen particles into the surrounding solvent. We will directly address this issue in the next section, which deals more specifically with the relationship between conductivity variations and the initial concentration of particles placed in aqueous suspension.

[7] The spacing between the lowest electrode and the glassware's bottom roughly correspond to the thickness of a dry sample.

[8] Results seen in fig.7.4 were obtained from a unique sample.

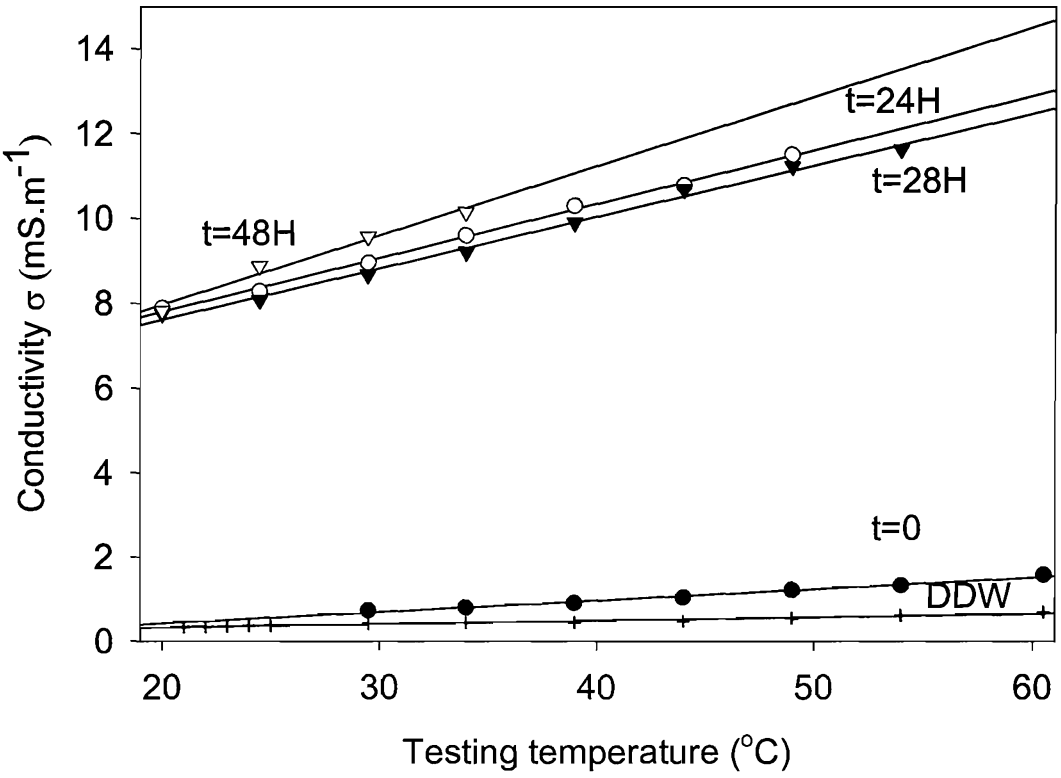

Figure 7.4: Variations of the conductivity of DDW and of a "pinched" sample of absorbent material as a function of temperature and immersion time.

Sample type	R^2
DDW	0,968
Pinched sample-0H	0,985
Pinched sample-24H	0,997
Pinched sample-28H	0,994
Pinched sample-48H	0,979

Table 7.1: Correlation data collected from plots that make up fig 7.4.

7.3.3 The effect of concentration on time-based conductivity measurements

From this section on, we prepared all our samples in a very specific way. Once calibration of the apparatus had been performed in both air and DDW, and enough time had elapsed to obtain stable readings, we immersed our sample in DDW and started to record the time. For temperature-based experiments, this preparation method had the advantage that the DDW was already at temperature, prior to immersing the sample in it. Once the sample had swollen, the electrode system was reintroduced.

Since our measurements were entirely manual, we gathered data points as rapidly as possible, consistent with the time constraints imposed by manually balancing the bridge. Consequently, individual measurements could only realistically be acquired every fifteen to thirty seconds, after about ninety seconds had elapsed. The sampling rate was then adjusted and reduced as time went on, and each experiment was systematically stopped after two hours.

Testing concentrations could easily be derived, since the dry weight of our sample and the starting quantity of DDW were both known. In this section, experiments are described in which the concentration of the swelling material is the main variable. Fig.7.5a contains data sets that were obtained for concentration levels ranging from 0.0033 to 0.104 grams of particles per gram of water (g/g); these particular experiments were all performed at 25°C. Fig.7.5a shows the relationships between concentration, conductivity and time. It demonstrates that the rate of change of conductivity varies with testing time, regardless of the concentration, at least in the concentration range covered here, which was determined by data sampling and sample preparation issues. Given the shape of our data, which we expect to be related to counterion diffusion in DDW, we decided to test the suitability of two mathematical functions as a means of describing our data sets. For the sake of simplicity, these will subsequently be referred to as Model I and Model II. Model I involves a single characteristic time, in combination with a linear component, whereas Model II contains two characteristic times.

$$\sigma = \sigma_o(1-\exp(-t/\tau)) + kt \qquad \text{(eq.7.2)}$$

$$\sigma = \sigma_1(1-\exp(-t/\tau_1)) + \sigma_2(1-\exp(-t/\tau_2)) \qquad \text{(eq.7.3)}$$

The reason for adopting this empirical mathematical procedure is to provide a means of comparing different families of data sets and, therefore, identifying the effect of concentration, temperature and sample ageing on the underlying physics. Evidently, before this can be done, it is necessary to decide which model is better.

Table 7.2 contains parameters obtained from these two models, as well as values for the standard error in the different parameters they contain. Table 7.2 also contains a parameter, which we have termed *MSR* (mean square residuals), which corresponds to the sum of the squares of the regression residuals, normalized using the number of degrees of freedom (n-n_o) conditioned by the model employed. Here, n and n_o respectively stand for the total number of data points acquired during a single

experiment, and the total number of independent variables found in each model. The *MSR* parameter is employed for variance analysis; in effect, it represents an alternative to the determination coefficient when it comes to comparing our two models. *MSR* values were manually computed by employing the residuals automatically provided by the Sigma Plot software.

$$MSR = (1/(n - n_0)) * \sum (residuals)^2 \qquad \text{(eq.7.4)}$$

From our data, it appears that Model II fully[9] converges only towards higher concentration values; otherwise this model does not give any reliable value for σ_2 and τ_2. Since convergence was not automatically achieved for all data sets, manual adjustments were made to minimize errors in the latter parameters, using an empirical trial and error method. Thus, values for σ_2 that were fixed manually[10] are reported in italics in Table 7.2. On the basis of their determination coefficient alone, it appears difficult to separate both models when our data are obtained at lower concentrations. *MSR* values are, however, consistently lower for Model I in this range of concentration. The values for the determination coefficient and the *MSR* indicate that Model II improves, relative to Model I, at higher concentrations, since the plots obtained at higher concentration depart more strongly from a linear-like behaviour at higher testing times. Still, the overall utility of the *MSR* values is greatly diminished by the fact that our data sets include a rather large number of data points, thus making for marginal differences between *MSR* values for the two models. This behaviour simply reflects the capability of a given model to reproduce the shape of our data. Thus, Model II is better at fitting data acquired at higher concentrations, since more pronounced deviation from a linear-like variation in conductivity appears as the concentration increases. Correlations between the various parameters that make up our model and sample concentration are presented graphically, from the data assembled in Table 7.2. Hence, although the point discussed above can be verified from fig.7.5a, it is more evident from fig.7.5b, which contains plots for both σ_o and σ_1. This figure demonstrates that the overall magnitude of these parameters generally increases in proportion to sample concentration, although this behaviour cannot be completely extended to Model II, since σ_1 deviates from linearity at higher

[9] By "fully", we mean automatically and completely.

[10] The manual adjustments to this parameter were chosen by looking at figures obtained from the fully converging data sets.

concentrations. Fig.7.5c shows the increase in the rate of change of conductivity at longer experimental times. From this figure, there appears to be a linear relationship between concentration and the rate of change of conductivity. The characteristic diffusion times, τ and τ_1, are shown graphically in fig.7.5d, where, it would appear that values for this parameter generally remain within a rather narrow range, although the data obtained at a concentration of 0.0033 g/g does seem rather small. In a sense, this behaviour was already predictable from fig.7.5a and, hence, we repeated this particular experiment once more. Still we obtained a similar result. Finally, we can discuss the existence of a secondary diffusion process quantified thanks to Model II. Fig.7.5e illustrates data obtained for τ_2; in view of our data points, the characteristic time for a secondary process is likely to equal or exceed the timescale of our experiments. However, given the magnitude of the error bars, it appears difficult to discuss its variations as a function of concentration. We will attempt to discuss the meaning of this term later on, especially since the two characteristic times for Model II could be strongly interdependent.

To summarize, conductivity levels do vary qualitatively with concentration, as we had anticipated and, provided that sample preparation allows the exchange surface to increase by a similar factor, our hypothesis for a conducting fraction of counterions diffusing out of swollen particles appear reinforced. The next section discusses the effect of temperature on similar conductivity measurements, since we wish to discuss the effect of thermal variations on the ensemble of parameters introduced above.

MODEL I				MODEL II			
(g/g)	Coefficient	Standard error	R^2/MSR	(g/g)	Coefficient	Standard error	R^2/MSR
0.0033				0.0033			
σ_o	0.0647	0.0012	0.990519	σ_1	0.0647	0.0022	0.986823
$1/\tau$	0.4167	0.0313	2.35E-05	$1/\tau_1$	0.4165	0.0378	2.39E-05
k	0.0013	0.0001		σ_2	*0.5*	*0.2098*	
				$1/\tau_2$	0.0029	0.0015	
0.0065				0.0065			
σ_o	0.1804	0.0027	0.995269	σ_1	0.1804	0.008	0.994616
$1/\tau$	0.1126	0.0038	3.13E-05	$1/\tau_1$	0.1126	0.0065	3.19E-05
k	0.0013	0.0001		σ_2	*0.778*	*1.061*	
				$1/\tau_2$	0.0018	0.0028	
0.013				0.013			
σ_o	0.2395	0.0042	0.99726	σ_1	0.2395	0.013	0.994519
$1/\tau$	0.1053	0.0038	7.17E-05	$1/\tau_1$	0.1053	0.0067	7.27E-05
k	0.0032	0.0001		σ_2	*1.000*	*0.5084*	
				$1/\tau_2$	0.0037	0.0026	
0.026				0.026			
σ_o	0.3297	0.0057	0.993851	σ_1	0.3027	0.0144	0.994255
$1/\tau$	0.1425	0.0062	2.13E-04	$1/\tau_1$	0.1576	0.0109	2.02E-04
k	0.0036	0.0001		σ_2	1.217	0.4404	
				$1/\tau_2$	0.0038	0.0018	
0.052				0.052			
σ_o	0.7761	0.0112	0.996967	σ_1	0.7317	0.0309	0.997104
$1/\tau$	0.1249	0.004	5.33E-04	$1/\tau_1$	0.1333	0.0074	5.17.5-04
k	0.0075	0.0002		σ_2	3.4505	1.7762	
				$1/\tau_2$	0.0026	0.0016	
0.104				0.104			
σ_o	1.4248	0.0401	0.992638	σ_1	0.9949	0.124	0.993675
$1/\tau$	0.0826	0.0044	3.64E-03	$1/\tau_1$	0.117	0.0154	3.18E-03
k	0.0104	0.0005		σ_2	2.1628	0.1517	
				$1/\tau_2$	0.0115	0.003	

Table 7.2: Regression data derived from Model I and Model II, relative to fig.7.5a.

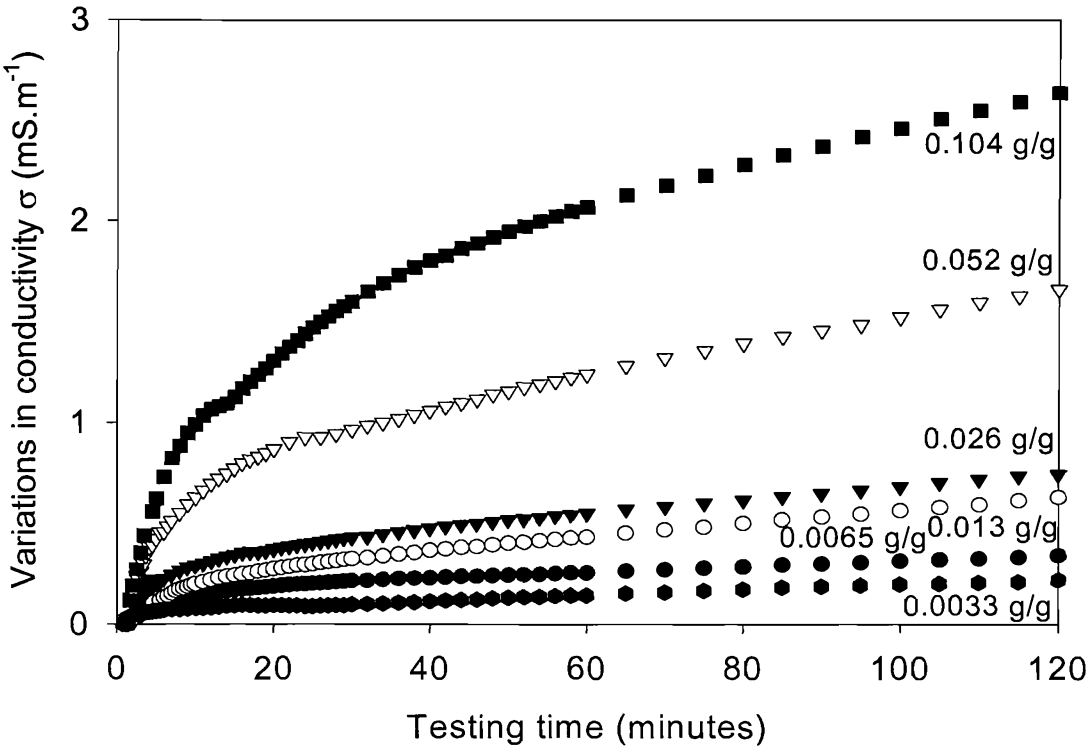

Fig.7.5a: Time and concentration variations in conductivity obtained for unaged samples. Concentration levels are reported on individual plots.

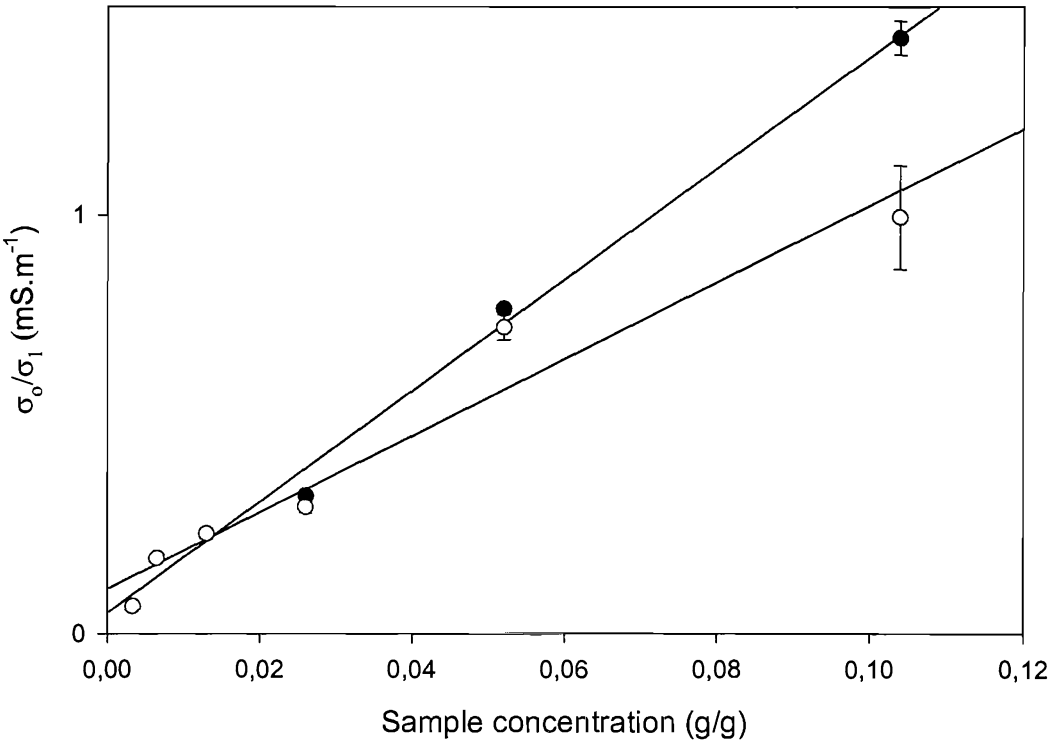

Figure 7.5b: Variations of σ_o or σ_1 with sample concentration. (Black dots represent data derived for Model I and coincide with data for Model II at low concentrations.)

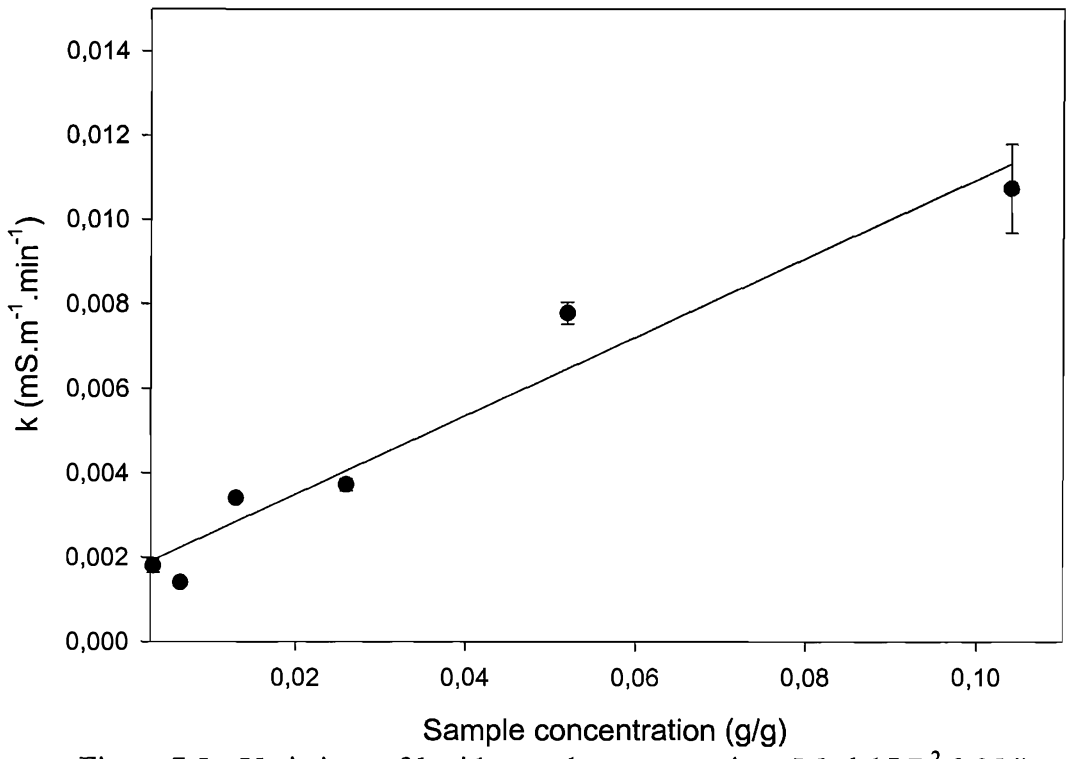

Figure 7.5c: Variations of k with sample concentration. (Model I-R^2:0.954)

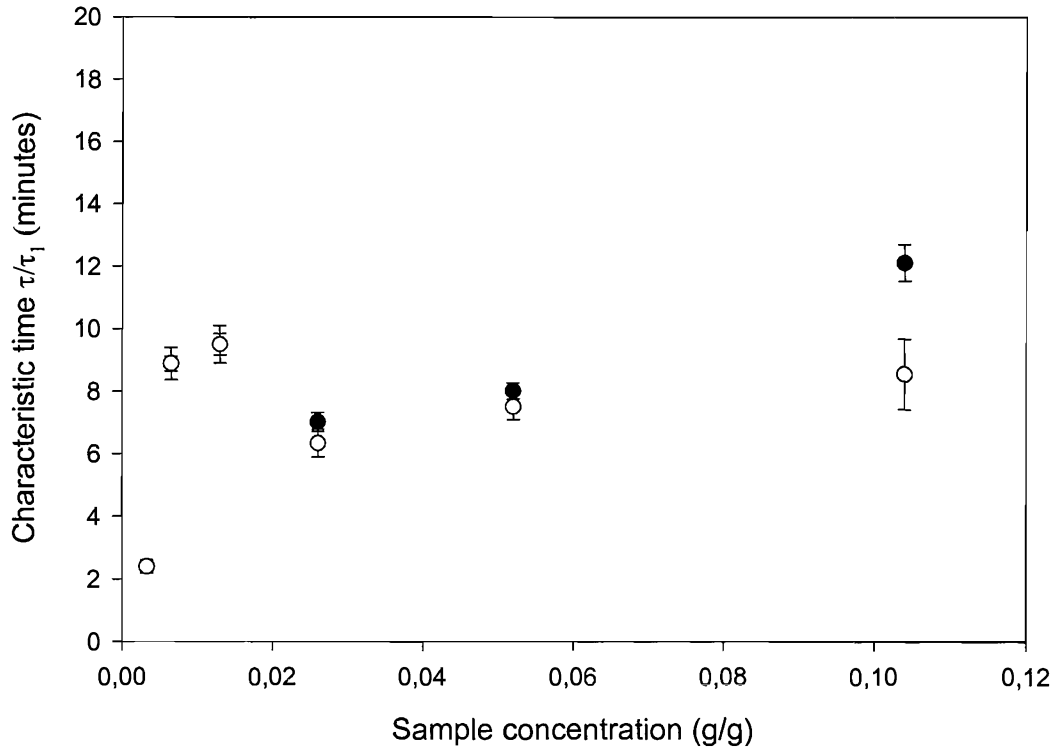

Figure 7.5d: Comparison between τ/τ_1 and sample concentration (Black dots represent data derived from Model I and coincide with data for Model II at low concentrations).

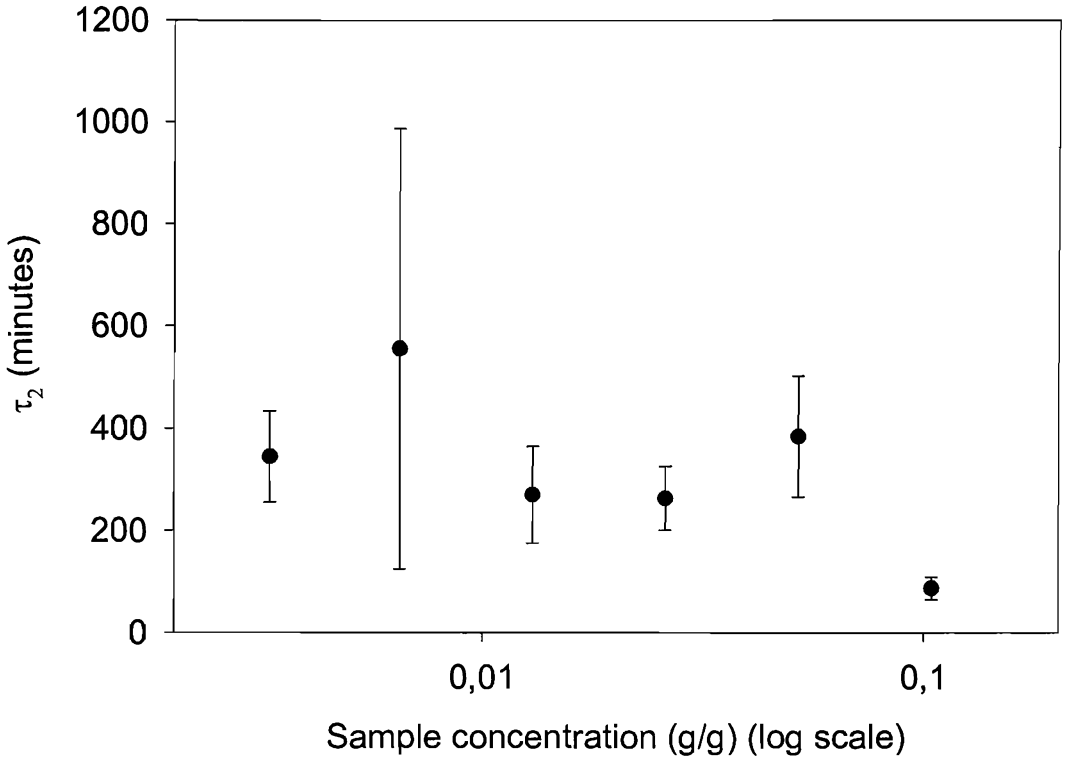

Figure 7.5e: Variations of τ_2 with sample concentration (from Model II).

7.3.4 The effect of temperature on conductivity measurements

We explored the effects of temperature on conductivity by performing a series of experiments in a narrow range of temperatures, situated between 20 and 40°C, at a fixed concentration of 0.013 g/g[11]. Fig.7.6a contains overlaid data obtained at 20, 25, 30, 35 and 40°C, from which we can see that the magnitude of conductivity increases with testing temperature. The slopes of the linear-like zones seen at longer testing times, globally, seem to increase with temperature as well. To quantify these observations, we used the mathematical models introduced in the preceding section, and Table 7.3 contains numerical parameters derived from our regressions. Both models describe our data well, since both determination coefficients and *MSR* values do not systematically favour either of the two models. Fig.7.6b shows the relationship between σ_o and testing temperatures. We observe a fairly linear relationship between these parameters, which is somewhat undermined by the data obtained at 30°C. Fig.7.6c highlights the correlation between the rate of change (k) for conductivity as a

[11] Higher temperature levels were envisaged but unwanted evaporation effects did not permit the acquisition of data above 40°C.

function of temperature, and again, a good correlation is found between these parameters. Fig.7.6d shows the temperature-independent character of the main characteristic time for both models, τ and τ_1. Finally, some values for τ_2 could be derived from Model II. Fig.7.6e reveals possible evidence of a secondary process. The associated characteristic time appears temperature-independent and its magnitude is comparable to the data shown in fig.7.5e. However, the error bars are large, especially in the case of regressions that did not fully converge.

At this point, we need to pose an important question. In view of our preceding results, why would a diffusion time not be influenced by temperature and concentration, at least, to some extent? To examine this matter, equivalent tests and models were used in the following section, which examines the effect of ageing on the various parameters that make up our two models.

MODEL I				MODEL II			
Temp (°C)	Coefficient	Standard error	R^2/MSR	Temp (°C)	Coefficient	Standard error	R^2/MSR
40°C				40°C			
σ_0	0.3937	0.0085	0.995266	σ_1	0.3937	0.0261	0.992792
$1/\tau$	0.1059	0.0049	0.000283	$1/\tau_1$	0.1059	0.0086	0.000288
k	0.0046	0.0001		σ_2	*1.5*	*0.9898*	
				$1/\tau_2$	0.0035	0.0031	
35°C				35°C			
σ_0	0.3511	0.0062	0.996863	σ_1	0.315	0.0185	0.997072
$1/\tau$	0.1003	0.0035	0.000138	$1/\tau_1$	0.1118	0.0075	0.000131
k	0.0039	0.0001		σ_2	1.4013	0.4919	
				$1/\tau_2$	0.0036	0.0017	
30°C				30°C			
σ_0	0.2435	0.0036	0.998615	σ_1	0.2003	0.0078	0.999023
$1/\tau$	0.1061	0.0033	4.75E-05	$1/\tau_1$	0.1327	0.0068	3.41E-05
k	0.0040	0.0001		σ_2	1.3082	0.1647	
				$1/\tau_2$	0.0042	0.0007	
25°C				25°C			
σ_0	0.2395	0.0042	0.99726	σ_1	0.2395	0.013	0.994517
$1/\tau$	0.1053	0.0038	7.17E-05	$1/\tau_1$	0.1053	0.0067	7.28E-05
k	0.0032	0.0001		σ_2	*1.000*	*0.5084*	
				$1/\tau_2$	0.0037	0.0026	
20°C				20°C			
σ_0	0.194	0.0042	0.997267	σ_1	0.1831	0.0139	0.997302
$1/\tau$	0.0899	0.0037	5.11E-05	$1/\tau_1$	0.0948	0.0077	5.13E-05
k	0.0027	0.0001		σ_2	*0.9*	*0.399*	
				$1/\tau_2$	0.0037	0.0023	

Table 7.3: Regression data derived from Model I and Model II, relative to fig.7.6a.

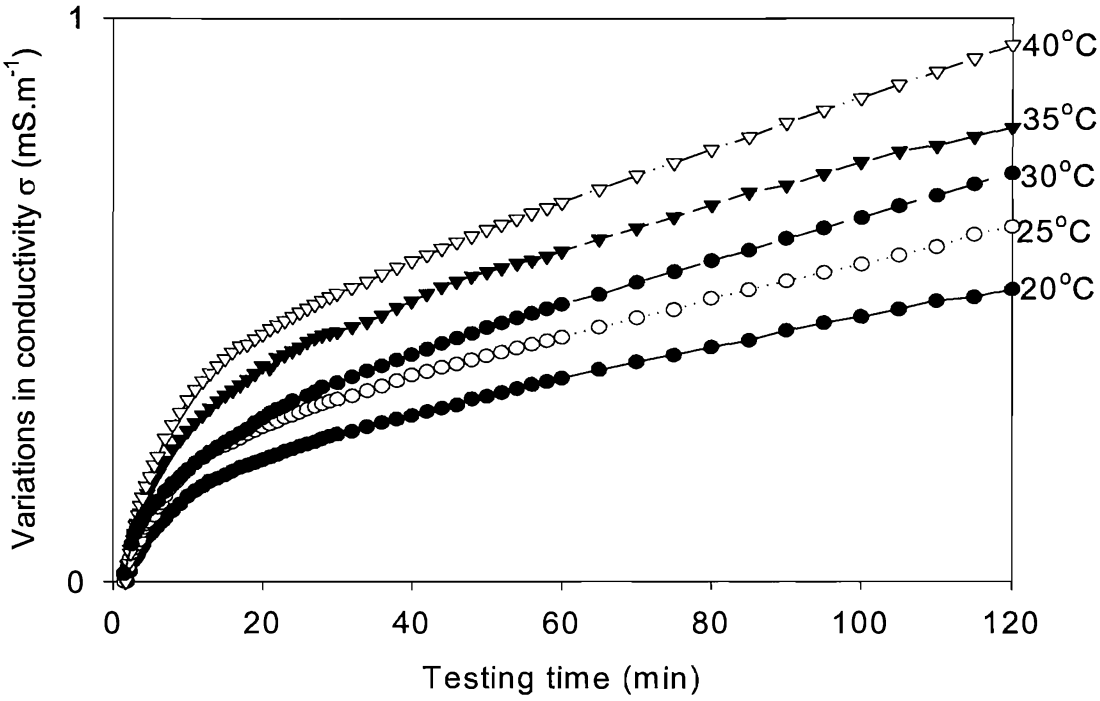

Figure 7.6a: Variations of the conductivity of unaged samples with time and temperature.

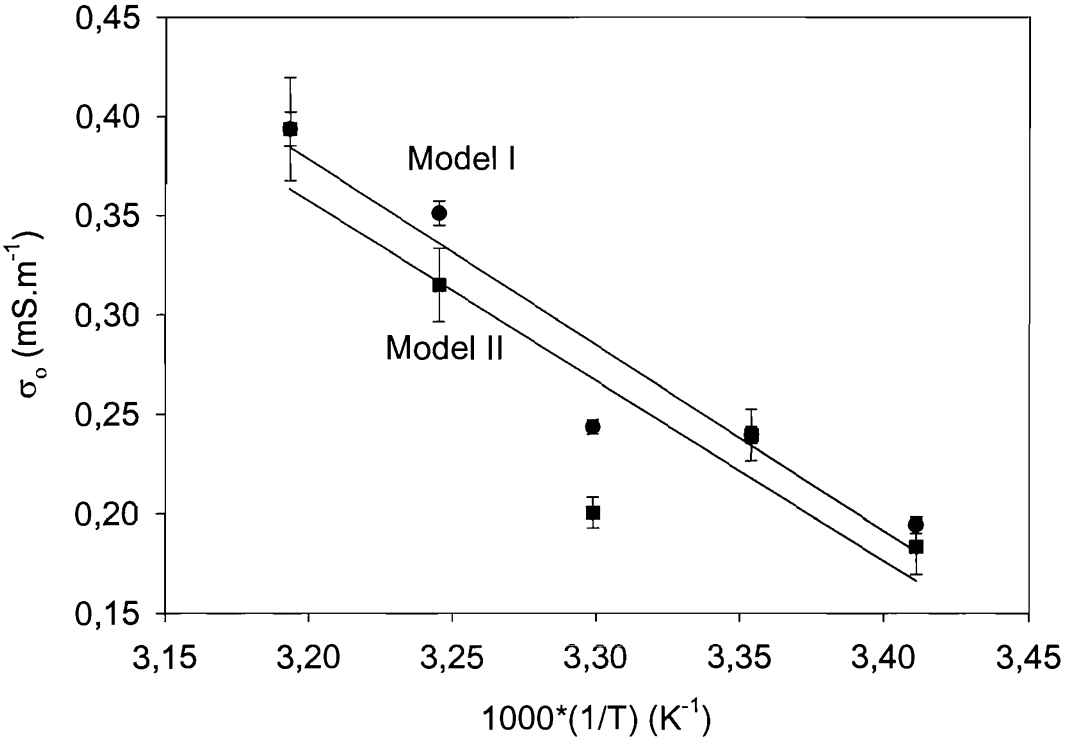

Figure 7.6b: Correlation between σ_o or σ_1 and reciprocal temperature. (R^2 values: 0.918 for Model I; 0.795 for Model II).

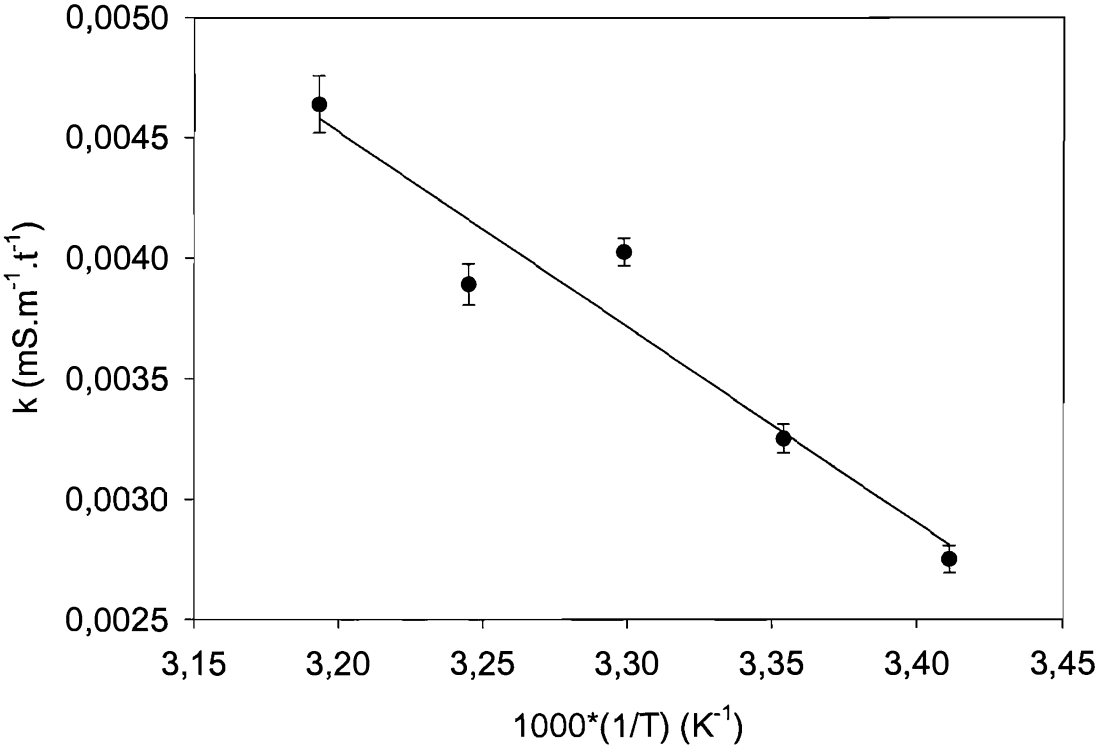

Figure 7.6c: Variations of k with temperature. (Model I-R^2:0.920)

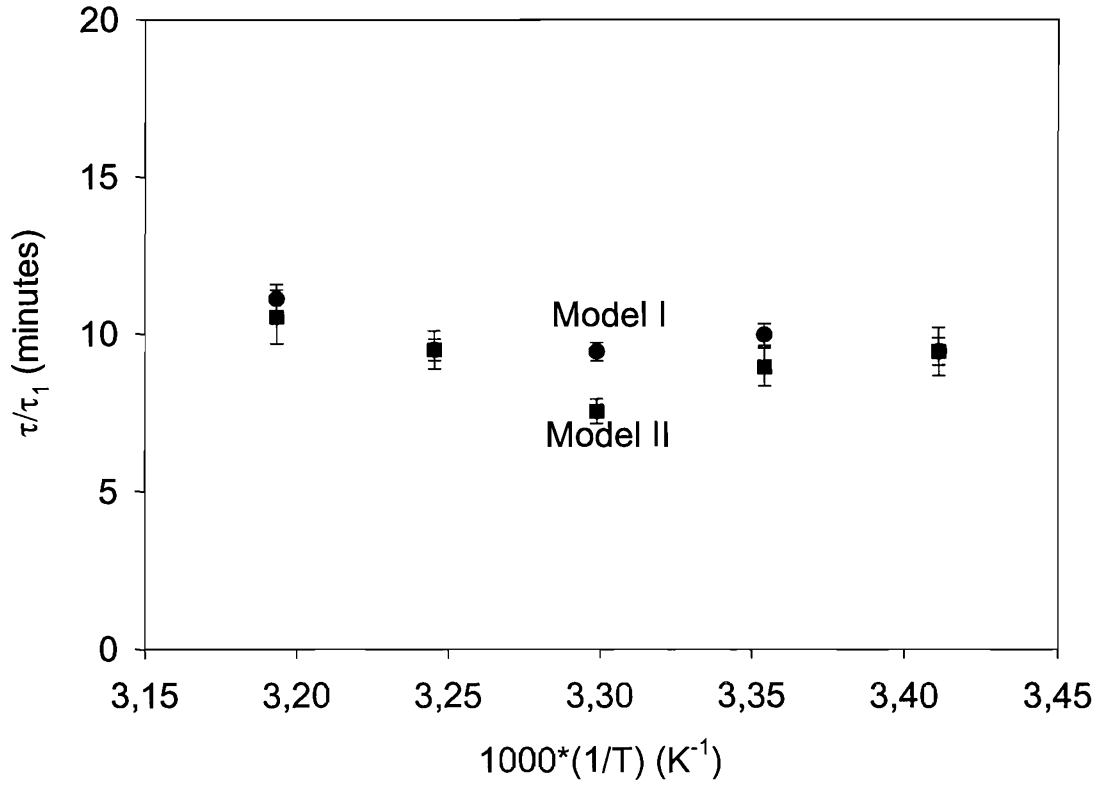

Figure 7.6d: Comparison between τ or τ_1 and sample concentration. (Data for Model I are the black round dots).

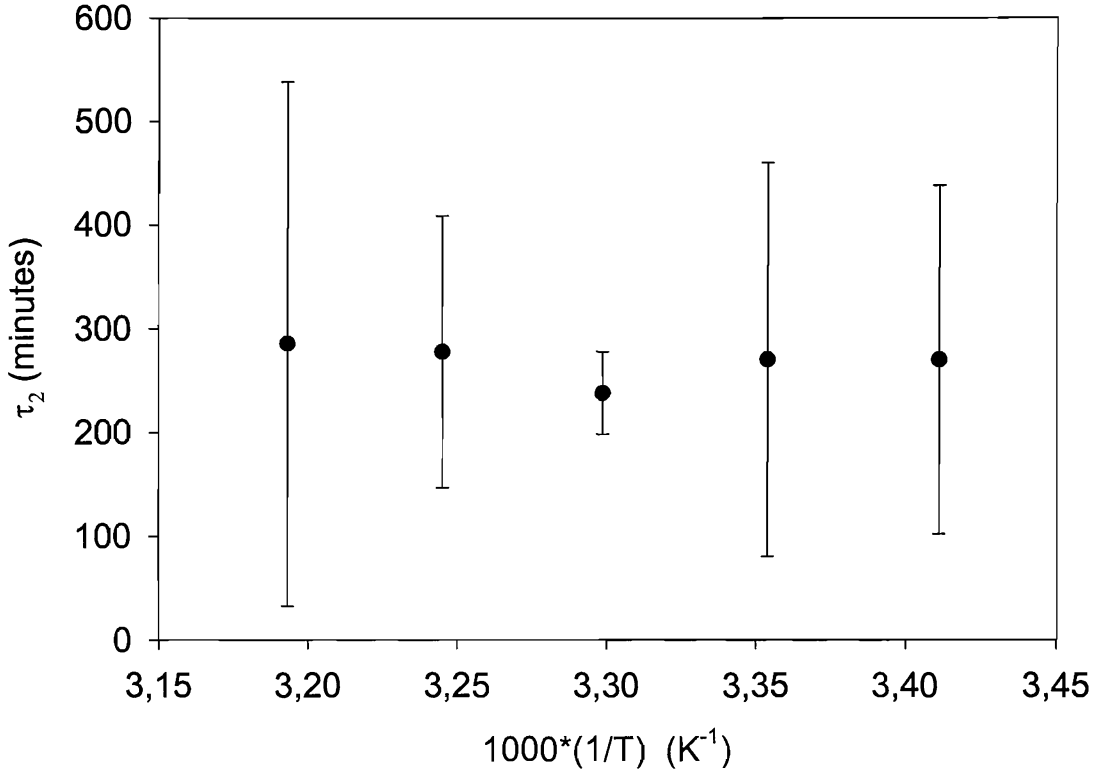

Figure 7.6e: Variations of τ_2 with temperature-(from Model II).

7.3.5 The effect of sample ageing on conductivity measurements

We undertook to test one series of aged samples that was originally prepared to carry out swelling measurements; namely, the (S90/O2) sample set. The reason behind this choice is simply that, out of the four sets of samples that were examined, this was likely to be the most altered. Our experiments were carried out on four aged specimens, including a (S90/O2/2W), a (S90/O2/4W), a (S90/O2/12W) and a (S90/O2/24W) sample, in addition to an unaged analogue, (REF). Starting concentrations and testing temperatures were nominally identical. Fig.7.7a and fig.7.7b show two different representations of the same data; fig.7.7a displays the data in on an absolute conductivity scale, whereas, in fig.7.7b, individual plots are offset for more clarity. A close examination of the data shown in fig.7.7a reveals that the conductivity is reduced for (S90/O2/2W) and (S90/O2/4W), relative to the other two aged specimens and the (REF) sample. The linear-like parts appear quite similar, except for the (S90/O2/12W) plot, which exhibits a lower slope than the other four. Visible shifts in the main characteristic time are predictable, since the initial parts of the plots appear steeper as the ageing time increases; fig.7.7b includes tangents as a guide for the eye.

Table 7.4, once again, presents all the numerical coefficients derived from our two models.

MODEL I				MODEL II			
Ageing Time (weeks)	Coefficient	Standard error	R^2/MSR	Ageing Time (weeks)	Coefficient	Standard error	R^2/MSR
0				0			
σ_o	0.2395	0.0042	0.99726	σ_1	0.2395	0.013	0.994517
$1/\tau$	0.1053	0.0038	7.17E-05	$1/\tau_1$	0.1053	0.0067	7.28E-05
k	0.0032	0.0001		σ_2	*1.000*	*0.5084*	
				$1/\tau_2$	0.0037	0.0026	
2				2			
σ_o	0.1825	0.003	0.998880	σ_1	0.1723	0.009	0.998905
$1/\tau$	0.0983	0.0033	1.47E-05	$1/\tau_1$	0.1042	0.0064	2.02E-05
k	0.0037	0.0001		σ_2	3.7179	2.853	
				$1/\tau_2$	0.0011	0.0009	
4				4			
σ_o	0.1277	0.0019	0.998897	σ_1	0.1219	0.0046	0.998926
$1/\tau$	0.1483	0.0057	4.28E-06	$1/\tau_1$	0.1572	0.0092	6.89E-06
k	0.0038	0.0001		σ_2	5.1562	3.6212	
				$1/\tau_2$	0.0008	0.0006	
12				12			
σ_o	0.2442	0.0027	0.997317	σ_1	0.2418	0.0066	0.997324
$1/\tau$	0.1610	0.0049	2.52E-05	$1/\tau_1$	0.163	0.0071	2.75E-05
k	0.0030	0.0001		σ_2	6.8638	16.4952	
				$1/\tau_2$	0.0004	0.0011	
24				24			
σ_o	0.2196	0.0028	0.997300	σ_1	0.2037	0.0057	0.997664
$1/\tau$	0.1999	0.0075	3.53E-06	$1/\tau_1$	0.2222	0.0114	9.84E-06
k	0.0040	0.0001		σ_2	1.924	0.526	
				$1/\tau_2$	0.0024	0.0008	

Table 7.4: Regression data derived from Model I and Model II, relative to fig.7.7a.

The apparent variation of σ_o from Model I with ageing is, we believe, due to uncertainties in sample preparation, such as qualitative changes in the exchange surface. Fig.7.7c shows a graphical representation of these values, from which, no trend emerges. We therefore consider that the latter parameter does not vary significantly with ageing. Fig.7.7d illustrates a similar point, in that the linear-like regions of our plots do not vary significantly with ageing either. If this interpretation is limited to Model I, it reflects rather well the qualitative appearance of our raw data. Next, fig.7.7e displays the values for τ and τ_1 as a function of ageing. For both models,

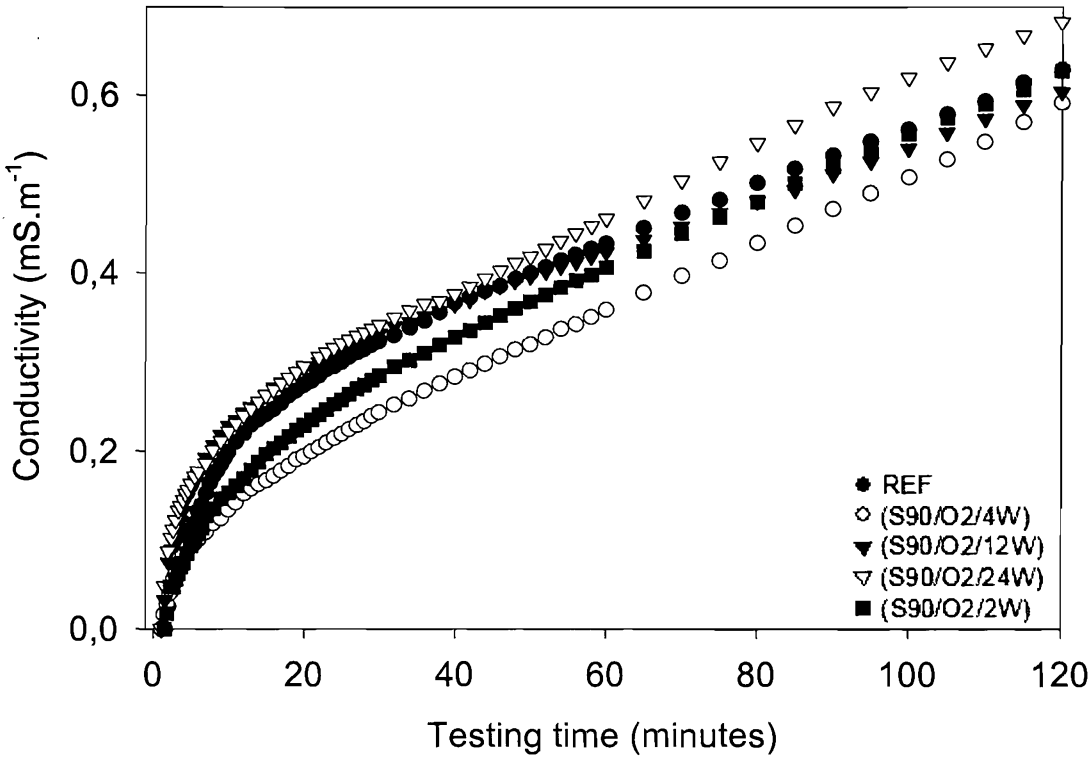

Figure 7.7a: Variations of the conductivity of unaged samples with ageing.

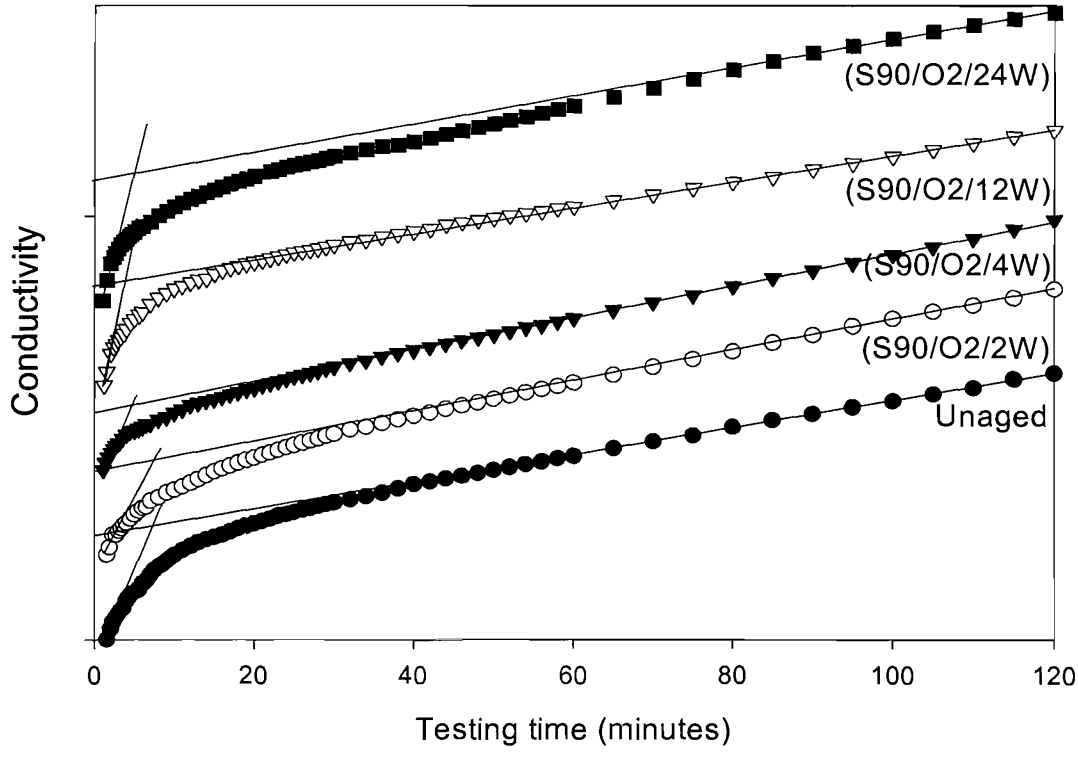

Figure 7.7b: Variations of the conductivity of unaged samples with ageing (offset along the y-axis).

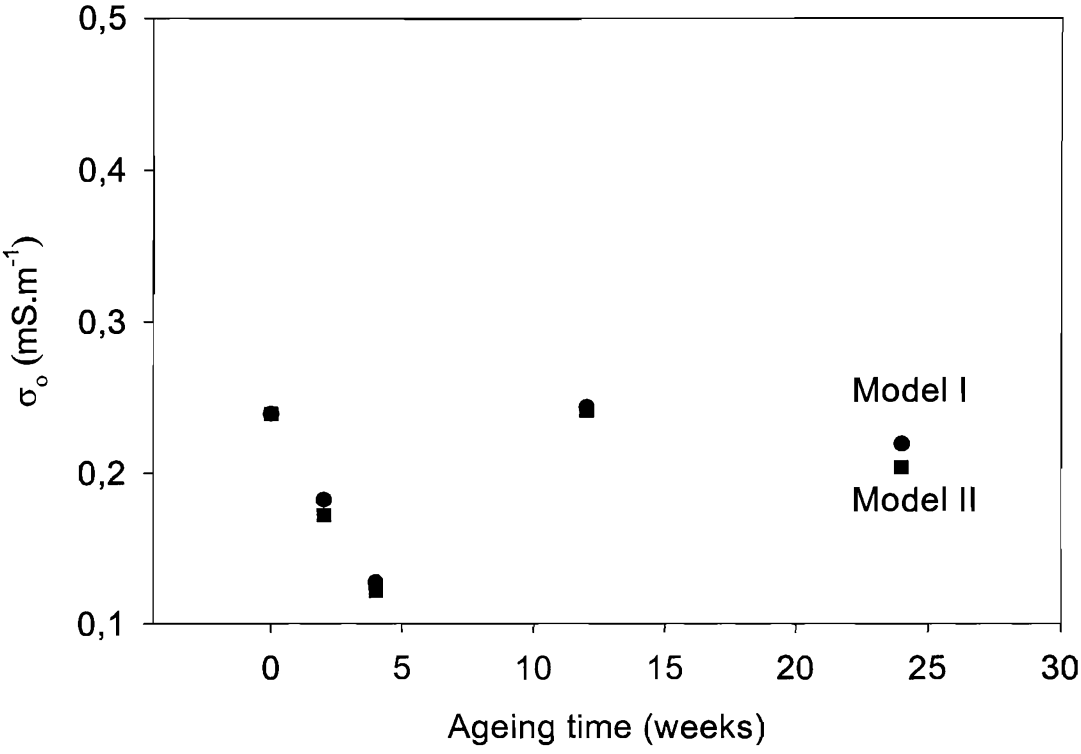

Figure 7.7c: Correlation between σ_o/σ_1 and sample ageing (data extracted from both models).

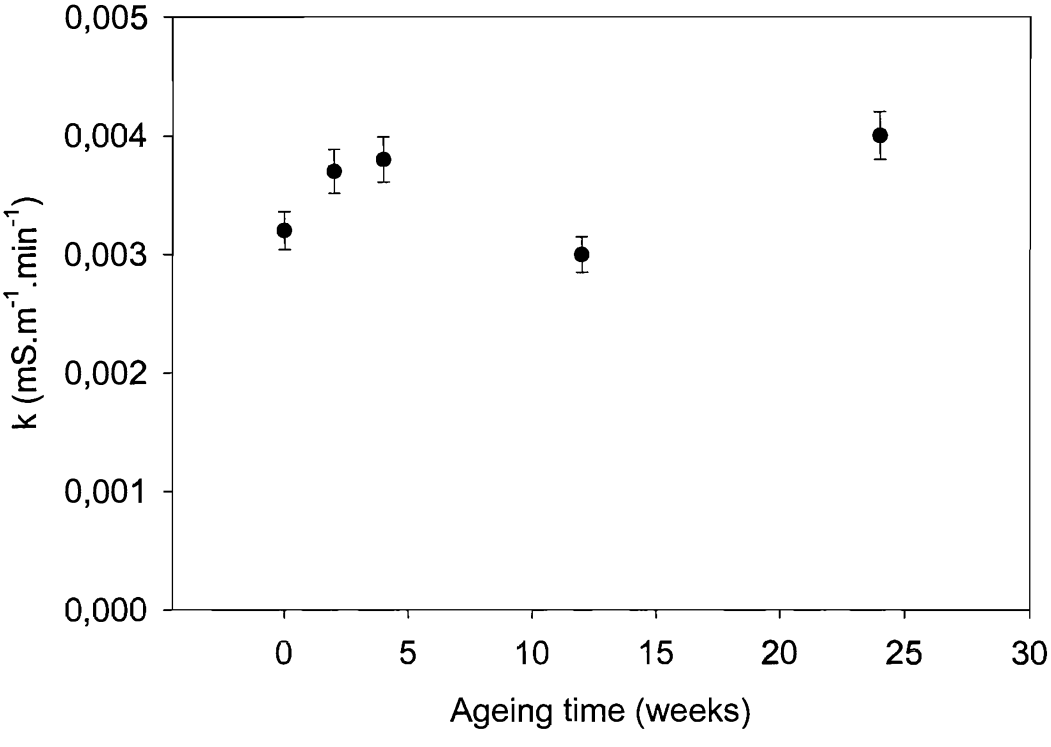

Figure 7.7d: Variations of k with ageing (Model I).

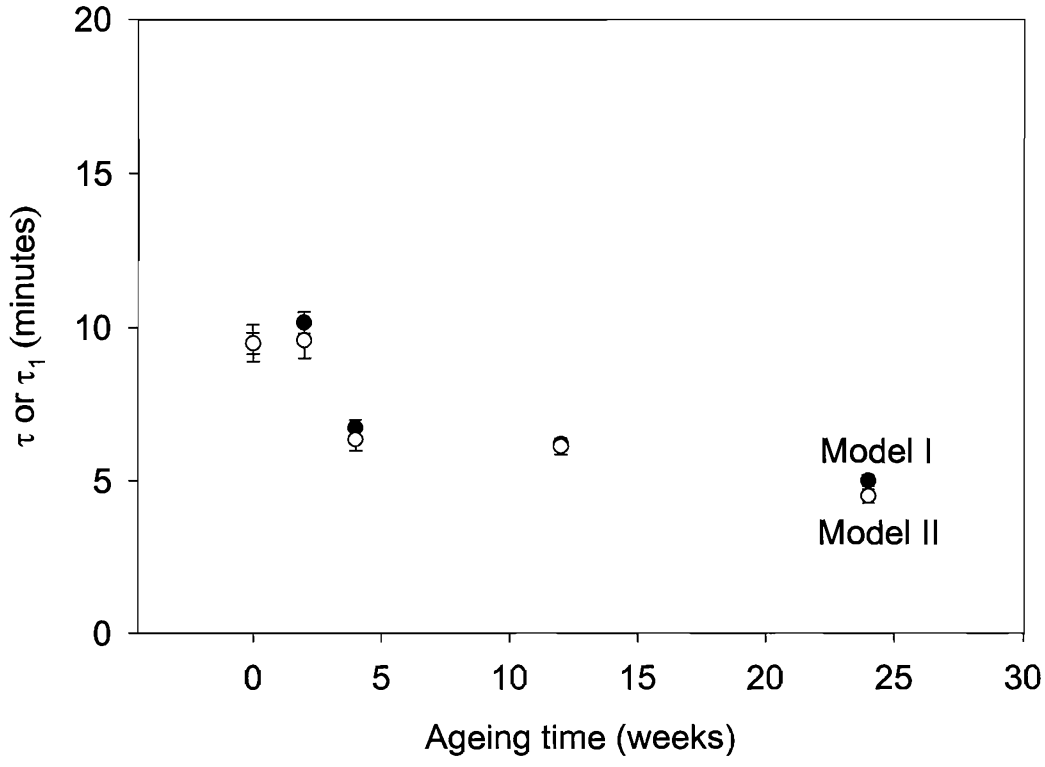

Figure 7.7e: Comparison between τ or τ_1 and sample concentration (data extracted from both models).

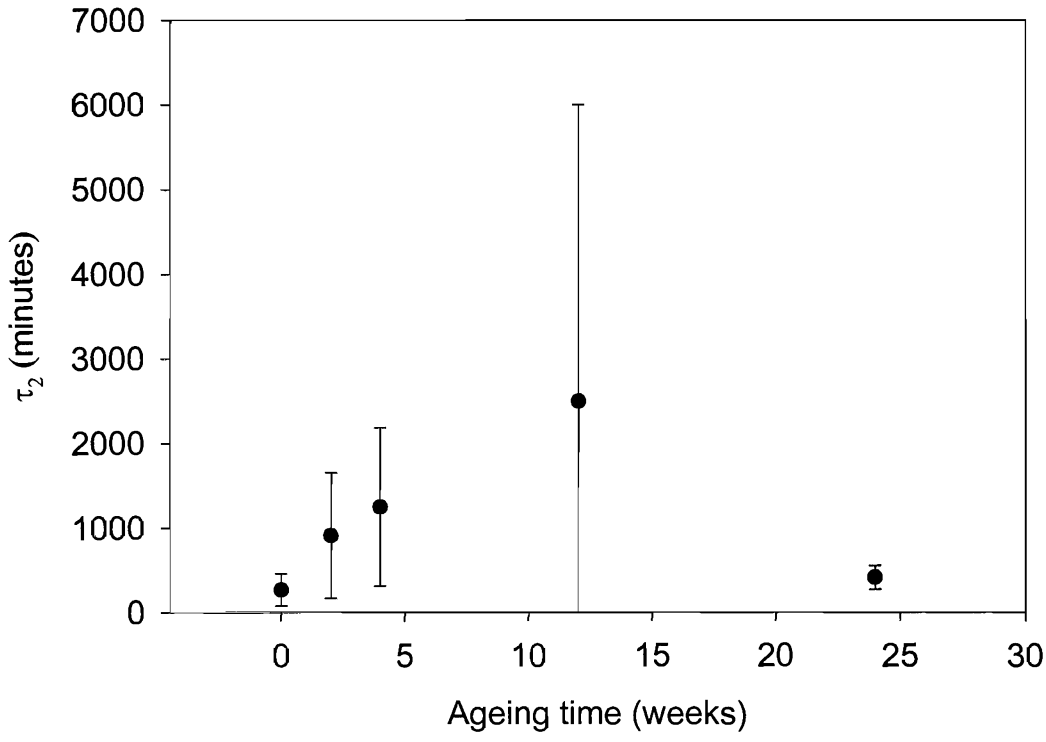

Figure 7.7f: Variations of τ_2 with ageing-(from Model II).

it appears that the principal characteristic time decreases progressively with ageing. Finally, fig.7.7f shows the variation of τ_2 with ageing. The error bars on these individual data points appear, globally, to be much larger than those in any other similar plot, and, thus these data should be treated with caution.

7.4 Further testing of mathematical models

Thus far, we have attempted only to explore the effect of different physical parameters on the models. It would seem that concentration, temperature and ageing conditions do affect the variation of solvent conductivity with time, and some qualitative changes could be seen simply by examining the data visually. The additional analysis provided by the calculation of *MSR* values is limited, since our data sets are large, the latter can alternatively indicate a slightly more pertinent fit for Model I or Model II. In the present section, we attempt to explore the shape of the response surface for both models in parameter space, which relates critically to the analysis, and, consequently, to parameter optimization in the physical sense rather than on simple statistical grounds. Specifically, we test the response of our model if we fix one or more parameters[12] and allow the model to compensate for this by adjusting other parameters.

7.4.1 Model optimization

The Sigma Plot software includes a function which automatically computes values for parameter dependencies; this feature is particularly useful for exposing conditions when numerical models exploit supernumerary degrees of freedom for a given regression. This is effectively the case for Model II, where σ_2 and τ_2 are fully dependent, according to the software. This behaviour is somewhat rectified for data that deviate from a linear-like behaviour. To illustrate this, Table 7.5 contains dependency values for the plots previously shown in fig.7.5a; the latter includes dependency parameters for both models, as a result of free-fit calculations. It also includes data for Model II which was optimized[13] manually. From Table 7.5, we can see that Model I is not fully constrained since dependency values vary between 0.3 and

[12] This was already done for Model II, by fixing values for σ_2 manually. It was the only way to "force" the convergence of the second term for this model.

[13] Data manually optimized were indicated by italics in the previous tables.

0.9. This is not the case, however, for Model II, when conductivity profiles do not exhibit pronounced deviations from a linear-like behaviour, at long testing times. This is the case when sample concentration is low; it manifests itself by dependency values adopting a numerical value of 1. This can be rectified to a degree by imposing values for σ_2[14] on the model. This might be because the second term of this model cannot locate local extrema, possibly because the precise form of the response surface in parameter space is too shallow to lead to convergence.

Sample type (g/g)	Model I		Model II		Rectified Model II	
	Param.	Depend.	Param.	Depend.	Param.	Depend.
0.0033	σ_o	0.950969	σ_1	0.99543		
	$1/\tau$	0.693156	$1/\tau_1$	0.920768		
	k	0.936408	σ_2	0.983927		
			$1/\tau_2$	0.997309		
0.0065	σ_o	0.891452	σ_1	0.98632		
	$1/\tau$	0.63076	$1/\tau_1$	0.862395		
	k	0.847159	σ_2	0.999779		
			$1/\tau_2$	0.999816		
0.013	σ_o	0.86671	σ_1	0.98037		
	$1/\tau$	0.580587	$1/\tau_1$	0.806675		
	k	0.814423	σ_2	0.999338		
			$1/\tau_2$	0.999487		
0.026	σ_o	0.912209	σ_1	0.990532	σ_1	0.993185
	$1/\tau$	0.705327	$1/\tau_1$	0.904709	$1/\tau_1$	0.919703
	k	0.863935	σ_2	1	σ_2	0.999637
			$1/\tau_2$	1	$1/\tau_2$	0.999738
0.052	σ_o	0.904958	σ_1	0.989032	σ_1	0.99062
	$1/\tau$	0.676846	$1/\tau_1$	0.885514	$1/\tau_1$	0.894122
	k	0.857171	σ_2	1	σ_2	0.999924
			$1/\tau_2$	1	$1/\tau_2$	0.999933
0.104	σ_o	0.727394	σ_1	0.911589	σ_1	0.91582
	$1/\tau$	0.308529	$1/\tau_1$	0.511156	$1/\tau_1$	0.513731
	k	0.682129	σ_2	1	σ_2	0.999108
			$1/\tau_2$	1	$1/\tau_2$	0.999215

Table 7.5: Dependency values for Model I and Model II.

[14] Manual values for σ_2 were obtained empirically and might not be the best possible values; still, customized regressions were satisfying in terms of error bars and marginally changed dependency values.

7.4.2 Optimization attempts involving different groups of data

Here, we wish to carry out further calculations using the data sets previously shown in fig.7.6a and fig.7.7a. The reason for focusing on these, and not the results shown in fig.7.5a, is because the latter relate to material testing more than forensic analysis. Specifically, we wish to know how stable our results are, and, thereby, how valid automated computations can be for our data. If we consider fig.7.6d, we can be reasonably confident that values for the primary characteristic time, τ, do not vary with the testing temperature. Conversely, we suppose that there is a linear relationship between the testing temperature and the magnitude of the conductivity, σ, (see fig.7.6b), and also for the constant k representing the rate of change in conductivity at longer testing times (see fig.7.6c).

To personalize calculations, we first employed an average value for τ whose average was calculated for both models. In addition, we alternatively employed discrete values extracted from regression lines as new inputs. Then, the different parameters that make up a model were fixed by following a permutation procedure; in this way, numerical computations differed from free fit analysis as a result of the imposition of one or many parameters. In the case of Model I, fig.7.8a, 7.8b and 7.8c respectively illustrate the outcome generated by imposing parameters on the temperature dependence of σ, τ and k; in each case, imposed parameters are indicated in the figure's legend. For clarity, data obtained from free fit computations are also included in the figures[15]. From these plots, it is evident that imposing the above constraints does not make the final data deviate strongly from their free fit counterpart, still:

- Fixing only τ does tend to linearize, to some extent, the data in fig.7.8a.
- Conversely, the different attempts to narrow the range in which τ is situated systematically resulted in distorting the free fit data, thus increasing the scatter between data points (see fig.7.8b).
- Fixing only σ tended to linearize slightly the data in fig.7.8c.

[15] Free fit data reported in fig.7.8a, 7.8b and 7.8c are those initially employed to build fig.7.6b, 7.6c and 7.6d respectively.

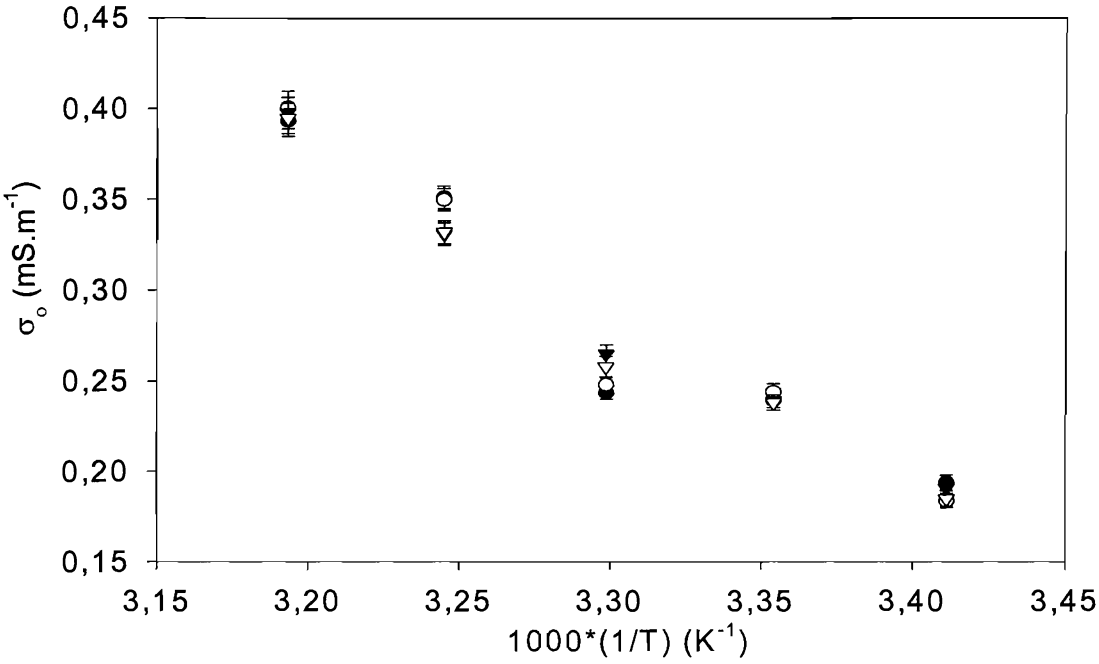

Figure 7.8a: Effect of imposed parameters on the correlation between σ_o and reciprocal temperature. (Round black dot- free fit; Round white dot-τ is imposed; Black triangle-k is imposed; White triangle- both k and τ are imposed)-Model I.

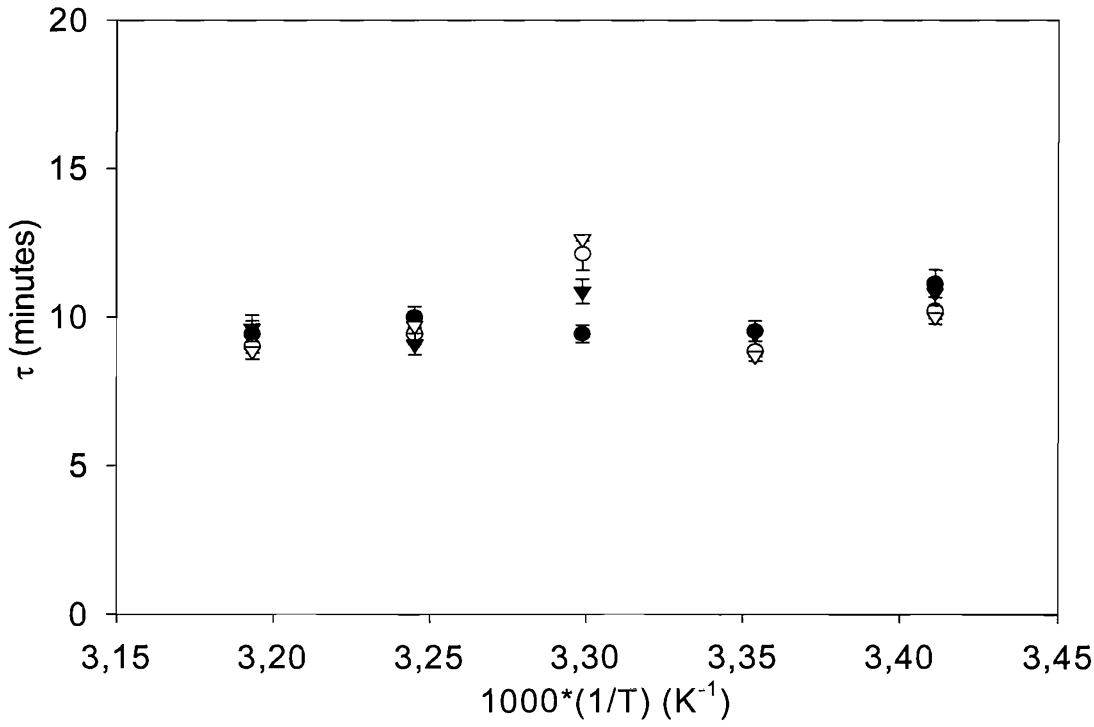

Figure 7.8b: Effect of imposed parameters on the correlation between τ and reciprocal temperature. (Round black dot- free fit; Round white dot-σ is imposed; Black triangle-k is imposed; White triangle- both k and σ are imposed)-Model I.

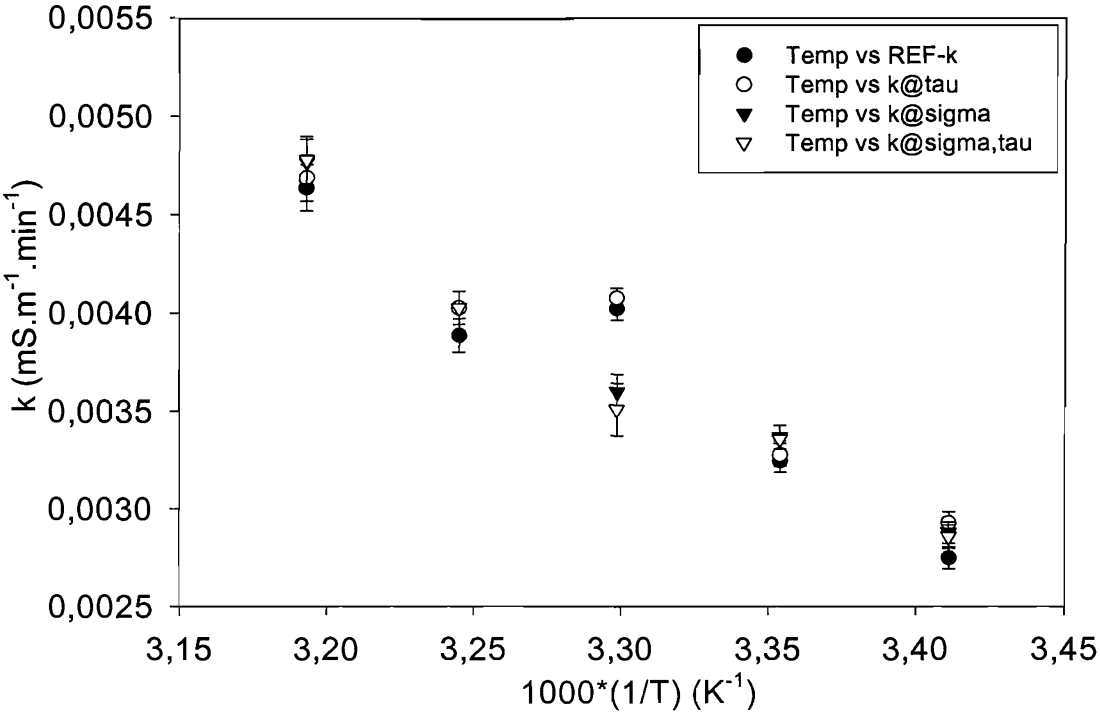

Figure 7.8c: Effect of imposed parameters on the correlation between k and reciprocal temperature. (Round black dot- free fit; Round white dot-τ is imposed; Black triangle-σ is imposed; White triangle- both σ and τ are imposed)- Model I.

Concerning Model II, we were particularly interested in exploring variations in the interdependency of characteristic times. This is specifically because fig.7.6e contains data that appears redundant with that shown in fig.7.6d for τ_1. The link between σ_2 and τ_2 is obvious. If we go back to the definition for our two models, we can utilize a Taylor series to find an equivalent to the second term for Model II. It gives:

$$\sigma \exp(-t/\tau)) = \sigma - (\sigma/\tau)t \qquad \text{(eq.7.4)}$$

Thereby, we can relate k to σ_2 and τ_2 since $k \sim \sigma_2/\tau_2$. This provides a straightforward means of comparing results obtained with the two models; indeed, from the results in Tables 7.1 to 7.3, it can be concluded that values for σ_2/τ_2 fall within a similar range to that of k. We could easily check that imposing higher values for σ_2 leads to lower values for τ_2. Hence, we examined directly how τ_1 influences τ_2 by imposing biased values for τ_1[16]on the model; fig.7.9a shows that variations in τ_1 of the order of 10% has virtually no effect on the resultant value for τ_2, at least, not in the same

[16] Values for $\tau_1 \pm 10\%$ were employed, and reported as such in the graph's legend.

proportion. Conversely, σ_1 exhibits a massive influence on σ_2 and, consequently, on τ_2. Fig.7.9b displays data obtained, as above, by adjusting σ_1 by ±P% and seeing the effect it has on σ_2. Only data obtained at 30 and 35°C are shown because convergence problems were encountered elsewhere for the second term contained in Model II. Convergence restrictions also conditioned the employed values for P.

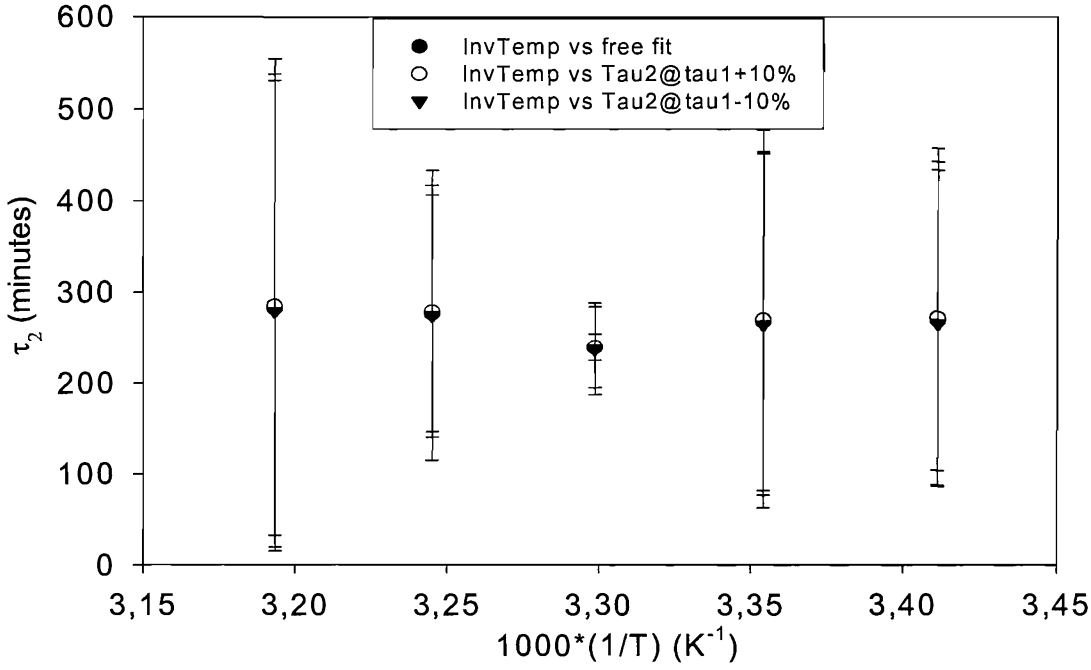

Figure 7.9a: Effect of variations in τ_1 over values for τ_2- Model II.

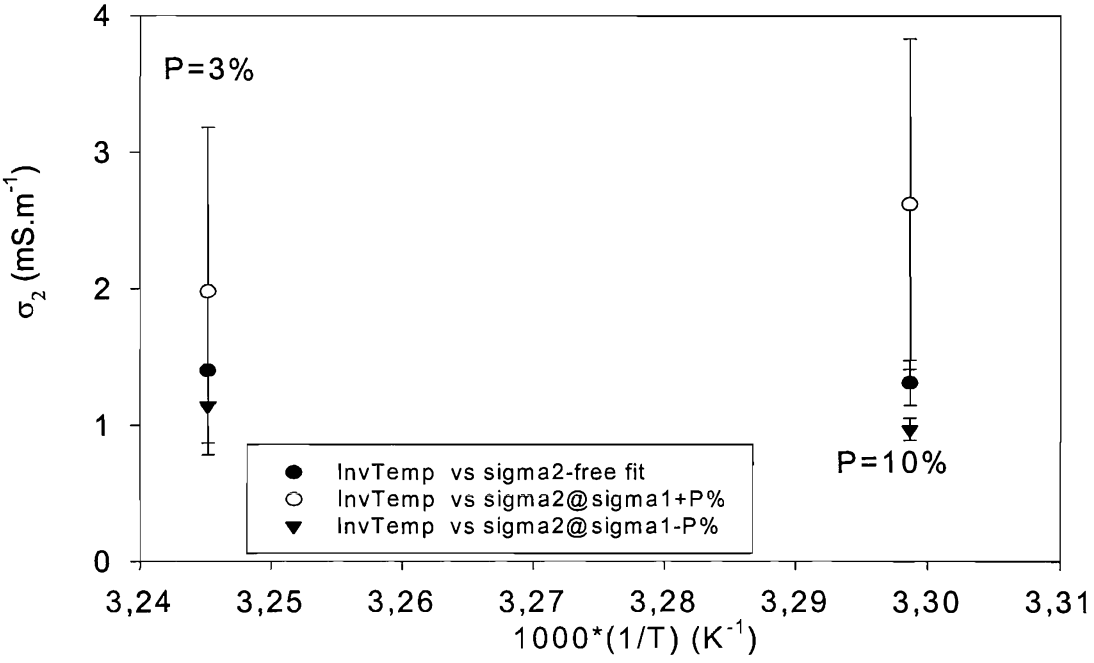

Figure 7.9b: Effect of variations in σ_1 over values for σ_2- Model II.

Finally, we wished to re-analyse the data obtained from the series of aged samples that make up fig.7.7a. Data shown in fig.7.7e indicates that there might be a decrease in the material's characteristic time with ageing. To explore this, two possible scenarios were envisaged:

(i) Where the primary characteristic time remains constant;

(ii) Where the latter decreases linearly with ageing time.

For this, we first input into Model II an average value for τ_1 and then discrete values extracted from the original linear regression. Neither approach proved successful; the second term of the model could not converge in most cases while, the few numerical values we could obtain were equivalent to that previously shown.

7.5 Global interpretation of our data

Even though the overall objective of this study concerned the effectiveness and long-lasting swelling capacities of our superabsorbent material, the goals for our experiments were twofold. By carrying out swelling and conductivity experiments, we both attempted to probe the nature of our material and conduct experiments that relate more specifically to water uptake, by introducing an additional accelerated ageing aspect into the work. Based upon the results presented above, we feel confident that our material relates to the general class of polyelectrolyte, as discussed in the literature. That is, the considered material is a superabsorbent network that releases a fraction of ions into its surroundings during long-term swelling [119,122,129]. From a theoretical point of view, the swelling behaviour of our material could correspond to a model such as an ideal sliding gel [132], whose thermodynamic equilibrium is reached once the distance between cross-links is maximized; that is, an object that maximizes its volume under the constraint that the number of bonds between chains and particles must remain constant [132]. The dynamic aspect of the swelling process would explain how conductivity levels vary for suspensions of swelling particles. We imagine that counterions are driven outside the swollen structure, thus contributing for a time to the atmosphere of counterions, which participate in conduction [129], before being lost to the solvent and replaced by more ions from the swollen particle. We propose that early electrostatic repulsion processes form the physical basis from which the main characteristic diffusion time originates. This would explain both the apparent

insensitivity of this parameter to thermal effects, but also its plausible reduction with ageing time. That is, scission reactions might "loosen" the original network, which would result in the observed increase in swelling ratio with ageing. In turn, this would allow the diffusion of excess counterions into the solvent to be accelerated, yet neither could this point be proved nor disproved by optimizing data acquired from our different models. The regions of our plots which deal with the variations in conductivity at longer time might then truly relate to a counterion extraction that reacts to thermal variations, once this preliminary process has occurred. Since simple observations have revealed that the collapse of the swollen particles typically necessitate times significantly longer than that addressed within our models, we can hypothetize that a secondary diffusion process implied by our second model, is somehow correlated to the collapse process of swollen particles. The latter might vary with the concentration in particles and relate, in a complex manner, to concurrent ionic association-dissociation processes, as presented by Vasilevskaya et al. [129]; these authors proposed a model where relative association probability increases with the ionic charge but decreases with temperature, and varies with the monomer size and solvent permittivity. Also, the kinetics for collapse are linked to the solvent's relative "goodness", and deswelling in a good solvent is expected to occur at a slow, almost constant rate [129]. From an experimental point of view, our conductivity tests intrinsically rely on the presence of an electrical field in order to measure the changes in conductivity of our samples. We know from the work of Gong et al. that electrically induced contractions do occur when electrical fields are applied to a sample [130]. Thus the timescale for physical shrinkage and the loss of counterions from inside a swollen particle must, to a certain extent, be affected by the very electrical field used to probe it. Gong et al. also showed that [130] the lowest frequency dependence for the conductivity of their system is situated above 10^3 Hz, and that relaxation times for counterions are to be found above 10^5 Hz.

7.6 Conclusions

Our study of this superabsorbent material has showed that both theoretical and experimental clues were required to understand how the material functions. It is important to reiterate that our material absorbs water to an enormous extent, but that this swelling strongly depends on pH and solvent quality. For example, swelling ratios

in tap water are about half those measured in DDW for an equivalent, unaged sample[17]. Although the conductivity of dilute suspensions of particles clearly varies over time, detailed interpretations of this rely greatly on better defined systems, as described in the literature.

Finally, we would like to stress once more that the main experimental difficulties encountered here are primarily linked to sample preparation effects, i.e. geometrical factors in addition to unresolved issues concerning the behaviour our material. Also, there might be additional effects on diffusion characteristics due to the application of an electrical field. The understanding of the latter point might, ultimately, prove to be of paramount importance given the potential application of this material within a high-voltage structure.

[17] A number of experiments were carried out with tap water, similarly to those presented in the above sections.

Chapter 8

Summary, future work and conclusions

8.1 Introduction

The originality of the research topic covered by this work relates to the understanding of the diffusant behaviour of liquid water into totally different model systems; our principal intention being to prevent detrimental water penetration within the very core of power cables, and thus, enhance their service lifespan by decreasing the occurrence of water-based electrical breakdowns. To achieve this goal, we assume that penetrant liquids must be stopped prior to diffusing in the intrinsically hydrophobic insulation XLPE layer that surrounds the core, and that this can be achieved by trapping and fixing water molecules using hydrophilic substances. In this context, we had to ensure that these materials can withstand the conditions under which they are supposed to fulfil their function.

8.2 Results summary

8.2.1 Microstructure and water uptake kinetics in LDPE-based samples

We started this work by exploring the effect of additives on the microstructure of LDPE-based model materials. A reliable insulator must be understood in terms of its microstructure, the latter being influenced as much by its thermal history as its chemical composition. By examining a temperature window under which isothermal crystallization can occur, we illustrated both the nucleating capacity of the included antioxidant and the effect of thermo-chemical crosslinking on crystallizability by comparing experimental results derived from the latter systems to those of a system exempt of such additives. From a purely theoretical prospective, one would expect that highly crystalline structures form effective barriers against penetrants such as water, implying that water diffusion essentially takes place within amorphous phases. Importantly, the experimental determination of water uptake kinetics within

LDPE-based samples showed that absorbed quantities depend strongly on solvent quality, and demonstrated that the presence of dissolved impurities can enhance water uptake such that the final concentration greatly exceeds the amount that would be anticipated on the sole basis of thermodynamics considerations. We could determine that, among all the tested samples, it is the crosslinked system which shows the greatest water uptake. Furthermore, the overwhelming effect of water contamination over water absorption is such that the testing of (EVA/LDPE) blends, aimed at making water quantities more detectable, did not prove as useful as we originally imagined. Water contamination does not, however, affect the concentration-independent character of the diffusion coefficient, which responds to a Fickian model regardless of the investigated sample type.

8.2.2 Long-term efficiency of water-trapping mechanisms

We tested two different water-trapping substances, one of which being a polysaccharide whose binding process with water molecules is based upon hydrogen bonding, whilst the other is a swelling polyelectrolytic substance. Both materials appeared capable of withstanding accelerated ageing conditions.

In spite of important thermally-enhanced depolymerisation processes, guar molecules retain their propensity of forming hydrogen-bonds with water molecules, since the lateral galactose groups that bear the hydroxyl groups involved in the hydration process, show a greater thermal stability than the glycosidic bonds; this behaviour can reliably be seen for ageing temperatures up to 90°C. The superabsorbent polymer also demonstrated excellent water-trapping stability, since swelling experiments showed that the material's capacity to absorb water does not diminish during ageing. Water-trapping is also very fast in the case of this material, and the mechanism through which the latter could lose its ability is attributable to the diffusion of counterions in the outer parts of the swelling particles and, thus, the reliable water-trapping capacity of this material appears concentration-dependent.

8.3 Proposed research program

The following sub-sections contain a proposal for further experimental work directly aimed at covering several points which were answered only speculatively in the previous chapters. A number of issues are also raised concerning a number of

complementary experimental routes that ought to be explored, in order to enlarge the scope of this thesis' research topic.

8.3.1 Morphology, molecular mobility and crystallinity of LDPE-based systems

The versatility of the DSC technique originates from the fact that an array of thermal programs can be employed to probe morphological variations induced by varying the thermal history of different samples. To complement our knowledge regarding the molecular motions taking place within LDPE-based materials, we could certainly employ a low-temperature DSC technique. It would also be of interest to probe the effect of extremely slow heating rates on the melting behaviour of materials considered in this thesis. From a technological standpoint, reverse engineering methods could be employed to investigate the morphological range characterizing XLPE-based samples extracted from different sections of an insulation layer. Paolini et al. followed this testing route [133] and their study provided a feedback on the effectiveness of the thermal events employed to process XLPE systems. For instance, the latter authors revealed that the crosslinking degree vary, depending on the distance from the conductor since radial thermal gradients are generated during curing processes. Surely, this has a direct incidence on the development of local morpho-mechanical properties, which could alternatively be tested using a mechanical technique such as that employed early on in this work. Earlier on, we suspected the latter technique to be limited in scope, especially because of the plausible existence of high-temperature relaxation processes that cannot be measured using this same technique; more specifically, melting processes linked to α relaxation features situated above 80°C are believed to be present. If this point was to be confirmed using a consistent testing route, this could prove crucial in terms of correlating such data to our DSC results.

Furthermore, experimental parameters such as crystallinity could be quantified precisely, using, for instance, combined X-ray and DSC methods. Such work may be needed prior to starting more refined work in the area of water diffusion in LDPE-based materials, by considering that only amorphous fractions of materials allow diffusion to occur.

8.3.2 Water uptake kinetics in LDPE-based compounds

A non-exhaustive list of straightforward experiments is provided here. These should be carried out to complement our understanding of water uptake mechanisms in

LDPE-based materials. First, multiple sorption experiments ought to be repeated on specimens presenting different thicknesses to verify the fact that diffusion processes in LDPE-based materials are truly Fickian. Certainly, the presence of mobile solvated ions appears to influence water uptake to a significant degree. Because of this, rigorous control of the impurity levels regarding the employed penetrant should also be considered. For instance, one could dissolve salts into DDW and evaluate the subsequent variations in sorption kinetics and saturation concentrations. Also, similar series of tests could be repeated using a range of (EVA/LDPE) samples, provided that their morphology and phase distribution is completely investigated. Obviously, experimental results could be reproduced using adapted numerical techniques and models. Again, a reverse engineering approach could be undertaken, i.e. similar experimental routes could be employed to test materials extracted from power cables.

Alternative water detection methods were employed by several workers. For example, several experimental methods dedicated to detecting small quantities of water in XLPE were employed by Ilstad [14]. This author employed three different methods, including the Karl Fischer titration method, a freezing method[1] and infrared spectroscopy. Similarly, Haridoss et al. [134] compared Karl Fischer titration results to infrared spectroscopy measurements. During the earliest stages of this work, we attempted to use the FTIR technique to detect absorbed water in 30 micron thick LDPE-based samples, but, without success. We wish to point out that the aforementioned workers employed millimetre-thick XLPE samples extracted from power cables, and this choice of sample type certainly explain their success. Less conventional detection methods also exist; for instance, we discovered that Sivadjian [135] employed a so-called hygrophotographic method, which is based upon wrapping special mercury and silver iodide plates in the material (sheath) whose permeability needs to be evaluated, which provides a gradual discoloration that allows the permeability to water vapour of the wrapping material to be quantified.

Further work should also be carried out to evaluate the fraction of penetrant subjected to clustering. For instance, one should use a device that permits varying relative water vapour pressure levels prior to employing a technique able to detect, or better still, differentiate water clusters from isolated water molecules.

[1] This method is based upon measuring vapour pressure variations induced by the evaporation of water in a closed volume.

8.3.3 Further testing of guar macromolecules

Depolymerisation kinetics is reported to vary as a function of sample concentration [105], and this is a point that ought to be addressed. Prior to exploring this issue, our own results could certainly be diversified by repeating viscometry tests on guar samples aged at further temperatures and, alternatively, at different ageing times. This would provide a means of constructing an extended version of the 3D graph shown in fig.5.11, thereby interpolating our data to larger temperature and ageing time ranges. Because of the depolymerisation issue raised above, we could carry out rheological measurements on guar samples whose concentration becomes a variable and, alternatively, submit samples to a wider range of ageing conditions. For instance, relative humidity levels could be controlled and varied to provide an alternative to the study of depolymerisation kinetics under purely dry or aqueous conditions, so that one can differentiate hydrolytic scission from thermally-enhanced and oxidation-based depolymerisation processes.

The most sensible issue to explore is that which covers guar's composition in terms of its galactose to mannose ratio. We are reasonably confident that, if the latter was to drift gradually towards that of locust bean, thermal effects could still, for a while, counteract the formation of hyperentanglements, in the same manner that preliminary heating steps are employed to fractionate [40] or recover locust bean samples. Alternative spectroscopy testing should be carried out on liquid-like samples. Some attempts were made, during the course of this work, to differentiate a GG and a LBG solution in the anomeric region, however, the spectral quality was such that we could not derive useful information from these. Extra efforts should be made towards developing adequate sample preparation procedures for such samples.

8.3.4 Further testing of the superabsorbent

Concerning our superabsorbent system, we give the priority to discovering its chemical nature prior to carrying out any further test; as for our failed attempts to follow swelling kinetics, we propose to employ a profile projection device coupled to a recording system to rule out observational difficulties.

Since water-trapping materials are supposed to operate in the presence of voltage gradients, we think it would be desirable to test the effect of a variable electric field on the behaviour of the material. Experimental work should be carried out to check the polarizability of the different elements that constitute such system. Indeed, the swelling

of polyelectrolytic superabsorbent behaviour is likely to be affected by the presence of an electric field [130]. Also, such materials are likely to be pressure sensitive, and alternative tests should be carried out to investigate this particular point.

8.3.5 Further experimental testing

Throughout this work, we specifically concentrated on identifying the physical processes by which water molecules can remain trapped within water-blocking substances. However, we did not evaluate the capacity of the above materials to literally prevent water diffusion in LDPE-based materials. Moreover, one could argue that aqueous substances will be even more concentrated in their vicinity; hence, concentration gradients might be greatly increased due to their presence. As a consequence, it is essential to see whether trapped water would diffuse preferentially within the trapping layer itself, that is, along the cable axis and not towards the insulation layer. Experimentally, we think it would be interesting to surround LDPE samples with either guar solutions, better still, swollen particles to explore the effect of this on diffusion kinetics. Certainly, the presence of mobile solvated ions appears to influence absorption to a significant degree. Once more, such tests could be performed by employing XLPE samples extracted from power cables, and numerical methods could possibly be implemented to reproduce and thereby probe the underlying physics.

8.4 Enlargement of the research topic

A key motivation for this study is to increase the lifespan of a power cable, without necessarily increasing manufacturing costs. While the results summarized above are encouraging, we are still far from having made sure that a water-trapping material can be implemented safely in a power cable. Alternative research guidelines might prove helpful to start some lateral thinking on topics close to our subject, so that the best possible technological alternative is eventually devised.

8.4.1 Monitored power cables and smart structures

Different strategies could be deployed to intervene prior to the occurrence of electrical breakdown. To do so, real-time monitoring systems based upon optical fibre technology could be embedded within cables. The latter technology offers an array of sensor-based properties, among which special fibres that can react to temperature,

strain or even humidity variations. Such systems could potentially monitor sheath continuity, levels of moisture absorption, temperature variations and mechanical stress levels. The real-time interpretation of data acquired via such monitoring system would, however, prove crucial. Also, technological problems regarding the loss of transmitted signals should first be addressed, whereas the long-term reliability of the sensing system should be probed critically. Thus, difficulties linked to signal attenuation over short distances would have to be considered. Then, the overall reliability of the sensing system addressed in the field of material science; for instance, the response of water-sensing fibres based upon deformation induced by a water-swelling gel-coated interface should be studied under conditions, i.e. ageing, similar to those employed to test our water-trapping systems. Adequate series of tests should be designed to answer these questions in a specific manner.

8.4.2 Irreversible consumption of water molecules

One might propose different alternatives to construct "smarter" power cables, such as those discussed above. Alternatively, instead of devising a water-trapping system, one could design a layer with components that react to the presence of water molecules. The irreversibility of such reactions would, however, need to be addressed as a matter of priority. Alternatively, modifications to the insulation layers may also be proposed, yet, one should consider the direct incidence such changes would generate on material breakdown and dielectric loss characteristics. The implementation of reacting particles such as in core-shell materials could certainly be employed to reduce the detrimental effect of penetrant diffusion, thus reducing the occurrence of water-treeing breakdowns. Again, chemical reactions could consume water molecules, or simply retain them preferentially via polar attraction methods. Obviously, the latter proposal resembles more the idea of blending polar materials with an ethylenic matrix in order to avoid the formation of isolated water clusters. In return, it must be acknowledged that materials modified in this manner will certainly be characterized by lower characteristics than "classical" XLPE compounds.

8.5 Final conclusions

A great deal of work remains to be done to guarantee the reciprocal compatibility of all the different materials enclosed in complex systems. Power cables provide a good

example of a structure presenting a high level of architectural complexity and, in spite of presenting opposite properties, hydrophilic materials are likely to protect hydrophobic systems from water-related hazards.

REFERENCES:

[1] Greenway G.R., PhD Thesis, University of Reading, Department of Physics, 2000.

[2] Gustaffsson B., Bostrom J.O., Dammert R.C. Angew Makromol Chem 1998;261/262(Nr4620):93-9.

[3] Black R.M. The history of electric wires and cables. Peter Peregrinus, 1983.

[4] Ciuprina F., Teissèdre G., Filippini J.C. Polymer 2001;42:7841-6.

[5] Boubakeur A., Mecheri Y., Bouberzou M. Ann Chim Sci Mat 2000;25:457-70.

[6] Mildner R.C., Slaughter R.J. "Cables and other dielectric applications" in: Polyethylene, the technology and uses of ethylene polymers. Interscience publishers, 1957.

[7] Kaminaga K., Ichihara M., Jinno M., Tanabe T., Fukunaga S., Kanaoka M., Takehana H. Electr Eng Jpn 1997;118(1):299-306.

[8] Dissado L.A., Fothergill J.C. Electrical degradation and breakdown in polymers. Peter Peregrinus, 1992.

[9] Shinozaki D.M., Cheng P.C., Haridoss S., Mitchell R., Fenster A. J Mater Sci 1991;26:6151-60.

[10] Ahmed M., Garwan M.A., Al-Ohali M.A., Hamouz Z., Soufi K., Minqin R., Rajta I., Watt F. Nucl Instrum Meth B 2003;210:548-53.

[11] Sutton S.J. - personal communication. NGT House – Warwick Technology Park, Gallows Hill, Warwick, CV34 6DA, UK.

[12] Official Newsletter of Lamar Electric Membership Corporation, May 2003.

[13] Horokhov Y.V., Nazim Y.V. J Wind Eng Ind Aerodyn 2001;89:1409-19.

[14] Ilstad E. Doktor Ingeniør dissertation, University of Trondheim, 1982.

[15] Nikolajevic S.V., Drca R. Electr Pow Syst Res 2001;60:9-15.

[16] Acedo M., Radu I., Frutos F., Filippini J.C., Notingher P. J Electrostat 2001;53:267-94.

[17] Radu I., Notingher P., Filippini J.C. J Electrostat 2000;48:165-78.

[18] Judeinstein P., Carmo Lanca M., Marat Mendes J., Rault J. Polymer 2000;41:8151-4.

[19] Meyer C.T. IEEE T Electr Insul 1983;EI 18(1):28-31.

[20] Nilsson U.H. "Development of water tree resistant XLPE compounds" in: Colloquium on "Recent advances in the understanding of water trees". Institution of Electrical Engineers (IEE), 1992.

[21] Watanabe K., Yagyu H., Sekii Y., Marumo M. IEEE T power deliver 1986;PWRD-1(1):27-33.

[22] Trotignon J-P., Verdu J., Dobraczynski A., Piperaud M. Précis des Matières plastiques. Nathan, 1996.

[23] Mayoux C. Angew Makromol Chem 1998;261/2:143-56.

[24] Bremner T., Rudin A. Polym Eng Sci 1992;32(14):939-43.

[25] Kind D., Karner H. High-voltage insulation technology; textbook for electrical engineers. Vieweg & Sohn, 1985.

[26] Yamazaki T., Seguchi T. J Pol Sci Part A Pol Chem 2000;38:3092-9.

[27] Yamazaki T., Seguchi T. J Pol Sci Part A Pol Chem 1999;37:349-56.

[28] Peacock A.J. Polymer communications 1987;28:259-60.

[29] Kirby A.J. The anomeric effect and related stereoelectronic effects at oxygen. Springer Verlag, 1983.

[30] Bayerlein F. "Technical Applications of galactomannans" in: Plant Polymeric Carbohydrates. Royal Society of Chemistry,1993.

[31] Daas P.J.H., Schols H.A., De Jongh H.H.J. Carbohyd Res 2000;329:609-19.

[32] Daas P.J.H., Grolle K., Van Vliet T., Schols H.A., De Jongh H.H.J. J Agr Food Chem 2002;50:4282-9.

[33] Garti N., Leser M.E. Polym Adv Technol 2001;12:123-35.

[34] Cheng Y., Prud'homme R.K. Biomacromolecules 2000;1:782-8.

[35] Kök M.S., Hill S.E., Mitchell J.R. Food Hydrocolloid 1999;13:535-42.

[36] Wientjes H.W., Duits M.H.G., Jongschaap R.J.J., Mellema J. Macromolecules 2000;33:9594-605.

[37] Simonet F., Garnier C., Doublier J-L. Carbohyd Polym 2002;47:313-21.

[38] Lai L.S., Tung J., Lin P.S. Food Hydrocolloid 2000;14:287-94.

[39] Robinson G., Ross-Murphy S.B., Morris E.R. Carbohyd Res 1982;107:17-32.

[40] Fernandes P.B. J Food Eng 1995;24:269-83.

[41] Vandamme Th.F., Lenourry A., Charrueau C., Chaumeil J-C. Carbohyd Polym 2002;48:219-31.

[42] Huggins M.L. J Phys Chem 1942;46:151-8.

[43] Flory P.J. J Chem Phys 1942;10:51-61.

[44] Saunders B.R., Vincent B. Adv Colloid Interfac 1999;80:1-25.

[45] Fedors R.F. Polymer 1980;21:207-12.

[46] MacCall D.W., Douglass D.C., Blyler L.L.Jr, Johnson G.E., Jelinski L.W., Bair H.E. Macromolecules 1984;17:1644-9.

[47] Jelinski L.W., Dumais J.J., Luongo J.P., Cholli A.L. Macromolecules 1984;17:1650-5.

[48] Barrie J.A. "Water in polymers" in: Diffusion in Polymers. Academic Press, 1968.

[49] Aminabhavi T.M., Thomas R.W., Cassidy P.E. Polym Eng Sci 1984;24(18):1417-20.

[50] Brown G.L. "Clustering of water in polymers" in: Water in Polymers. ACS, 1980.

[51] Murrell J.N., Jenkins A.D. Properties of liquids and solutions, (2nd ed.). Wiley, 1994.

[52] Starkweather H.W.Jr. Macromolecules 1975;8(4):476-9.

[53] Misra A., David D.J., Snelgrove J.A., Matis G. J Appl Polym Sci 1986;31:2387-98.

[54] Ugalde J.M., Alkorta I., Elguero J. Angew Chem Int Ed 2000;39(4):717-20.

[55] Utschick H. Methods of thermal analysis. Applications from inorganic chemistry,organic chemistry, polymer chemistry and technology. Ecomed verlagsgesellschaft AG&co. KG, 1999.

[56] Sinclair I.R. Sensors and transducers, a guide for technicians. BSP professional books, 1988.

[57] Patzelt W.J. Polarized light microscopy, (3rd ed.). Ernst Leitz Wetzlar GmbH, 1985.

[58] Delly J.G. Photography through the microscope, (9th ed.). Eastman Kodak Company, 1988.

[59] Huggins M.L. J Am Chem Soc 1942;64:2716-8.

[60] Kraemer E.O. Ind Eng Chem 1938;30:1200-3.

[61] Paula D.L., Lampman G.M., Kris G.S. Introduction to spectroscopy, (3rd ed.) Brooks/Cole, 2001.

[62] Coleman M.C., Painter P.C. "Infrared Analysis" in: Polymer Characterization Techniques and Their applications to blends. Oxford University Press, 2003.

[63] Bower D.I., Maddams W.F. The vibrational spectroscopy of polymers. Cambridge University Press, 1989.

[64] Krishnan R.S. "Historical Introduction" in: The Raman effect; vol.1, principles. Marcel Dekker, 1971.

[65] Hsu H-W. Separations by centrifugal phenomena, techniques of chemistry, vol.XVI. Wiley,1981.

[66] Hosier I.L., Vaughan A.S., Swingler S.G. J Mater Sci 1997;32:4523-31.

[67] Capaccio G., Golz W., Rose L.J. "The influence of morphology and polymer structure on the water-treeing resistance of crosslinked polyethylene" in: ETG Conf. Proc.16/Long term performance of high voltage insulations. Verlay, 1985.

[68] Raharimalala V., Poggi Y., Filippini J.C. IEEE T Dielect El In 1994;1(6):1094-103.

[69] Yamazaki T., Seguchi T. J Pol Sci Part A Pol Chem 1997;35:279-84.

[70] Yamazaki T., Seguchi T. J Pol Sci Part A Pol Chem 1997;35:2431-9.

[71] Phillips P.J., Vantansever A. Polymer 1989;30(4):710-7.

[72] Phillips P.J., Kao Y.H. Polymer 1986;27(11):1679-86.

[73] Kao Y.H., Phillips P.J. Polymer 1986;27(11):1669-78.

[74] Gohil R.M., Phillips P.J. Polymer 1987;27(11):1687-95.

[75] Gohil R.M., Phillips P.J. Polymer 1987;27(11):1696-704.

[76] Woodward A.E., Sauer J.A. "Dynamic mechanical behaviour of partially crystalline polymers" in: Physical properties of polymers. SCI monograph 5. Soc Chem Ind, 1959.

[77] Sirotkin R.O., Brooks N.W. Polymer 2001;42:9801-8.

[78] Nitta K.H., Tanaka A. Polymer 2001;42:1219-26.

[79] Boyd R.H. Polymer 1985;26:1123-33.

[80] Boyd R.H. Polymer 1985;26:323-47.

[81] Young R.J. "Strength and toughness" in: Comprehensive polymer science. (Volume 2). Pergamon, 1989.

[82] Cowie J.M.G. Polymers: Chemistry and physics of modern materials. Blackie Academic & Professional, 1991.

[83] Danch A., Osoba W., Stelzer F.Eur Pol J 2003;39:2051-8.

[84] Mandelkern L. Crystallization of polymers. Mac-Graw Hill, 1964.

[85] Crank J. and Park G.S. "Methods of measurement" in: Diffusion in Polymers. Academic Press, 1968.

[86] Dautray R., Lions J-L. Mathematical analysis and numerical. Methods for science and technology. Volume 6, Evolution problems II. Springer Verlag, 1993.

[87] Raff R.A.V., Allison J.B. Polyethylene. Interscience publishers, 1956.

[88] Fujita H. "Organic vapors above the glass transition" in: Diffusion in Polymers. Academic Press, 1968.

[89] Iordanskii A.L., Kamaev P.P., Ol'Khov A.A., Wasserman A.M. Desalination 1999;126:139-45.

[90] Devallencourt C., Marais S., Saiter J.M., Labbé M., Métayer M. Pol Testing 2002;21:253-62.

[91] Cheng Y., Brown K.M., Prud'homme R.K. Int J Biol Macromol 2002;31:29-35.

[92] Cheng Y., Brown K.M., Prud'homme R.K. Biomacromolecules 2002;3:456-61.

[93] Tayal A., Khan S.A. Macromolecules 2000;33:9488-93.

[94] Azero E.G., Andrade C.T. Polym Test 2002;21:551-6.

[95] Lai V.M-F., Lii C.-yi, Hung W-L., Lu T-J. Food Chem 2000;68:319-25.

[96] Casas J.A., Mohedano A.F., Garcia-Ochoa F. J Sci Food Agric 2000;80:1722-7.

[97] Beer M.U., Wood P.J., Weisz J. Carbohyd Polym 1999;39:377-80.

[98] Wang Q., Ellis P.R., Ross-Murphy S.B. Carbohyd Polym 2002;49:131-7.

[99] Chen J., Park H., Park K. J Biomed Mater Res 1999;44:53-62.

[100] Van Waser J.R., Lyons J.W., Kim K.Y., Colwell R.E. Viscosity and flow measurement, a laboratory handbook of rheology. (2nd printing). Interscience publishers,1966.

[101] Hall H.T., Fouss R.M. J Am Chem Soc 1951;73:265-9.

[102] Barlow R.J. Statistics, a guide to the use of statistical methods in the physical sciences. Wiley, 1989.

[103] Sudduth R.D. J Appl Polym Sci 1997;66:2319-32.

[104] Taylor J.R. An Introduction to Error Analysis. Oxford University Press, 1982.

[105] Bradley T.D., Mitchell J.R. Carbohyd Polym 1988;9:257-67.

[106] Bradley T.D., Ball A., Harding S.E., Mitchell J.R. Carbohyd Polym 1989;10:205-214.

[107] Hamley I.W. – Introduction to soft matter. Polymers, colloids, amphiphiles and liquid crystals. Wiley, 2000.

[108] Goycoolea F.M., Morris E.R., Gidley M.J. Carbohyd Polym 1995;27:69-71.

[109] Ferguson M.J., Jones G.P. J Sci Food Agric 2000;80:166-70.

[110] Colombani M.P., Ceccarini A., Carmignani A. J Chromatogr A 2002;968:79-88.

[111] Mrozek M.F., Weaver M.J. Anal Chem 2002;74:4069-75.

[112] Bell A.F., Barron L.D., Hecht L. Carbohyd Res 1994;257:11-24.

[113] Proniewicz L.M., Paluskiewicz C., Weselucha-Birczinska A., Baranski A., Dutka D. J Mol Struct 2002;614:345-53.

[114] Proniewicz L.M., Paluskiewicz C., Weselucha-Birczinska A., Majcherchjyk H., Baranski A., Konieczna A. J Mol Struct 2001;596:163-9.

[115] Zhbankov R.G., Firsov S.P., Grinshpan D.D., Baran J., Marchewka M.K., Ratajczak H. J. Mol. Struct. 2003;645:9-16.

[116] Kizil R., Irudayaraj J., Seetharaman K. J Agric Food Chem 2002;50:3912-8.

[117] Shingel K.I. Carbohyd Res 2002;337:1445-51.

[118] Zhbankov R.G., Firsov S.P., Korolik E.V., Petrov P.T., Lapkovki M.P., Tsarenkov V.M., Marchewka M.K., Ratajczak H. J Mol Struct 2000;555:85-96.

[119] Kramarenko E.Y., Khoklov A.R., Yoshikawa K. Macromolecules 1997;30: 3383-8.

[120] Omidian H., Hashemi S.A., Sammes P.G., Meldrum I. Polymer 1998;39(26): 6697-704.

[121] Bottcher C.J.F. Theory of electric polarization. Vol.1, dielectrics in static fields. Elsevier,1973.

[122] Kuhn P.S. Physica A 2002;311:50-8.

[123] Kim S.J., Lee C.K., Lee Y.M., Kim I.Y., Kim S.I. React Funct Polym 2003;55:291-8.

[124] Mitsumata T., Suemitsu Y., Fujii K., Fujii T., Taniguchi T., Koyama K. Polymer 2003;44:7103-111.

[125] Chen J., Shen J. J Appl Pol Sci 2000;75:1331-8.

[126] Liu M.,Guo T. J Appl Pol Sci 2001;82:1515-20.

[127] Wallmersperger T., Kroplin B., Gulch R.W. Mech Mater 2004;36:411-20.

[128] Seidel J., Pinkrah V.T., Mitchell J.C., Chowdhry B.Z., Snowden M.J. Thermochim Acta 2004;414:47-52.

[129] Vasilevskaya V.V., Men'shikova L.V. Polym Gels Netw 1998;6:149-61.

[130] Gong J.P., Komatsu N., Nitta T., Osada Y. J Phys Chem B 1997;101:740-5.

[131] Gallagher T.J. Simple dielectric liquids. Clarendon Press, 1975.

[132] De Gennes P-G. Physica A 1999;271:231-7.

[133] Paolini Y., Ronca G., Feijoo J.L., Da Silva E., Ramirez J., Muller A.J. Macromol Chem Phys 2001;202:1539-47.

[134] Haridoss S., Tobazéon R., Crine J-P. Appl Spectrosc 1988;42(1):186-8.

[135] Sivadjian J., "Permeability of plastics and rubbers to water and water vapour, as measured by the hygrophotographic method" in: Physical properties of polymers – SCI monograph No 5. Soc. Chem. Ind., 1959.

Appendix IV-1

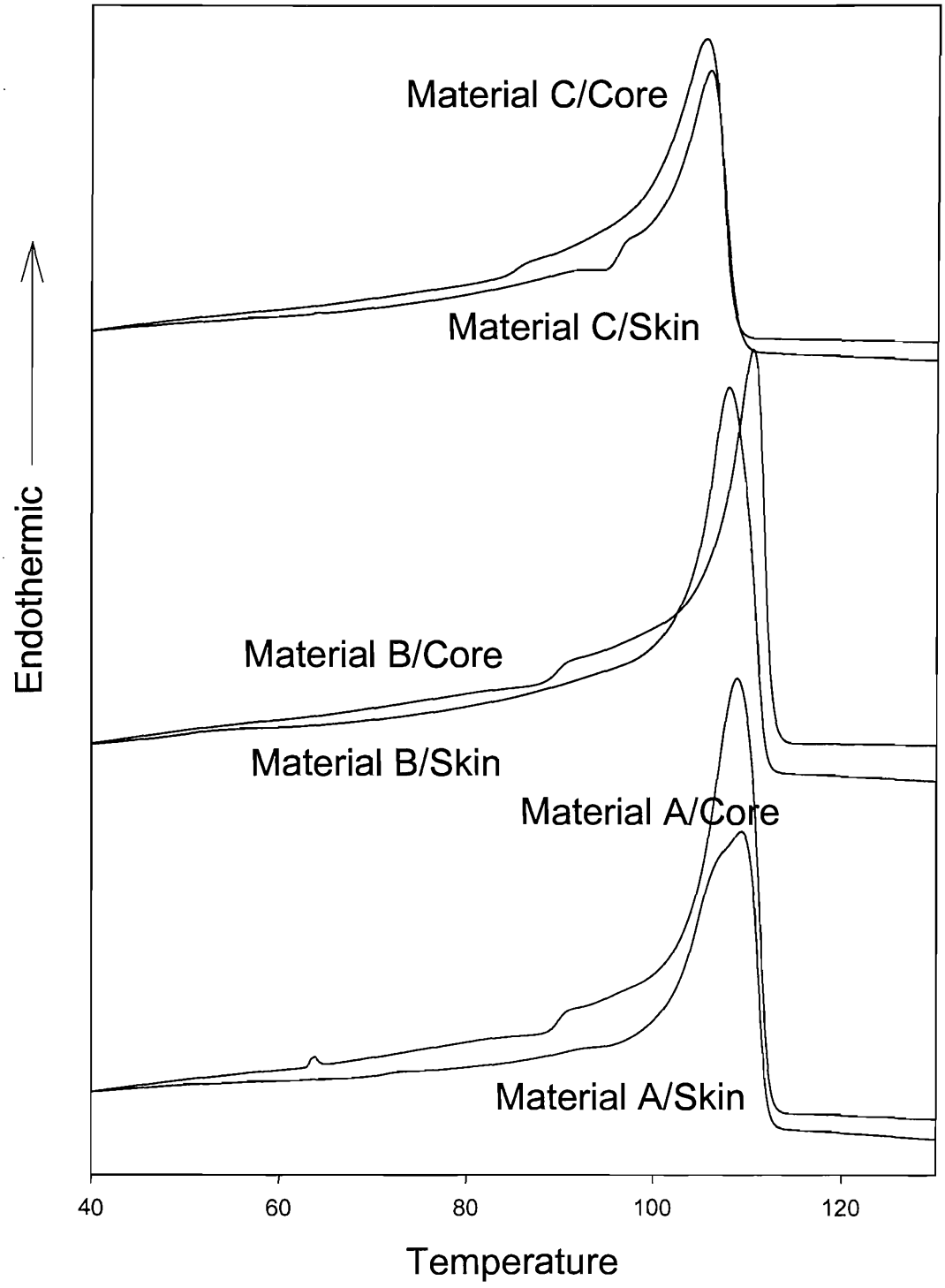

DSC melting traces obtained from the skin and core of millimetre-thick (Mat.A/SQ), (Mat.B/SQ) and (Mat.C/X/SQ) samples similar to those destined to being tested mechanically or during water sorption experiments.

Appendix VII-1

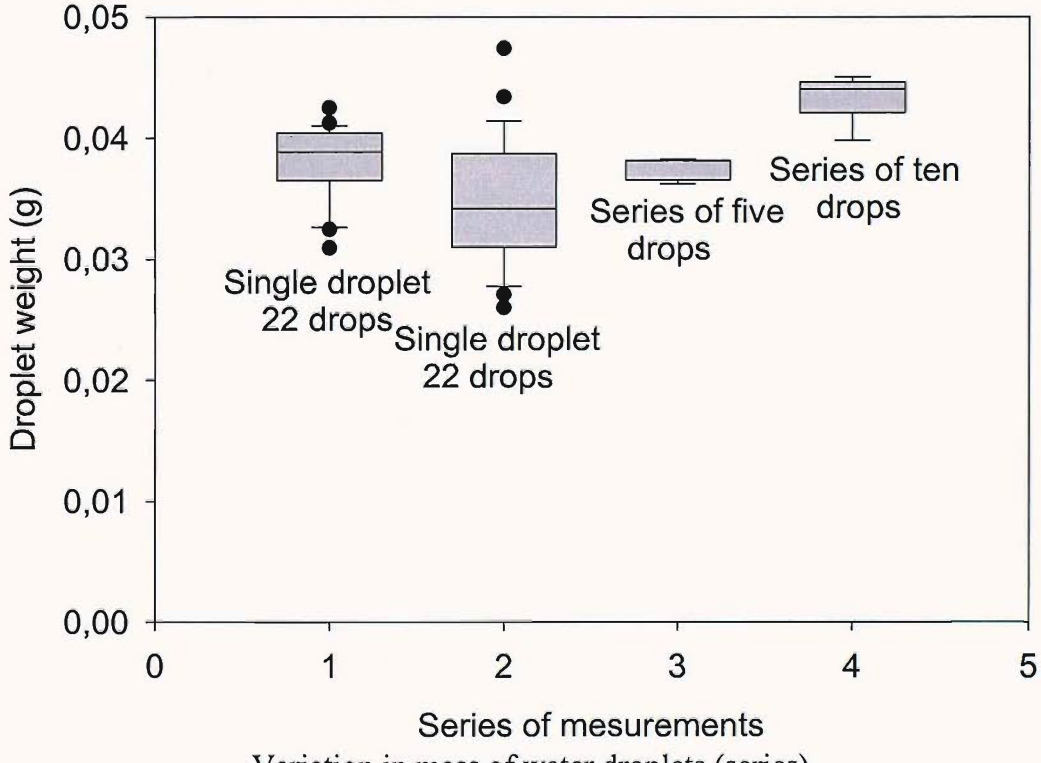

Variation in mass of water droplets (series).